Influences on the location of the Earth's magnetopause

Thesis submitted for the degree of

Doctor of Philosophy

at the University of Leicester

by

Katie M. Raymer

Radio and Space Plasma Physics Group

Department of Physics and Astronomy

University of Leicester

June 2018

Influences on the location of the Earth's magnetopause

Katie M. Raymer

Abstract

The magnetopause is the boundary that separates the Earth's magnetic field from the interplanetary magnetic field (IMF) and largely prevents solar wind plasma from entering the magnetosphere. It shields the Earth from space weather and understanding what affects its location is vital as we become more dependent on ground-, air- and space-based technologies.

To study influences on the location of the magnetopause, an automated magnetopause crossing detection routine is developed which can determine the location of the magnetopause using a combination of plasma and magnetic field data. The technique is applied to almost two solar cycles of data (1996 - 2015) from the Geotail spacecraft, producing a database of over 8000 magnetopause crossings. The crossings are normalised for solar wind dynamic pressure and the magnetopause is modelled with the functional form of the Shue *et al.* [1997, 1998] empirical model.

Solar cycle effects on the shape and location of the magnetopause are investigated and the model is compared to models defined by previous authors. Magnetopause location varies significantly throughout the solar cycle. We find that the model developed in this thesis characterises magnetopause location most accurately during solar minima but is less accurate during the increased solar activity observed in the declining phase of solar cycle 23.

Finally, we compare the model magnetopause predictions with observations for a variety of solar wind and magnetospheric conditions. We find that the direction of the B_Z component of the IMF has a stronger influence on the dayside magnetopause when the solar wind dynamic pressure is weaker. The quantity of open magnetic flux in the magnetosphere orders the dayside magnetopause location. We also examine the effect of the ring current on magnetopause location and results indicate that the dayside magnetopause is eroded and magnetotail is more inflated when the ring current is stronger.

Declarations

I, Katie Raymer, declare that the work presented in this thesis is my own. Information taken from other sources and material which is reproduced has been suitably referenced. The following scientific paper has been submitted for publication:

Raymer, K. M., S. E. Milan, S. M. Imber, M. Lester and T. Nagai (2018), Solar wind and magnetospheric influences on the shape and location of the Earth's magnetopause, *J. Geophys. Res. Space Weather*, under review.

To my family and friends

Acknowledgements

Firstly, I would like to thank my supervisors, Suzie and Steve. Thank you for your guidance and support over the years, for putting up with me panicking about making silly mistakes in my code, for all your wisdom and knowledge on the magnetopause, for encouraging me to (and letting me!) go to so many conferences and workshops all over the world, and for supporting me when I ran away to Parliament for three months. Suzie, you really are an inspiration and I hope that one day, when you are an astronaut, you wave at me from space! Steve, thank you for never taking things too seriously, for all the house white in Babs, and for always being there for me especially whenever Suzie was lost up a mountain.

Working in RSPP has been fantastic. You are a lovely bunch of crossword, cake and Babs loving people, and you really have made my time in Leicester doing my PhD great. A special shout out goes to all my office pals over the years: Gabby, Greg, Sam and Tom of F64a (I guess I'll forgive you for forgetting to water my plants...), and Rosie, Roger and Matt of F59 (I'll never forget that Ganymede is 8% larger than Mercury!). Thank you to all my earthlings in Earth Club for helping me set it up and for its continuation after I have left. Another shout out needs to go to all the inspirational physics ladies in the group: Bea, Jenny, Angeline, Gabby, Rosie, Jasmine, Maria, Katie H, Alexandra, Harneet and Naomi, thank you for all your advice, inspiration and sangria evenings (and for being excellent hair plaiters and bakers!). And thank you to everyone else I haven't mentioned - you all have made the last 3 and a half years unforgettable!

I'd also like to thank all the amazing people I have met at conferences and workshops all over the world. I have made so many friends and have so many fond memories. There are a few I will never forget like singing along to songs from Frozen at the back of a coach with the SuperDARN crew (little did I know that one of them would be my future external examiner...).

A massive thanks to all of my wonderful friends who have helped me more than they'll ever realise, especially Rosie (my BBF and PhD sis), Liz, Tom, Abi and Jess. Thank you all so much for being there for me through the ups and downs. You mean the world to me.

Finally, and most importantly, I want to thank my family. Mum and Dad, Mary and Grandma, thank you so much for your unwavering support throughout my life. I would not be where I am today without you.

Now on to the next chapter...

Contents

List of Figures

List of Tables

Chapter 1

Introduction

This thesis is concerned with the solar wind and magnetospheric influences on the shape and location of the Earth's magnetopause. The magnetopause is the boundary between the terrestrial magnetic field and the magnetosheath, comprising shocked solar wind plasma, and the interplanetary magnetic field. It acts as a barrier which shields the Earth from space weather; the solar activity that affects the near-Earth space environment. Space weather conditions can vary on both short- and long-timescales and can have differing levels of effect. For example, extreme space weather events can produce beautiful brightenings of the auroras at the northern and southern poles, but they can also disrupt ground-, air- and space-based technologies, such as power grids, aviation and satellites. Solar activity also changes over an approximately 11-year period known as the solar cycle. The most recent two solar cycles, with which this thesis is concerned, contained some highly unusual features that have provided a unique opportunity to study the magnetopause. In order to improve our understanding of how space weather impacts the Earth and develop forecasting capabilities, expanding our knowledge on how the magnetopause is affected by different space weather conditions is vital.

In this chapter, the fundamental physics which underpins the behaviour of space plasmas is presented. This provides the framework for understanding how the solar wind, magnetosphere and ionosphere couple, and what causes the location of the magnetopause to vary. In addition, the necessary solar physics and magnetospheric configuration and dynamics are introduced. In Chapter 2, the instrumentation and datasets used in both this thesis and in the previous research carried out in the field, are discussed. A review of the literature

with particular focus on previous methods of identifying the magnetopause location and modelling the magnetopause forms Chapter 3. The work contained in Chapter 4 discusses the methods used to identify the location of the magnetopause in this thesis, as well as the development of a new magnetopause model. Chapters 5, 6 and 7 focus on different physical processes that influence magnetopause location. Finally, conclusions and possible future work are considered in Chapter 8.

1.1 Motion of charged particles in magnetic and electric fields

To describe the dynamics of a plasma, the simplest approach is to consider the motion of each individual charged particle independently; known as the *single particle motion* description. This approach neglects the collective behaviour of the particles, and can only be used when the plasma can be approximated as collisionless, and where charged particle effects on the external magnetic field are negligible [Baumjohann & Treumann, 1997].

The equation of motion for a particle with charge q and mass m, in an electromagnetic field can be obtained by combining Newton's second law, $\mathbf{F} = m\mathbf{a}$, with the Lorentz force, $\mathbf{F} = q(\mathbf{E} + \mathbf{v} \times \mathbf{B})$, to give

$$m\frac{d\mathbf{v}}{dt} = q(\mathbf{E} + \mathbf{v} \times \mathbf{B}) \tag{1.1}$$

where $\mathbf{E}$ is the electric field vector, $\mathbf{B}$ is the magnetic field vector and $\mathbf{v}$ is the particle's velocity vector.

The motion of charged particles is strongly influenced by the electromagnetic field that penetrates the plasma. Maxwell's equations describe the relationship between the particles and the electromagnetic field. In their differential forms, Maxwell's equations are

$$\nabla \cdot \mathbf{E} = \frac{\rho_{\mathrm{q}}}{\varepsilon_0} \qquad \text{Gauss' law for electricity} \tag{1.2}$$

$$\nabla \cdot \mathbf{B} = 0 \qquad \text{Gauss' law for magnetism} \tag{1.3}$$

$$\nabla \times \mathbf{E} = -\frac{\partial \mathbf{B}}{\partial t} \qquad \text{Faraday's law} \tag{1.4}$$

$$\nabla \times \mathbf{B} = \mu_0 \mathbf{j} + \varepsilon_0 \mu_0 \frac{\partial \mathbf{E}}{\partial t} \qquad \text{Ampère-Maxwell law} \tag{1.5}$$

where ρ_q is the charge density, ε_0 is the permittivity of free space in a vacuum (8.854×10^{-12} F m^{-1}), μ_0 is the permeability of free space in a vacuum (1.257×10^{-6} m kg s^{-2}A^{-2}), and **j** is the current density.

The first two equations define the sources of electromagnetic fields. Equation 1.2 is known as Gauss' law for electricity and shows that the source of the electric field is related to the electric space charge density, ρ_q, which is the difference between the charge densities of electrons and ions. The second equation, equation 1.3, is known as the "no monopoles" law or Gauss' law for magnetism. It indicates that there are no sources or sinks of magnetic field and therefore magnetic field lines always close.

The next two expressions show that electric and magnetic fields are not independent, but are coupled by their spatial and temporal variations. Faraday's law is given in equation 1.4 and it describes the electric field that is induced in the presence of a time-varying magnetic field. Finally, the Ampère-Maxwell relation is defined in equation 1.5 and it relates a current system, **j**, to the magnetic field. The first term on the right-hand side of the Ampère-Maxwell, $\mu_0\mathbf{j}$, where **j** is the conduction current, describes the magnetic field circling the current flow. When the electric field varies slowly with time, which is a good approximation for most space plasma phenomena, the second term, $\varepsilon_0\mu_0\frac{\partial \mathbf{E}}{\partial t}$, which describes the displacement current, can be neglected giving $\nabla \times \mathbf{B} = \mu_0\mathbf{j}$, forming Ampère's law.

In the following sections, the implications of the equation of motion (equation 1.1) under different magnetic and electric field conditions will be discussed.

1.1.1 Gyromotion

In the absence of an electric field ($\mathbf{E} = 0$), assuming that the magnetic field is uniform and steady along the Z-direction ($\mathbf{B} = B\hat{\mathbf{z}}$), and the velocity **v** has three components (v_x, v_y, v_z), equation 1.1 can be expressed in each of its Cartesian components as follows

$$\frac{dv_x}{dt} = \frac{qB}{m}v_y \tag{1.6a}$$

$$\frac{dv_y}{dt} = -\frac{qB}{m}v_x \tag{1.6b}$$

$$\frac{dv_z}{dt} = 0 \tag{1.6c}$$

Differentiating equation 1.6a and substituting equation 1.6b yields

$$\frac{d^2v_x}{dt^2} = \left(\frac{qB}{m}\right)\frac{dv_y}{dt} = -\left(\frac{qB}{m}\right)^2 v_x$$
$$\frac{d^2v_x}{dt^2} + \left(\frac{qB}{m}\right)^2 v_x = 0 \tag{1.7}$$

which is the equation for simple harmonic motion, with gyrofrequency, ω_g,

$$\omega_g = \frac{qB}{m} \tag{1.8}$$

A similar equation for v_y can be found by performing a similar differentiation and substitution.

The particles therefore gyrate around a field line, with a gyrofrequency, ω_g. The direction of gyration depends on the particle's charge. In the configuration shown in Figure 1.1a. where magnetic fields are directed out of the page, the positively charged particle gyrates clockwise and the negatively charged particle gyrates anti-clockwise. This forms current loops which produce a magnetic field which opposes that of the background field, $\mathbf{B}$. They gyrate with a gyroradius, r_g,

$$r_g = \frac{v_\perp}{|\omega_g|} = \frac{mv_\perp}{|q|B} \tag{1.9}$$

where $v_\perp = \sqrt{v_x^2 + v_y^2}$ is the velocity perpendicular to $\mathbf{B}$. It can further be shown that when $\mathbf{E} = 0$ and the magnetic field is steady, the velocity of the particle remains constant. From the equation of motion given by equation 1.1

$$m\frac{d\mathbf{v}}{dt} = q(\mathbf{v} \times \mathbf{B}) \tag{1.10}$$

Taking the dot product with $\mathbf{v}$ on both sides yields

$$\begin{aligned} m\mathbf{v} \cdot \frac{d\mathbf{v}}{dt} &= m\frac{d}{dt}\left(\frac{1}{2}\mathbf{v}\cdot\mathbf{v}\right) \\ &= \frac{d}{dt}\left(\frac{1}{2}mv^2\right) \\ &= q\mathbf{v}\cdot(\mathbf{v}\times\mathbf{B}) \end{aligned} \tag{1.11}$$

$$\text{where } \mathbf{v}\cdot(\mathbf{v}\times\mathbf{B}) = 0$$
$$\Rightarrow \frac{d}{dt}\left(\frac{1}{2}mv^2\right) = 0$$

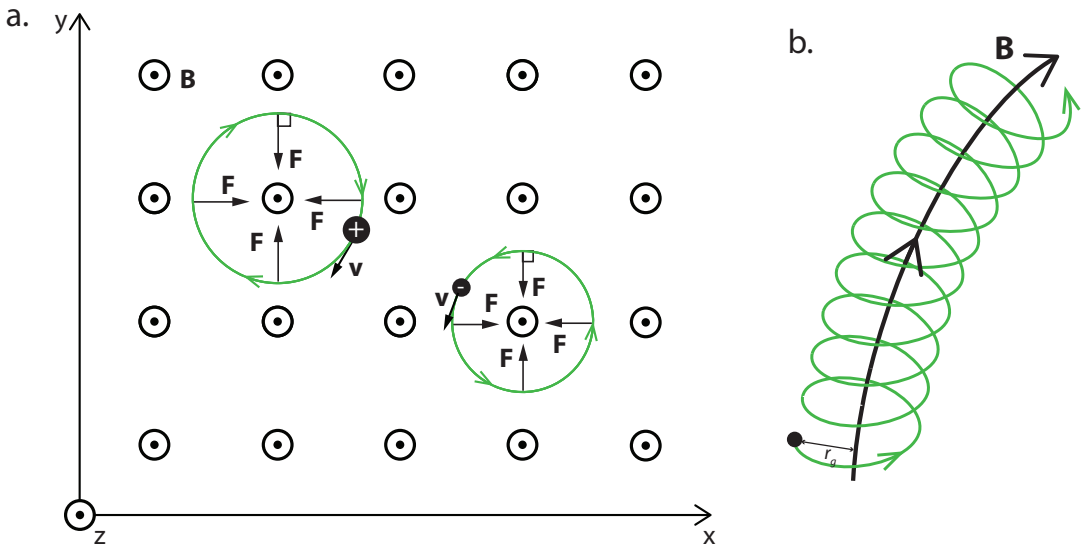

Figure 1.1: a. Sketch of the motion of positively and negatively charged particles in a steady uniform magnetic field, $\mathbf{B}$, with no electric field. The direction of the force the particles feel is shown by the arrowed lines labelled $\mathbf{F}$ and the trajectory is shown by the green arrowed line. b. Sketch of a particle's gyromotion along a magnetic field line. The particle's trajectory is shown by the green arrowed line.

This shows that the kinetic energy of the particle does not change with time, implying that

$$v = \sqrt{v_{\perp}^2 + v_{\parallel}^2} = \text{constant} \tag{1.12}$$

where $v_{\perp}$ is the component of $\mathbf{v}$ perpendicular to $\mathbf{B}$ and $v_{\parallel}$ is parallel to $\mathbf{B}$.

The centre of the orbit is described as the *guiding centre*. When there is a parallel component to the velocity, the particle will travel along the field line in a helical trajectory, as shown in Figure 1.1b. Another way to represent particle motion is to define the *pitch angle*, α, which describes the angle that the particle's velocity vector makes to the magnetic field line or guiding centre

$$\alpha = \tan^{-1}\left(\frac{v_{\perp}}{v_{\parallel}}\right) \tag{1.13}$$

When α is $0°$, the particle travels along $\mathbf{B}$, and when it is $90°$, its trajectory is circular.

1.1.2 Magnetic mirroring

In this section, we will consider the scenario where a charged particle is moving into a region of increasing magnetic field strength, that is a converging magnetic field. This configuration is shown in Figure 1.2. In this diagram, the gradients in $\mathbf{B}$ and $v_{\parallel}$ are along the z-axis. The Lorentz force ($q\mathbf{v} \times \mathbf{B}$), labelled $\mathbf{F}$ in the diagram, is perpendicular to the magnetic field, $\mathbf{B}$, so has a component pointing away from the direction of increasing field. This component causes $v_{\parallel}$ to reduce as the particle moves into a stronger magnetic field, but as equation 1.12 must remain true, $v_{\perp}$ must increase. Eventually, $v_{\parallel}$ decreases until there is no parallel motion along the field and the direction of the particle's trajectory reverses. This type of motion is known as *magnetic mirroring*, or bounce motion.

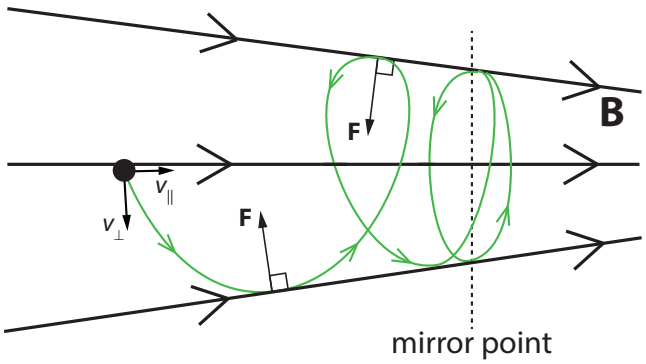

Figure 1.2: Sketch showing the trajectory of a charged particle in a converging magnetic field.

The point along the field where the particle is mirrored, B_m, can be deduced using a quantity known as the *first adiabatic invariant*. The first adiabatic invariant is as follows

$$\frac{v_{\perp}^2}{B} = \text{constant} = \frac{v_{\perp 0}^2}{B_0} \tag{1.14}$$

where $v_{\perp 0}^2$ and B_0 are measured at some specified initial point. Both the particle velocity and the first adiabatic invariant are conserved. Combining equations 1.14 and 1.12 yields

$$\begin{aligned} v_{\parallel}^2 &= v^2 - v_{\perp}^2 \\ &= v^2 - v_{\perp 0}^2 \left(\frac{B}{B_0}\right) \end{aligned} \tag{1.15}$$

The particle will mirror at B_m where the parallel velocity decreases to 0,

$$v^2 = v_{\perp 0}^2 \left(\frac{B_m}{B_0}\right)$$
$$\Rightarrow B_m = B_0 \left(\frac{v}{v_{\perp 0}}\right)^2 \tag{1.16}$$

The mirror point can also be described using the pitch angle, α, which was defined in equation 1.13. The first adiabatic invariant becomes

$$\frac{v_\perp^2}{B} = \frac{v^2 \sin^2 \alpha}{B} = \text{ constant}$$

or, as v is constant,

$$\frac{\sin^2 \alpha}{B} = \text{ constant} \tag{1.17}$$

As the particle approaches the mirror point, $\alpha \rightarrow 90^\circ$ as v is constant. The constant in equation 1.17 becomes

$$\frac{\sin^2 \alpha}{B} = \frac{\sin^2 \alpha_m}{B_m} = \frac{1}{B_m} \tag{1.18}$$

which can be rearranged to give the field strength at the mirror point,

$$B_m = \frac{B}{\sin^2 \alpha} \tag{1.19}$$

Equation 1.19 implies that the mirror point of a particle does not depend on the type of particle, i.e. its mass or charge, or on its velocity, but it only depends on the pitch angle, the angle at which the velocity vector makes to the guiding centre.

1.1.3 $\mathbf{E} \parallel \mathbf{B}$

When there is no electric field, the velocity of a charged particle along a magnetic field line is constant (as shown by equation 1.12). When an electric field is introduced, this is no longer necessarily true. Similar to the previous sections, we assume $\mathbf{B} = B\hat{z}$, and introduce $\mathbf{E} = E_\parallel \hat{z}$. A parallel electric field occurs when there is a charge separation along the magnetic field direction. The velocity along the field, equation 1.6c becomes

$$\frac{dv_z}{dt} = \frac{q}{m} E_\parallel \tag{1.20}$$

which becomes on integration

$$v_z = v_{z0} + \frac{qE_\parallel}{m} t \tag{1.21}$$

The dependence of v_z on q means that positively charged particles accelerate in the direction of $\mathbf{E}$, and negatively charged particles accelerate in the opposite direction. Eventually the charge separation is reduced and $E_{\|}$ becomes zero. Generally, in this thesis we are interested in space plasmas where $E_{\|} = 0$.

1.1.4 $\mathbf{E} \times \mathbf{B}$ drift

If the electric field is perpendicular to the magnetic field, such that $\mathbf{E} = E_{\perp}\hat{y}$ (as shown in Figure 1.3), then a particle initially at rest will be accelerated due to the electric field in the y direction. As the velocity of the particle begins to increase, the particle starts to gyrate due to the Lorentz force, $q\mathbf{v} \times \mathbf{B}$ (the second part of equation 1.1). As the Lorentz force on the particle begins to increase, the particle is accelerated in the x direction causing it to turn. The turning continues until $v_y = 0$ and when the Lorentz force is opposite to and larger than the $q\mathbf{E}$ term of equation 1.1. After this point, the particle continues to turn whilst moving against $\mathbf{E}$, decelerating, until it comes to a rest. The motion then repeats itself, and the particle drifts in the positive x direction. The resultant flow of the particles has an average *drift velocity*

$$\mathbf{v}_E = \frac{\mathbf{E} \times \mathbf{B}}{B^2} \tag{1.22}$$

The average drift velocity does not depend on charge, mass or initial conditions.

In the frame of reference moving with the particle drift, the particles would appear to gyrate in circles, like the motion described in section 1.1.1. In this frame, the particles experience $\mathbf{B}$ as before, but feel no effect from the electric field. There is no perpendicular electric field in this frame. Therefore, the electric field is dependent on the frame of reference the particles are observed in. When a plasma drift is observed, $\mathbf{v}$, in that frame of reference there will also be an observed electric field, such that

$$\mathbf{E} = -\mathbf{v} \times \mathbf{B}. \tag{1.23}$$

1.1.5 Gradient and curvature drifts

In the terrestrial magnetospheric physics, it is often unrealistic to consider a homogeneous magnetic field. Usually the magnetic fields we are interested in have gradients and often they are curved. In section 1.1.2 it was shown that particles mirror when there is a gradient

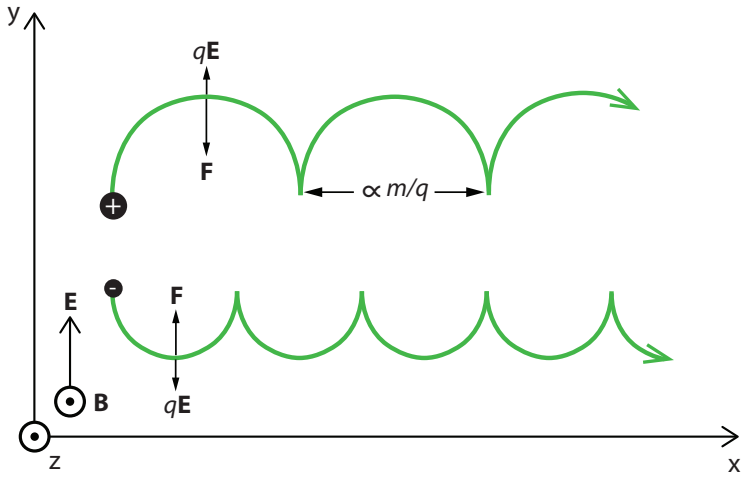

Figure 1.3: Sketch showing the trajectory of positively and negatively charged particles in a uniform magnetic field with a uniform perpendicular electric field. The particles exhibit $\mathbf{E} \times \mathbf{B}$ drift.

in the magnetic field strength parallel to $\mathbf{B}$. In this section, we will consider what happens to the particles when the gradient in the magnetic field is perpendicular to $\mathbf{B}$.

Figure 1.4a. shows the configuration of the system. As the particles gyrate, they will experience differing magnetic field strengths. As the particles move into regions of higher magnetic field strength, their gyroradius (equation 1.9) will decrease, and as they move into regions of lower magnetic field strength, their gyroradius will increase. The change in gyroradii causes the guiding centre to shift in a direction perpendicular to both $\mathbf{B}$ and ∇B, resulting in the positive and negative charges drifting in opposite directions. This drift is known as *gradient-B drift*. The gradient-B drift velocity is given by

$$\mathbf{v}_{\nabla \mathbf{B}} = \frac{m v_\perp^2}{2qB^3}(\mathbf{B} \times \nabla B) = \frac{W_\perp}{qB^3}(\mathbf{B} \times \nabla B) \tag{1.24}$$

where $W_\perp = \frac{1}{2} m v_\perp^2$ is the perpendicular kinetic energy. Equation 1.24 shows that the ions and electrons drift in opposite directions, and that the gradient drift velocity is proportional to the perpendicular kinetic energy. Particles that have higher kinetic energies will drift faster as they will have a larger gyroradius and will experience larger inhomogeneity in the magnetic field.

When the magnetic field lines are curved, that is the field direction changes along $\mathbf{B}$, the particles will experience *curvature drift*. Under these conditions, the gyrating particles expe-

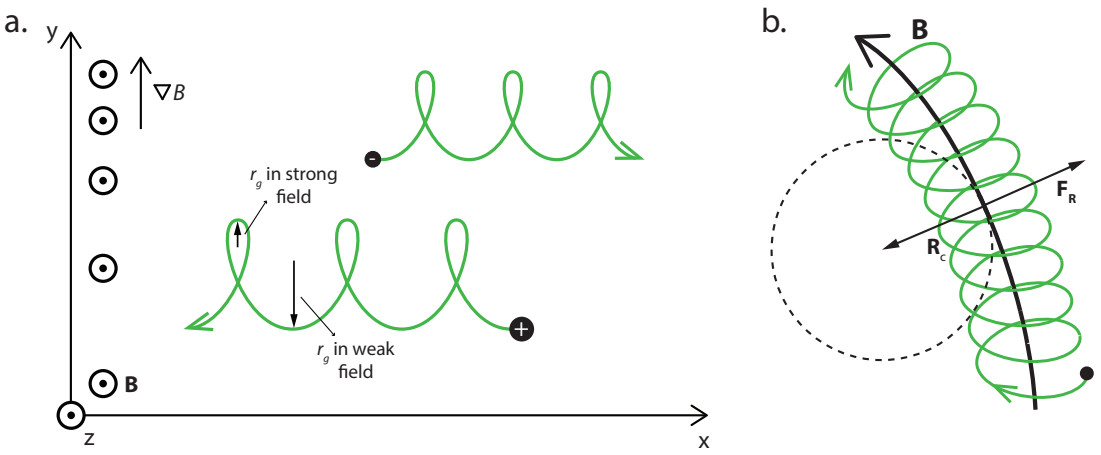

Figure 1.4: a. Sketch showing the motion of positively and negatively charged particles experiencing gradient-B drift. b. The centrifugal force felt by a particle moving along a curved field line.

rience a centrifugal acceleration directed away from the centre of the field line curvature (see Figure 1.4b.). Similar to the gradient-B drift, the gyroradius of the particles increases as the particle moves away from the curvature of the field, which causes the particles to drift perpendicular to the field and the radius of curvature with a drift velocity given by

$$\mathbf{v_{curv}} = \frac{mv_{\parallel}^2}{q}\frac{\mathbf{R}_c \times \mathbf{B}}{R_c^2 B^2} = \frac{2W_{\parallel}}{q}\frac{\mathbf{R}_c \times \mathbf{B}}{R_c^2 B^2} \tag{1.25}$$

where $\mathbf{R}_c$ is the local radius of curvature of the field lines. The curvature drift is proportional to the parallel particle energy, $W_{\parallel}$, and perpendicular to the magnetic field and its curvature. Therefore, there is a flow in the $\mathbf{R_C} \times \mathbf{B}$ direction.

In a dipolar, or approximately dipolar field like that of Earth, particles will undergo both gradient and curvature drifts. In the Earth's magnetosphere, these drifts are in the same direction and so they can be considered as one gradient-curvature drift or total magnetic drift.

1.1.6 Drifts in the Earth's magnetosphere

The Earth's magnetic field is approximately dipolar inside of about 6 R_E (Earth radii), which means the total field strength is lowest at the equator and the field lines converge in both the northern and southern hemispheres. Under this configuration, the particles gyrate along the

magnetic field lines as shown in Figure 1.5a. As the field converges in both hemispheres, they will bounce back and forth between their mirror points and are said to be trapped. These trapped energetic particles form the *radiation belts*, or the *Van Allen belts* [Baumjohann & Treumann, 1997]. However, particles can escape. Particles with small equatorial pitch angles will mirror closer to the Earth. If the mirror point lies within the Earth's atmosphere, they will collide with neutral particles and will be absorbed by the atmosphere. If these particles are energetic enough, this collision will produce an *aurora*. The particles that are lost from the trapping region are described as being within the *loss cone*.

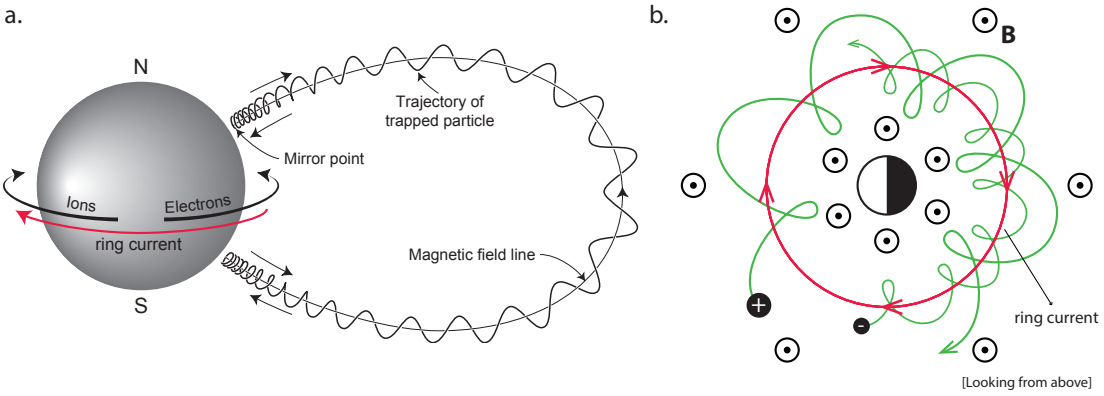

Figure 1.5: a. Sketch showing the motion of ions and electrons trapped on closed field lines in the Earth's magnetosphere. Adapted from Baumjohann & Treumann [1997]. b. Ion and electron drifts which create the ring current.

As well as gyrating and bouncing, the particles undergo a slow azimuthal drift as a result of the gradient-curvature drift which dominates in the Earth's dipole magnetic field. Positively and negatively charged particles drift oppositely as can be seen in Figure 1.5b. At the Earth, ions drift westward while the electrons drift eastward, resulting in a westward current known as the *ring current* (indicated by the red arrowed line in the Figure 1.5a. and b.).

1.2 Magnetohydrodynamics

Another technique used to describe the dynamics of a plasma is to consider the bulk motion of the plasma. This approach is known as *magnetohydrodynamics*, or MHD. It neglects all

single particle aspects and treats the plasma as a single conducting fluid with macroscopic variables such as average velocity, temperature and density.

1.2.1 Equations of motion

In a one-fluid MHD approximation, it is assumed that the plasma consists of two species of particles, electrons and ions (where subscripts *e* and *i* will be used to denote each species respectively). In a quasi-neutral plasma, the fluid number density, *n*, fluid mass, *m*, fluid velocity, $\mathbf{V}$, and mass density, ρ are given by

$$n = n_e = n_i \tag{1.26}$$

$$m = m_e + m_i \approx m_i \tag{1.27}$$

$$\mathbf{V} = \frac{m_i n_i \mathbf{v}_i + m_e n_e \mathbf{v}_e}{m_e n_e + m_i n_i} \approx \mathbf{v}_i \tag{1.28}$$

$$\rho = n_e m_e + n_i m_i \tag{1.29}$$

where it can be assumed that the electron mass, m_e is negligible in comparison to the ion mass. Electron fluid velocity can be neglected in the one-fluid MHD approach because the ion mass is much larger than the electron mass, and so the ions are the dominant species.

The *continuity equation* is then given by

$$\frac{\partial \rho}{\partial t} + \nabla \cdot (\rho \mathbf{V}) = 0 \tag{1.30}$$

This is the continuity equation for the total fluid and it does not discriminate between particle species. It shows that in a classical and non-relativistic plasma, mass is conserved.

If we consider Newton's second law, the momentum equation can be derived. The forces acting on the particles are made up of both internal and external forces. The internal electrostatic forces cancel due to Newton's third law, and so we are left with only the external forces to consider. The forces that need to be considered are gravity, pressure of the surrounding medium, and electromagnetic forces. Combining these forces gives the *general equation of motion*

$$\rho \frac{d\mathbf{V}}{dt} = \rho \mathbf{g} - \nabla P + \rho_q \mathbf{E} + \mathbf{j} \times \mathbf{B} \tag{1.31}$$

where P is the pressure ($P = P_i + P_e$), ρ_q is the charge density (departure from quasi-neutrality), and $\mathbf{j}$ is the current density. This gives the rate of change of the centre of mass velocity of a plasma element.

This equation can be simplified by showing that some of the terms are negligible when compared to others. For example, the electric force term, $\rho_q \mathbf{E}$, is negligible in comparison to the magnetic force term, $\mathbf{j} \times \mathbf{B}$, for non-relativistic situations.

1.2.2 Ohm's law

The *generalised Ohm's law* of a plasma describes the evolution of current density, $\mathbf{j}$, in an electromagnetic field. It can be determined from the manipulation of the continuity equation (equation 1.30) and the equation of motion (equation 1.31). For space plasmas, Ohm's law can be simplified to

$$\mathbf{j} = \sigma(\mathbf{E} + \mathbf{v} \times \mathbf{B}) \tag{1.32}$$

where σ is the plasma conductivity, given by

$$\sigma = \frac{n_e e^2}{m_e \nu_c} \tag{1.33}$$

where ν_c is the collision frequency between ions and electrons. In an ideal MHD plasma, there are no collisions, so as $\sigma \to \infty$, equation 1.32 becomes

$$\mathbf{E} = -\mathbf{v} \times \mathbf{B} \tag{1.34}$$

1.2.3 Frozen-in flow approximation

An important consequence of Ohm's law is the *induction equation* which describes the changes in magnetic field. The induction equation can be determined from rearranging Ohm's law (equation 1.32) for the electric field, taking the curl of both sides and substituting Faraday's law (equation 1.4) to give

$$\frac{\partial \mathbf{B}}{\partial t} = \nabla \times (\mathbf{v} \times \mathbf{B}) + \frac{1}{\mu_0 \sigma} \nabla^2 \mathbf{B} \tag{1.35}$$

where the first term on the right-hand side is the convective term and the second is the diffusive term.

When the magnetic field varies slowly with respect to the particles' gyroradii and gyroperiods, the diffusion term becomes negligible and the plasma is dominated by convection. In this scenario, the motions of the plasma are tied to the magnetic field lines and vice versa. This is known as the *frozen-in flow approximation* or Alfvén's theorem [Alfvén, 1943]. When

the frozen-in flow approximation applies, plasmas from different sources cannot mix and different magnetic field lines stay separated, making it possible to identify a field line by the plasma that is frozen to it. The identifiable field lines are known as a *flux tube*, which is essentially a theoretical cylinder which contains a constant amount of magnetic flux.

1.2.4 Magnetic reconnection

The frozen-in flow approximation breaks down when the diffusive term in equation 1.35 dominates. In this scenario, the magnetic field is no longer frozen into the plasma and may slip or diffuse across the plasma, allowing field lines to *reconnect*. The consequences of this are greatest at the boundary between two magnetic fields which are oppositely directed as shown in Figure 1.6. Such a topology exists around thin current sheets like the magnetopause and the current sheet in the magnetotail (both of which will be discussed in greater detail in section 1.4). Figure 1.6 shows the magnetic reconnection configuration which occurs at the dayside magnetopause.

Reconnection is driven by the inflow of plasma (blue arrows in the figure). The diffusion of field lines through the plasma allow them to reconnect (indicated by the pink cross). This results in an X-type configuration. There is high magnetic tension in the newly connected field lines and as the diffusion term acts to smooth out gradients in the field, there is an outflow of plasma in the form of jets (indicated by the green arrows). The newly connected field lines contain a mix of plasma from both sides of the current sheet. As the gradients in the magnetic field become less sharp, the diffusion term of the induction equation decreases. To balance the system, more plasma moves into the diffusion region and reconnection continues.

1.3 The Sun and the solar wind

As well as emitting electromagnetic radiation which bathes the Earth with heat and light, the Sun also emits the *solar wind*. The solar wind is a continuous stream of high-speed particles which blows out from the solar corona into interplanetary space filling the entire solar system, carving out a region surrounding the Sun called the *heliosphere*. The Sun has a magnetic field which is, to a first approximation, a dipolar during solar minimum. The

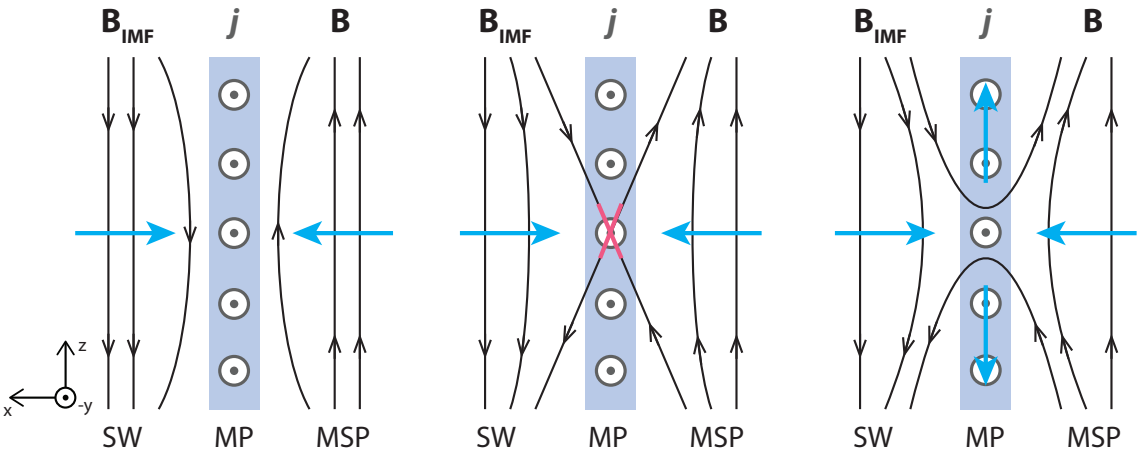

Figure 1.6: Diagrams illustrating magnetic reconnection at the dayside magnetopause. The Sun's magnetic field, $\mathbf{B_{IMF}}$, embedded in the solar wind (SW) is oppositely directed to the magnetospheric (MSP) magnetic field, B. The two magnetic fields with their frozen-in plasma are separated by the magnetopause (MP) current sheet (grey). Blue arrows show the motion of the magnetic field lines and frozen-in plasma, and the pink cross shows the location of the reconnection site.

solar wind and the Sun's magnetic field are frozen-in (as discussed in section 1.2.3), which enables the Sun's magnetic field to permeate the entire heliosphere. This is known as the *interplanetary magnetic field* (IMF). In this section, the origins and structure of the solar wind and IMF will be briefly discussed.

Similar to winds found on Earth, the solar wind is driven by a difference in pressure, but this difference is between the Sun's upper atmosphere and interplanetary space [Moldwin, 2008]. The solar corona is a hot and high density region of the Sun's upper atmosphere, and it provides the energy needed for the plasma to escape the Sun's atmosphere. However, the plasma cannot escape at all latitudes. At the equator, the Sun's magnetic field is closed with both footprints on the Sun. This closed region of field lines contains hot, high-density coronal plasma which is trapped. At the poles, the Sun's dipole is more radial as the field lines are stretched out into interplanetary space. In these regions, known as coronal holes, the solar wind is able to escape the solar corona. The plasma found in these high-latitude coronal holes is much cooler and more tenuous, and it is the main source of solar wind

outflow.

As shown in section 1.2.3, the motions of the plasma are tied to the magnetic field lines and vice versa. At the Sun, the energy density of the IMF is low in comparison to that of the outflowing solar wind, so the solar wind carries the IMF with it. If there was no solar wind outflow, the Sun's magnetic field would be approximately dipolar. The flow of solar wind however, distorts the field and stretches out the field lines radially. After some time, each field line points radially inwards or outwards as seen in Figure 1.7a. Oppositely directed field lines at the equator will create an azimuthal current sheet separating them (as described by Ampère's Law, equation 1.5).

It is also necessary to consider the rotation of the Sun when determining the topology of the IMF, since the footprint of each magnetic field line is frozen to the Sun's surface. The Sun has a rotation period of approximately 27 days. As the Sun rotates, the point where an element of solar wind plasma leaves the surface moves anti-clockwise when viewing from above the Sun (see Figure 1.7b.). As the plasma and magnetic field are frozen-in, the field lines are bent into a spiral as the plasma element moves further away from the Sun with respect to the original point where the plasma left the surface. The spiral pattern produced is known as an Archimedean spiral, or the *Parker Spiral* [Parker, 1958] (see Figure 1.7c.).

At 1 AU, where the Earth orbits the Sun, the Parker spiral impacts the Earth at approximately 45° to the Sun-Earth line, from the late morning direction. As indicated in Figure 1.7c., the direction of the IMF is divided into sectors (red dashed lines) according to solar and anti-solar directions [Baumjohann & Treumann, 1997]. The sectors are separated by current sheets. The current sheet is tilted with respect to the ecliptic plane at the sector boundaries, but far above and below the ecliptic plane it turns into horizontal direction, analogous to a ballerina skirt. The Earth orbits the Sun with an azimuthal velocity of approximately 30 km s^{-1}. This means the solar wind impacts the Earth's magnetosphere with an aberration of around 5° from the radial direction, sometimes known as the *windsock effect*. When the solar wind velocity is higher, this angle decreases. When the solar wind reaches the Earth, it typically has a velocity of 450 km s^{-1}, electron density and temperature of 5 cm^{-3} and 10^5 K, and the IMF is of the order 5 nT [Baumjohann & Treumann, 1997].

The solar wind is not steady or uniform but is highly variable both on short and long timescales. In the next two sections, space weather and its impact on the terrestrial system

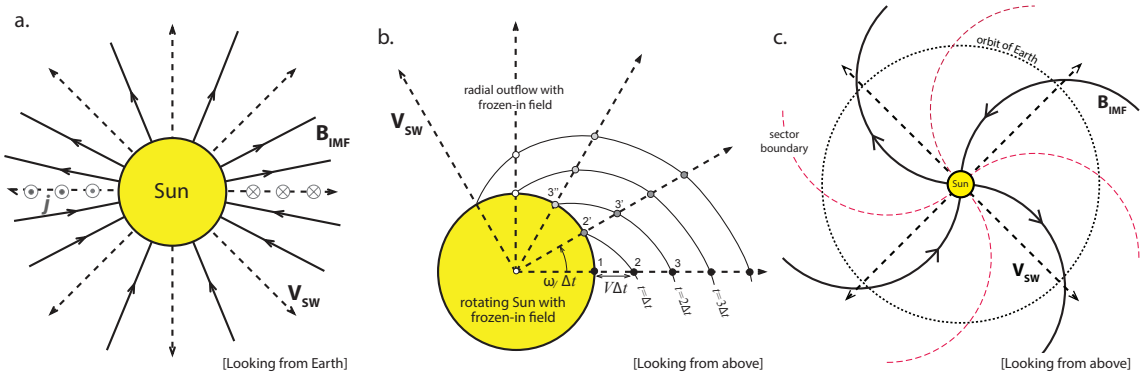

Figure 1.7: a. A diagram of the radial component of the interplanetary magnetic field (IMF) with an azimuthal current sheet separating the oppositely directed fields. b. A diagram of the azimuthal component of the IMF. The numbers indicate how an element of plasma flows out from the Sun over time *t*. c. Parker Spiral structure of the IMF [Baumjohann & Treumann, 1997].

will be discussed, followed by the solar cycle.

1.3.1 Space weather

Space weather refers to the solar activity that affects the near-Earth space environment. There are numerous different types of space weather phenomena that can impact and cause havoc in the near-Earth space environment, including solar flares, energetic particles or cosmic rays, coronal mass ejections and corotating interaction regions. Solar flares are highly-energetic ejections of particles and electromagnetic radiation including X-rays, which can cause communication issues on Earth, or in the most extreme scenarios, can cause radio blackouts [e.g. Moldwin, 2008; Eastwood *et al.*, 2017]. Cosmic rays consist of energetic particles. When high-energy cosmic rays hit the near-Earth space environment they can cause damage to satellites and are very dangerous for astronauts. The phenomena that directly impact the Earth's magnetopause, of which we are concerned with in this thesis, will be briefly introduced here.

Coronal mass ejections (CMEs) are responsible for the most extreme space weather effects at the Earth [Webb & Howard, 2012]. An observation of a CME is shown in Figure 1.8a. They form when the Sun's magnetic field reconfigures causing a large portion of the solar

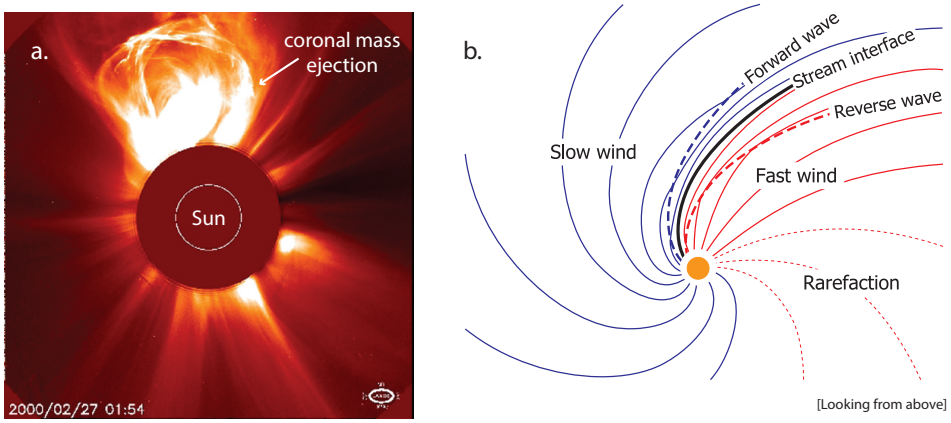

Figure 1.8: a. A coronal mass ejection as observed by the SOHO satellite. [Image credit: SOHO ESA and NASA]. b. A sketch of a corotating interaction region from Owens & Forsyth [2013].

corona containing magnetic field and plasma, to blast away into the heliosphere [Moldwin, 2008; Webb & Howard, 2012]. As a CME travels through the solar system, its magnetic field expands, which commonly has the form of a helical magnetic structure known as a flux rope. CMEs often have a shock and a high-density pile up of plasma in front of them due to slower solar wind plasma being "swept up". Fast CMEs can cause a phenomenon at Earth known as geomagnetic storms (which will be discussed in detail in Chapter 3).

Another type of space weather event that can have damaging effects at the Earth is known as a *corotating interaction region* (CIR). CIRs occur when fast solar wind (red) catches up with slow solar wind (blue) ahead of it, and a spiral-shaped stream interface (black line) forms as seen in Figure 1.8b. [Owens & Forsyth, 2013]. When the solar wind is quasi-steady, the stream interface region will corotate with the Sun.

1.3.2 Solar cycle

The polarity of the Sun's magnetic field reverses every 11 years and this cyclic behaviour is known as the *solar cycle*. The solar cycle is characterised by the waxing and waning of the number of sunspots on the solar surface, regions or patches of strong magnetic field that appear darker on the surface of the Sun as they are cooler than the surrounding surface [Moldwin, 2008]. The magnetic field strength in a sunspot is sufficiently strong to choke

the convective heat flow, which leaves it cooler than its surroundings [Hathaway, 2015]. Solar activity and variability also change over the solar cycle. The most active and energetic interval is described as *solar maximum*, whilst the period of lowest activity is called *solar minimum*. By convention, solar cycles end and begin at solar minimum.

Sunspots can be seen with the naked eye during hazy skies, or by using a telescope. This has allowed for centuries of observations of sunspots. In 1844, Heinrich Schwabe was the first to report that observations of sunspots over the previous 18 years varied over an approximately 10-year cycle [Schwabe, 1844]. Figure 1.9 shows solar cycle observations spanning 1750 to the present day. During this time, sunspots have been observed daily from a number of different observatories. Sunspots can last hours, days or even months [Moldwin, 2008], with the total number varying over the semi-regular 11-year cycle. How sunspots are measured and counted will be discussed in section 2.2.3.

The number of sunspots, or regions of intense magnetic fields, changes over the solar cycle because the Sun's magnetic field changes. The Sun's magnetic field is generated and modulated by a dynamo. At solar minimum, the solar magnetic field is well ordered and dipolar. Over the course of the solar cycle, the Sun's magnetic field slowly reverses polarity. At solar maximum, the Sun's magnetic field is most disordered and highly structured. In the descending phase of the solar cycle, which occurs after solar maximum, the Sun's magnetic field returns to its dipole configuration. This reversal of polarity occurs over an 11-year cycle, with a complete magnetic cycle occurring over 22 years. The 22-year cycle is sometimes known as the Hale cycle, named after the solar astronomer who discovered it [Hale *et al.*, 1919]. The reversal in polarity is also observed in the polarity of sunspot pairs: the leading spots in each hemisphere have opposite polarities, which reverse every 11-years. As solar activity varies with sunspot numbers, or the solar cycle, space weather also follows this cycle. More severe space weather events occur at solar maximum, whilst during solar minimum, the space weather conditions are much quieter.

The number of sunspots, or level of solar activity, varies significantly between solar cycles. For example, in the top panel of Figure 1.9, there is a large difference between the number of sunspots observed in the solar cycles occurring before 1800 and the following few solar cycles occurring after 1800. Using cosmogenic ice-core data as a proxy for the solar cycle, it is possible to observe variations in solar cycles over the last 10,000 years [e.g.

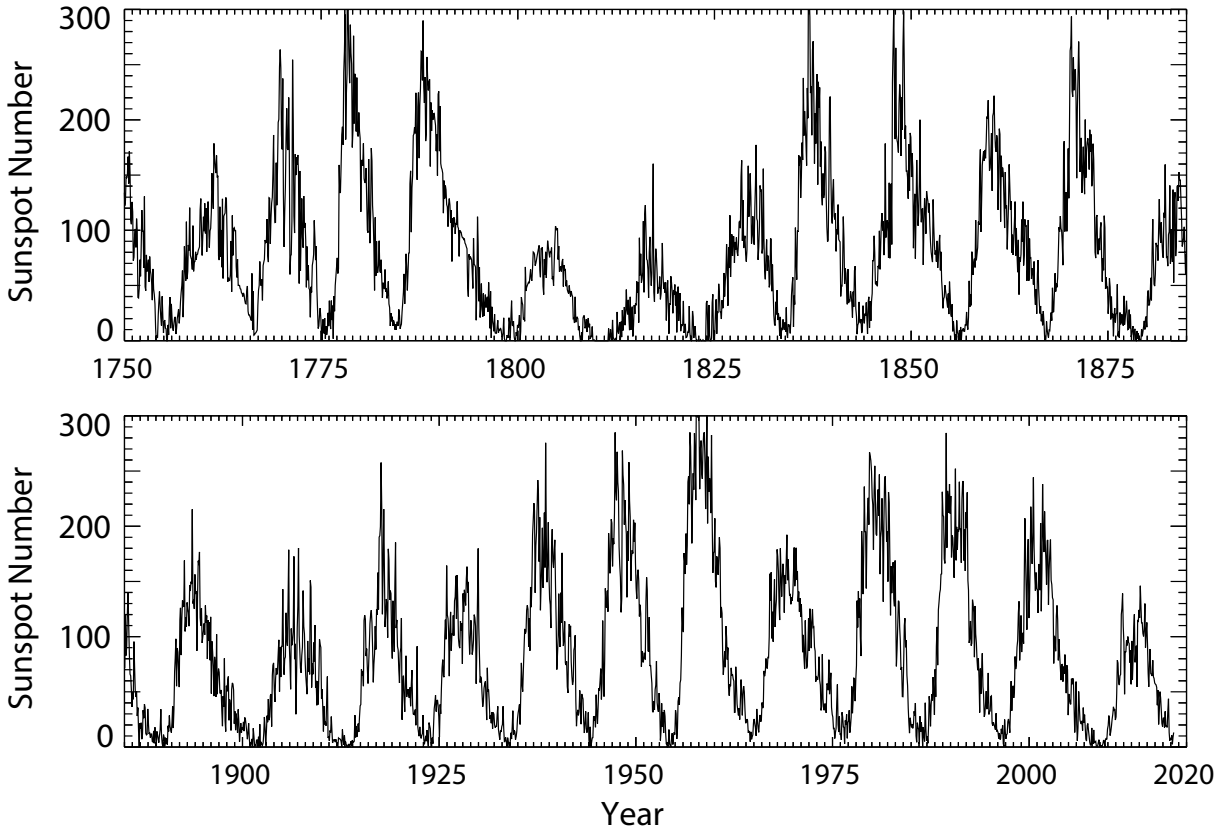

Figure 1.9: Monthly International Sunspot Numbers from 1750 to May 2018 from SILSO World Data Center [2016].

Usoskin, 2017; Beer *et al.*, 2017]. This proxy data has shown that solar cycles vary over a much longer timescale and undergo grand minima and maxima phases. The most well-known of these phases is called the Maunder Minimum [Eddy, 1976], which took place over a 70-year period from 1645 to 1715. Many scientists believe we are entering the next grand minimum of solar activity. This will be discussed in greater detail in section 3.2.

1.4 The Magnetosphere

As the solar wind and frozen-in IMF expands into the solar system, it eventually meets the Earth's magnetic field with its frozen-in plasma. When the two plasmas meet, they cannot mix and a thin current sheet, called the *Chapman-Ferraro current* or the *magnetopause*, forms

at the interface [Chapman & Ferraro, 1931]. This will be expanded on in section 1.4.2. The solar wind compresses the terrestrial magnetic field on the dayside, causing the terrestrial field to increase in strength. This increases the magnetic pressure being exerted on to the solar wind, resulting in the solar wind coming to a stop at the dayside equator. Elsewhere, the solar wind and IMF slip around the sides of the terrestrial field. This forms a cavity called the *magnetosphere*. In the remaining sections we will explore the configuration of the magnetosphere, the magnetopause, and the other currents and flows that result from this configuration.

1.4.1 Magnetospheric configuration

Figure 1.10 shows the basic configuration of the Earth's magnetosphere. As the highly supersonic solar wind hits the magnetosphere, a shock wave forms upstream, known as the *bow shock*. As the plasma passes through the bow shock it is slowed, compressed and heated. This shocked solar wind plasma forms the *magnetosheath*. The density in the magnetosheath is about 4 times the density of the solar wind plasma [Baumjohann & Treumann, 1997]. Near the Earth's magnetosphere, the solar wind typically has a density of 7 cm^{-3} and so the magnetosheath plasma density will be of the order 30 cm^{-3}. The standoff distance to the bow shock is approximately 14 R_E. The magnetopause separates the magnetosheath and the magnetosphere. At the nightside magnetosphere, the magnetic field is stretched into a tail-like formation known as the *magnetotail*.

1.4.2 The Magnetopause

1.4.2.1 The Chapman-Ferraro current

The magnetopause current, also called the Chapman-Ferraro current, forms because Ampère's law (equation 1.5) states that if there is a gradient in $\mathbf{B}$, a current must exist. The IMF is weak in comparison to the terrestrial magnetic field, so across the boundary the gradient is directed Earthwards across the subsolar magnetopause. From Ampère's law, the current, $\mathbf{j}$, is parallel to $\nabla \times \mathbf{B}$, so the current at the subsolar magnetopause where the terrestrial field is directed northwards flows duskwards (as shown in Figure 1.11a.). At higher latitudes and in the magnetotail, the terrestrial field is directed southwards, reversing the direction of the

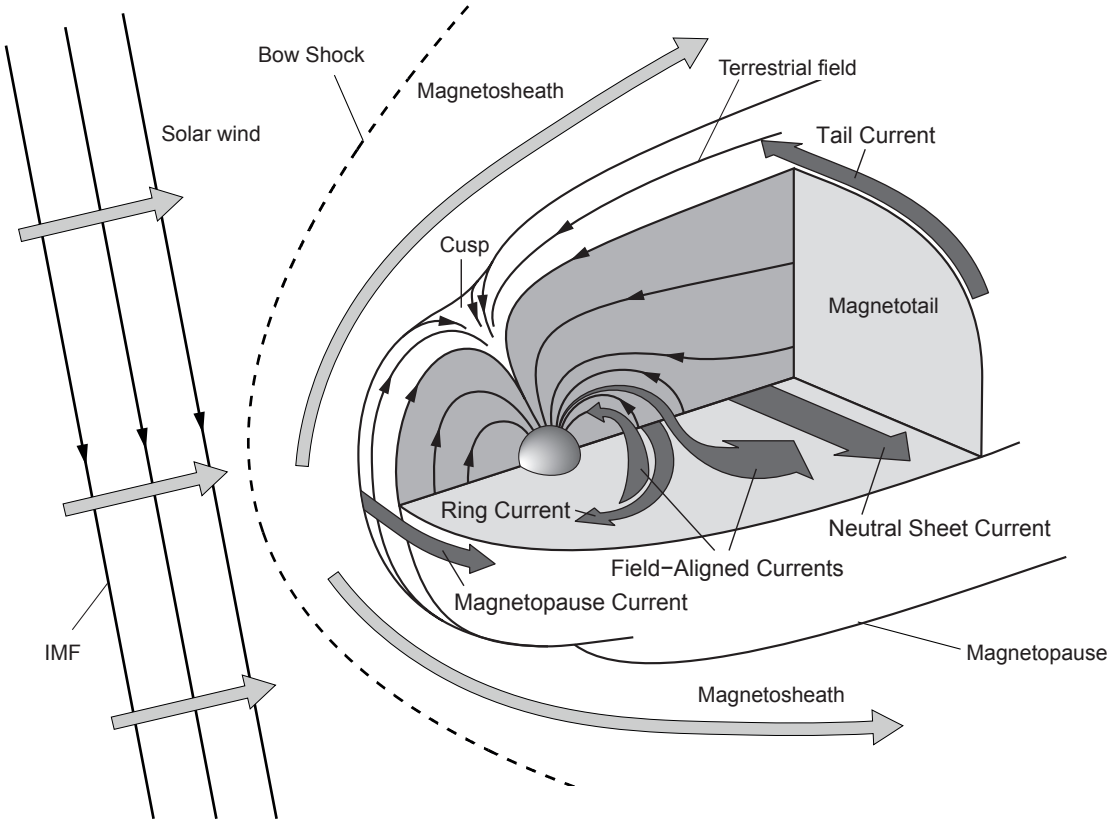

Figure 1.10: The Earth's magnetosphere. Large light grey arrows show the solar wind flow. Large dark grey arrows indicate the currents that form in the magnetosphere. Adapted from Baumjohann & Treumann [1997] and Hunt [2016].

gradient. The magnetopause current in these regions flows dawnwards.

The Chapman-Ferraro current itself produces a corresponding magnetic field. The generated field is directed northwards in the vicinity of the magnetopause nose, the same direction as the dipolar magnetospheric field. The Chapman-Ferraro current therefore compresses the magnetospheric field and increases the dipolar field strength. The magnetic field strength just inside the magnetopause is twice the strength of the undisturbed dipole strength, of the order 60 nT [Baumjohann & Treumann, 1997].

We can further understand Chapman-Ferraro currents by considering the motions of the charged particles as they encounter the magnetopause boundary. As the IMF is very weak it can be assumed that solar wind particles have effectively infinite gyroradii and that

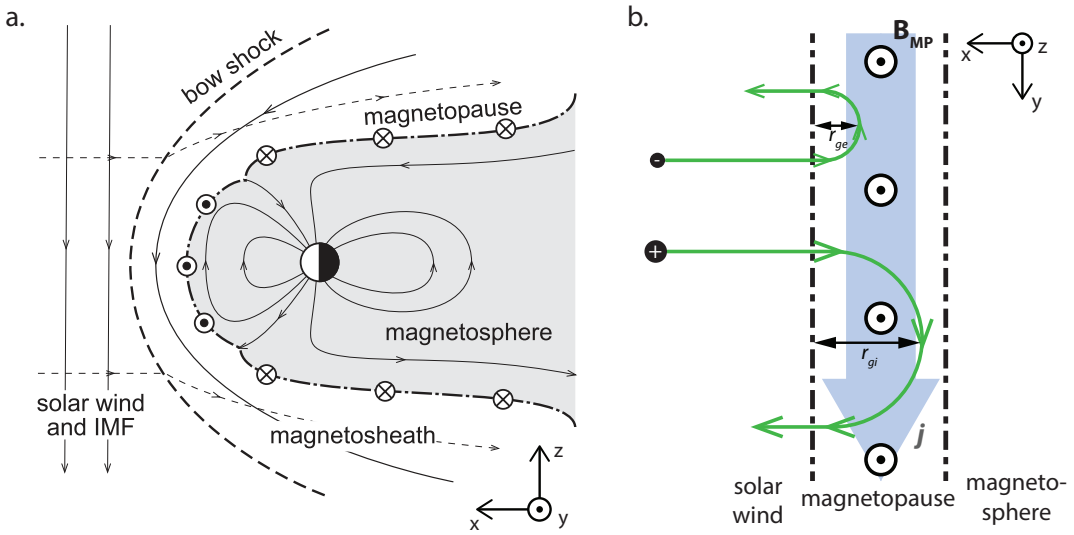

Figure 1.11: a. Schematic showing the Earth's magnetosphere with the Chapman-Ferraro current. b. Diagram showing the trajectories of solar wind particles as they encounter the dayside magnetopause. Adapted from Baumjohann & Treumann [1997].

they move with the solar wind flow. When the particles encounter the terrestrial magnetic field, which is much stronger than the IMF, the particle gyroradii suddenly decrease, and the particles are essentially reflected from the magnetopause boundary. This motion is displayed in Figure 1.11b. As shown in section 1.1.1, ions and electrons gyrate in opposite directions. Therefore, within the magnetopause there is a relative drift between opposite charges along the magnetopause, which gives rise to the Chapman-Ferraro current. In addition, Figure 1.11b. also indicates that the magnetopause has a finite width of the order of an ion gyroradius.

1.4.2.2 Magnetopause standoff distance

The location of the magnetopause is mainly controlled by the pressure balance between the solar wind and IMF on one side, and the magnetospheric plasma and field on the other. From the equation of motion (equation 1.31) and evoking Ampère's law it can be shown that,

$$\rho\frac{d\mathbf{V}}{dt} = \rho\mathbf{g} - \nabla(P + \frac{B^2}{2\mu_0}) + \frac{1}{\mu_0}(\mathbf{B}.\nabla)\mathbf{B} \tag{1.36}$$

By assuming equilibrium ($\frac{d\mathbf{V}}{dt} = 0$), gravity is negligible ($\mathbf{g} = 0$) and magnetic tension is negligible ($\frac{1}{\mu_0}(\mathbf{B}.\nabla)\mathbf{B} = 0$), equation 1.36 becomes

$$\nabla\left(P + \frac{B^2}{2\mu_0}\right) = 0 \tag{1.37}$$

This implies that the sum of the gas and magnetic pressures is a constant in space and that it is equal on either side of the magnetopause. Therefore,

$$P_{SW} + \frac{B_{SW}^2}{2\mu_0} = P_{MP} + \frac{B_{MP}^2}{2\mu_0} \tag{1.38}$$

where the subscripts SW and MP refer to the solar wind and magnetopause respectively. Since the IMF is very weak, to a first approximation, the contribution of the IMF to the pressure balance can be neglected. Additionally, the magnetospheric plasma pressure can be neglected because it is much less than the field pressure. Equation 1.37 simplifies to

$$P_{SW} = \frac{B_{MP}^2}{2\mu_0} \tag{1.39}$$

This means the force per unit area of the solar wind flow balances the force per unit area of the compressed magnetospheric field.

Since the main energy of the solar wind flow comes from the bulk flow of the ions, it is sufficient to neglect the thermal pressure and only consider the *solar wind dynamic pressure*, or *ram pressure*

$$P_{Dyn} = n_{SW} m_i V_{SW}^2 = \rho V_{SW}^2. \tag{1.40}$$

As discussed in the previous section, the magnetic field strength at the subsolar magnetopause is twice the strength of the dipole field ($B_{MP} = 2B_{dipole}$). The dipole field strength is given by

$$B_{dipole} = B_{eq}\left(\frac{R_E}{R_{MP}}\right)^3 \tag{1.41}$$

where B_{eq} is the equatorial magnetic field strength and R_{MP} is the magnetopause standoff distance. Inserting equations 1.39 and 1.40 into equation 1.38 and rearranging for R_{MP}, yields

$$R_{MP} = \left(\frac{B_{eq}^2}{\mu_0 \rho V_{SW}^2}\right)^{\frac{1}{6}} R_E$$

or,

$$R_{MP} \propto P_{Dyn}^{-1/6} \tag{1.42}$$

As the magnetopause standoff distance varies with the sixth root, it is not very sensitive to changes in the solar wind dynamic pressure. For typical solar wind and magnetospheric conditions, (i.e. $n_{SW} = 5$ cm^{-3}, $V_{SW} = 400$ km s^{-1}, and $B_{eq} = 31,000$ nT) the magnetopause subsolar standoff distance is approximately 10 R_E.

Away from the subsolar magnetopause, the solar wind flow pressure falls off as $\cos^2\theta$ where θ is the angle between the flow direction and the normal to the magnetopause. This means that the magnetopause boundary flares out downtail. The radius of the magnetopause flanks can be determined by considering the thermal pressure of the solar wind, P_{th}. At the flanks, the solar wind velocity is tangential to the magnetopause, so the ram pressure reduces to zero. The thermal pressure of the solar wind is given by

$$P_{th} = \gamma n_{SW} k_B T_{SW} \tag{1.43}$$

where γ is the ratio of the specific heats which is 5/3 for an ideal monoatomic gas, k_B is the Boltzmann constant and T_{SW} is the solar wind temperature. The magnetopause flank radius, R_{flank} is therefore given by

$$R_{flank} = \left(\frac{K B_{eq}^2}{2\mu_0 \gamma n_{SW} k_B T_{SW}} \right)^{\frac{1}{6}} \tag{1.44}$$

where K is a constant. Under the typical conditions described above, where $K = 2$ (as discussed in section 1.4.2.1, the magnetic field strength at the subsolar magnetopause is twice the dipole field strength) and $T_{SW} = 1.3 \times 10^5$ K, the theoretical magnetopause flank radius at the dawn-dusk meridian is $R_{flank} \approx 1.8 R_{MP}$ [Baumjohann & Treumann, 1997]. However, observations of the flank magnetopause at the dawn-dusk meridian is less than this, approximately 14 R_E. Observations further show that at the dawn-dusk meridian flank magnetopause, there is still a normal flow velocity component and hence the ram pressure does not diminish to zero. Therefore, the magnetosphere is still inflating in this region, and it is not until much further downtail that the flow is parallel to the tail magnetopause.

As alluded to in Figure 1.10, the magnetopause is not symmetrical in the equatorial and meridional planes. In the equatorial plane, the magnetopause is a smooth curve that extends from the dayside magnetopause into the magnetotail. In the meridional plane however, the tangent to the magnetopause is discontinuous in regions known as the *polar cusps* (where the northern cusp is indicated in Figure 1.10).

1.4.3 Magnetospheric flows

So far, we have only considered the case where the solar wind plasma is frozen-in to the IMF, and the magnetospheric plasma is frozen-in to the terrestrial magnetic field. However, as discussed in section 1.2.4, the frozen-in flow approximation breaks down when gradients in the magnetic field are comparable to the particle gyroradii. At the magnetopause nose, magnetic field gradients occur on spatial scales comparable to the particle gyroradii (see section 1.4.2.1). Figure 1.6 illustrates the magnetic reconnection that occurs at the dayside magnetopause when the IMF B_Z component is directed southwards. When the interplanetary field reconnects with the magnetospheric field, solar wind plasma can enter the magnetosphere. We refer to these reconnected field lines as "open", such that one end of the field line is connected to the geomagnetic field, and the other end is connected to the solar wind. As the open field lines leave the reconnection site (as shown in the right panel in Figure 1.6), the frozen-in flow conditions are satisfied again. These newly opened field lines contain a mix of solar wind and magnetospheric plasma, and as the field lines reconfigure, magnetic energy is converted into particle energy, and the plasma becomes heated and accelerated. The solar wind plasma flows down the field lines into the poles where they are mirrored close to Earth. These regions are the polar cusps (the northern cusp is shown in Figure 1.10). As the solar wind flows around the magnetosphere, the newly opened magnetic field lines that are connected to both the Earth and the IMF, are dragged anti-sunwards by the solar wind into the nightside magnetosphere. The mirrored particles then flow back along the field lines, away from the planet.

In the magnetotail, the magnetic field lines become stretched and they form the northern and southern *magnetospheric lobes*. The kinetic energy associated with the solar wind plasma is converted into magnetic energy and magnetic field pressure forces in the lobes push the field lines and plasma into lower latitudes. Most of the magnetotail plasma is concentrated in the 10 R_E-thick mid-plane in the magnetotail, in a region known as the *plasma sheet*. The footprints of the field lines that thread the plasma sheet extend down to the high-latitude *ionosphere*. It is the plasma sheet electrons which precipitate into the ionosphere along these field lines and collide with and ionise neutrals in the atmosphere which forms the Earth's *aurora*. The *polar cap* lies inside the auroral oval, such that the field line footprints in the polar caps map out to the magnetospheric lobes [Baumjohann & Treumann, 1997].

The stretched magnetic field lines in the northern and southern lobes are oppositely directed, or anti-parallel. Therefore, magnetic reconnection occurs in the magnetotail, closing the open field lines and leaving a stretched terrestrial field line with footprints at the poles earthwards of the reconnection site, and a solar wind field line downtail of the reconnection site. This can take place anywhere between 100-200 R_E downtail [Baumjohann & Treumann, 1997]. Due to magnetic tension, plasma is accelerated earthwards, and the closed stretched field lines and plasma move sunwards returning to the dayside magnetopause. If the IMF B_Z component remains southwards, the closed field line will reconnect with the IMF again, forming a cyclical motion of the magnetic field and plasma. This is known as the *Dungey cycle* and will be reviewed in greater detail in section 3.1.1 [Dungey, 1961, 1963]. Magnetic reconnection can also occur at high-latitudes between the magnetospheric field and northward directed IMF B_Z.

1.4.3.1 Substorms

For simplicity, we have so far considered the dayside and nightside reconnection rates to be in equilibrium. However, generally, this is not the case. The quantity of magnetic flux that is reconnected at the dayside magnetopause depends on how fast the solar wind is flowing and the magnitude of the southward component of the IMF B_Z as well as how long it remains southwards. IMF B_Z is only orientated southwards approximately half the time, therefore there will be periods during which the magnetosphere is very quiet, and periods when it is very active. Eventually, all opened magnetic field lines must be closed in the magnetotail. However, the rate of reconnection at the dayside magnetopause does not have to equal the rate of reconnection in the magnetotail, only the average rates need to be equal.

Most field lines that are opened at the dayside magnetopause and convected to the magnetotail are not closed via reconnection instantaneously. Open field lines get added to and stored in the magnetotail lobes until the magnetic flux density becomes high and the field lines are compressed into the centre. After about an hour, the field lines suddenly reconnect and there is an explosive release of energy [Baumjohann & Treumann, 1997]. This process is known as a *substorm* and is illustrated in Figure 1.12.

Substorms are typically broken down into three phases: growth, expansion and recovery (upper, middle and lower schematics in Figure 1.12, respectively). Usually lasting an hour,

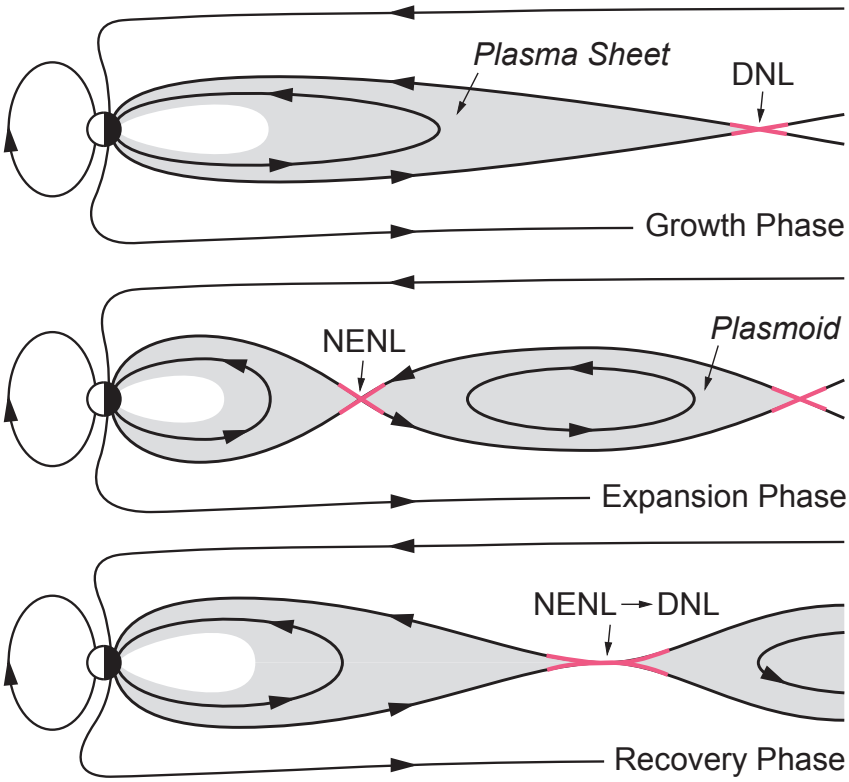

Figure 1.12: Schematic illustrating the growth, expansion and recovery phases of a magnetospheric substorm. The reconnection sites are indicated in pink. DNL refers to the distant neutral line and NENL refers to the near-Earth neutral line. Adapted from Baumjohann & Treumann [1997].

the growth phase typically occurs after a sustained period of southward directed IMF B_Z in combination with a low nightside reconnection rate. Some reconnection occurs in a region known as the *distant neutral line* (DNL in Figure 1.12). However, most of the open magnetic flux accumulates in the magnetotail lobes. As more flux is added, the plasma pressure increases and the plasma sheet thins [Coroniti & Kennel, 1973]. The *near-Earth neutral line* forms towards the end of the growth phase at approximately 20-30 R_E downtail (referred to as NENL in Figure 1.12).

Lasting typically for 30-60 min, the substorm expansion phase occurs next. The expansion phase is characterised by a dramatic increase in the magnetic reconnection rate at the NENL, which causes a dipolarisation of the magnetic field in the tail, and an explosive

brightening of the auroral oval as hot plasma is injected into the ionosphere. In the large region between the two neutral points, phenomena known as *plasmoids* form. The magnetic field lines in a plasmoid form closed loops or helical structures and are lost downtail. The substorm recovery phase lasts around 1-2 hours. Magnetic reconnection at the NENL ends and the magnetosphere returns to its quiet state.

1.4.4 Magnetospheric currents

Many current systems occur in the magnetosphere due to spatial gradients in the magnetic field. We have already discussed Chapman-Ferraro current, or magnetopause current (section 1.4.2.1) and mentioned the ring current (section 1.1.6). Figure 1.13 shows the configuration of the currents in the magnetosphere.

The ring current, as mentioned previously, is carried by ions trapped in the radiation belt and was first introduced by [Störmer, 1907]. It exists at all times but increases in magnitude during geomagnetic storms (which will be explained in greater detail in section 3.1.5). The ring current is often described in two parts: the symmetric ring current which consists of ions drifting on closed drift paths, and the *partial ring current* which lies on open field lines and closes in the ionosphere.

In the magnetotail, a current known as the *cross-tail current* flows between the two magnetotail lobes in the plasma sheet. The magnetic field that populates the northern lobe is directed earthwards towards the northern pole, whilst the magnetic field that populates the southern lobe is directed tailwards and away from the southern pole. A current must exist as a result of Ampère's law (equation 1.5). The magnetopause currents that flow on the surface of the magnetotail, also known as the *tail current*, close through the cross-tail current as illustrated in Figure 1.13b.

There are also a number of currents that form in the Earth's ionosphere, however most of these are beyond the scope of this thesis. The final currents shown in Figure 1.13c. are the *field-aligned currents* (FACs), or *Birkeland currents*. FACs flow along magnetic field lines and connect magnetospheric current systems with ionospheric current systems. FACs are broken down into *Region 1* and *Region 2* current systems, indicated by the blue and red lines respectively in the figure. Region 2 currents are closed by the partial ring current in the near-Earth equatorial plane. Region 1 currents are polewards of the Region 2 currents and

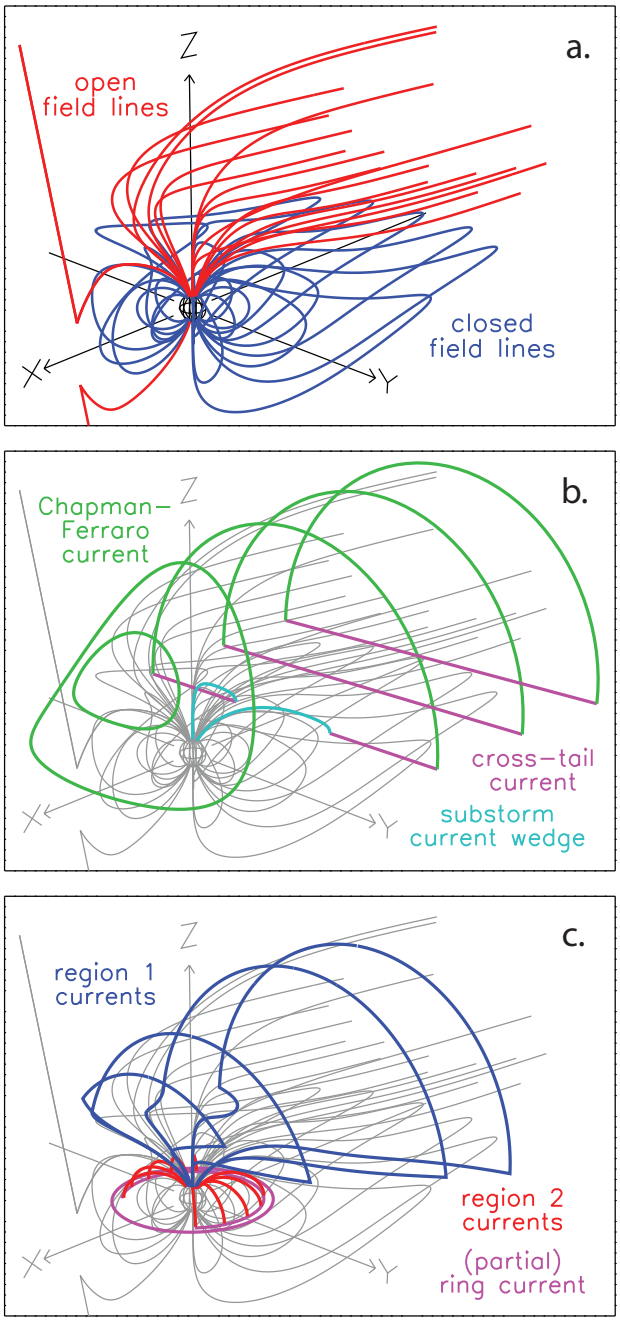

Figure 1.13: a. Schematic showing the open (red) and closed (blue) magnetic field line configuration in the Earth's magnetosphere. b. Diagram indicating the location of the Chapman-Ferraro currents (green), cross-tail current (pink) and the substorm current wedge (light blue). c. Schematic illustrating the locations Region 1 (blue) and Region 2 (red) field-aligned currents, and the (partial) ring current (pink). [Milan *et al.*, 2017].

close on the magnetopause.

1.5 Summary

This chapter has presented all the background space plasma physics relevant for the rest of this thesis. This will provide the context for studying the intricacies of the Earth's magnetopause, and what influences its location. In the following chapter, the relevant instrumentation and datasets will be discussed in order to provide the framework for reviewing the literature in Chapter 3. The remaining chapters will present the research that has been carried out to investigate what influences the location of the magnetopause.

Chapter 2

Instrumentation and datasets

In Chapter 2, the data, instrumentation and coordinate systems used in this thesis are described. The main dataset used is measured by the Geotail spacecraft and hence the mission and instruments are described in detail. Other datasets used in this study include solar wind data from the OMNI dataset, auroral data from the Imager for Magnetopause-to-Aurora Global Exploration (IMAGE) spacecraft, the SYM-H index as measured by ground-based magnetometers, ionospheric convection from the Super Dual Auroral Radar Network (SuperDARN), and solar activity measured by the International Sunspot Number. Finally, the coordinate systems are defined.

2.1 Space-based instrumentation

2.1.1 Geotail

2.1.1.1 Overview of the mission

The Geotail mission is a joint programme of the Institute of Space and Astronautical Science (ISAS) of Japan and the National Aeronautics and Space Administration (NASA) of the USA [Nishida, 1994]. The principal objective of the Geotail mission was to study the dynamics of the Earth's magnetotail at a wide range of distances downtail to address the issues of energy input, storage, release and conversion. Geotail was launched on 24$^{\text{th}}$ July 1992 into an equatorial orbit with an apogee that reached distances of 220 R_E (Earth radii). The first phase lasted two years until autumn 1994 and focused on the distant magnetotail. The apogee was

reduced during the second phase in order to study magnetic reconnection during substorms. The orbital apogee and perigee were reduced to ∼30 R_E and ∼8-10 R_E, respectively. The orbital perigee also allows for the study of the dayside magnetopause boundary. This study comprises data from the second phase of the mission, from January 1996 to December 2015. These orbital characteristics mean that Geotail frequently skims the dayside magnetopause boundary and samples the magnetotail at distances up to 25 R_E downtail.

A schematic of the configuration of the Geotail satellite is displayed in Figure 2.1. Geotail is cylindrical in shape with a diameter of 2.2 m and height of 1.6 m. It has two 6 m long booms that separate the magnetometers from the main body. It contains four 50 m long antennas that measure the electric field up to 800 kHz. It has a spin rate of 20 rpm. Onboard data recorders measure continuously, and data is sent to the NASA Deep Space Network and the Usuda Deep Space Center of ISAS. Geotail has seven scientific instruments on board which are listed in Table 2.1 with a brief description.

The magnetic field data used in this thesis are obtained from Geotail's high-resolution Magnetic Field experiment (MGF) [Kokubun *et al.*, 1994]. Geotail's Low Energy Particle experiment (LEP) provides the ion data used in this study [Mukai *et al.*, 1994]. These instruments are described in greater detail in the following sections.

2.1.1.2 Magnetic Field experiment

The Magnetic Field experiment measures the magnetic field in the frequency range below 50 Hz. It consists of two fluxgate magnetometers and a search coil magnetometer which are described in the following sections [Kokubun *et al.*, 1994].

Fluxgate magnetometer

Typically, a fluxgate magnetometer consists of a ring core that is made out of a highly magnetically permeable alloy. Two electrically conductive coils are wrapped around the coil; a drive coil and a sense coil which fully encloses the drive coil, as seen in Figure 2.2. A square wave current is applied to the drive coil to generate a magnetic field in the core. Any external magnetic field will contribute to the total field in the core. This produces a net change in flux across the sense coil which induces a voltage that is modulated at twice the drive frequency. If there is no external magnetic field, no voltage is induced.

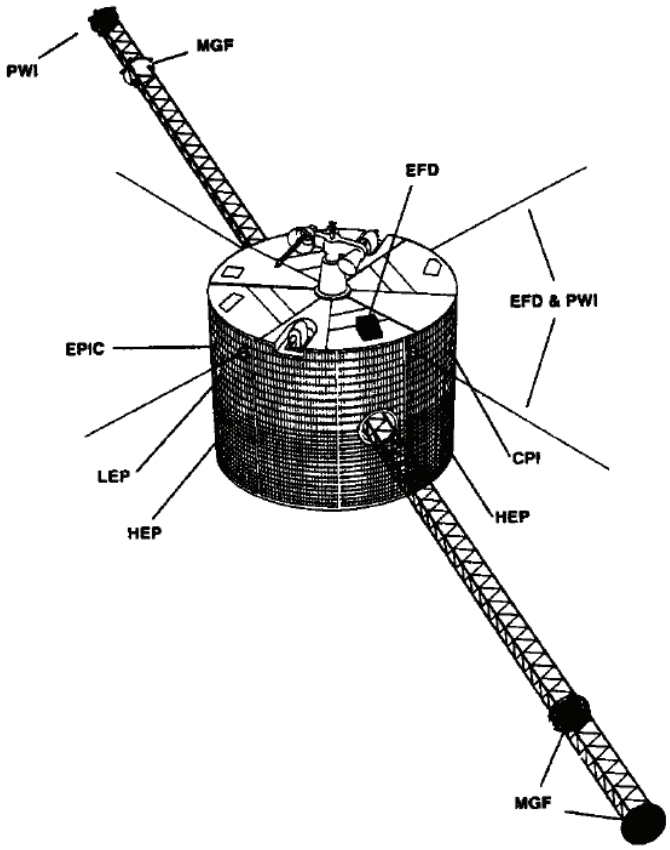

Figure 2.1: A schematic of Geotail from Nishida [1994]. See Table 2.1 for instrument descriptions.

The size and phase of the induced voltage under the influence of an external magnetic field provides information about the magnitude and direction of the external magnetic field. The fluxgate magnetometers onboard Geotail have seven dynamic ranges from $\pm$16 nT to $\pm$65,536 nT (full scale) which are switched between automatically [Kokubun *et al.*, 1994]. They have a sampling rate of 128 Hz.

Search coil magnetometer

A search coil magnetometer consists of a high permeability core with a fine wire wound round it thousands of times [Hospodarsky, 2016]. In the presence of an external time-varying magnetic field, a time-varying voltage is induced due to Faraday's law (equation 1.4). The coil output is attached to a preamplifier, which amplifies the induced voltage and conditions the signal so it can be transmitted to the main electronics via a low-frequency

Instrument	Brief description
Electric Field Data (EFD)	Spherical probe and wire antenna Electron boomerang Ion emitter
Magnetic Field (MGF)	Fluxgate Search coil
Low Energy Particle (LEP)	Ion/electron 3-dim vel. distribution Solar wind ions Ion mass/energy spectrum
Comprehensive Plasma Instrument (CPI)	Ion/electron 3-dim vel. distribution Solar wind ions Ion mass/energy spectrum
High Energy Particle (HEP)	Low energy particles Ion/electron burst Medium energy ion isotope ratio High energy ion isotope ratio
Energetic Particles and Ion Composition (EPIC)	Ion charge state/mass/energy Ion mass and energy Electron energy
Plasma Wave Instrument (PWI)	Frequency sweep Multichannel analyser Waveform capture

Table 2.1: A list of the scientific instruments onboard the Geotail satellite (from Nishida [1994]).

radio receiver. The basic design of a search coil magnetometer is shown in the schematic in Figure 2.3. The main difference between a fluxgate magnetometer and a search coil magnetometer is that a fluxgate magnetometer is more sensitive to static and low fields, whereas a search coil magnetometer can measure high frequencies.

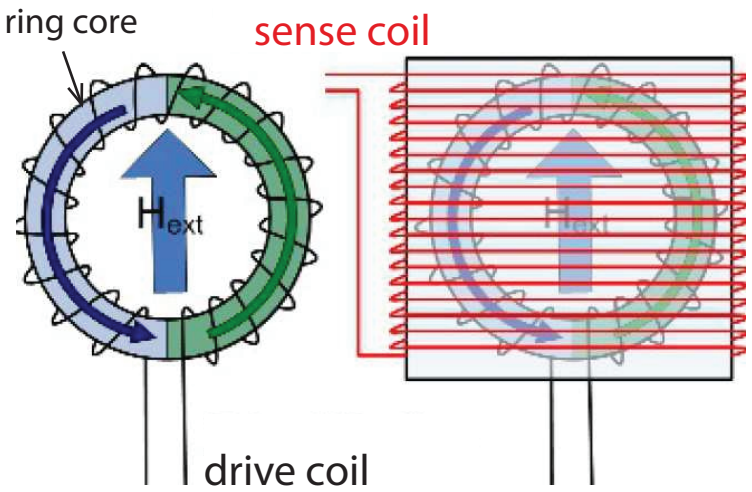

Figure 2.2: Schematic of a fluxgate magnetometer. The diagram on the left shows the ring core with the drive coil wrapped around it. Blue and green arrows indicate the induced fields. H_{ext} describes the external magnetic field. The diagram on the right shows the sense coil which encloses the ring core and drive coil. Adapted from Imperial College London.

2.1.1.3 Low Energy Particle experiment

The Low Energy Particle (LEP) experiment consists of three sensors: an Energy-per-charge Analyser (LEP-EA), which measures three-dimensional velocity distributions and their moments of hot plasmas; a Solar Wind ion analyser (LEP-SW), which measures three-dimensional velocity distributions and moments of the solar wind ions with fine energy and angular resolutions; and finally, an energetic-ion Mass Spectrometer (LEP-MS), which measures three-dimensional determinations of the ion composition [Mukai *et al.*, 1994].

Electrostatic potential analyser

The LEP-EA is an electrostatic analyser and consists of two quadrispherical electrostatic analysers, the inner measures electrons (LEP-EA-e) and the outer measures positive ions (LEP-EA-i) both separately and simultaneously. It has a field of view of $10^\circ \times 145^\circ$ and an energy range of several eV Q^{-1} to 43 keV Q^{-1}. The inner and outer analysers have equal voltages applied to them with opposite polarities. The analysers allow charged particles with specific energies, charge and incident angles to travel through them and be measured. It is capable of calculating velocity moments every spin, although due to telemetry constraints,

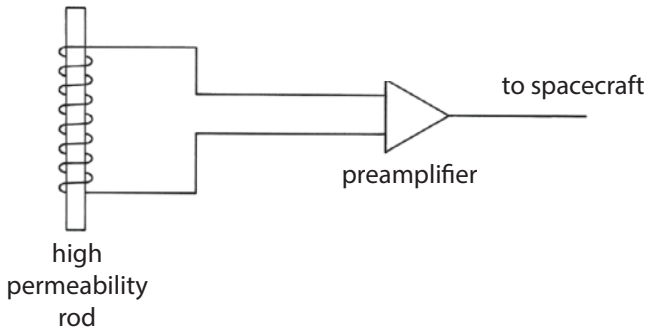

Figure 2.3: Basic schematic of a search coil magnetometer. A wire is wrapped round a high permeability rod. It is attached to a preamplifier, which amplifies the induced voltage before being transmitted to the spacecraft electronics. Adapted from Hospodarsky [2016].

it can only calculate three-dimensional velocity distributions every four spins.

The LEP-SW is also an electrostatic analyser and has a similar design to the LEP-EA but uses a 270° spherical electrostatic analyser with a field of view of $5° \times 60°$. It measures ions in the energy range of 0.1 keV Q^{-1} to 8 keV Q^{-1}. Like the LEP-EA, it is capable of calculating velocity moments every spin period but can only resolve three-dimensional velocity distributions every four spins due to telemetry constraints.

Mass spectrometer

The LEP-MS is an energetic-ion mass spectrometer that determines three-dimensional distributions of different ion species simultaneously over the energy range of 0.1 to 25 keV Q^{-1}. The mass spectrometer consists of an inlet collimator, tandem (spherical and poloidal) electrostatic analysers, a magnetic analyser and MCP detectors [Mukai *et al.*, 1994]. A microprocessor can determine the counts for five different ion species (H^+, He^{2+}, He^+, O^{2+} and O^+), background counts and total counts.

2.1.2 OMNI

The OMNI dataset has been used in this study to determine the solar wind parameters. OMNI data are publicly available and can be found on the NASA Goddard Space Flight Center website. High (1-minute and 5-minute) and low (1-hour) resolution data is available. In this study, we make use of the high resolution, 1-minute data. It comprises magnetic

field and plasma data from spacecraft in orbit about the L1 Lagrange point 225 R_E in front of the Earth and in geocentric orbit. During the 20-year period investigated in this study, magnetic field and plasma data are obtained from the Advanced Composition Explorer (ACE), Wind, Geotail and Interplanetary Monitoring Platform-8 (IMP-8) satellites. The dataset also includes energetic particle fluxes, geomagnetic activity index (SYM-H) and sunspot numbers.

To support solar wind-magnetosphere coupling studies, the OMNI dataset is time-shifted to a point closer to the magnetosphere. This point is chosen to be the bow shock nose. The measurements are processed using a set routine that assumes that each solar wind measurement lies along a phase front that propagates first past the spacecraft and then the bow shock. The phase front normal direction uses magnetic field and solar wind propagation speed to time shift the data to the location of the bow shock nose. The location of the bow shock at the time the phase front reaches it is determined using the Farris & Russell [1994] model and the Shue *et al.* [1997] magnetopause model. Due to the Earth's orbital motion about the sun, solar wind flow aberration is included in determining the location of the bow shock.

2.1.3 IMAGE

The Imager for Magnetopause-to-Aurora Global Exploration (IMAGE) spacecraft was operational between June 2000 and October 2005 [Burch, 2000; Mende *et al.*, 2000a]. It has an elliptical polar orbit that enables the spacecraft to observe the Earth's auroral ovals. During the years 2002 and 2003, IMAGE's orbit changed from observing the Northern aurora to observing the Southern aurora causing a several-month gap in the dataset.

IMAGE has three Far Ultraviolet (FUV) instruments. This includes two spectrographic imagers (SI), SI12 and SI13 [Mende *et al.*, 2000b], and a Wideband Imaging Camera (WIC) [Mende *et al.*, 2000a,c]. The SI12 instrument measures aurora produced by proton precipitation and the WIC camera primarily measures aurora produced by electron precipitation. Both SI12 and WIC make measurements at a 2-minute cadence for 10 hours of each 14-hour orbit [Burch, 2000]. The apogee of IMAGE is at approximately 44,000 km. To observe the entire auroral oval at this altitude, the FUV imagers have fields of view of $17^\circ \times 17^\circ$ (WIC) and $15^\circ \times 15^\circ$ (SI).

2.1.4 ECLAT

IMAGE data has been processed for easy usage as part of the European Cluster Assimilation Technology (ECLAT) project [Shukhtina & Gordeev, 2015]. The ECLAT processed data includes measurements of the total auroral emission, maximum auroral brightness, auroral radius and polar cap flux. In this thesis, polar cap flux and auroral radius have been used and will be briefly explained here.

The raw images have a resolution of 128 $\times$ 128 pixels but are reduced to a 40 $\times$ 40 spatial grid fixed in geomagnetic latitude and magnetic local time in order to extract global information. The images are then spatially and temporally averaged, which helps to increase the signal to noise ratio in images where the oval is very faint, and to "fill in the gaps" during times where full coverage is not available. Auroral boundaries are then identified from these processed images by fitting circles of different radii. The circle which corresponds to the brightest pixels in the image is then used to describe the size of auroral oval. The inner boundary of the auroral oval is used to define the open closed field line boundary (OCB). Under quiet conditions this is a good approximation, however during more disturbed times significant but weaker emission can occur polewards of the inner boundary. Under these conditions, an additional step is included to identify the poleward boundary of the weaker emission. If the magnetic field is assumed to be dipolar, integrating over the area inside the auroral oval gives the polar cap flux.

2.2 Ground-based instrumentation

2.2.1 SYM-H

The Symmetric Horizontal (SYM-H) index measures disturbances in the symmetric portion of the horizontal (H) component magnetic field near the equator [Wanliss & Showalter, 2006]. It measures the magnetic perturbation produced by the ring current. During geomagnetic storms, the ring current becomes enhanced and the accompanying induced magnetic field causes a decrease which opposes the terrestrial magnetic field at the equator, and hence equatorial magnetometers observe a reduction in the Earth's magnetic field strength (a decrease in SYM-H). The indices are measured by ground-based, mid-latitude magnetometer stations

and are calculated at a high temporal resolution of 1-minute. The SYM-H index has been available since 1981 and is considered to be a higher resolution version of the similarly-calculated Disturbed storm time (*Dst*) index, in which only hourly values are available [Wanliss & Showalter, 2006]. Figure 2.4 shows the locations of the stations used to calculate the both indices. SYM-H is derived from only six stations each month, which are chosen based on availability and data quality (more information can be found on the World Data Centre for Geomagnetism, Kyoto website).

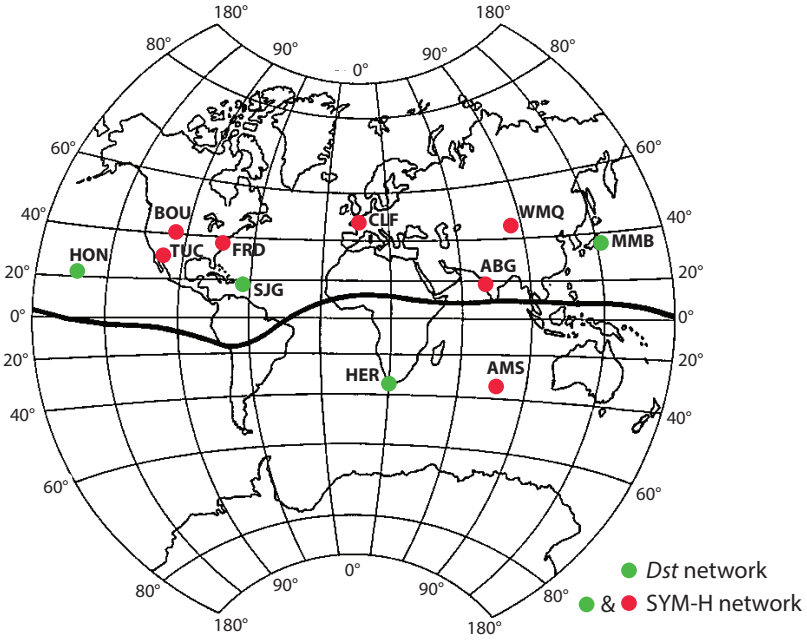

Figure 2.4: A map showing the locations of the ground-based magnetotmeters which are used to calculate the SYM-H and *Dst* indices.

To calculate the index, the background magnetic field and the solar quiet daily variation are first subtracted from the measurements [Iyemori, 1990; Wanliss & Showalter, 2006]. This is followed by a transformation of the coordinates to a magnetic dipole coordinate system, which assumes that the ring current flows parallel to the dipole equatorial plane. Finally, the six-station average of the longitudinal symmetric magnetic field component is calculated from the averages of the disturbance component at each minute and latitudinal corrections are made. A more detailed description of how the SYM-H index is calculated can be found in Iyemori [1990].

2.2.2 SuperDARN

The Super Dual Auroral Radar Network (SuperDARN) consists of more than 30 high-frequency (HF) radars located in the northern and southern hemispheres [Greenwald *et al.*, 1995; Chisham *et al.*, 2007]. SuperDARN radars primarily measure the convection of plasma in the ionosphere and aid with the study of a wide range of magnetospheric, ionospheric and atmospheric phenomena. Figure 2.5 shows the current radars in operation and their fields-of-view. Signals are transmitted from the radars in the frequency range of 8-20 MHz. In normal operation mode, each radar looks in 16 beam directions and combined they cover a spatial range of 52°. The data have a temporal resolution of 2 minutes.

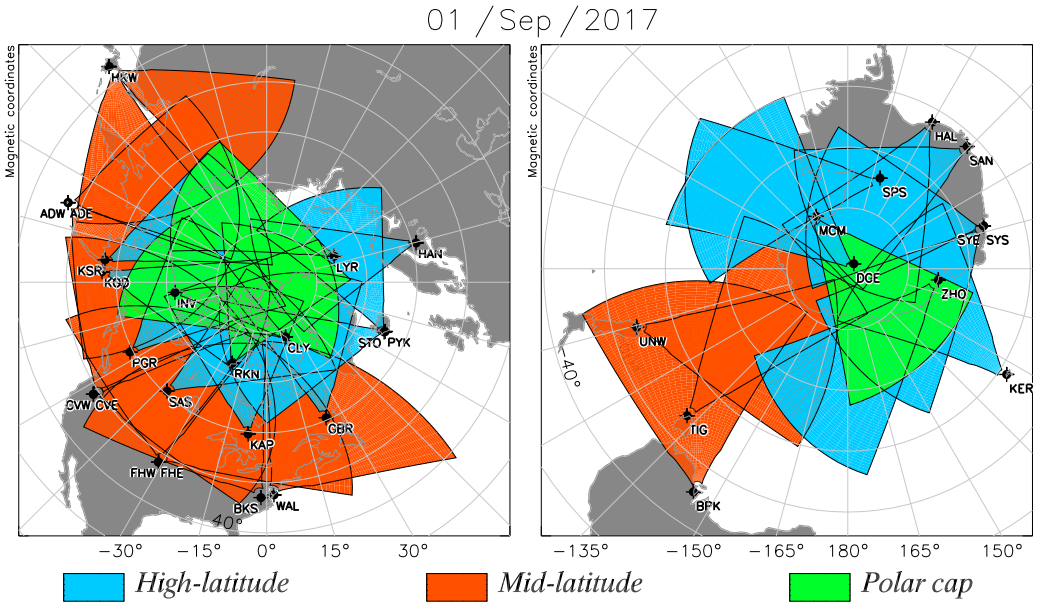

Figure 2.5: Maps showing the locations and fields-of-view of the SuperDARN radars in operation in 2017 in the northern (left) and southern (right) hemispheres from VirginiaTech. Colours indicate high-latitude, mid-latitude and polar cap radars.

SuperDARN measures the line-of-sight velocity of the plasma irregularities in the E and F regions of the ionosphere that scatter the radar signal. There are two main types of plasma instabilities present in the E and F regions of the ionosphere which can lead to scatter of a radar signal. The first, which occurs in the E region, is due to the ions colliding with the neutrals while the electrons convect with the $\mathbf{E} \times \mathbf{B}$ drift velocity. The second, which occurs in the F region, is due to the gradient-drift instability which produces irregularities moving at the convection velocity. When measurements of line-of-sight velocities from multiple

locations are combined, the overall $\mathbf{E} \times \mathbf{B}$ drift motion of the plasma can be calculated.

2.2.2.1 Map potential technique

The map potential technique combines all of the available SuperDARN radar data at a given time in one hemisphere into a global two-dimensional ionospheric convection map [Ruohoniemi & Baker, 1998; Chisham & Pinnock, 2002; Grocott *et al.*, 2012]. It uses the line-of-sight velocities of the plasma to constrain a spherical harmonic fit of the electrostatic potential. Where data coverage is limited, a statistical electrostatic potential model parameterised by upstream solar wind conditions is used to help constrain the fit [Ruohoniemi & Greenwald, 1996]. The final potential map is weighted so that the model is only used in regions where there is no data. An example SuperDARN potential map from 2nd March 2002 is shown in Figure 2.6. Noon is at the top of the figure, and dusk is to the left. The coloured dots indicate the location of the SuperDARN observations, with the colour, direction and length of the line corresponding to the velocity of the modelled flow. The black contours are the ionospheric potential. The interplanetary magnetic field (IMF) used by the model is indicated in the top right of the figure.

2.2.2.2 Heppner-Maynard Boundary

The Heppner-Maynard Boundary (HMB) represents the latitudinal extent of the ionospheric convection pattern. Below the HMB, the flow is dominated by corotation, and above it is dominated by convection. The HMB is derived from SuperDARN radar observations and is based on criteria defined by Heppner [1977] and Heppner & Maynard [1987]. In their studies, the low-latitude convection boundary is defined as the latitude at which the electric field showed a clear departure from low- and mid-latitude values. Heppner [1977] required a change of at least 5 mV m^{-1} in the dawn-dusk electric field measured by the OGO-6 spacecraft, whereas Heppner & Maynard [1987] required a minimum change of 2 - 3 mV m^{-1} in the horizontal electric field measured by the DE2 satellite. To determine the HMB from SuperDARN data, a minimum threshold of three SuperDARN data points with velocity greater than 100 m s^{-1} which lie on or below the boundary must be satisfied, ensuring that the HMB encircles the ionospheric convection. The velocity requirement corresponds to an electric field of approximately 5 mV m^{-1}.

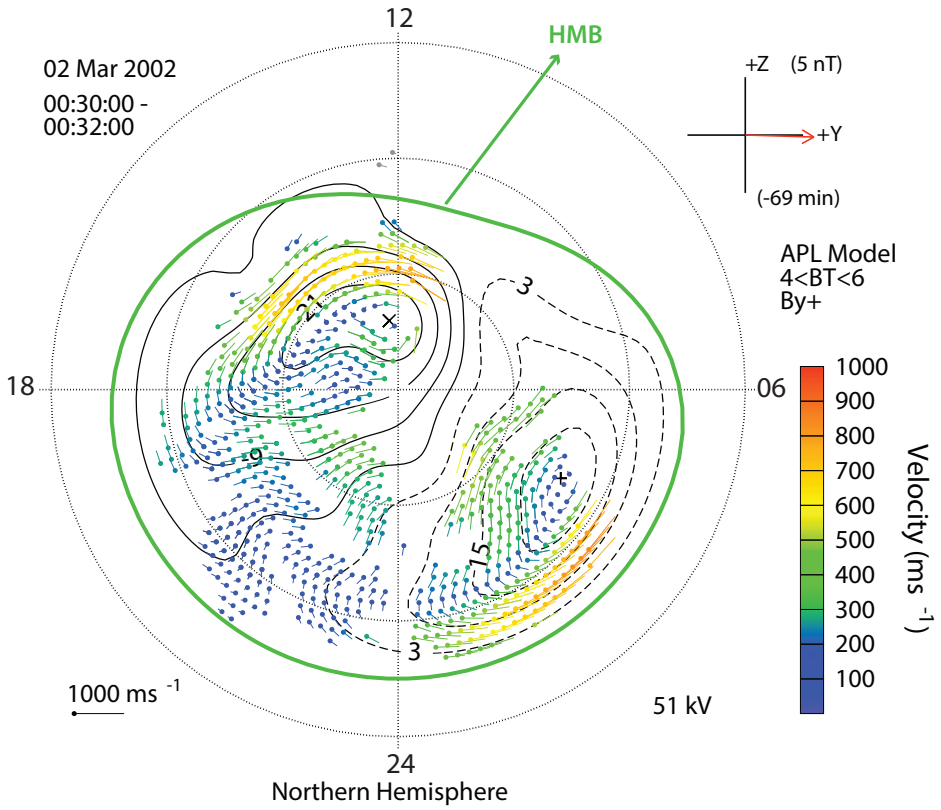

Figure 2.6: An example potential map calculated from SuperDARN data from 00:30 UT on 2nd March 2002. Noon is at the top of the map and dusk to the left. SuperDARN observations are indicated by the coloured dots, with the colour and vector direction corresponding to flow velocity. The ionospheric potential is indicated by the black lines and the IMF conditions fed into the model are shown at the top right. The Heppner Maynard Boundary is shown by the solid green line. It crossed the midnight meridian at 65° magnetic latitude. Adapted from Imber *et al.* [2013a].

In Figure 2.6, the solid green line shows the location of the HMB, indicating the equatorward edge of the radar observations. Since its shape is nonuniform, its latitude is taken as the intersection of the HMB with the midnight meridian [Shepherd & Ruohoniemi, 2000].

In this thesis, the HMB has only been used between January 1996 to December 2012 as this dataset was readily available. Figure 2.7 shows the northern hemisphere SuperDARN radars that were in operation during this period and used to determine the HMB location. The fields of view are shown in Figure 2.7a. and the years of operation and magnetic latitudes 2.7b. The main array located at high-latitudes, indicated by blue, was constructed first

between 1993 and 2001. Mid-latitude radars, known as StormDARN, were added next to measure ionospheric convection during geomagnetically active times when the auroral oval expands to lower latitudes. The polar cap radars, known as PolarDARN, shown in green were built in 2007 and 2008. By 2012, the were 18 northern hemisphere radars in operation.

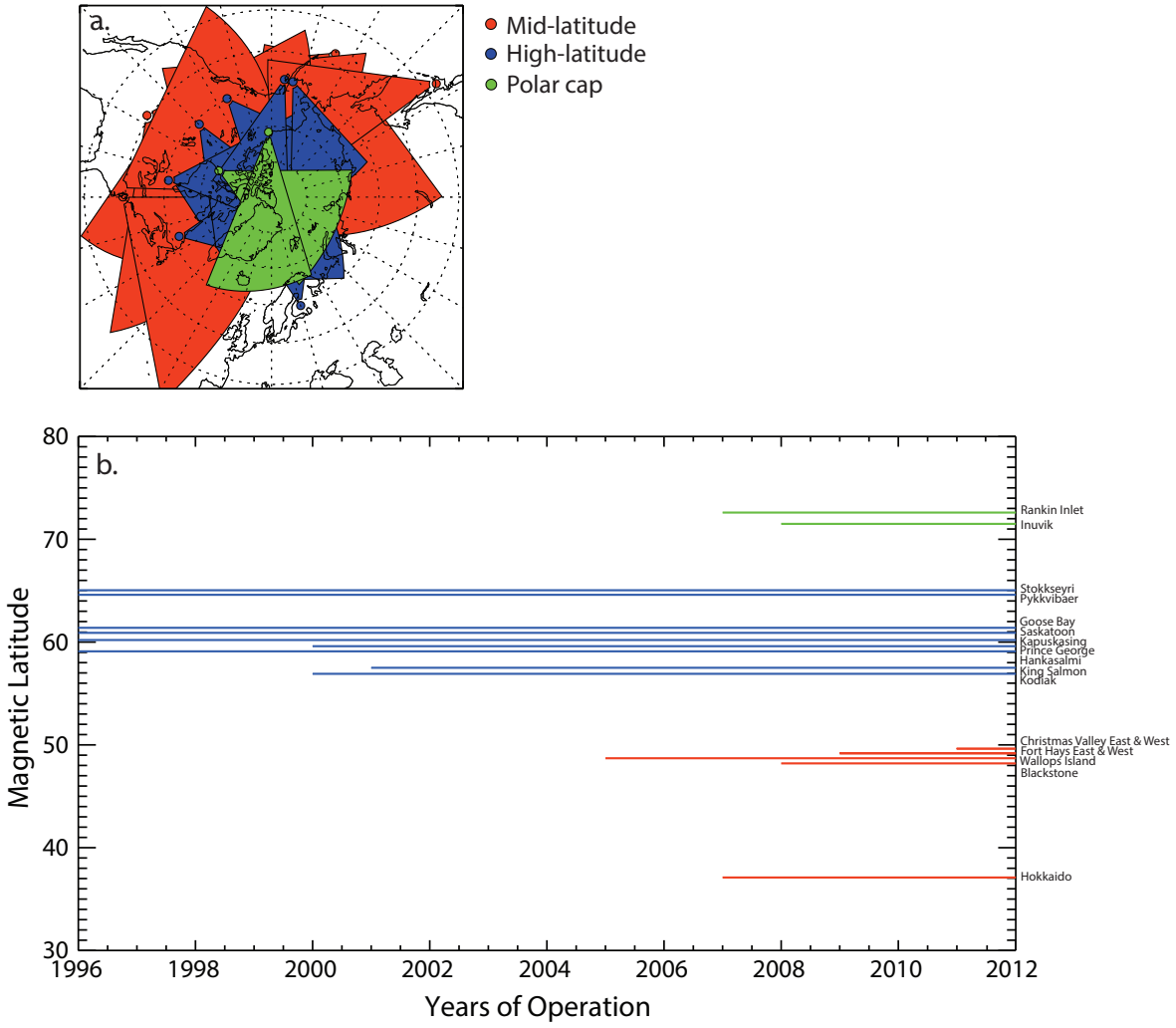

Figure 2.7: a. The fields of view of the northern hemisphere SuperDARN radars in operation on 31 December 2011 at 00 UT. The mid-latitude or StormDARN radars are shown in red, the high-latitude or main array radars are shown in blue, and the polar cap or PolarDARN radars are shown in green. b. The years of operation and magnetic latitude for each of the northern hemispheric SuperDARN radars. Both panels are adapted from Imber *et al.* [2013a] and Imber *et al.* [2013b].

2.2.3 International Sunspot Number

Sunspot numbers are often used as a proxy for solar activity and the solar cycle (as discussed in section 1.3.2). The highest number of sunspots are observed during solar maximum, and the lowest during solar minimum. Although other sunspot number measurements do exist (for example, the Boulder Sunspot Number and the American Association of Variable Star Observers (AAVSO)), the International Sunspot Number has been used in this study [Hathaway, 2015]. The International Sunspot Number has been obtained daily since 1849 [Wolf, 1861].

Rather than identifying individual sunspots, the "relative" sunspot number, R, is identified which counts sunspot groups

$$R = k(10g + n) \tag{2.1}$$

where k is a correction factor for the observer, g is the number of identified sunspot groups, and n is the number of individual sunspots. The recorded sunspot number for each day was made by the primary observer. J. R. Wolf was the primary observer from 1849 to 1893. His correction factor, k, was set at 1.0. He was followed by A. Wolfer, however their observing periods overlapped by 16 years. Wolfer had different instruments and had slightly different identification criteria, so he consistently observed a higher number of sunspots. He, and subsequent observers, had a correction factor of 0.6. Since 1981, the International Sunspot Number has been measured by the Royal Observatory of Belgium with S. Cortesi as the primary observer SILSO World Data Center [2016]. Instead of using numbers from a single observer, a weighted average of many observers is used, but with a correction factor associated with the primary observer. In 2015, the reference observer was changed to from Wolf to Wolfer, thus removing the 0.6 correction factor. This has meant that all sunspot numbers have been scaled to modern day values.

2.3 Coordinate systems

In geophysics, many different coordinate systems are used. The main coordinate systems used in this thesis are discussed below.

2.3.1 Geocentric Solar Magnetic coordinates

The Geocentric Solar Magnetic (GSM) coordinate system is defined as follows: the x-axis is a line that connects the centre of the Earth with the centre of the Sun, with positive x in the sunwards direction; the z-axis is the projection of the Earth's magnetic dipole axis on the plane perpendicular to the x-axis, with positive z directed northwards; and the y-axis completes the right-handed set, with positive y in the direction opposite to the Earth's motion around the Sun (duskwards). The GSM coordinate system is generally used for studying the Sun's effects on the magnetosphere.

2.3.2 Geocentric Solar Ecliptic coordinates

Geocentric Solar Ecliptic (GSE) coordinates are defined as follows: like the GSM coordinate system, the x-axis is along the Sun-Earth line, with positive x directed sunwards; the z-axis is perpendicular to the plane containing the Earth's orbit around the Sun, with positive z pointing northwards; and the y-axis completes the right-handed set, with positive y directed duskwards. y is directed opposite to the Earth's orbital motion.

Chapter 3

Literature Review

In this chapter, the literature relevant to Chapters 4, 5, 6, and 7 will be discussed, outlining the current understanding of the solar wind-magnetosphere-ionosphere system and how this affects magnetopause location. Various aspects of solar wind-magnetosphere-ionosphere coupling will be reviewed including the Dungey cycle, the expanding-contracting polar cap paradigm, methods of quantifying the amount of open magnetic flux in the magnetosphere and the dayside magnetic reconnection rate, geomagnetic storms and the ring current, and the solar cycle. Following this, an overview of previous magnetopause models will be presented, including a section that will discuss the models used in this thesis. Next, how previous studies have identified magnetopause crossings will be considered. Finally, the motivations and aims of this study will be presented.

3.1 Solar wind-magnetosphere-ionosphere coupling

Both external solar wind and internal magnetospheric parameters influence magnetopause location and shape. Therefore, it is important to understand how the systems are coupled in order to characterise the magnetopause.

3.1.1 The Dungey cycle

The model proposed by Jim Dungey in 1961, now known as the *Dungey cycle*, provided the theoretical framework to understand the large-scale structure and dynamics of the solar wind-magnetosphere-ionosphere system [Dungey, 1961, 1963]. In this model, magnetic

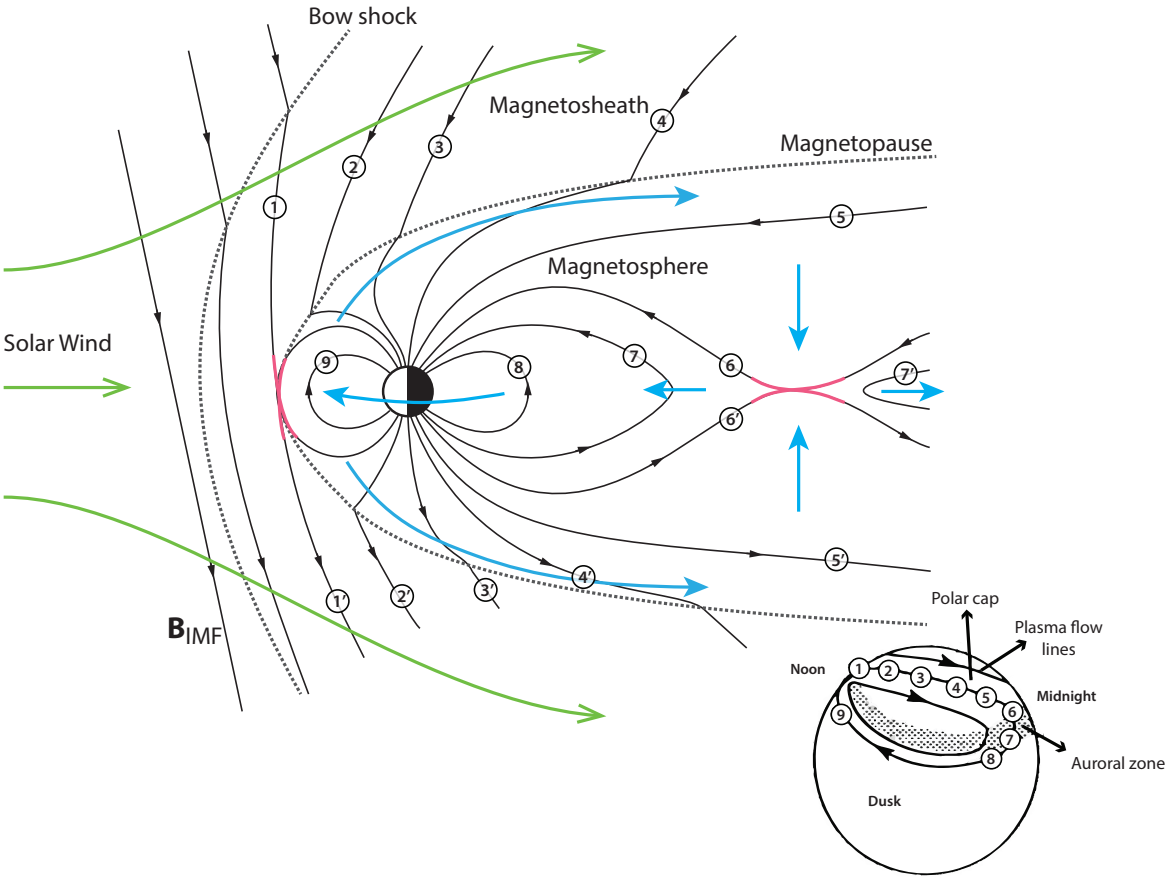

Figure 3.1: Schematic of the open magnetosphere model in the noon-midnight meridian plane. The bow shock and magnetopause boundaries are indicated by grey dotted lines. Blue arrows show the bulk plasma flow directions and black arrowed lines represent magnetic field lines. The solar wind is indicated by green arrows. The field lines are numbered to show the succession of the field lines through the Dungey cycle. Low latitude reconnection takes place at the subsolar point of the magnetopause under a southward directed IMF, B_{IMF} (1, 1'). Field lines then reconnect in the magnetotail (6, 6') and then return to the dayside magnetopause. Reconnection sites are indicated by the pink parts of the field lines. The inset shows the northern ionospheric projection of the cycle. Adapted from Hughes [1995] and Sandhu *et al.* [2016]

reconnection drives the convection in the magnetosphere (see section 1.2.4 for more detail on magnetic reconnection). When the IMF B_Z component is directed southwards, such that the magnetic shear across the dayside magnetopause is high, magnetic reconnection takes place at the subsolar magnetopause [Dungey, 1961]. When the IMF B_Z component is directed northwards, magnetic reconnection takes place at high-latitudes [Dungey, 1963].

Dungey further proposed that magnetic reconnection takes place in the magnetotail at the neutral sheet between opposite directed magnetic fields [Dungey, 1961]. This model is illustrated in Figure 3.1. Dayside and magnetotail reconnection (illustrated by the pink parts of the lines in the figure) leads to the circulation of magnetic field and the plasma (blue arrows and numbers). Under ideal MHD, Alfvén's theorem applies (as discussed in section 1.2.3). The plasma is frozen-in to the magnetic field lines, and hence the Dungey cycle drives plasma around the magnetosphere as well as the magnetic field lines.

In 1961, another competing theory was proposed by Axford & Hines [1961]. They suggested that ionospheric convection was driven by a purely viscous interaction between the solar wind and a closed terrestrial magnetosphere. The interaction is analogous in appearance to a falling raindrop. The ionospheric convection produced is similar to the twin-cell convection pattern described by the Dungey cycle, describing all auroral and magnetospheric phenomenon. Although, it is generally accepted that the Dungey cycle is the dominant source of convection in the magnetosphere, Cowley [1982] showed that viscous interactions also play a role in the convection in the Earth's magnetosphere.

3.1.2 Expanding/contracting polar cap model

Since the Dungey cycle model of the magnetosphere was proposed, studies have shown that the dayside and magnetotail reconnection rates are not always balanced [e.g. Coroniti & Kennel, 1973; Siscoe & Huang, 1985; Freeman & Southwood, 1988; Cowley & Lockwood, 1992; Milan, 2009, 2015]. Considerations of the temporal variability lead to the *expanding/contracting polar cap* paradigm (ECPC) [Russell, 1972; Siscoe & Huang, 1985; Cowley & Lockwood, 1992; Lockwood & Cowley, 1992; Taylor *et al.*, 1996; Milan *et al.*, 2003, 2006; Lockwood *et al.*, 2009c], which will be explained in this section.

Russell [1972] first suggested that the polar cap, the area of open magnetic flux at the poles, expands and contracts with the quantity of open magnetic flux in the magnetosphere. Holzer & Slavin [1978] noted that the size of the dayside and nightside magnetosphere might be moderated by magnetic reconnection. Siscoe & Huang [1985] studied dayside and nightside merging rates and suggested each would dominate under different conditions, and the polar cap would change in size correspondingly. In 1992, Cowley & Lockwood [1992] proposed the idea of the ECPC model. In this model, during intervals of southward IMF,

reconnection at the dayside magnetopause will add open magnetic flux to the magnetosphere and cause an expansion of the polar cap. In their theory, after some time, reconnection would take place in the magnetotail, and as dayside reconnection slows down, the polar cap contracts. This is demonstrated in Figure 3.2. Ionospheric convection for dayside magnetopause reconnection is displayed in Figure 3.2a., and nightside magnetotail reconnection in Figure 3.2b. The black solid circle illustrates the equatorward edge of the polar cap, known as the open/closed field line boundary (OCB). The ionospheric projection of the reconnection site, or merging gap, is shown by the black dashed lines. The direction of the ionospheric plasma flow streamlines is shown by the arrowed lines. The large white arrows show that the polar cap is expanding in Figure 3.2a. and contracting in 3.2b.

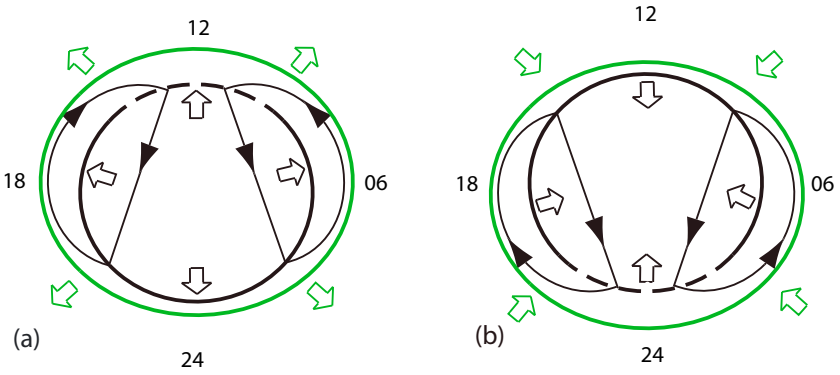

Figure 3.2: Ionospheric convection pattern driven by a. low latitude dayside reconnection and b. magnetotail reconnection. Noon is at the top, with dusk to the left in both panels. The open/closed field line boundary (OCB) is represented by the black circle, which encircles the region of open magnetic field lines. The dashed section of the circle marks the ionospheric projection of the reconnection sites, known as the merging gap. The direction of the ionospheric plasma flow streamlines is indicated by the arrowed lines. The large white arrows show the expansion (a.) and contraction (b.) of the polar cap. The Heppner-Maynard Boundary (HMB) is represented by the green oval, and the large green arrows show the motion of the HMB as the polar cap expands and contracts. Adapted from Imber *et al.* [2013a,b].

How much the polar cap expands or contracts by depends on the change in the amount of open magnetic flux in the magnetosphere, F_{PC}. Therefore, the rate of expansion of the polar cap can be determined by finding the difference between the rate of magnetic reconnection

at the dayside magnetopause, ϕ_D, and the rate of reconnection in the magnetotail, ϕ_N

$$\frac{dF_{PC}}{dt} = \phi_D - \phi_N = \frac{d}{dt}\int_{PC} \mathbf{B}.\mathbf{dS} \tag{3.1}$$

Equation 3.1 is a form of Faraday's law (equation 1.4), where **B** is the ionospheric magnetic field vector and the integral is taken over the polar cap area. ϕ_D and ϕ_N are indicated in the schematic shown in Figure 3.3. The footprints of the open magnetic field lines (blue) map to the polar cap, which is enclosed by the auroral oval (yellow). Φ_D is dependent on upstream solar wind conditions [e.g. Caan *et al.*, 1977; Perreault & Akasofu, 1978; Meng & Makita, 1986; Milan *et al.*, 2007, 2012]. If ϕ_D dominates over ϕ_N (i.e. under southward IMF conditions), the polar cap will expand. Therefore, ϕ_D can be estimated from the rate of expansion of the polar cap after a southward turning of the IMF, assuming ϕ_N is zero [Milan *et al.*, 2012]. Quantifying ϕ_D will be discussed in greater detail in section 3.1.4.

Magnetic reconnection in the magnetotail is generally considered to be the magnetospheric response to dayside driving whereby open magnetic flux which has accumulated in the tail is closed [e.g. Cowley & Lockwood, 1992; Lockwood & Cowley, 1992; Milan *et al.*, 2003, 2007, 2008; Gordeev *et al.*, 2011]. Both Cowley & Lockwood [1992] and [Lockwood & Cowley, 1992] noted that different substorm phases coincide with the expansion/contraction of the polar cap (see section 1.4.3.1 for greater detail on substorms). The expansion of the polar cap is associated with the substorm growth phase driven by dayside reconnection adding magnetic flux into the magnetosphere, whilst the contraction of the polar cap is associated with the substorm expansion phase, during which nightside reconnection dominates.

An electrostatic potential difference exists across the polar cap [e.g. Cowley & Lockwood, 1992; Lockwood & Cowley, 1992]. Assuming that the expanding/contracting polar cap remains circular, Lockwood [1991] calculated that the rate of antisunwards transport of magnetic flux across the dawn-dusk meridian, known as the cross-polar cap potential, or the electrostatic potential, usually denoted as Φ_{PC}, is given by

$$\Phi_{PC} = \frac{1}{2}(\phi_D + \phi_N). \tag{3.2}$$

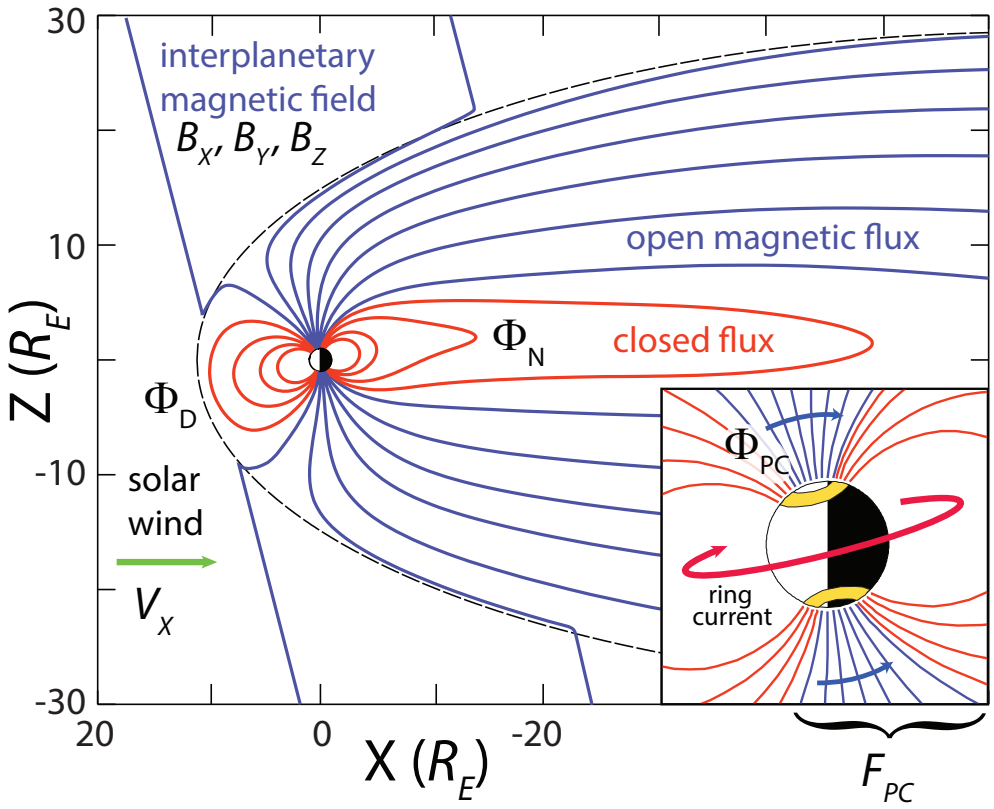

Figure 3.3: A schematic showing the magnetosphere. Closed and open magnetic field lines are denoted by red and blue lines, respectively. ϕ_D and ϕ_N quantify the rate at which flux is opened at the dayside and closed at the nightside, respectively. ϕ_D depends on the solar wind speed, V_{SW} and the strength and orientation of the IMF, B_{IMF}. The inset panel indicates the relationship between the footprint of the open magnetic flux, F_{PC}, and the size of the polar caps, the dim ionospheric regions encircled by the auroral ovals (yellow in the figure). The ring current is shown by a red arrow. Adapted from Milan *et al.* [2012].

3.1.3 Quantifying open magnetic flux

Understanding what affects the rate of change of the polar cap area is an important tool in understanding global magnetospheric dynamics. It is difficult to measure changes in the amount of open magnetic flux, $\frac{F_{PC}}{dt}$, in the magnetosphere because the dayside and nightside reconnection rates, ϕ_D and ϕ_N, are typically not equal and are difficult to quantify. Therefore, many studies have investigated the use of proxies to estimate the amount of open magnetic flux in the magnetosphere. It has been shown that the location of the open/closed field line boundary (OCB), changes in the location of the auroral ovals, magnetospheric and

ionospheric current systems, and ionospheric convection all respond to changes of the quantity of open flux in the magnetosphere. Different proxies that are commonly used will be discussed in this section.

The location of the OCB can be used as a proxy for determining the quantity of open magnetic flux in the magnetosphere. F_{PC} is defined by the area enclosed by the OCB (equation 3.1). The OCB moves due to the ECPC paradigm, which means that to determine its location, measurements must be made over all MLTs. Typically, the location of the OCB can be determined from either in situ plasma observations from polar orbiting satellites [e.g. Newell *et al.*, 1991] or global auroral imagery [e.g. Milan *et al.*, 2003; Hubert *et al.*, 2006; Østgaard *et al.*, 2007; Boakes *et al.*, 2009; Milan, 2009; Milan *et al.*, 2009a; Longden *et al.*, 2010]. The OCB latitude can be identified from satellites via the type of precipitating particle population the satellite observes. Trapped electrons with high energies are found on closed field lines [e.g. Evans & Stone, 1972], whilst low energy plasma, known as polar rain [Winningham & Heikkila, 1974], is found on open field lines. It has been possible to determine the location of the OCB to a relatively high precision since the 1980s from, for example, the DMSP satellites (Defense Meteorological Satellite Program) [e.g Hardy *et al.*, 1984; Newell *et al.*, 1991]. However, measurements of the OCB from in situ satellites are disadvantaged in that they can only provide information about the polar cap at a single point in time and cannot tell us about the total polar cap area or its temporal variation.

Alternatively, auroral images or measurements of magnetospheric and ionospheric current systems can be used to determine the location of the OCB. It is assumed that most auroras and field-aligned currents (FACs) lie on closed field lines away from the cusp regions (see section 1.4.4 for greater detail on FACs). Hence, the OCB is coincident with the poleward boundary of the auroral ovals and the FACs. It was determined in a large-scale statistical study by Boakes *et al.* [2009] that the OCB, on average, is located 5° poleward of the proton auroral oval. The circumference of the dim region inside of the auroral ovals can also be used as a proxy for the OCB [Milan *et al.*, 2003]. Auroral images from satellites in highly elliptical polar orbits can provide a global image of every few minutes over time periods of hours, enabling the study of the OCB over extended periods of time. However, the camera resolution, viewing angle, dayglow, and assumptions about the relationship between the auroral oval and the OCB all affect accuracy. In addition, the availability of high-quality

global auroral images is limited. In this thesis, auroral images from the IMAGE spacecraft which was in orbit between 2000 and 2005 are used (see section 2.1.3 for detail on the IMAGE mission). After 2008, when the POLAR mission ended, there are no global auroral images available. Observations of FACs show that they move equatorward with expansions of the polar cap [Zmuda *et al.*, 1970; Iijima & Potemra, 1978]. More recently, Clausen *et al.* [2012, 2013] have shown that the Region 1 Birkeland currents can be used as a proxy for the location of the open flux region.

As it is not always possible to determine the location of the OCB from auroral imagery or satellite measurements, another proxy that can be used is the Heppner-Maynard Boundary (HMB) [Imber *et al.*, 2013a,b]. The HMB represents the latitudinal extent of the ionospheric convection [Heppner, 1977; Heppner & Maynard, 1987] and is calculated from SuperDARN convection maps (see section 2.2.2.2 for a discussion of how the HMB is calculated). The HMB expands and contracts with the polar cap, as indicated by the green oval in Figure 3.2, with large green arrows illustrating the motion. In a large statistical study carried out by Imber *et al.* [2013a] it was found that, on average, the HMB defined at midnight is located 2.2° equatorward of the proton auroral oval, which in turn is located on average 5° equatorward of the OCB, as discussed earlier [Boakes *et al.*, 2009]. In the example data shown in Figure 3.4, the HMB is located 2° equatorward of the auroral latitude. Imber *et al.* [2013a] advise that the HMB only be used as a proxy for the polar cap area for large-scale statistical studies when auroral measurements are unavailable as the latitude of the HMB is only accurate up to $\pm 0.5°$.

3.1.4 Quantifying dayside reconnection

The primary driver of the dynamics in the magnetosphere is low-latitude reconnection at the dayside magnetopause occurring between the Earth's magnetic field and the IMF [Dungey, 1961]. Therefore, being able to measure how much magnetic flux is being added to the magnetosphere, the dayside reconnection rate, ϕ_D, will be a valuable tool to help understand how the magnetopause location and shape changes with open flux content.

Many studies have attempted to relate upstream solar wind conditions to magnetospheric activity by developing solar wind-magnetosphere coupling functions [e.g. Perreault & Akasofu, 1978; Kan & Lee, 1979; Vasyliunas *et al.*, 1982; Scurry & Russell, 1991; Siscoe *et al.*,

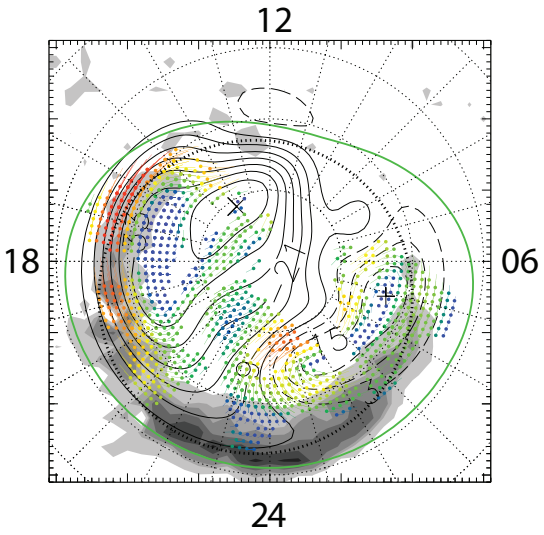

Figure 3.4: Examples of proton auroral observations, SuperDARN observations and the Heppner-Maynard Boundary (HMB) which have been projected onto a polar grid with noon at the top and dusk to the left from the 30th December 2001. Proton auroral data measured by the SI12 instrument onboard the IMAGE spacecraft (see section 2.1.3 for detail) are indicated in black. The dotted black line shows the circle of maximum brightness (see Milan *et al.* [2009b] for methods). The SuperDARN observations from the same day at 02:44 UT are indicated by coloured dots and the flow velocity is indicated by the colour, length, and direction of the line. The ionospheric potential is illustrated by the black contours (see section 2.2.2.1 for detail). The HMB is shown by the solid green line. Adapted from Imber *et al.* [2013a].

2002; Newell *et al.*, 2007; Borovsky, 2008; Milan *et al.*, 2012]. Early examples of coupling functions were typically based on upstream solar wind velocity and magnetic field strength. Later studies have considered upstream solar wind measurements in combination with in situ spacecraft observations, ground-based observations and auroral images. In this thesis, the coupling function developed by Milan *et al.* [2012] is used.

Milan *et al.* [2012] developed their coupling function by first identifying intervals from IMAGE spacecraft observations when the nightside reconnection rate was low or non-existent so that changes in F_{PC} can be attributed to the dayside reconnection rate alone. F_{PC} is estimated from images of the auroral oval taken by the Far Ultraviolet Imager (FUV) on the IMAGE spacecraft. They use the functional form

$$\phi_D = \Lambda N^{\alpha} V_X^{\beta} B_{YZ}^{\gamma} \sin^{\delta} \frac{1}{2}\theta \tag{3.3}$$

where Λ, α, β, γ, and δ are determined by fitting OMNI solar wind data to the polar cap observations. V_X is the velocity of the solar wind in GSM coordinates, B_{YZ} is the transverse component of the IMF ($B_{YZ}^2 = B_Y^2 + B_Z^2$), and θ is the clock angle, the angle between the IMF vector projected into the GSM Y-Z plane and the Z axis, i.e. $\theta = tan^{-1}(B_Y/B_Z)$. Milan *et al.* [2012] find

$$\phi_D = L_{eff}(V_X) V_X B_{YZ} \sin^{\frac{9}{2}} \frac{1}{2}\theta \tag{3.4}$$

$$L_{eff}(V_X) = 3.8 R_E (\frac{V_X}{4 \times 10^5 m s^{-1}})^{\frac{1}{3}} \tag{3.5}$$

where L_{eff} is the effective length of the reconnection site modulated by the solar wind velocity. Milan *et al.* [2012] test their function (equation 3.4) against other coupling functions and find that their function fits the variability in the polar cap area the best. They further compare their coupling function with SuperDARN cross-polar cap potential, Φ_{PC} (equation 3.2), measurements [Chisham *et al.*, 2007] which can also be used as a proxy for the dayside reconnection rate. They find a general agreement between their results and the Φ_{PC} measurements. For these reasons, the coupling function described by Milan *et al.* [2012] is used in this thesis to estimate the dayside reconnection rate.

3.1.5 Geomagnetic storms

The term "geomagnetic storm" or "magnetic storm" was first used in the mid-1800s to describe observations of large magnetic disturbances and decreases in the horizontal component of the terrestrial magnetic field [Chapman & Bartels, 1940]. Generally, geomagnetic storms are defined as periods of intense solar wind-magnetosphere coupling usually associated with extreme solar wind conditions, during which the solar wind deposits large amounts of energy and solar wind plasma into the magnetosphere, causing enhancements in the ring current [e.g. Akasofu *et al.*, 1963; Gosling *et al.*, 1990; Gonzalez *et al.*, 1994; Kamide *et al.*, 1998; Daglis *et al.*, 1999; Daglis & Kozyra, 2002; Hutchinson *et al.*, 2011]. The drivers and observational signatures, and the storm/substorm relationship are presented in this section.

Geomagnetic storms or magnetic storms result from intense periods of solar wind-magnetosphere coupling. During sustained periods of southward directed IMF and high solar wind velocities, dawn-to-dusk electric fields drive magnetospheric convection [e.g.

Tsurutani *et al.*, 1992; Kamide, 1992; Gonzalez *et al.*, 1994; Kamide *et al.*, 1998]. The solar wind ram pressure also plays a role in ring current energisation [Gonzalez *et al.*, 1989]. The solar wind events which are generally thought to cause geomagnetic storms are coronal mass ejections (CMEs) and co-rotating interaction regions (CIRs) (see section 1.3.1 for more detail on CMEs and CIRs).

CMEs are huge explosions of magnetic field and plasma from the Sun's corona, occurring most frequently during solar maximum [Webb & Howard, 1994]. CIRs on the other hand, occur when fast and slow stream regions form spirals in the equatorial plane that corotate with the Sun. If there is a large gradient in the velocity of the streams, forward and reverse shock waves form [Smith & Wolfe, 1976]. CIRs occur most during the declining phase of the solar cycle when higher solar wind velocities are observed. It has been shown that CMEs cause the most intense storms [Gosling *et al.*, 1991; Taylor *et al.*, 1994; Hutchinson *et al.*, 2011] and that CIRs cause weaker storms [Taylor *et al.*, 1994; Tsurutani *et al.*, 1995; Hutchinson *et al.*, 2011].

Low-latitude ground-based magnetometers measure the intensity of the storm-time ring current (see section 2.2.1 for more detail on the index used in this thesis). The indices most commonly used to measure the ring current are Dst and SYM-H. Both indices are a general measure of the southward magnetic deflection at the equator caused the magnetic perturbation produced by the westward-flowing ring current. Both have been in operation for a long time; hourly *Dst* values have been available since 1963, whilst 1-minute SYM-H values have been available since 1981 [Wanliss & Showalter, 2006]. It has been shown that the differences between Dst and SYM-H measurements arise from the difference in methods used to determine the values [Iyemori *et al.*, 2010]. Generally, it is agreed that SYM-H provide a higher resolution version of the Dst index [e.g. Reeves, 2003; Hutchinson *et al.*, 2011].

Geomagnetic storms undergo three phases; an initial, main and recovery phase, as indicated by the characteristic storm shown in Figure 3.5. The initial phase is triggered by an enhancement in the solar wind ram pressure typically caused by a CME or CIR. This enhancement compresses the magnetic field at the dayside magnetopause, resulting in an increase in magnetic field strength associated with the magnetic perturbation produced by enhanced magnetopause currents. A small positive increase in the SYM-H trace is observed,

as seen in the figure. The main phase depends on the duration that the IMF B_Z component remains southward, as well as its strength. Southward directed IMF drives magnetic reconnection at the dayside magnetopause, allowing large amounts of energy to be deposited into the Earth's magnetosphere [Kozyra *et al.*, 1998]. The ring current becomes enhanced which causes the equatorial magnetic field to decrease, as illustrated by the drop in SYM-H in Figure 3.5. The recovery phase is usually initiated by the IMF B_Z component becoming less southward or turning northward, or the solar wind velocity reducing, resulting in decreased driving at the dayside magnetopause. Reconnection in the magnetotail via substorms enables the system to return to normal conditions [Gonzalez *et al.*, 1994; Daglis *et al.*, 1999]. The geomagnetic storm illustrated in Figure 3.5 represents an ideal case where each phase is very clear. Often storms are less well defined than the one shown in the figure, but follow the general structure outlined above.

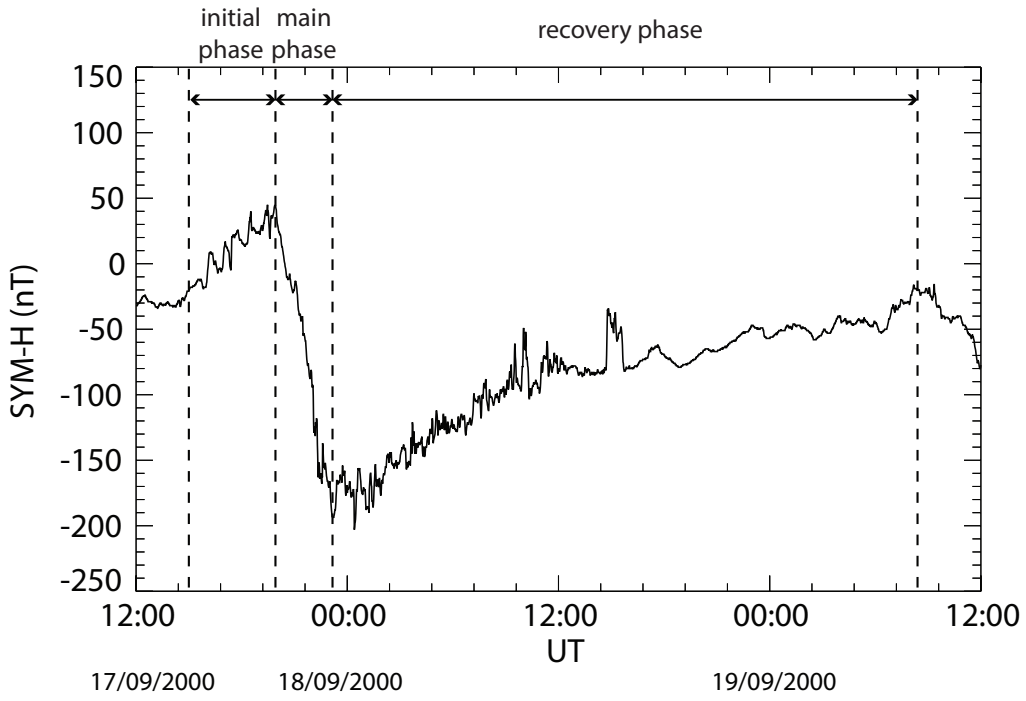

Figure 3.5: The SYM-H trace of a typical geomagnetic storm. The storm occurred on 17th September 2000. The three phases are indicated on the trace by vertical dashed lines. Adapted from Hutchinson *et al.* [2011].

Previous authors have classified the intensity of geomagnetic storms by defining different Dst or SYM-H ranges [e.g. Yokoyama & Kamide, 1997; Zhang *et al.*, 2006; Hutchinson *et al.*,

2011]. Hutchinson *et al.* [2011] define weak, moderate, and intense storms in SYM-H based on the *Dst* classifications described by Yokoyama & Kamide [1997]. Equivalent SYM-H indices are calculated by comparing the magnitude of storms in *Dst* and SYM-H [Wanliss & Showalter, 2006]. Weak storms are defined as -150 nT < SYM-H $\leq$ -80 nT, moderate storms as -300 nT < SYM-H $\leq$ -150 nT, and intense storms as SYM-H $\leq$ -300 nT [Hutchinson *et al.*, 2011]. The characteristic storm in Figure 3.5 would be classed as a moderate storm, for example.

For many years, the relationship between substorms and geomagnetic storms was much debated [e.g. Kamide *et al.*, 1998]. Substorms and storms are related because they both result from periods of southward directed IMF B_Z. In an early paper studying the relationship, Chapman [1962] reported that storms were a superposition of intense substorms. Later studies carried out during the 1990's, when spacecraft measurements were more readily available, showed that substorms and storms are separate phenomenon [e.g. Gonzalez *et al.*, 1994; Kamide *et al.*, 1998; Gonzalez *et al.*, 1999], and that geomagnetic storms do not result from a period of multiple substorms. Although increased substorm activity is often observed during geomagnetic storms [e.g. Tsurutani *et al.*, 1992], substorms occur independently of geomagnetic storms, and geomagnetic storms do not cause increased and intense substorm activity [e.g. Gonzalez *et al.*, 1994].

3.2 Solar cycle

Solar activity, as measured by various parameters, varies over an approximately 11-year cycle (see section 1.3.2 for more detail) [e.g. Hathaway, 2015]. The two most recent solar cycles, solar cycle 23 and 24, contained several unusual features such as an extended and deep solar minimum, and the weakest solar activity since the early 20st century. Typical observations of various solar wind parameters over the solar cycle will be discussed in this section, as well as characteristics of solar cycles 23 and 24.

3.2.1 Solar cycles 23 and 24

The period of study in this thesis (1st January 1996 - 31st December 2015) occurs during solar cycle 23 and 24. Table 3.1 indicates the start times of the two cycles (solar minimum)

and when solar maximum occurred. Figure 3.6 depicts the sunspot numbers over the period being studied. The section highlighted in blue is solar cycle 23 and the section highlighted in red is solar cycle 24. The solar minimum that happened at the end of solar cycle 23 contained several highly unusual features. The solar minimum was the longest and deepest of the space age (see Figure 1.9), with the longest number of consecutive spot-free days since 1913. There was a significant reduction in the solar wind velocity and density [McComas *et al.*, 2008], and the heliospheric magnetic field was the weakest observed in recent years [Lockwood *et al.*, 2009a,b]. Furthermore, the polar magnetic field was observed to be the lowest since 1975, when routine photospheric magnetic field measurements began [Wang *et al.*, 2009].

Solar cycle	Start	Maximum
23	August 1996	November 2001
24	December 2008	April 2014

Table 3.1: Start dates and maxima of solar cycles 23 and 24.

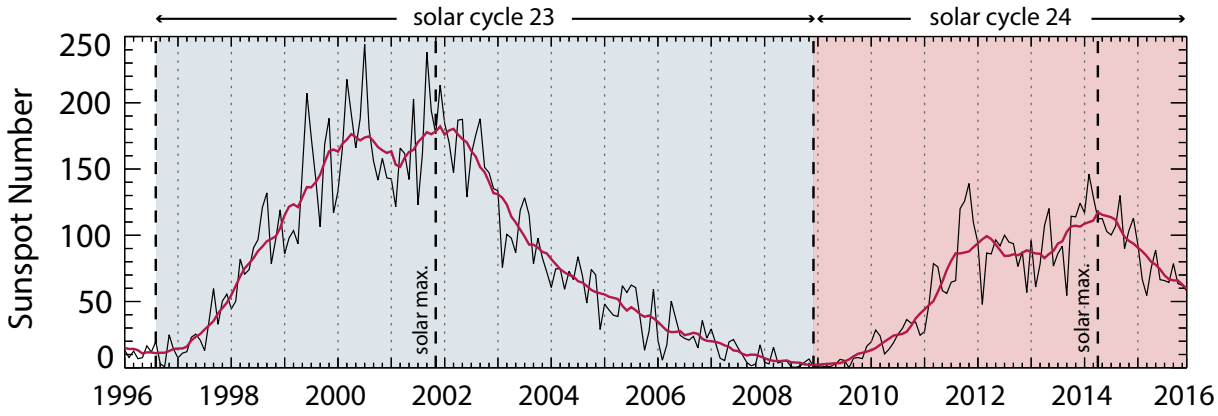

Figure 3.6: Sunspot numbers from January 1996 to December 2015. The black line indicates the monthly mean sunspot numbers, whilst the red line indicates the sliding 12-month mean sunspot numbers. Solar minima and maxima are illustrated by the black dashed lines. Solar cycle 23 is highlighted in blue and solar cycle 24 is highlighted in red. Sunspot numbers are from SILSO World Data Center [2016].

Solar cycle 24 began in 2008 and is still ongoing at the time of writing this thesis. Its maximum is much lower than the previous solar cycle and it is the lowest solar maximum in approximately a century, with an average of 120 sunspots at maximum in 2014. It is

characterised by a double peak, of which, the second peak is larger than the first [Javaraiah, 2017]. Solar cycle 24 is in the descending phase at the end of the time interval included in this thesis.

Since 1985, average solar activity has been declining [Lockwood & Fröhlich, 2007]. Prior to this however, it is believed that the Sun was in a Grand Solar Maximum of activity. In a study carried out in 2008 that looked at Grand Solar Maxima detected from cosmogenic ice-core data over almost 10,000 years, it was estimated that the current Grand Solar Maxima would only last a further 15-36 years, and solar activity would decline over the next two or three cycles [Abreu *et al.*, 2008]. The low solar activity of solar cycle 24 appears to support this prediction. It has been suggested that the Sun is now entering a Grand Solar Minimum, during which solar activity is greatly reduced [e.g. Usoskin, 2017]. The most famous solar minimum is known as the Maunder Minimum which occurred in the late 17th century [e.g. Eddy, 1976; Usoskin *et al.*, 2015]. During such minima, solar activity reduces and very few sunspots are observed [Cliver *et al.*, 1998; Usoskin *et al.*, 2001]. For example, it was estimated that the solar wind velocity during the Maunder Minimum was uniform and slow, with approximate velocities of 250-275 km s^{-1}, which is nearly half the average velocities seen in modern times [Lockwood & Owens, 2014]. Predictions based on solar and heliospheric parameters during the current solar cycle suggest that Maunder Minimum conditions are likely to descend within the next 40 years [Owens *et al.*, 2011].

Magnetopause location is strongly dependent on upstream solar wind conditions and therefore, it is important to understand how solar wind parameters vary with solar cycle. Parameters such as solar wind velocity, dynamic pressure and IMF strength have been observed to vary over the solar cycle [e.g. Neugebauer, 1975; Gosling *et al.*, 1976; Fairfield, 1979; Grzedzielski & Lazarus, 1993; Fairfield, 1995; Richardson *et al.*, 1996]. Since the two most recent solar cycles contained unusual behaviour such as the long solar minimum at the end of solar cycle 23 and the relatively weak activity in solar cycle 24, they have provided a unique opportunity to study magnetopause location under relatively quiet conditions.

3.3 Magnetopause location

It was first established by Chapman & Ferraro [1931] that the most important controlling factor of magnetopause location and shape is solar wind dynamic pressure (see section 1.4.2.2). At the nose of the magnetopause, the ram pressure of the solar wind is in balance with the magnetic pressure exerted by the terrestrial magnetic field [Schield, 1969]. Consequently, variations in upstream ram pressure cause changes in magnetopause position and shape [e.g. Chapman & Ferraro, 1931; Sibeck *et al.*, 1991; Sotirelis & Meng, 1999].

Magnetopause shape is also strongly influenced by the direction and magnitude of the north-south component of the IMF (B_Z) [e.g. Aubry *et al.*, 1970, 1971; Maezawa, 1974; Fairfield, 1991, 1995; Sibeck *et al.*, 1991; Roelof & Sibeck, 1993; Sibeck *et al.*, 2000]. When IMF B_Z is orientated southwards, reconnection takes place at the dayside magnetopause eroding magnetic flux in this region and causing the nose of the magnetopause to move closer to the planet. The newly opened magnetic flux is convected to the magnetotail [Dungey, 1961; Mead & Beard, 1964; Milan *et al.*, 2004], and inflates the nightside magnetosphere. After some time, the open magnetic flux is closed by reconnection in the magnetotail and is convected back to the dayside.

Many empirical models have been developed to describe and predict the position and shape of the Earth's magnetopause [e.g. Fairfield, 1971; Holzer & Slavin, 1978; Sibeck *et al.*, 1991; Petrinec *et al.*, 1991; Roelof & Sibeck, 1993; Petrinec & Russell, 1993; Kuznetsov & Suvorova, 1996; Petrinec & Russell, 1996; Elsen & Winglee, 1997; Shue *et al.*, 1997, 1998; Kuznetsov & Suvorova, 1998; Kawano *et al.*, 1999; Kalegaev & Lyutov, 2000; Chao *et al.*, 2002; Verigin *et al.*, 2009; Dmitriev *et al.*, 2011]. They are generally built from large numbers of magnetopause crossings identified by in situ spacecraft observations and are typically parameterised by the solar wind dynamic pressure and IMF B_Z. Elliptical functions that depend on magnetopause standoff distance and eccentricity parameters are often used to describe the shape. Ellipsoid models are limited however, as they must close and hence cannot represent an open magnetosphere [Fairfield, 1995]. Parabolic functions are also often used and rotational symmetry is usually assumed.

Some studies have investigated the impact of other parameters on magnetopause location. It was suggested that large asymmetries would be introduced at the near-Earth high-

latitude magnetopause if the effect of dipole tilt angle was taken into account [e.g. Petrinec & Russell, 1995; Sotirelis & Meng, 1999; Eastman *et al.*, 2000; Boardsen *et al.*, 2000; Dmitriev & Suvorova, 2000; Šafránková *et al.*, 2004; Lin *et al.*, 2010]. Some of these studies have developed empirical models that are asymmetric and three-dimensional which are parameterised by the dipole tilt angle, as well as the solar wind ram pressure and IMF B_Z. These models are able to reproduce the indentations made by the magnetic cusps.

The magnetopause crossing datasets used to develop the empirical models described above primarily contain dayside magnetopause crossings, with far fewer magnetopause crossings at the flanks and downtail. Magnetic reconnection on the dayside magnetosphere drives large-scale dynamics, and hence the dayside magnetopause has been more extensively studied with several missions focussing on observing this region. This has provided a more extensive database of magnetopause crossings at the dayside than at the flanks or downtail region, however models based largely on dayside magnetopause crossings may not be as accurate in characterising the magnetotail. A further limitation of these models is that many do not include extreme events, or only include crossings from a limited time period during part of the solar cycle.

3.3.1 Shue *et al.* [1997, 1998] and Lin *et al.* [2010] models

In later chapters, the functional form and methods employed by Shue *et al.* [1997, 1998] are applied to develop a simple model to predict magnetopause location based on magnetopause crossings identified in this study. Models defined by Shue *et al.* [1997, 1998] and Lin *et al.* [2010] are then compared with observations of magnetopause location (determined from spacecraft data) and with the empirical model developed in this study. The Shue *et al.* [1997, 1998] and Lin *et al.* [2010] models will be presented and discussed here.

3.3.1.1 Shue *et al.* [1997, 1998] models

Shue *et al.* [1997, 1998] models the magnetopause location using a parabolic function. It is a relatively simple function and describes the shape and location of the Earth's magnetopause using two inputs; the subsolar standoff distance and the flaring of the magnetotail. This function is axisymmetric around the aberrated Sun-Earth line and therefore does not describe the magnetopause at high latitudes. However, it is satisfactory because the

spacecraft exploited in this study primarily orbits in the equatorial plane and does not pass through the magnetic cusps. The function is defined as follows [Shue *et al.*, 1997, 1998]

$$r = r_0 \left(\frac{2}{1 + \cos\theta} \right)^{\alpha} \tag{3.6}$$

where r is the radial distance and θ is the solar zenith angle, r_0 is the magnetopause standoff distance, and α describes the level of flaring in the magnetotail. It has the flexibility to produce both an open and closed magnetopause depending on the value of α. Figure 3.7 illustrates how the function given in equation 3.6 varies with increasing r_0 for a fixed value of α (a.), and how the function varies with increasing α with a fixed value of r_0 (b.).

Shue *et al.* [1997] obtain functions for r_0 and α that depend on solar wind dynamic pressure and IMF B_Z using a bivariant best fit. They are developed from 553 magnetopause crossings identified from International Sun-Earth Explorer (ISEE) 1 and 2, Active Magnetospheric Particle Tracer Explorers/Ion Release Module (AMPTE/IRM), and Interplanetary Monitoring Platform (IMP) 8 primarily during the years 1977 to 1987. They fit the function to the identified magnetopause crossings using the linear least squares technique. The magnetopause crossings are separated into overlapping bins for B_Z and P_{Dyn}. The magnetopause crossings from which their model is developed are mainly found in the equatorial plane. The model developed is valid for the ranges -18 nT $< B_Z <$ 15 nT and 0.5 nPa $< P_{Dyn} <$ 8.5 nPa. Solar wind data are obtained from the IMP 8 and ISEE 3 spacecraft which primarily orbited in the solar wind. The solar wind data has a resolution of 5 minutes. The functions for r_0 and α are as follows

$$r_0 = \begin{cases} (11.4 + 0.013B_Z)P_{Dyn}^{-1/6.6} & B_Z \geq 0 \\ (11.4 + 0.14B_Z)P_{Dyn}^{-1/6.6} & B_Z < 0 \end{cases} \tag{3.7}$$

$$\alpha = (0.58 - 0.010B_Z)(1 + 0.010P_{Dyn}) \tag{3.8}$$

The dependence of r_0 on B_Z changes depending on whether B_Z is directed northwards (B_Z > 0 nT) or southwards (B_Z < 0 nT). When the IMF B_Z component is directed southwards, there is a greater gradient in the function which accounts for dayside magnetopause erosion as a consequence of magnetic reconnection. When the IMF B_Z component is directed northwards, some magnetic flux is added back to the dayside magnetosphere

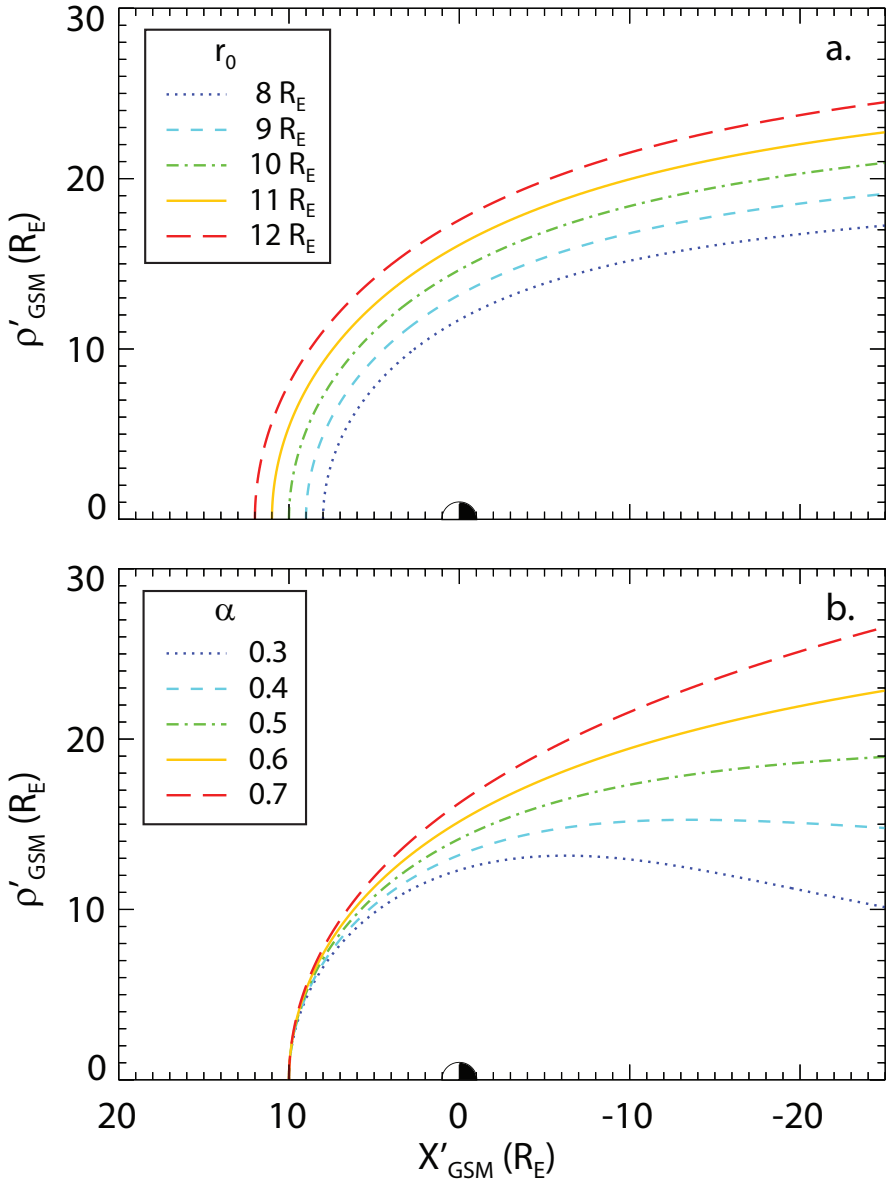

Figure 3.7: Graphical representation of how the function given by Equation 3.6 varies with a. fixed α ($\alpha = 0.5$) with varying r_0, and fixed r_0 ($r_0 = 10R_E$) with varying α. The function is plotted in the $X'_{GSM} - \rho'_{GSM}$ plane (where ρ' is defined as $\sqrt{Y'^2_{GSM} + Z^2_{GSM}}$). Adapted from Shue *et al.* [1997].

via high-latitude magnetic reconnection [e.g. Gosling *et al.*, 1991; Song & Russell, 1992]. A power law of -1/6.6 with respect to the solar wind dynamic pressure is found by Shue *et al.* [1997] for the magnetopause standoff distance. This differs from the theoretical prediction of -1/6 (for a dipole magnetic field); however, the authors suggest that this could be due to either the thermal pressure inside of the magnetosphere, or neglecting magnetic pressure in the solar wind. The magnetopause crossing database used to develop the Shue *et al.*

[1997] model only includes 21 magnetopause crossings beyond 10 R_E downtail due to gaps in the magnetospheric and solar wind datasets. This may introduce some inaccuracies to the prediction of the magnetopause location in this region.

As the Shue *et al.* [1997] model cannot predict magnetopause location under extreme solar wind conditions, they later re-visited their work to assess its prediction capabilities during a magnetic cloud event that occurred on 11$^{\text{th}}$ January 1997 [Shue *et al.*, 1998]. During this event, the dayside magnetopause was located inside geosynchronous orbit. They found that although their model could predict the dayside magnetopause fairly accurately, predictions at the flanks were less accurate. To improve their model, a hyperbolic tangent function was introduced to their r_0 fit for B_Z, and a natural logarithm was introduced to their α fit for P_{Dyn} to prevent r_0 and α from becoming unphysical during extreme events. The new model is given below

$$r_0 = 10.22 + 1.29\tanh[0.184(B_Z + 8.14)]P_{Dyn}^{-1/6.6} \tag{3.9}$$

$$\alpha = (0.58 - 0.007B_Z)[1 + 0.024\ln(P_{Dyn})] \tag{3.10}$$

Figure 3.8 illustrates the Shue *et al.* [1998] model under different solar wind conditions. In panel a. the solar wind dynamic pressure is varied between 0.5 nPa and 4.5 nPa, whilst keeping the IMF B_Z component constant at 0.0 nT. Panel b. shows the magnetopause location under varying IMF B_Z between - 5.0 nT and 5.0 nT, whilst keeping the solar wind dynamic pressure constant at 2.5 nPa. As can be seen in the figure, solar wind dynamic pressure has a greater effect on magnetopause location at all MLTs than IMF B_Z. Under different IMF B_Z values, the nose of the magnetopause does not vary greatly, but the flanks flare under southward B_Z.

3.3.1.2 Lin *et al.* [2010] model

The other model that will be used in later chapters was defined by Lin *et al.* [2010]. The Lin *et al.* [2010] model is three-dimensional and predicts magnetopause location based on solar wind dynamic and magnetic pressures (P_{Dyn} and P_M), IMF B_Z, and dipole tilt angle (ϕ). The model is developed from a database of 980 magnetopause crossings detected at all latitudes during the years 1994 to 2008 by a variety of spacecraft including Cluster, Time

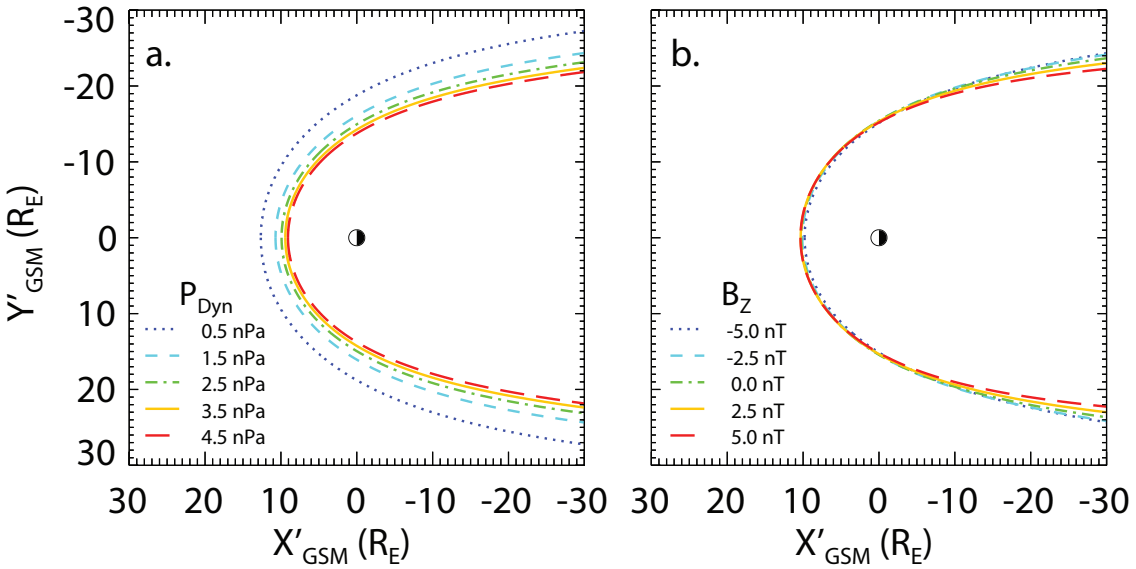

Figure 3.8: The Shue *et al.* [1998] model of magnetopause location under a. varying solar wind dynamic pressure with constant B_Z ($B_Z = 0$ nT), and b. varying IMF B_Z with constant solar wind dynamic pressure ($P_{Dyn} = 2$ nPa). The magnetopause is shown in the X-Y plane, although it would be identical in X-Z as the Shue *et al.* [1998] model is axis-symmetric.

History of Events and Macroscale Interactions during Substorms (THEMIS), Geotail, IMP 8, Interball, TC1, Polar, Los Alamos National Laboratory (LANL), GOES and a database of 1482 Hawkeye magnetopause crossings detected during the years 1974 to 1978 which are used to define the indentations caused by the cusps. This model is able to predict the asymmetries of the magnetopause, and the depth and location of the indentations near the magnetic cusps.

The Lin *et al.* [2010] model is developed on the basis of the Shue *et al.* [1997, 1998] function and employs the Levenberg-Marquardt method for non-linear multiparameter fitting (see Lin *et al.* [2010] for greater detail). The function contains 21 coefficients which are listed in the paper. They find a power law index defining how r_0 depends on P_{Dyn} of -1/5.15, which is lower than the theoretical prediction of -1/6. Figure 3.9 illustrates the Lin *et al.* [2010] model for varying solar wind dynamic pressure (0.5 nPa to 4.5 nPa), with a constant IMF B_Z of 0.0 nT (panels a. and c.), and varying IMF B_Z (-5.0 to 5.0 nT), with a constant solar wind dynamic pressure of 2 nPa (panels b. and d.). In their model, as the solar wind dynamic pressure increases, the magnetopause decreases in size but remains self-similar, as can be seen in Figure 3.9 in panels a. and c. On the other hand, as the IMF B_Z becomes

more southward, the dayside magnetopause moves closer to the planet indicative of erosion of magnetic flux, and the nightside magnetopause inflates, as can be seen in Figure 3.9 panels b. and d. Under northward IMF B_Z, the magnetopause location and shape does not change showing that it does not depend on the strength of B_Z.

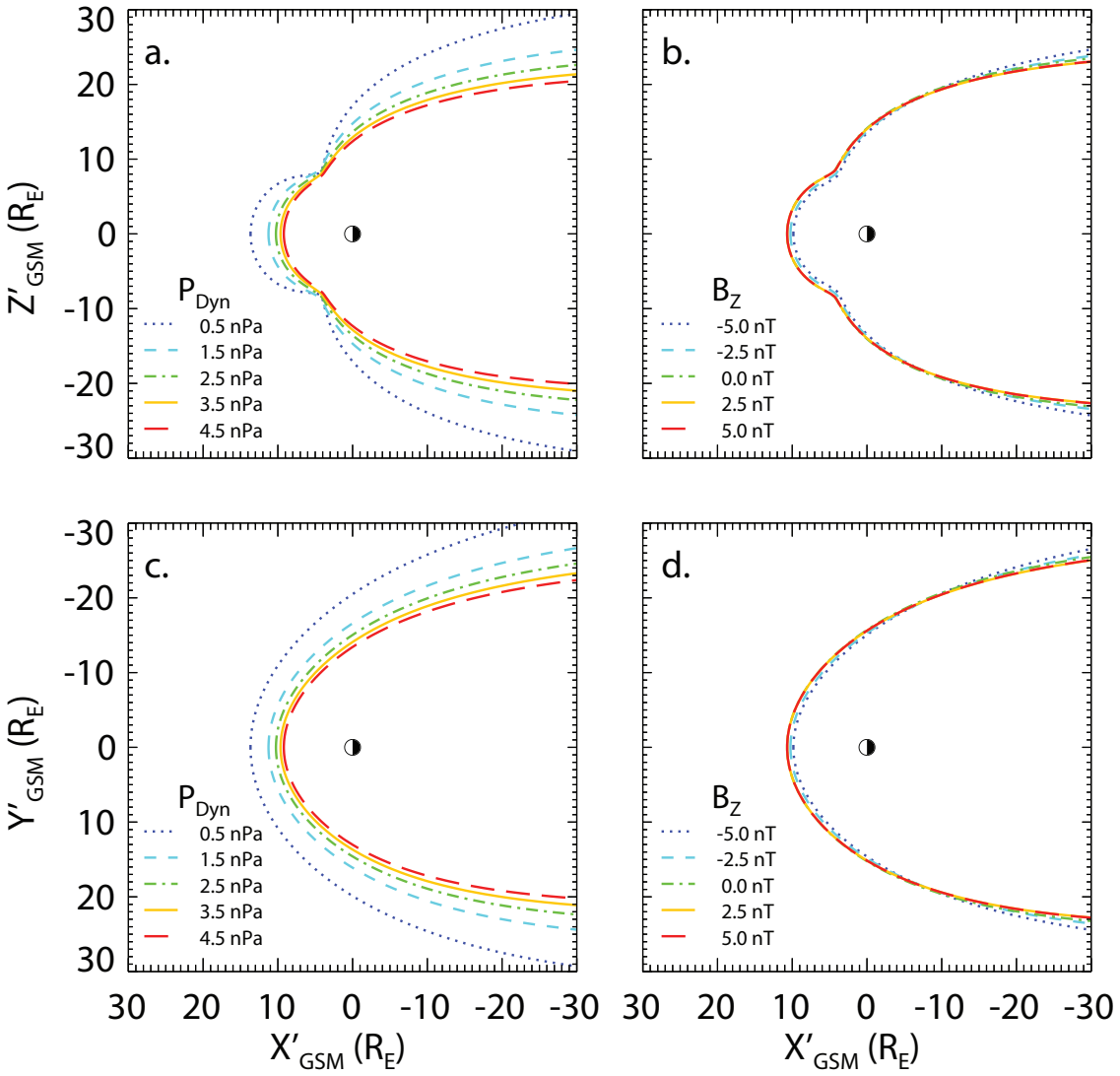

Figure 3.9: The Lin *et al.* [2010] model of magnetopause location under a. varying solar wind dynamic pressure with constant B_Z ($B_Z = 0$ nT) in the X-Z plane, and b. varying IMF B_Z with constant solar wind dynamic pressure ($P_{Dyn} = 2$ nPa) in the X-Z plane. Panels c. and d. are the same as a. and b. but in the X-Y plane. The dipole tilt angle is set to zero in all panels and the magnetic pressure is kept constant.

3.4 Determining magnetopause location

To understand how the magnetopause responds to a combination of both varying upstream solar wind conditions and internal magnetospheric conditions, its location must be determined. Typically, when a spacecraft encounters the magnetopause it observes a change in direction and magnitude of the magnetic field. Most previous studies utilise magnetic field data to identify magnetopause crossings, partly because detecting a magnetopause encounter in this way is relatively straightforward, but also because magnetic field data are commonly available. Some studies use plasma data either in a combination with magnetic field data, or to check the magnetopause crossings identified from magnetic field data. Chapter 1 details the typical magnetic field and plasma conditions observed on either side of the magnetopause boundary.

Depending on both the spacecraft's trajectory and where on the magnetopause boundary it crosses, the spacecraft might pass through the magnetopause quickly, or it might skim the boundary and cross it multiple times. It was first reported that the magnetopause boundary can vary in thickness from around 400 km to 1000 km by Berchem & Russell [1982], however later studies have found that magnetopause thickness can vary from 500 km to 1500 km, and that the flanks are typically thicker than the dayside magnetopause [Haaland *et al.*, 2014]. It is well established in the literature that Kelvin-Helmholtz instabilities form at the magnetopause flanks and downtail, and this will cause a variation in thickness [e.g. Sonnerup, 1980; Haaland *et al.*, 2014]. Furthermore, the magnetopause is in constant motion with velocities ranging from 10 km s^{-1} to 80 km s^{-1} primarily due to changes in upstream conditions, but also as a consequence of surface waves [Berchem & Russell, 1982; Haaland *et al.*, 2014].

Magnetopause boundary crossings are often identified either visually [e.g. Haaland *et al.*, 2014], or through the use of an automated routine [e.g. Ivchenko *et al.*, 2000; Case & Wild, 2013]. A magnetopause crossing identified by one observer may not be identified by another. Automated routines have the benefit that they can be easily applied to large datasets and so are less labour-intensive, however the criteria used to identify magnetopause crossings are still defined by an observer.

3.4.1 Ivchenko *et al.* [2000] and Case & Wild [2013] routines

In this thesis, the magnetopause crossing detection method is developed from criteria presented by Ivchenko *et al.* [2000] and Case & Wild [2013]. Their work will be reviewed in this section.

3.4.1.1 Ivchenko *et al.* [2000] routine

Like many previous studies, Ivchenko *et al.* [2000] identify magnetopause traversals from magnetic field data. They applied their method to two and a half years (1995 to 1997) of magnetic field measurements from the Geotail spacecraft to study the magnetopause. Ivchenko *et al.* [2000] detected 1369 magnetopause crossings at the dayside magnetopause and near the magnetopause flanks ($X_{GSM} \geq$ -5 R_E). Ivchenko *et al.* [2000] use the following four criteria to determine when Geotail passed through the magnetopause boundary:

1. The transition should be completed within 30 seconds.
2. The standard deviation of the magnetospheric magnetic field is required to be less than 40% of the magnetic field on the magnetosheath side of the assumed boundary.
3. the northward component of the magnetospheric magnetic field is required to exceed 10 nT.
4. The northward component of the magnetospheric magnetic field is required to be at least a factor of 1.3 times greater than the corresponding magnetosheath component.

If two magnetopause crossings occurred within 40 s of each other they are not included in the dataset. The magnetic field data for each detected magnetopause crossing was visually inspected and if there was uncertainty, the crossings were not included. Some magnetopause crossings were further cross-checked with plasma data.

3.4.1.2 Case & Wild [2013] routine

Case & Wild [2013] exploited 8 years of magnetic field measurements from the Cluster mission (2002 to 2010) to compare magnetopause location with four models. The four Cluster spacecraft have an elliptical polar orbit meaning that the Cluster spacecraft were able to pass through the magnetopause at a wide range of latitudes. Because of this, Case

& Wild [2013] modified the Ivchenko *et al.* [2000] magnetopause crossing detection criteria and applied their adapted routine at the dayside magnetopause ($X_{GSM} \geq 0\ R_E$).

Case & Wild [2013] use a running average method to identify magnetopause crossings from Cluster data. In their study they look at two 3-minute intervals of magnetic field data separated by a 32 second interval (equivalent to eight spins of the Cluster spacecraft). The intervals are then tested against a modified version of Ivchenko *et al.* [2000] criteria, listed below:

1. The transition across the magnetopause boundary should be completed within 32 s.
2. Multiple magnetopause crossings should not occur within 10 min.
3. The standard deviation of the 3 min window of magnetosheath magnetic field must be greater than 4.5 on average, and it must be a factor of 2.5 times larger than the standard deviation of the 3 min window of magnetospheric magnetic field.
4. At low latitudes the B_Z and at high latitudes the B_r components of the magnetospheric magnetic field must be greater than 10 nT.
5. The particular magnetospheric magnetic field component, as determined by criterion 4, must be a factor of at least 1.3 times greater than the corresponding magnetosheath magnetic field component.

If all of the criteria are met, then a magnetopause crossing is detected and the three intervals are shifted by 10 min. If a magnetopause crossing is not detected, the time intervals are shifted by 4 s. Criterion 2 means that multiple magnetopause crossings are not included in their database and the first detection of the magnetopause represents the magnetopause location. Case & Wild [2013] note that a threshold of 10 nT for the observed terrestrial magnetic field is a conservative estimate in criterion 4, and enforce that it must be greater than 1.3 times the observed magnetosheath magnetic field to avoid identifying small changes in the magnetic field as magnetopause crossings. However, this could mean that when the IMF has a similar orientation to the terrestrial magnetic field (under northward B_Z), magnetopause crossings would be underrepresented. Case & Wild [2013] identify 2640 magnetopause crossings during which OMNI data are available.

3.5 Motivation and aims

The magnetopause is the barrier between the Earth's magnetic field and the incoming solar wind and embedded interplanetary magnetic field (IMF). It shields the Earth from harmful space weather events that can affect ground-, air- and space-based technologies like power grids, transport, and satellite communications. Therefore, understanding where it is and what causes its location to vary is of utmost importance to improve our understanding and predictive capabilities of space weather and hence is the main motivation of this study.

Although the magnetopause has been studied extensively before, the aims of this thesis are to study the magnetopause over the two most recent solar cycles, look at long-term variations in its location and shape, and to investigate the effects of other solar wind and magnetospheric processes. To carry out this study on the magnetopause, data from the Geotail spacecraft has been used. Geotail was chosen because its orbital properties mean that it frequently crosses both the dayside and nightside in the equatorial plane, and it has been in orbit for 26 years at the time of this thesis, meaning we are able to perform a long-term study. More detail about Geotail can be found in section 2.1.1.

To achieve the aims of this thesis, a new magnetopause crossing detection routine is developed that can identify magnetopause crossings much further downtail that previous studies (Chapter 4). We use the methods and criteria discussed by Ivchenko *et al.* [2000]; Case & Wild [2013] and develop new criteria that can be applied downtail. Using an automated routine to identify magnetopause crossings has the benefit that it can be applied to a long period of data making it much less labour-intensive than identifying magnetopause crossings by eye. This automated routine could be used further with other datasets, which could increase the number of identified magnetopause crossings and cover distances even further downtail.

The magnetopause crossing dataset is then used to develop a new simple empirical magnetopause model using similar methods to Shue *et al.* [1997] (Chapter 4). A new model is developed rather than using a model developed by previous authors because it is able to more accurately describe the magnetopause crossings identified in this study than models developed using different datasets. This is verified in Chapter 5, in which we compare the predictive capabilities of our model and models defined by Shue *et al.* [1998]; Lin *et al.* [2010].

The magnetopause crossing dataset identified in this study contains a greater number of magnetopause crossings than previous studies and includes crossings from much further downtail than previous studies, during the two most recent solar cycles.

Solar cycle 23 and 24 were unique in that they were relatively weaker than previous solar cycles and contained an extended and deep solar minimum. The new model and magnetopause crossings are used to investigate long-term changes in magnetopause location and shape over these two solar cycles (Chapter 5). Comparisons between the predicted magnetopause and actual magnetopause location are made and conclusions about what affects shape and location are drawn (Chapter 6).

Finally, it is the aim of this study to investigate how other solar wind and magnetospheric processes affect magnetopause shape and location (Chapter 7). We examine the effects of IMF B_Z and dayside reconnection rate, under different solar wind dynamic pressure strengths. We also investigate the effects of the amount of open flux content inside the magnetosphere and ring current strength.

Background theory, instrumentation and datasets, and a review of the literature relevant to this thesis have been presented in Chapters 1, 2 and 3. The next chapter presents the magnetopause crossing identification and magnetopause model (Chapter 4). The following three chapters utilise the results presented in Chapter 4 to investigate the shape and location of the magnetopause further. Firstly, solar cycle influences on the shape and location of the magnetopause (Chapter 5) are discussed, followed by an analysis of the differences between the observed and modelled location of the magnetopause (Chapter 6), and finally solar wind and magnetospheric influences on the shape and location of the magnetopause are presented (Chapter 7). Conclusions from this thesis and future work are discussed in Chapter 8.

Chapter 4

Magnetopause crossing identification and magnetopause model

In this chapter, criteria are developed to identify when the Geotail spacecraft passes through the magnetopause. All magnetopause crossings detected by the routine are presented and methods to develop a simple model of magnetopause location are discussed.

4.1 Magnetopause crossing identification

The conditions in the magnetosphere and in the magnetosheath are very different. In the equatorial plane near the magnetosheath, the magnetosphere is comprised of a strongly northward terrestrial magnetic field with a low-plasma density. The magnetic field in the magnetosheath is more turbulent and has a much higher plasma density. A set of criteria to determine when a spacecraft crosses the magnetopause can be established from understanding the properties in the two regions.

4.1.1 Detection criteria

The automated routine used in this study to determine when Geotail traverses the dayside magnetopause is based on detection criteria defined by Ivchenko *et al.* [2000] and Case & Wild [2013] (see section 3.4.1 for a review of the literature). A similar running average method to that employed by Case & Wild [2013] is used in this investigation to identify magnetopause crossings. The Geotail data is separated into a 3-minute interval, followed

by a 36 second (three plasma measurements) interval and finally another 3-minute interval. The automated routine determines whether there are magnetospheric conditions in one of the 3 min intervals, magnetosheath conditions in the other 3-minute interval and a crossing taking place over the 36 second interval. If a magnetopause crossing is not found, the three intervals are shifted by 12 seconds to the next data point and are tested against the criteria. If all the criteria are satisfied, then a magnetopause crossing is identified.

At the nightside and flanks of the magnetopause, conditions can be very different to those observed at the magnetopause nose. Consequently, two different sets of criteria are used to identify a magnetopause crossing depending on where Geotail encountered the magnetopause.

4.1.1.1 Magnetopause nose crossings ($X_{GSM} \geq 5\ R_E$)

Although plasma data are available from Geotail, they have not been used at the magnetopause nose region ($X_{GSM} \geq 5\ R_E$) since it is difficult to determine magnetopause crossings from plasma measurements due to the subsolar stagnation point. At the stagnation point the component of the magnetosheath plasma velocity in the Earth-Sun direction gradually decreases to zero and sharp plasma density gradients are observed due to the pile-up of solar wind plasma in front of the magnetopause. The magnetic field is compressed due to the draping of field lines around the magnetopause nose and magnetic pressure increases. This leads to the magnetosheath plasma being squeezed out of the flux tubes into the magnetosheath flanks diluting the magnetosheath plasma density at the nose [Baumjohann & Treumann, 1997]. The location of the pile-up region depends on the incoming solar wind conditions; thus, magnetopause crossings have been identified from magnetic field measurements in this region.

The criteria for detecting magnetopause nose crossings are modified from those described by Ivchenko *et al.* [2000] and Case & Wild [2013] and are as follows:

1. The crossing must take place within the 36 second interval.

2. The standard deviation of the total magnetic field strength in the magnetosheath interval must be greater than 4.5 nT, and it must be at least 2.5 times larger than the standard deviation of the total magnetic field strength of the magnetosphere interval.

3. The total magnetic field strength in the magnetosphere 3 minute interval must be greater than that of the magnetosheath.

4. The average B_Z component of the magnetic field in the magnetosphere 3 min interval must be greater than or equal to 10 nT, and be 1.3 times larger than the average of magnetosheath 3 min interval. 10 nT is a conservative estimate of the Earth's magnetic field, it is generally expected to be higher.

The above criteria ensure that there is a sharp change in magnetic field strength as Geotail passes through the boundary, that the magnetic field in the magnetosheath is fluctuating more than the magnetospheric magnetic field, and the average magnetic field in the magnetosphere is larger than in the magnetosheath and directed northward. Unlike Case & Wild [2013], in this thesis multiple magnetopause crossings have been included in the database. By doing this, we ensure that the identified magnetopause crossing is not the innermost or outermost crossing depending on whether Geotail was traversing into the magnetosheath or magnetosphere, respectively. How multiple magnetopause crossings are dealt with will be discussed in greater detail in section 4.2.1.

Example magnetic field and plasma data are shown in the left panels in Figure 4.1 along with the orbital path of Geotail on the right. Panels a.-d. show the magnetic field strength in the Z_{GSM} direction, the total magnetic field strength, the velocity of the plasma in the X_{GSM} direction, and the density of the plasma observed by Geotail, respectively for a 2 hour period on 11$^{\text{th}}$ February 1997. The red dotted line indicates the magnetopause crossing identified by the algorithm described in this section. During the first hour of this example interval Geotail is located inside the magnetosphere, which is determined by the strongly northward magnetic field, approximately 0 km s^{-1} velocity and low density. At around 05:00 UT, Geotail traverses the magnetopause boundary. At the time of the traversal there is a sharp change in the direction of the B_Z component of the magnetic field. The total magnetic field strength becomes more varied as Geotail enters the magnetosheath. In this example, only a single magnetopause crossing is found.

Panel e. shows the orbital path taken by Geotail during the corresponding period, indicated by the dotted line. The Sun is to the left of the panel in the positive X'_{GSM} direction (where the apostrophe indicates that the coordinate system has been rotated to correct for

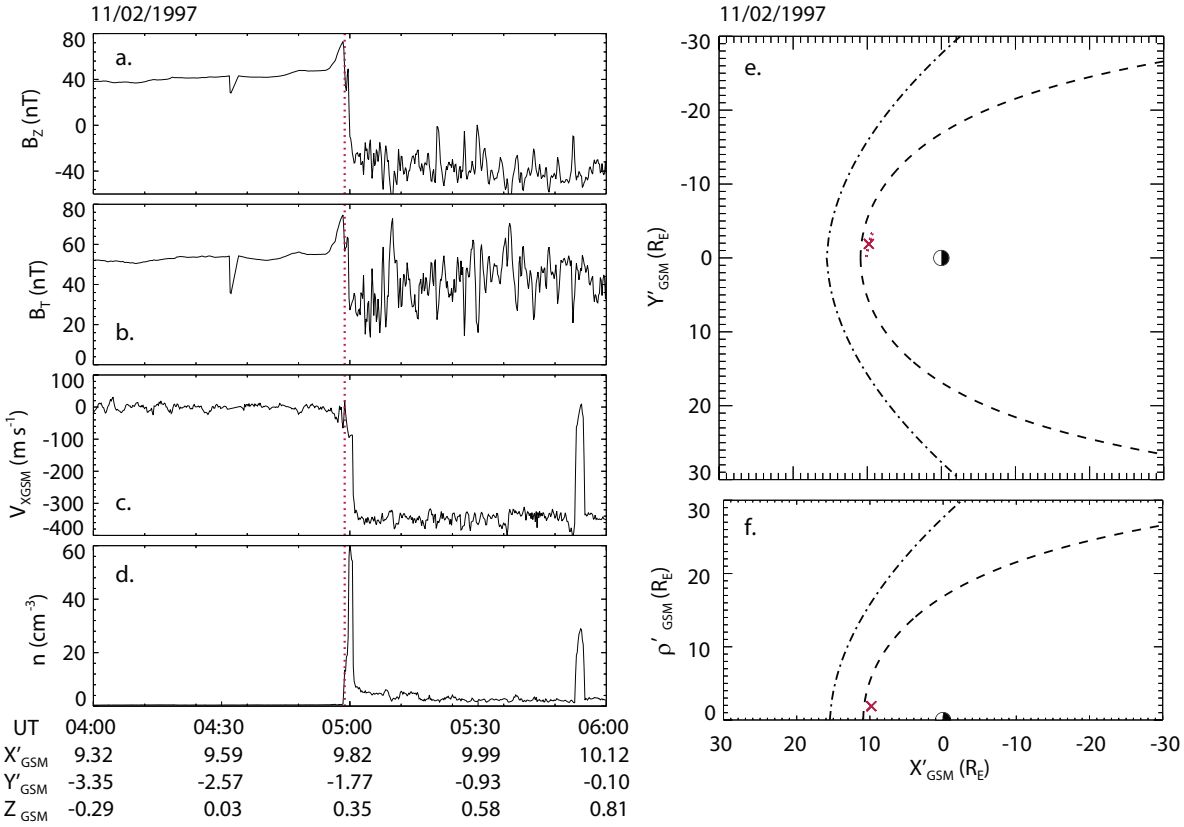

Figure 4.1: a. shows the magnetic field strength in the Z direction, b. the total magnetic field strength, c. the velocity of the plasma in the X_{GSM} direction, and d. the density of the plasma during a 2-hour period on 11$^{\text{th}}$ February 1997. e. shows the orbital path of Geotail (dotted arrowed line) for the same time period as the panels on the left. The locations of the magnetopause crossings detected by the algorithm are indicated by the red crosses. The dot dash line indicates a model bow shock [Peredo *et al.*, 1995] and the dashed line represents a model magnetopause [Shue *et al.*, 1998]. Average solar wind conditions from this time interval have been used as an input for both models. f. shows the location of the magnetopause crossing in the $X'_{GSM} - \rho'$ plane, where ρ' is defined as $\sqrt{Y'^2_{GSM} + Z^2_{GSM}}$.

the motion of the Earth around the Sun and is explained in more detail in section 4.1.2.1). The dashed lines show a model bow shock [Peredo *et al.*, 1995] and a model magnetopause [Shue *et al.*, 1998]. The average solar wind conditions from this period are used as the input into both models. The location of the magnetopause crossing identified by the automated routine is shown by the red cross. In this example, the magnetopause was found slightly more compressed than expected by the model. Panel f. shows the location of the magne-

topause crossing in cylindrical coordinates, where ρ' is defined as $\sqrt{Y'^2_{GSM} + Z^2_{GSM}}$.

4.1.1.2 Flank and magnetotail crossings ($X_{GSM} < 5\ R_E$)

The criteria for detecting flank and magnetotail crossings ($X_{GSM} < 5\ R_E$) are based primarily on plasma measurements and are developed in this study. The criteria allow magnetopause crossings to be identified much further downtail than previous studies. They are described as follows:

1. The average plasma bulk velocity in the X_{GSM} direction in the magnetospheric 3 minute interval must be greater than -100 km s^{-1} and the average velocity in the magnetosheath 3 minute interval must be less (more negative) than -100 km s^{-1}.

2. The difference in bulk plasma velocity in the X_{GSM} direction over the 36 second interval must be greater than 100 km s^{-1}.

3. The average plasma density in the magnetospheric interval must be less than 3 cm^{-3} and in the magnetosheath the average must exceed 1 cm^{-3}.

4. The standard deviation of the total magnetic field strength in the magnetosheath 3 minute interval must be greater than the standard deviation of the total magnetic field strength in the magnetosphere 3 minute interval.

A threshold of -100 km s^{-1} for the mean velocity inside the magnetosphere has been set in the first criterion because although the plasma flow should be stagnant ($\sim$0 km s^{-1}) in this region, it allows for any small changes in the flow to be smoothed and not register as a magnetopause crossing. As Geotail enters the magnetosheath, the observed velocities should be anti-sunwards and hence a mean velocity of -100 km s^{-1} is a conservative estimate. The second criterion checks there is a sharp change in the direction of the plasma flow as Geotail passes through the boundary. The plasma density inside the magnetosphere near the boundary is approximately 0-1 cm^{-3}, so the threshold set in the third criterion for the average in the magnetospheric interval prevents any small changes from being identified as a crossing. The plasma density in the magnetosheath is typically greater than 10 cm^{-3} depending on upstream solar wind conditions.

Example magnetic field and plasma data are shown in the left panels in Figure 4.2 along with the orbital path of Geotail on the right. Panels a.-d. show the magnetic field strength in the Z_{GSM} direction, the total magnetic field strength, the velocity of the plasma in the X_{GSM} direction, and the density of the plasma observed by Geotail, respectively. Magnetopause crossings identified by the algorithm described in this section are denoted by dotted red lines. At the beginning of the time period, Geotail is located inside the magnetosphere, as indicated by a northward directed B_Z, combined with a strong total magnetic field, and low plasma density and velocity. At approximately 12:30 UT Geotail crosses the magnetopause boundary into the magnetosheath on the dawn side. The magnetosheath contains shocked solar wind plasma characterised by very turbulent magnetic field and plasma parameters. Geotail crosses the magnetopause multiple times as indicated by further dashed red lines. Around 20:00 UT, Geotail crosses the bow shock and enters the solar wind. At the time of the magnetopause crossings, Geotail was located at $X'_{GSM} \approx 1\ R_E$ (where the dash denotes the aberrated GSM coordinate and will be explained in the following section), and so the nightside criteria were implemented to identify the magnetopause crossings in this case.

Panel e. shows the orbital path taken by Geotail during the corresponding period, indicated by the arrowed, dotted line. The Sun is to the left of the panel in the positive X'_{GSM} direction. Panel f. shows the location of the magnetopause crossing in cylindrical coordinates, where ρ' is defined as $\sqrt{Y'^2_{GSM} + Z^2_{GSM}}$. The dashed lines show a model bow shock [Peredo *et al.*, 1995] and a model magnetopause [Shue *et al.*, 1998]. The average solar wind conditions from this period are used as the input into both models. The observed magnetopause crossings are indicated by red crosses. The locations of these crossings show that the magnetopause was moving when Geotail encountered it. In panel e., the model magnetopause is located at a larger radial distance than the observed position. As Geotail was located slightly out of the equatorial plane when it encountered the magnetopause during this period, plotting the magnetopause crossing locations in cylindrical coordinates (f.) will allow us to compare the magnetopause crossings with the predicted location. As can be seen in the figure, the model is closer to the magnetopause crossing location. It will be important to carry out the future analysis in cylindrical coordinates rather than in one plane to mitigate these effects. As mentioned earlier, how multiple magnetopause crossings are dealt with will be discussed in greater detail in section 4.2.1.

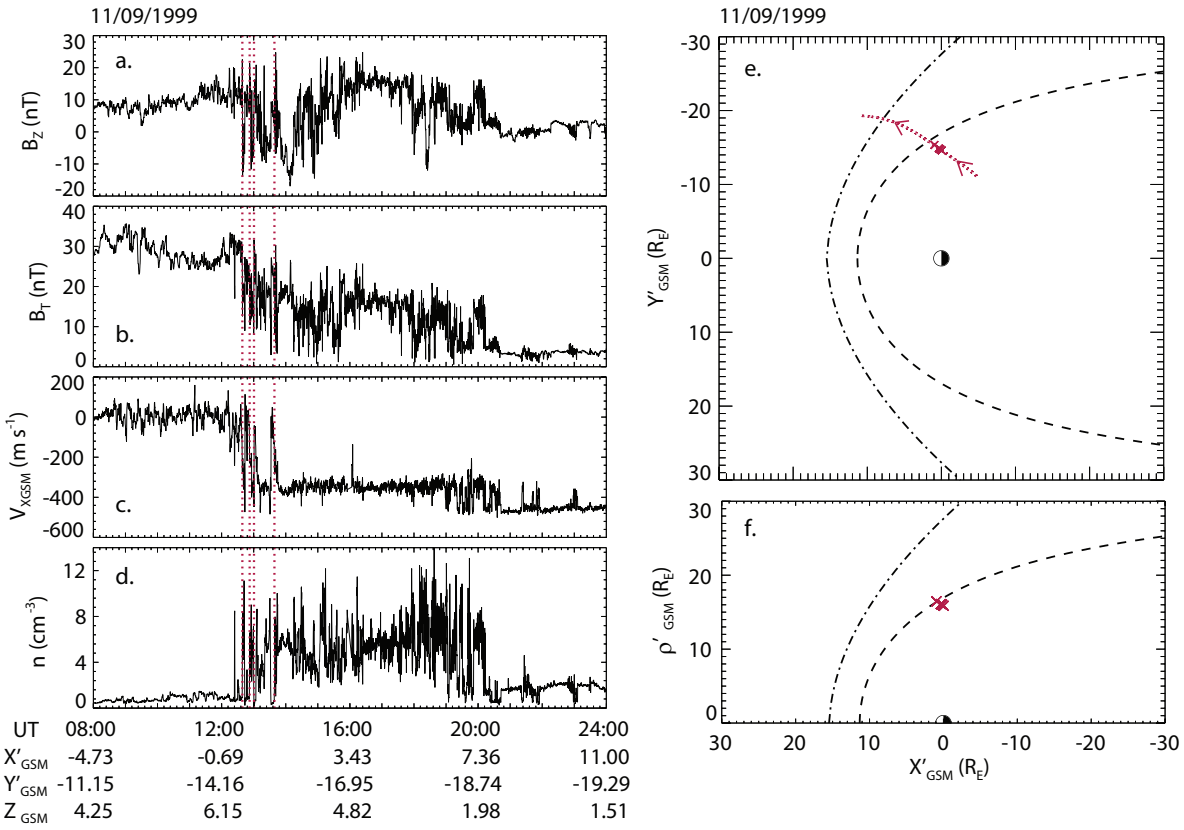

Figure 4.2: Panel a. shows the magnetic field strength in the Z direction, b. the total magnetic field strength, c. the velocity of the plasma in the X_{GSM} direction, and d. the density of the plasma during a 16-hour period on 11th September 1999. The panel on the right (e.) shows the orbital path of Geotail (dotted arrowed line) for the same time period as the panels on the left. The locations of the magnetopause crossings detected by the algorithm are indicated by the red crosses. The dot dash line indicates a model bow shock [Peredo *et al.*, 1995] and the dashed line represents a model magnetopause [Shue *et al.*, 1998]. Average solar wind conditions from this time interval have been used as an input for both models. f. shows the location of the magnetopause crossing in the $X'_{GSM} - \rho'$ plane, where ρ' is defined as $\sqrt{Y'^2_{GSM} + Z^2_{GSM}}$.

4.1.2 Results

The magnetopause crossing detection routine is applied to 20 years of Geotail data to produce a database of 8548 magnetopause crossings with corresponding upstream solar wind data from the OMNI database. In this section we shall discuss the properties and features of the complete set of magnetopause crossings after correcting for the apparent aberration caused by the motion of the Earth around the Sun.

4.1.2.1 Correcting for the motion of the Earth around the Sun

Before the magnetopause crossings can be used to develop a model, they must be rotated in the X-Y plane to correct for the motion around the Sun (see section 1.3). The Earth orbits around the Sun with a velocity of approximately 30 km s^{-1}. This causes an aberration of the X-Y plane. All crossings have been rotated into the aberrated GSE coordinate system to correct for this deviation before transforming the aberrated GSE coordinates into the GSM coordinate system. The coordinates are transformed using the following equations [Slavin & Holzer, 1981]

$$\theta' = \tan^{-1}\left(\frac{V_{ES}}{V_{SW}}\right) + \cos^{-1}\left(\frac{X_{GSE}}{r}\right) \qquad Y_{GSE} > 0 \tag{4.1}$$

$$\theta' = \tan^{-1}\left(\frac{V_{ES}}{V_{SW}}\right) - \cos^{-1}\left(\frac{X_{GSE}}{r}\right) \qquad Y_{GSE} < 0 \tag{4.2}$$

where θ' is the angle between the Sun-Earth line and a radial distance r, ($r = \sqrt{X_{GSE}^2 + Y_{GSE}^2}$), V_{ES} is the velocity of the Earth around the sun (approximately 30 km s^{-1}), and V_{SW} is the velocity of the solar wind which is provided by the OMNI dataset. The results are shown in Figure 4.3, where the grey diamonds indicate the magnetopause crossings before transforming the coordinates, and the black stars show the magnetopause crossings after the transformation. Aberration does not have a major effect on the dayside magnetosphere, however in the magnetotail correcting for aberration typically means that the magnetosphere undergoes a rotation of approximately 3-4° in the equatorial plane.

4.1.2.2 Complete set of magnetopause crossings

The complete set of magnetopause crossing locations are shown in Figure 4.4. The four panels show the locations and density of magnetopause crossings in 1×1 R_E bins in four different planes. Panel a. displays the magnetopause crossings in the $X'_{GSM} - Y'_{GSM}$ (or equatorial) plane as viewed from the magnetic north pole, with the Sun to the left, where X' and Y' denote the aberrated coordinates. Panel b. shows the noon-midnight meridian ($X'_{GSM} - Z_{GSM}$), again with the Sun to the left. Panel c. shows the view of the Earth from the Sun ($Y'_{GSM} - Z_{GSM}$), and finally panel d. shows the crossings in the $X'_{GSM} - \rho'$ plane, where ρ' is defined as $\sqrt{Y'^2_{GSM} + Z^2_{GSM}}$. There are a greater number of crossings detected

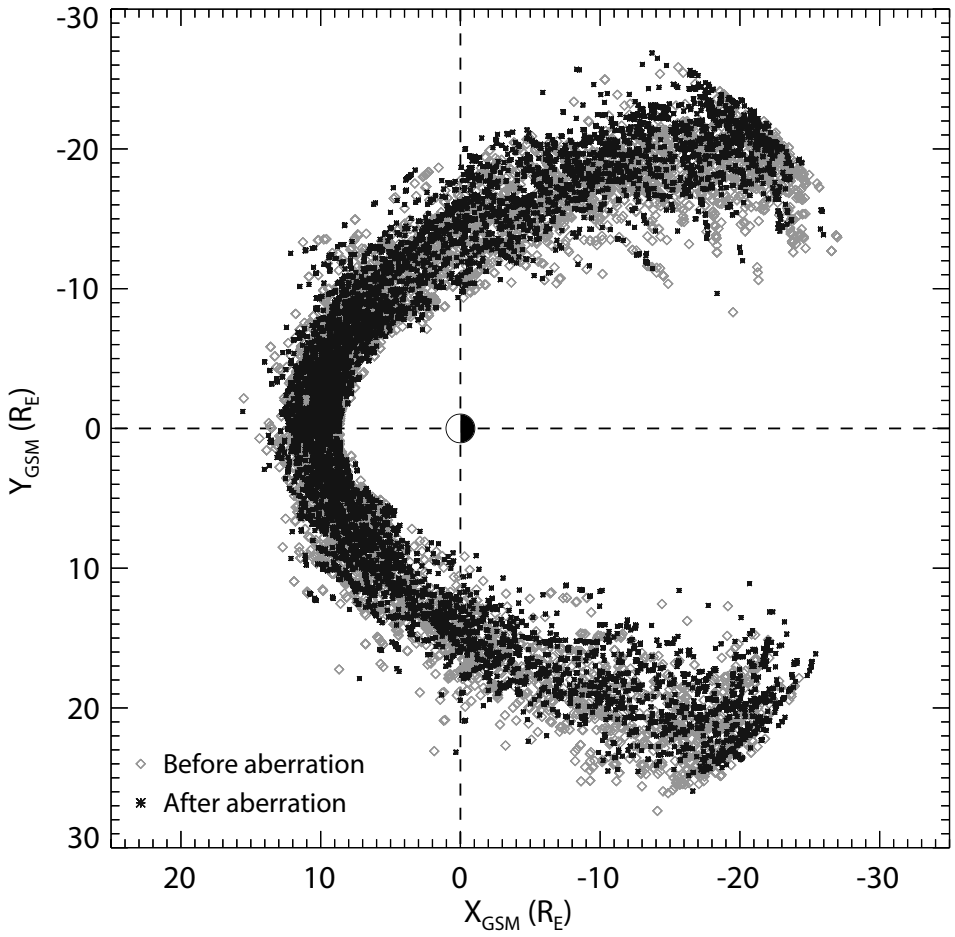

Figure 4.3: Identified magnetopause crossings in the $X_{GSM} - Y_{GSM}$ plane before and after the crossings are rotated to account for the motion of the Earth around the sun.

at the dayside magnetopause primarily due to Geotail's orbit. When its perigee is located at the dayside, Geotail skims and cuts through the magnetopause nose, but does not cross the nightside magnetopause, and hence more magnetopause crossings are observed on the dayside. Although Geotail's orbit is mainly confined to the equatorial plane, in later years its orbit has risen slightly out of the equatorial plane, as can be seen in panel c. There is good coverage at both the dawn and dusk magnetosphere.

It is well documented that the magnetopause is in constant motion, mainly as a consequence of varying upstream solar wind conditions, but also due to the presence of surface waves, and hence Geotail typically crosses the magnetopause multiple times per orbit.

Implementing an automated magnetopause crossing detection routine such as that used

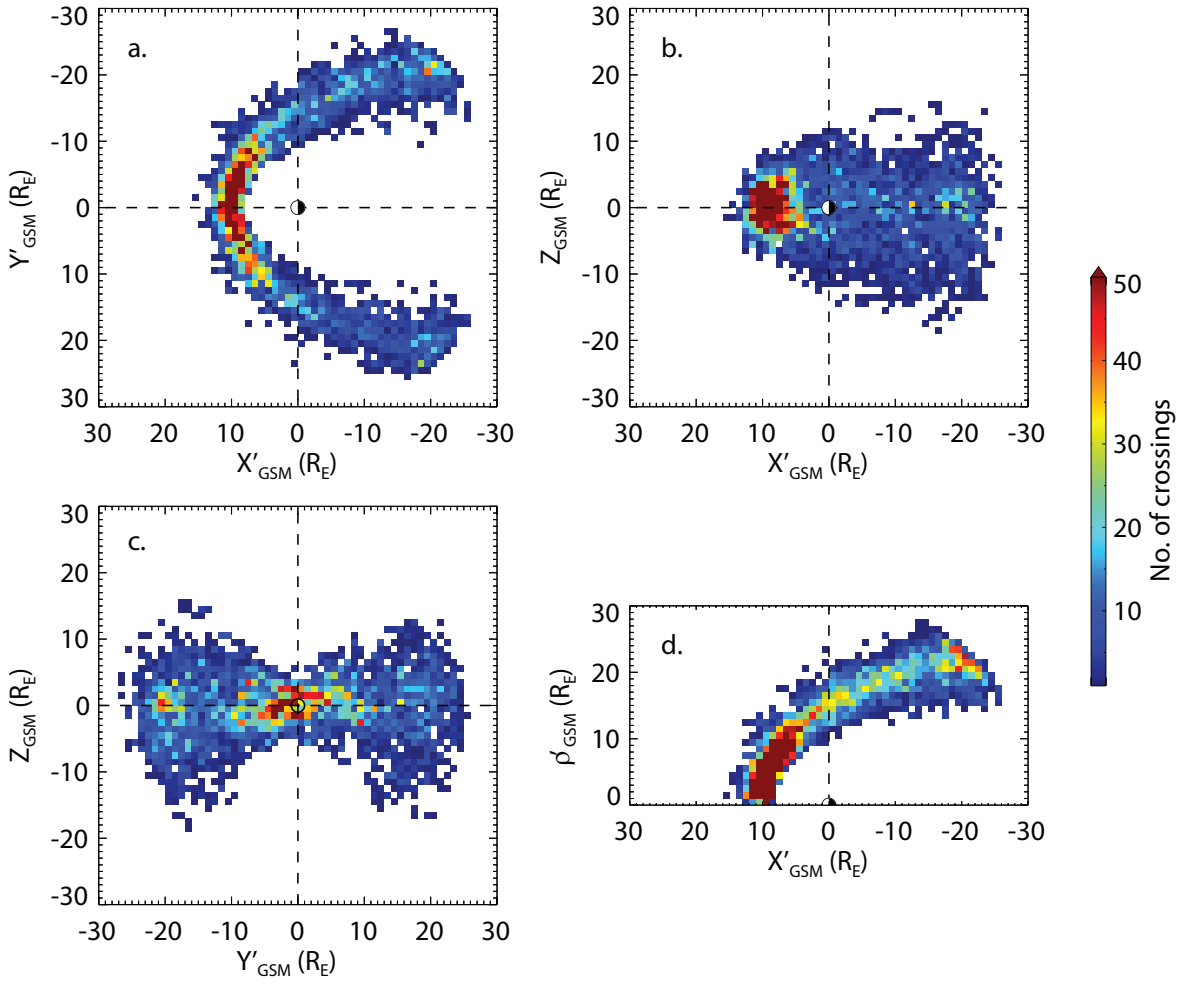

Figure 4.4: Observed Geotail magnetopause crossings in the a. $X'_{GSM} - Y'_{GSM}$ plane; b. $X'_{GSM} - Z_{GSM}$ plane; c. $Y'_{GSM} - Z_{GSM}$ plane; and d. $X'_{GSM} - \rho'_{GSM}$ plane (where ρ' is defined as $\sqrt{Y'^2_{GSM} + Z^2_{GSM}}$). The magnetopause crossings have been rotated to correct for the apparent aberration caused by the Earth's motion around the Sun. The colours represent the number of magnetopause crossings found in each 1×1 R_E bin.

in this study will reduce some selection bias compared with a "by-eye" approach, but the detection criteria is still user defined. All magnetopause crossings identified by the algorithm were visually inspected to remove any incorrectly identified crossings. Approximately 1.7% of identified crossings were incorrect and these were removed from the database. Incorrect magnetopause crossings were typically caused by plasma irregularities or data gaps. Finally, we removed any crossings from the dataset from periods when OMNI data was unavailable.

4.2 Defining the new model

To study how the shape and location of the magnetopause changes with solar wind and magnetospheric parameters, a simple empirical model was developed. The following section discusses problems that arise due to the coverage and orbit of Geotail, the techniques used to create the model, and the results.

4.2.1 Accounting for biases in the dataset

Before we can parameterise the magnetopause crossings with solar wind dynamic pressure to define a new model, biases within the database must be considered. Geotail has an elliptical orbit which means that some orbital bias will be introduced into the identified magnetopause crossings. Figure 4.5 shows how many hours the spacecraft was located in a 1×1 R_E bin over the 20-year period studied in this study. As can be seen in the figure, the dwell times are high at apogee as this is where Geotail is travelling most slowly, resulting in more magnetopause crossings being identified in this region (see Figure 4.4d.). Another limitation caused by Geotail's orbital characteristics is that magnetopause crossings will only be identified in regions where Geotail visits. For example, this means that near apogee, magnetopause crossings are only detected when the magnetotail is compressed, and not when it is inflated. To address these orbital biases in the magnetotail that could affect the fitting procedure which will be described in the next section, we removed any magnetopause crossings that occurred beyond a point downtail. Figure 4.6 illustrates the procedure implemented. The red dotted line shows the point beyond which the magnetopause crossings were removed, with the removed magnetopause crossings shaded in grey. The red dotted line was found by calculating the average magnetopause location for the entire magnetopause crossing database (shown by the black dashed line) and finding the normal to this average magnetopause at an arbitrary radial distance of 25 R_E. This process reduces the total number of magnetopause crossings to 8050.

The number of magnetopause crossings identified at the dayside magnetopause is higher than at the flanks and magnetotail for a number of reasons. The dayside magnetopause coincides with Geotail's perigee where the dwell times are high (see Figure 4.6) making it more probable that magnetopause crossings will be identified as more time is spent in that

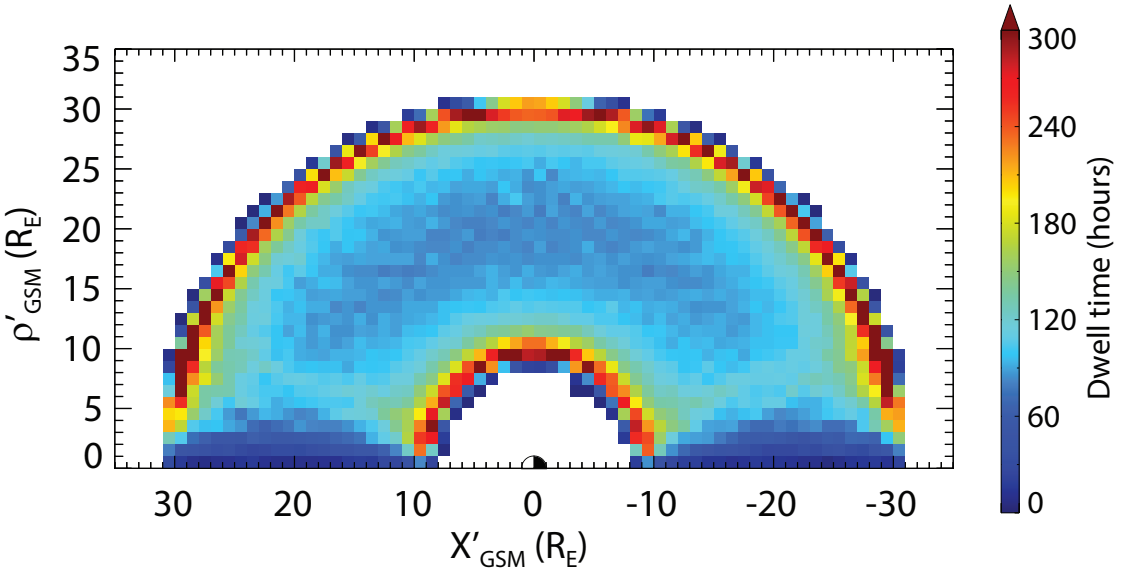

Figure 4.5: The 1×1 R_E colour coded bins indicate how long Geotail spent in that particular bin over the 20 years studied in the $X'_{GSM} - \rho'_{GSM}$ plane.

region. A perigee of 8-10 R_E also means that Geotail will skim the dayside magnetopause and multiple magnetopause crossings are likely to be identified. It is well documented that the magnetopause is in constant motion, mainly as a consequence of varying upstream solar wind conditions, but also due to the presence of surface waves [e.g. Berchem & Russell, 1982; Haaland *et al.*, 2014], and hence Geotail typically crosses the magnetopause multiple times per orbit. Case & Wild [2013] implemented a criterion that multiple magnetopause crossings should not occur within a 10-minute interval. This could mean that the magnetopause crossing that their algorithm identifies is either the innermost or the outermost crossing, depending on whether the spacecraft was traversing into the magnetosheath or magnetosphere, respectively. This could lead to biases in their magnetopause crossing database. Another method that could be applied to remove multiple magnetopause crossings would be to take an average of the multiple magnetopause crossings. This produces an average magnetopause crossing location where no magnetopause was observed. These methods have not been implemented as these could cause bias in the data set, and so we have included multiple magnetopause crossings in our study.

Unfortunately, Geotail's orbital properties means that magnetopause crossings will not

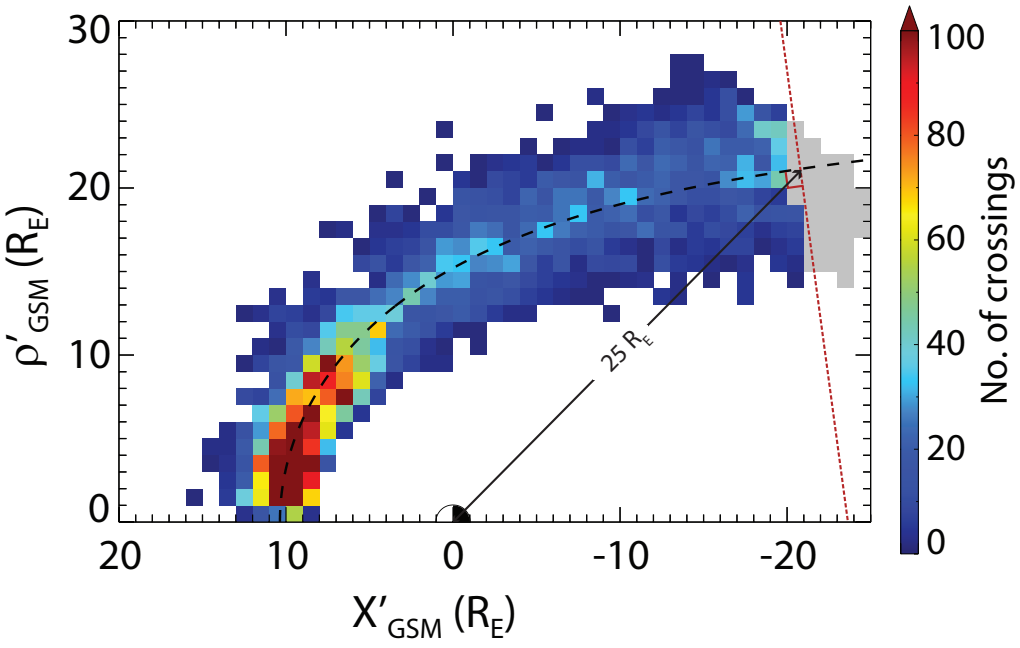

Figure 4.6: Identified magnetopause crossings in the $X'_{GSM} - \rho'_{GSM}$ plane. 1×1 R_E colour coded bins indicate the total number of magnetopause crossings identified in each bin. The black dashed line shows the average magnetopause location and the red dotted line shows the point which is normal to the average magnetopause. All magnetopause crossings beyond this normal have been removed from the database and are shaded grey in the figure.

be observed inside of 8 R_E and therefore our model will not be capable of predicting magnetopause location during extreme events that compress the dayside magnetopause.

Figure 4.7 indicates the resulting magnetopause crossing dataset. This reduces the total number of magnetopause crossings to 8050. Removing magnetopause crossings at a radial distance of $X'_{GSM} = 25$ R_E downtail was also considered, however it was felt that this would still introduce biases to the fitting procedure.

To account for orbital biases due to the spacecraft spending more time in some locations than others, the magnetopause crossing locations are normalised by the dwell time of the spacecraft in the particular location. This also reduces the bias caused by multiple magnetopause crossings, as many are identified where Geotail spends more time. By dividing the number of magnetopause crossings detected in each 1×1 R_E bin by the amount of time Geotail spent in the same bin (the dwell time), a probability of finding the magnetopause in a particular bin can be calculated. The results are shown in Figure 4.8. This probability is

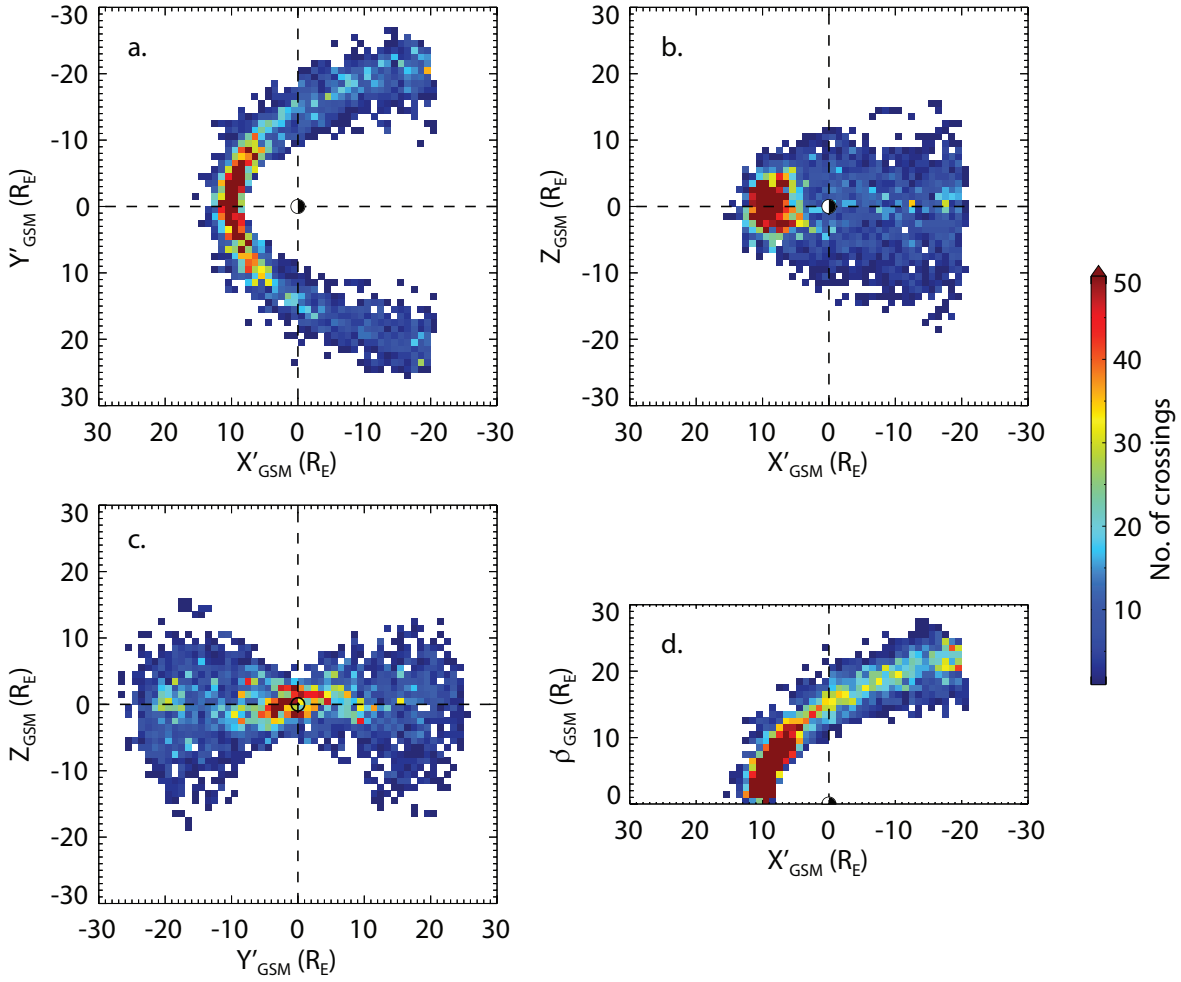

Figure 4.7: Identified magnetopause crossings in the a. $X'_{GSM} - Y'_{GSM}$ plane; b. $X'_{GSM} - Z_{GSM}$ plane; c. $Y'_{GSM} - Z_{GSM}$ plane; and d. $X'_{GSM} - \rho'_{GSM}$ plane (where ρ' is defined as $\sqrt{Y'^2_{GSM} + Z^2_{GSM}}$). Magnetopause crossings identified at the normal to the average magnetopause at $X'_{GSM} = 25\ R_E$ downtail have been removed. The colours represent the number of magnetopause crossings found in each $1 \times 1\ R_E$ bin.

then used to weight the magnetopause crossings.

4.2.2 Fitting process

Solar wind dynamic pressure is known to have a large influence on magnetopause location and shape, as discussed in section 1.4.2.2 where we calculated the magnetopause standoff distance. Figure 4.9 shows the 8050 identified magnetopause crossings that will be used

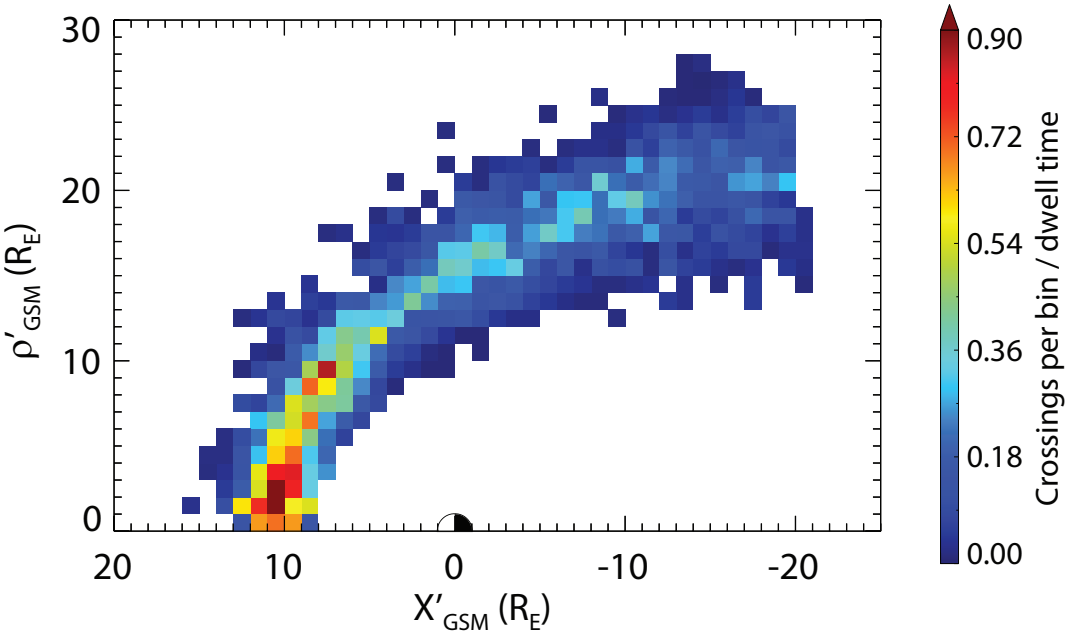

Figure 4.8: 1×1 R_E colour coded bins show the probability density map of Geotail locations. It is calculated from finding the ratio between how many magnetopause crossings found in a particular bin to how long Geotail spent in the bin.

for the fitting, colour coded with the solar wind dynamic pressure from the OMNI dataset (section 2.1.2) measured at the time of the magnetopause crossing. If OMNI data were unavailable at the time of the crossing, we look for available data up to 10 minutes after the crossing took place. If there is data available, an average is taken over this 10-minute interval. The difference between the solar wind dynamic pressure measured at the bow shock and the pressure measured downtail should not be large. It would take the solar wind approximately 12 minutes to reach a distance of 20 R_E downtail depending on upstream conditions. The propagation time from the upstream spacecraft to Geotail has not been considered in this study as it would have to be estimated for each magnetopause crossing independently.

Figure 4.9 shows that the solar wind dynamic pressure has a clear and strong effect on magnetopause location. When the solar wind ram pressure is weak, the magnetopause is more inflated and when the solar wind ram pressure is high, the magnetopause is compressed. The influence of solar wind dynamic pressure is greatest at the dayside magnetopause where the solar wind flow is normal to the magnetopause surface. Even at the flanks and in the

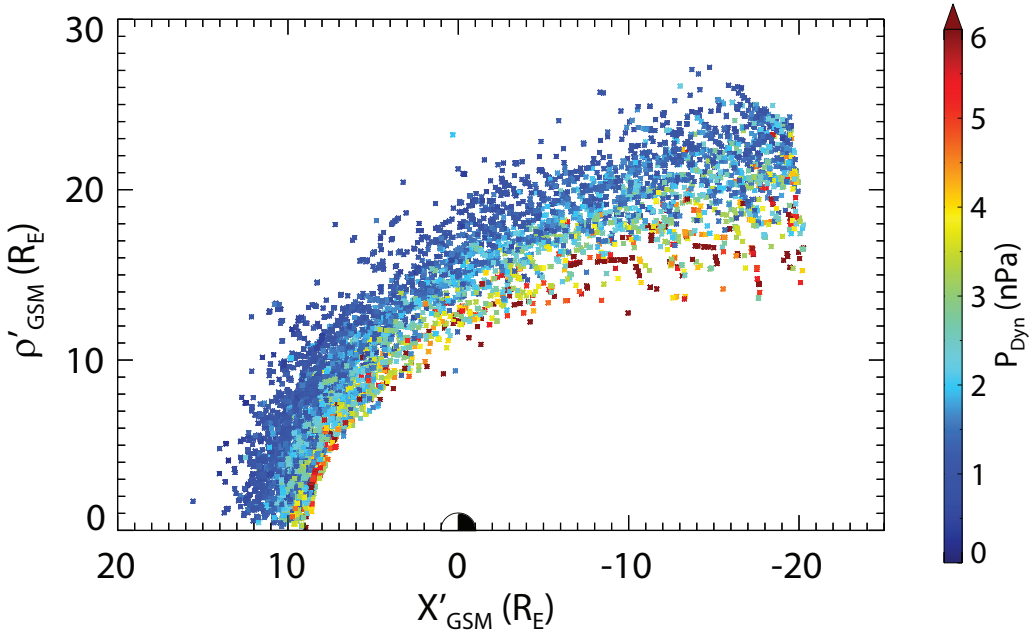

Figure 4.9: The identified magnetopause crossings in the $X'_{GSM} - \rho'_{GSM}$ plane (where ρ' is defined as $\sqrt{Y'^2_{GSM} + Z^2_{GSM}}$). Magnetopause crossings have been colour coded with the solar wind dynamic pressure which was provided by the OMNI dataset.

magnetotail, where we would expect the effect of solar wind dynamic pressure to diminish as the solar wind flow becomes tangential to the magnetopause, there is still a strong solar wind dynamic pressure dependence.

In this section, we develop a simple empirical model based on solar wind dynamic pressure to describe the magnetopause crossing database we have identified. We decided to develop a new model using the magnetopause crossings identified in this thesis, rather than using a model developed by any of the previous authors listed in section 3.3, because we have identified a much larger magnetopause crossing database than previous studies: covering further downtail, a greater number of extreme events, and nearly two solar cycles, both of which were relatively quiet in comparison to previous solar cycles. As Geotail orbits primarily in the equatorial plane, we do not need to consider the effects that the magnetospheric cusps have on magnetopause location. The Shue *et al.* [1997, 1998] model is developed from a smaller database of magnetopause crossings, over a shorter period during a solar cycle that was much stronger than the two solar cycles (solar cycle 23 and 24) from which we have Geotail data, and with limited coverage of the nightside magnetopause.

Comparison with other models would not, therefore, be able to describe the magnetopause crossings we have observed with as great an accuracy as the model that we will develop.

We use the function described by Shue *et al.* [1997, 1998] to develop the model (see section 3.3.1.1 for more detail). It is given by

$$r = r_0 \left(\frac{2}{1 + \cos\theta} \right)^{\alpha} \tag{4.3}$$

where r is the radial distance and θ is the solar zenith angle, r_0 is the magnetopause standoff distance, and α describes the level of flaring in the magnetotail. Equation 4.3 is fitted to the magnetopause crossings to obtain the functional forms of the magnetopause standoff distance, r_0 and the flaring of the magnetotail, α in terms of solar wind dynamic pressure.

To parameterise for solar wind dynamic pressure, the magnetopause crossings are separated by dynamic pressure into 1 nPa wide overlapping bins which are shifted by 0.5 nPa, ranging from 0 nPa to 9 nPa. These bin sizes were chosen because even at higher dynamic pressures, there were a sufficient number of magnetopause crossings for fitting. The difference, Δ, between the magnetopause crossing location and the function given by equation 4.3 is calculated by finding the perpendicular offset as follows

$$\Delta = \sqrt{(X_{Geo} - X_{func})^2 + (\rho_{Geo} - \rho_{func})^2} \tag{4.4}$$

where X_{Geo} and ρ_{Geo} describe the position of Geotail, and X_{func} and ρ_{func} describe the position of the magnetopause as predicted by the function in the $X'_{GSM} - \rho'$ plane. The simple diagram shown in Figure 4.10 illustrates how the perpendicular offsets are measured. The sum of the squared differences is calculated. r_0 and α are then independently varied until the sum of the squared differences is minimised. This is implemented for each pressure range to find a value for r_0 and α which most closely describe the observed magnetopause crossings. Other methods and techniques to find the best fit to the magnetopause crossings were trialled, but this procedure produced the best results.

The panels in Figure 4.11 and 4.12 show the total number of magnetopause crossings and coverage in each solar wind dynamic pressure range.

There are far fewer magnetopause crossings in higher solar wind dynamic pressure ranges than for lower solar wind dynamic pressures, although despite this, the magnetopause crossings locations cover both the dayside and nightside fairly evenly. As discussed

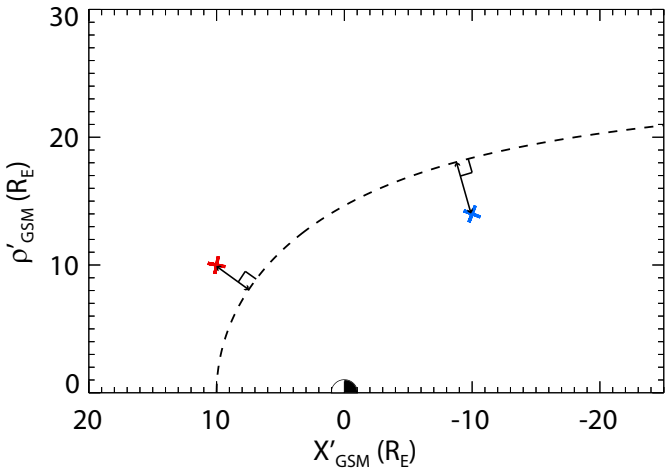

Figure 4.10: An example of how the fitting procedure works. Crosses represent example magnetopause crossings and the dashed line shows the function (Equation 4.3) with a trial r_0 and α value. Δ is calculated from the square root of the squared perpendicular offset.

previously, more magnetopause crossings have been identified at the dayside magnetopause than the nightside caused by Geotail's orbit.

To account for orbital bias in the fitting procedure, the probability density map shown in Figure 4.8 is used to weight the magnetopause crossings by dwell time before carrying out the fitting.

4.2.3 Results and discussion

Figure 4.13 shows the best fit r_0 and α values, respectively, as a function of solar wind dynamic pressure. Panel c. shows the number of magnetopause crossings that went into each solar wind dynamic pressure bin. The colours indicate the results without considering biases caused by Geotail's orbit in the fitting procedure (blue), and with considering biases in the fitting procedure (pink). Similar to the methods of Shue *et al.* [1997], a power law curve has been fitted to the data points in panel a., and a straight line has been fitted to the data points in panel b. to obtain the following equations for r_0 and α before considering orbital bias (shown by the blue dashed lines in Figure 4.13)

$$r_0 = 10.838 P_{Dyn}^{-1/8.85} \pm 0.021 R_E \tag{4.5}$$

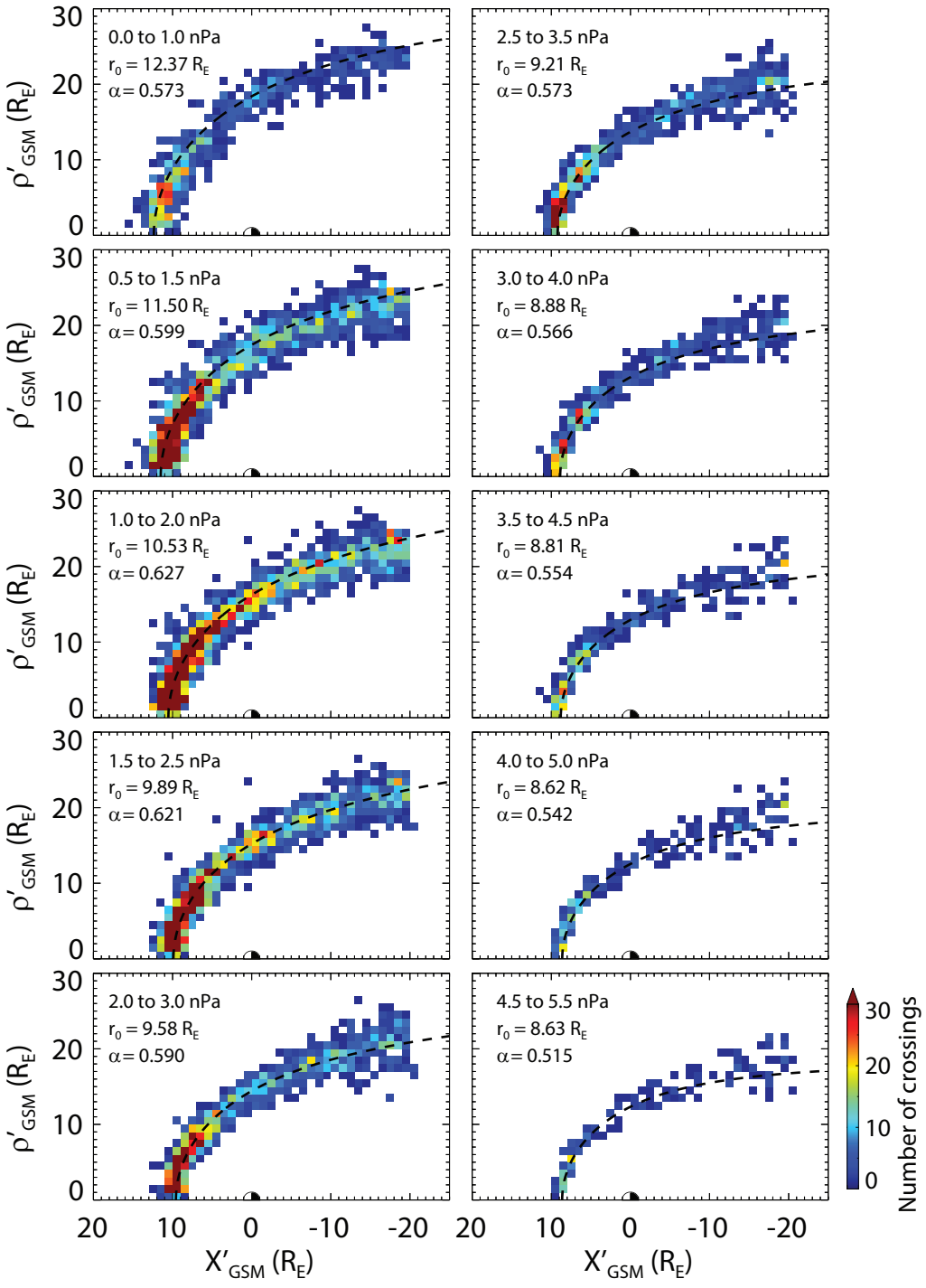

Figure 4.11: The number of magnetopause crossings in a 1×1 R_E bin separated by solar wind dynamic pressure in the $X'_{GSM} - \rho'_{GSM}$ plane.

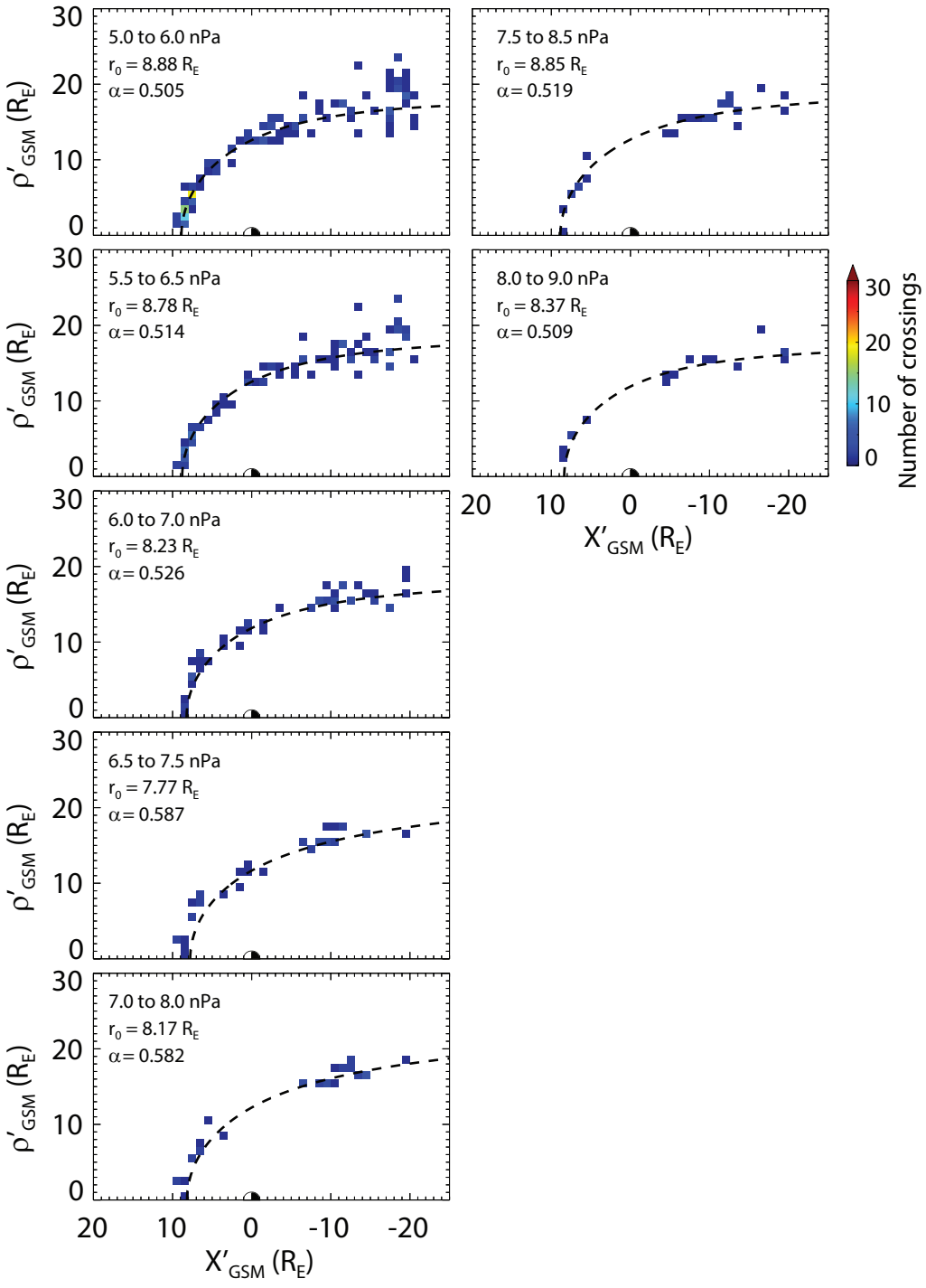

Figure 4.12: The number of magnetopause crossings in a 1×1 R_E bin separated by solar wind dynamic pressure in the $X'_{GSM} - \rho'_{GSM}$ plane.

$$\alpha = 0.610 - 0.011 P_{Dyn} \pm 0.015 \tag{4.6}$$

where the errors indicated are the standard error.

The power law index in equation 4.5 is greater than the theoretical prediction given by equation 1.41 in section 1.4.2.2 ($r_0 \propto P_{Dyn}^{-1/6}$). This relation assumes the magnetospheric field is dipolar and so some differences are expected. However, the results given by equation 4.5 imply that there is a much weaker dependence on solar wind dynamic pressure relative to the theory.

As the results presented are significantly different from the theoretical prediction and previous models, the analysis has been repeated after taking orbital biases into account. This is achieved by weighting the magnetopause crossings with dwell time. The resulting equations for r_0 and α are obtained (shown by the pink dotted lines in Figure 4.13)

$$r_0 = 11.08 P_{Dyn}^{-1/6.75} \pm 0.037 R_E \tag{4.7}$$

$$\alpha = 0.605 - 0.010 P_{Dyn} \pm 0.031 \tag{4.8}$$

After weighting the magnetopause crossings, the power law index given in equation 4.7 is much closer to the theoretical prediction and to other models. For example, other models derive exponents of: -1/6.6 [Shue *et al.*, 1997], -1/5.15 [Lin *et al.*, 2010], and -1/4.8 [Dušik *et al.*, 2010] (see section 3.3 for more detail).

The empirical model developed here describes magnetopause location under different solar wind dynamic pressures. As Geotail had an equatorial orbit, the model can only be used to describe magnetopause location in this plane. It is well-documented that the magnetopause is asymmetric in the equatorial and north-south planes. Under the same external conditions, the magnetopause is smaller in the north-south direction compared to at the equator. To characterise magnetopause location in the north-south direction, the magnetospheric cusps would also need to be considered.

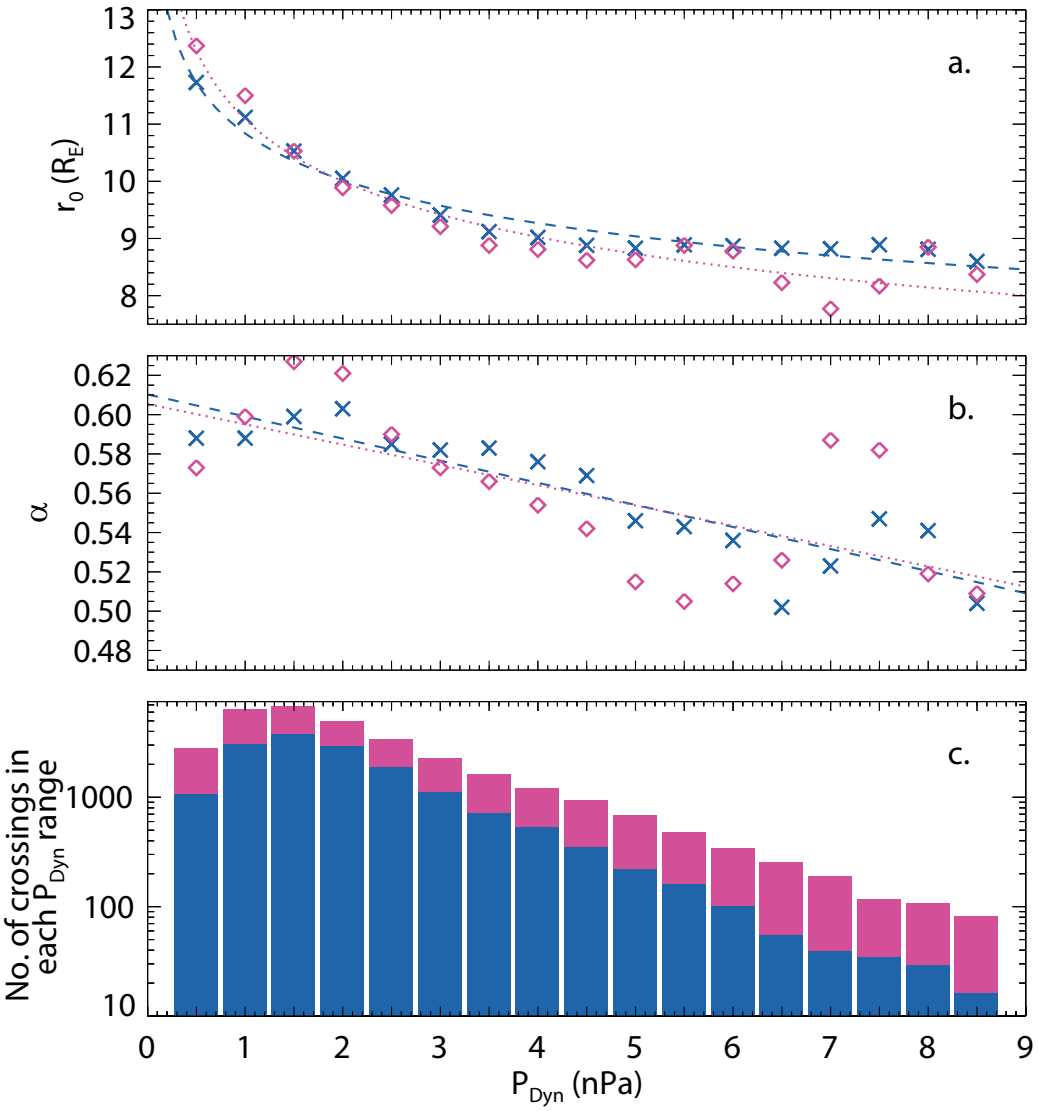

Figure 4.13: a. The standoff distance, r_0, as a function of solar wind dynamic pressure. b. The level of flaring in the magnetotail, α, as a function of solar wind dynamic pressure. c. The number of magnetopause crossings in each solar wind dynamic pressure range. The colours indicate the results without taking orbital bias into account (blue) and with taking orbital bias into account (pink).

4.3 Summary

In this chapter, we have developed an automated routine to identify magnetopause crossings from over 20 years of Geotail magnetic field and plasma observations. The automated routine is based on criteria first presented by Ivchenko *et al.* [2000] and Case & Wild [2013].

After removing some magnetopause crossings from the database to account for biases that are caused by Geotail's orbit, there are 8050 magnetopause crossings available for analysis. The magnetopause crossings are then used to create a simple magnetopause model to predict the location of the magnetopause using the functional form defined by Shue *et al.* [1997, 1998]. We trial developing the model with the magnetopause crossings both unweighted and weighted by the length of time Geotail spends in a particular region. This model is able to predict the location of the magnetopause based on the upstream solar wind dynamic pressure. It is not capable of predicting the magnetopause under conditions that cause the magnetopause to be compressed inside of 8 R_E due to Geotail's orbital properties.

Since the model only takes solar wind dynamic pressure into account, and no other solar wind or magnetospheric parameters, it will only be used to provide an approximate location for the magnetopause in this study. To improve the model, other parameters would need to be considered. In the following chapters, the model will be first used to study how magnetopause location varies over the solar cycle. Following this, the detected magnetopause crossings are compared with the predicted locations for a variety of upstream solar wind and magnetospheric conditions.

Chapter 5

Solar cycle influences on the shape and location of the magnetopause

5.1 Introduction

Variations in upstream solar wind conditions cause large changes in the location and shape of the magnetopause. Solar wind dynamic pressure and the interplanetary magnetic field (IMF) are known to vary over the solar cycle [Fairfield, 1979, 1995] (see section 3.2 for more detail). Consequently, the average shape and location of the magnetopause will also vary with solar cycle. For example, solar wind dynamic pressure peaks during the declining phase of the solar cycle, and therefore it is expected that the magnetopause will be more compressed during this phase. Conditions during the solar cycle can vary drastically, however, and the most recent solar cycle contained several highly unusual features, such as an extended, deep solar minimum which had profound implications for the dynamics of the Earth's magnetosphere. The long-term dataset (20 years) provided by Geotail has given us a unique opportunity to compare the magnetopause location during two very different minima and examine how the magnetopause responds to very low solar activity.

The magnetopause crossing dataset developed in this study spans 20 years allowing for the study of magnetopause location over the two most recent solar cycles (23 and 24). In this chapter, we will investigate how the shape and location of the magnetopause varies each year and study the identified magnetopause crossings in more detail. We will further examine long-term characteristics of the magnetopause and draw comparisons between the

model developed in this study (see section 4.2) with models developed by Shue *et al.* [1998] and Lin *et al.* [2010] (see section 3.3.1). A brief overview of the instruments and methods used will be recapped in the next section, followed by the results and discussion, and finally a summary.

5.2 Instruments and methods

Magnetic field and plasma data from the Geotail spacecraft have been used to investigate how magnetopause location changes with solar cycle (see section 2.1.1 for greater detail on the instruments and the mission). Geotail has an elliptical orbit in the equatorial plane that has remained relatively constant over the 20 years investigated in this study. Solar wind data is required as an input for the models used and for looking at the long-term changes over the solar cycles. This data, covering the duration of the Geotail mission, is provided by the OMNI dataset and is available at a time resolution of 1 minute. Finally, the international sunspot numbers are used to determine the phases of the solar cycle [SILSO World Data Center, 2016].

Magnetopause crossings are identified using the automated routines for the dayside and nightside magnetopause (described in section 4.1.1). The magnetopause crossings are aberrated to account for the motion of the Earth around the Sun (section 4.1.2.1), and magnetopause crossings beyond a line which is normal to the average magnetopause at 25 R_E are removed (section 4.2.1). This results in a dataset of 8050 magnetopause crossings. The magnetopause crossing dataset is used to develop a simple relationship to describe magnetopause location based on solar wind dynamic pressure (section 4.2). We use the function described by Shue *et al.* [1997, 1998] to develop the new model. The function is given by

$$r = r_0 \left(\frac{2}{1 + \cos\theta} \right)^{\alpha} \tag{5.1}$$

where r is the radial distance and θ is the solar zenith angle, r_0 is the magnetopause standoff distance, and α describes the level of flaring in the magnetotail.

We trial calculating functions for r_0 and α in two different ways, firstly by leaving the magnetopause crossings unweighted, and secondly by weighting the magnetopause crossings by dwell time. The weighting method provides much better results and will be used in

analysis presented here. However, we will also present the unweighted model for comparative purposes.

r_0 and α are determined by first weighting the magnetopause crossings by how long Geotail spends in a 1×1 R_E spatial bin, then by separating the magnetopause crossings into solar wind dynamic pressure ranges and fitting the function to each pressure range (see section 4.2.2 for detail). The resulting equations for r_0 and α are as follows

$$r_0 = 11.082 P_{Dyn}^{-1/6.75} \pm 0.037 R_E \tag{5.2}$$

$$\alpha = 0.605 - 0.010 P_{Dyn} \pm 0.031 \tag{5.3}$$

Unlike other models discussed in the literature review of this thesis (section 3.3), the model developed in this study is only parameterised by solar wind dynamic pressure. Solar wind dynamic pressure has a much greater influence on magnetopause size and shape than the direction and magnitude of IMF B_Z. This can be seen in Figures 3.7 and 3.8 in section 3.3 which show the effect of changing dynamic pressure and IMF B_Z on magnetopause location as predicted by the Shue *et al.* [1998] and Lin *et al.* [2010] models. In this thesis, since the simple empirical model will only be used to provide an approximate indication of expected magnetopause location, the effects of other parameters on magnetopause location have not been included in the model as they are much smaller.

As well as using the model developed in this thesis, models defined by Shue *et al.* [1998] and Lin *et al.* [2010] will also be compared to the observed magnetopause location. The model developed by Shue *et al.* [1998] depends on solar wind dynamic pressure and IMF B_Z, whilst the model developed by Lin *et al.* [2010] depends on these parameters as well as the magnetic pressure and dipole tilt angle (both models are described in greater detail in section 3.3.1). To see how the magnetopause shape and location varies with solar cycle and to see how well the models describe the observed magnetopause, the standoff distance, r_0, and the magnetotail radius in the $X_{GSM} - Z_{GSM}$ plane calculated at 20 R_E downtail will be plotted as a function of time.

5.2.1 Average magnetopause location

To investigate how the observed location of the magnetopause varies each year, the Shue *et al.* [1997, 1998] function, equation 5.1, is fitted to the weighted magnetopause crossings without parameterising by solar wind dynamic pressure. This process is applied to each year individually to see qualitatively how magnetopause location varies. A value for r_0 and α is calculated for each year of magnetopause crossings. Similar to the previous fitting process (section 4.2.2), to account for orbital biases, magnetopause crossings have been weighted by how long Geotail spends in a particular spatial bin for each year.

5.3 Results and discussion

The results and discussion are separated into two sections. Firstly, the magnetopause crossings and average location of the magnetopause for each year will be explored. Secondly, the solar cycle variations observed in the solar wind parameters and in the magnetopause locations as predicted by the models will be discussed. Comparisons between the models will also be made.

5.3.1 Yearly variations in the location of the magnetopause

The magnetopause crossings identified in each year of the 20-year period investigated in the thesis are presented in Figures 5.1 and 5.2. The panels have been labelled with the year, and the magnetopause crossings have been plotted in the aberrated $X'_{GSM} - \rho'$ plane (where ρ' is defined as $\sqrt{Y'^2_{GSM} + Z^2_{GSM}}$) and the colour represents the solar wind dynamic pressure strength. The dashed black curve indicates the average magnetopause location for each year which is found by fitting the Shue *et al.* [1997, 1998] function to each individual year of crossings (section 5.2.1). The grey dotted curve indicates the average magnetopause location over the whole 20-year period and is calculated from fitting the Shue *et al.* [1997, 1998] function to the entire database of weighted magnetopause crossings. The best fit standoff distance, r_0 is found to be 10.39 R_E and the best fit flaring in the magnetotail, α is found to be 0.56 for the entire dataset. This has been included on each panel to allow for easier comparison between individual years.

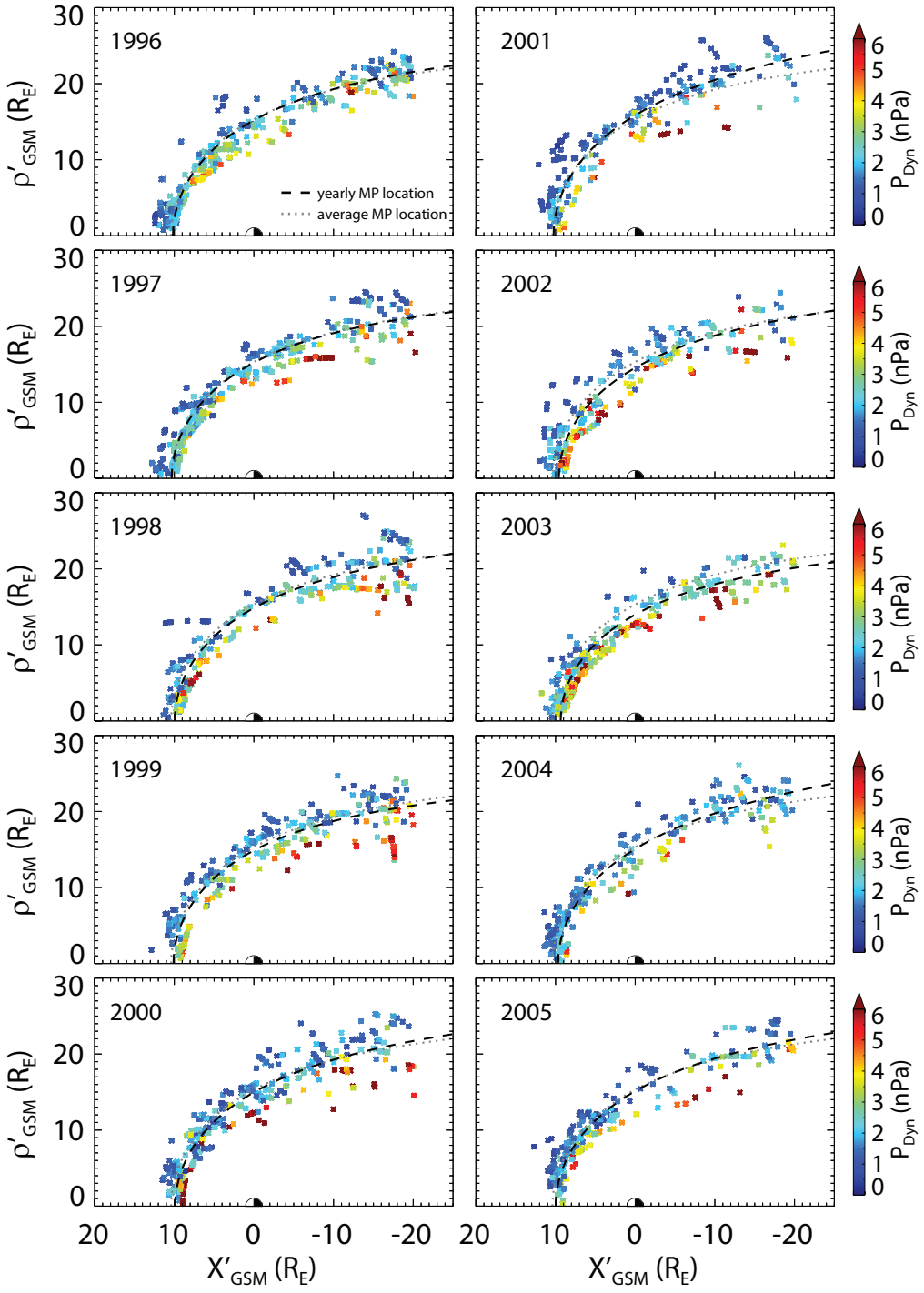

Figure 5.1: The panels indicate magnetopause crossings identified in the years 1996 to 2005, and are colour coded by solar wind dynamic pressure. The Shue *et al.* [1997, 1998] function has been fitted to each year of weighted magnetopause crossings to find the best fit location of the magnetopause indicated by the black dashed line. The average location of the magnetopause is shown by the dotted grey line.

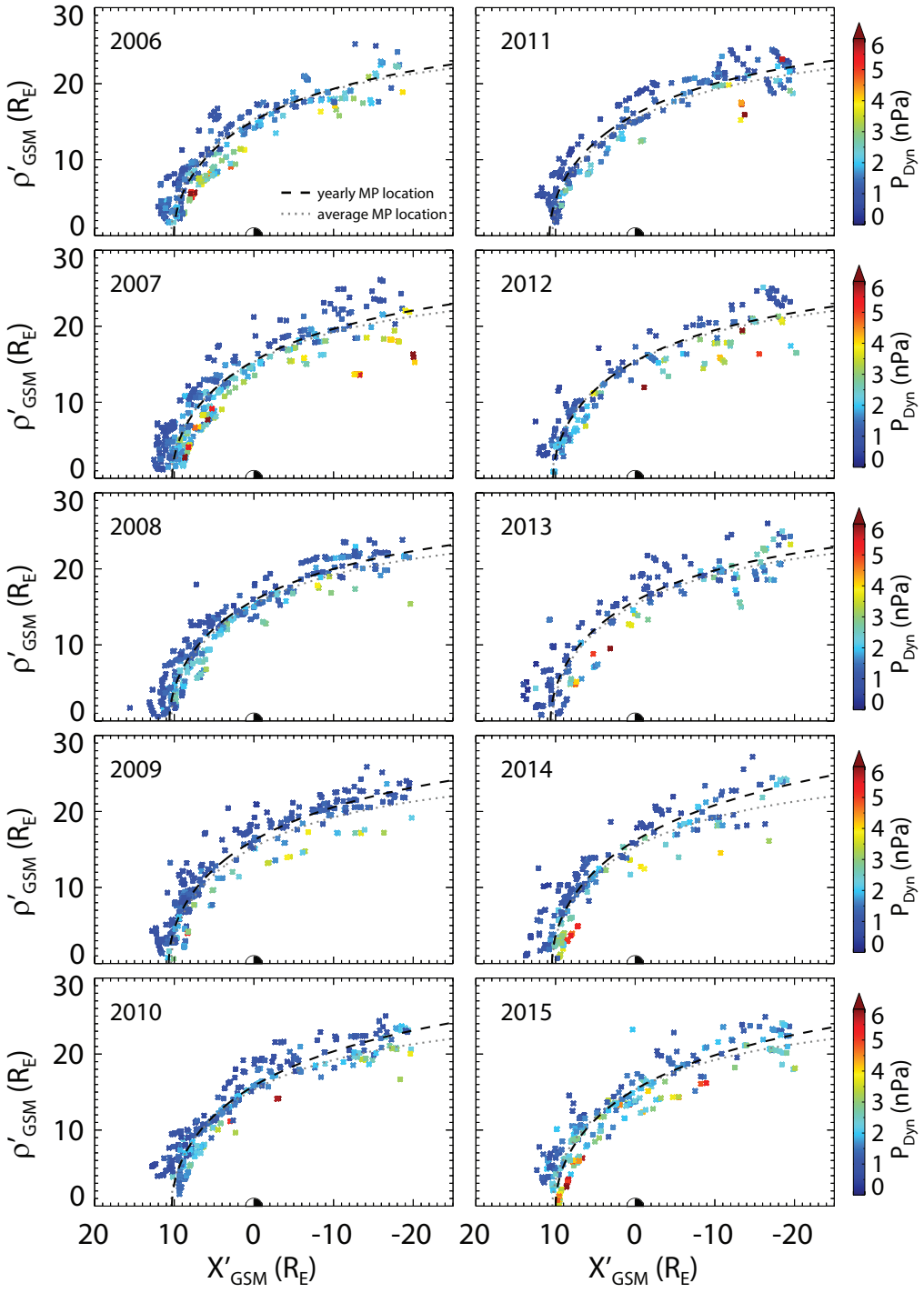

Figure 5.2: The panels are the same as Figure 5.1, but for the years 2006 to 2015.

The individual number of magnetopause crossings for each year and the weighted best fit r_0 and α values are listed in table 5.1. These are calculated by weighting the magnetopause crossings by how long Geotail spends in a 1×1 R_E spatial bin. Over the 20 years, the total number of identified magnetopause crossings varies from a minimum of 223 in 2013

to a maximum of 563 in 1996. Geotail's orbit takes around 5 to 6 days to complete and, over the course of a year, the orbital apogee covers all MLTs. As an approximation, it is expected that Geotail will cross through the magnetopause boundary at least twice for the majority of orbits, which equates to approximately 120 to 150 magnetopause crossings per year. However, Geotail typically crosses the magnetopause boundary multiple times per orbit because the boundary is in constant motion and when the orbital perigee is located at the dayside magnetopause, Geotail skims the boundary and passes through it multiple times. The total number of magnetopause crossings identified each year does not follow any pattern although there fewer crossings in the later years. The magnetopause crossings are weighted before any analysis is carried out, and therefore the differences in numbers of magnetopause crossings should not have a large effect on any analysis.

From 1996 to 1999, the yearly magnetopause location and the average magnetopause location for the whole dataset are very similar. As we approach solar maximum, the number of magnetopause crossings with corresponding high solar wind dynamic pressures increases. In 2001, the magnetosphere is more inflated than the average magnetopause location for the whole dataset. This likely caused by the large variability in the positions of the identified magnetopause crossings. In 2002 and 2003, the magnetosphere is compressed due to the high solar wind dynamic pressures observed during this period. From 2006 through to 2015, the observed solar wind dynamic pressures are generally lower and as a result, the magnetosphere is more expanded than the average magnetopause location for the whole dataset. This reflects the fact that the solar minimum that occurred at the end of solar cycle 23 and the activity during solar cycle 24 was much weaker than the previous cycle.

Investigating such an extensive dataset allows us to make comparisons between different solar cycle phases. The period of study starts during the solar minimum that occurred between solar cycle 22 and 23. The next solar minimum took place around 12 years later, in 2008 and 2009. This solar minimum was much deeper than the previous and magnetopause crossings with weaker solar wind dynamic pressures were observed. The magnetosphere was more inflated during the second solar minimum compared to the first. At the first solar minimum (1996), the best fit r_0 and α values are 10.16 R_E and 0.58 respectively, whereas the best fit r_0 and α values during the second solar minimum increase to 10.69 R_E and 0.60 in 2009. Similar behaviour is observed when comparing the solar maxima of solar cycles 23

Year	Number of crossings	r_0 (R_E)	α
1996	563	10.16	0.58
1997	534	10.32	0.56
1998	436	9.94	0.58
1999	427	10.09	0.56
2000	473	9.88	0.60
2001	293	10.24	0.63
2002	387	9.59	0.60
2003	483	9.35	0.58
2004	404	9.67	0.64
2005	387	9.98	0.60
2006	391	10.05	0.59
2007	562	10.26	0.59
2008	452	10.60	0.58
2009	417	10.69	0.60
2010	400	10.29	0.62
2011	332	10.75	0.57
2012	236	10.29	0.58
2013	223	10.62	0.57
2014	298	10.44	0.63
2015	352	9.98	0.62

Table 5.1: The number of magnetopause crossings, the dayside magnetopause standoff distance, r_0, and the flaring of the magnetotail, α for each year.

and 24. The magnetopause is more compressed during the first solar maximum compared to the second solar maximum. We are also able to compare the declining phases of the two solar cycles. During the declining phase, the highest solar wind velocities, and hence dynamic pressures, are observed. The magnetopause undergoes a slightly larger compression during the first declining phase (2003 to 2006) than the second (2015), however the

period investigated only includes one year of the second declining phase. During 2003 the best fit r_0 and α values are 9.35 R_E and 0.58 respectively, whereas in 2015 the best fit r_0 and α values are slightly higher; 9.98 R_E and 0.62 respectively.

5.3.2 Long-term solar cycle variations

Figures 5.3 and 5.4 display the sunspot numbers, different solar wind and magnetospheric parameters, and model predictions over the 20-year period investigated in this thesis. Figure 5.3a. shows the average international sunspot number determined from taking the mean over a 12-month sliding window, provided by SILSO World Data Center [2016]. The sunspot number is used to describe the 11-year solar activity cycle, where the end of a cycle occurs at solar minimum (see section 1.3.2 for more detail). The period in this study extends almost two solar cycles; solar cycle 23 and 24. Both solar cycles are characterised by unusual behaviour. Solar cycle 23 began in 1996 and peaked during the years 2000 to 2002. The solar minimum occurred between 2007 to 2010 and was the deepest and longest of the space age, with a low heliospheric magnetic field, and a significant reduction in the solar wind speed and density [Owens *et al.*, 2011, and references therein]. Solar cycle 24 is characterised by much lower activity relative to recent solar cycles, with an average of 120 sunspots at maximum in 2014. Solar cycle 24 is in the descending phase at the end of the time interval utilised in this study. See section 3.2 for more detail on solar cycles 23 and 24.

The magnetopause subsolar standoff distance, r_0, and the radius of the magnetotail estimated from four models are displayed by different lines in panels b. and c. in Figure 5.3 respectively. The radius of the modelled magnetotail is calculated at 20 R_E downtail. The pink dot-dash lines represent r_0 and the magnetotail radius as predicted by the empirical model developed in this study which depends on solar wind dynamic pressure. The model shown by the pink dot-dash lines is calculated after weighting the magnetopause crossings by how long Geotail spends in a 1×1 R_E spatial bin. For comparison, the dot-dashed blue lines represent the model developed in this study without weighting the magnetopause crossings. The dashed purple lines represent r_0 and the tail radius as predicted by the Shue *et al.* [1998] model, which requires solar wind dynamic pressure and IMF B_Z as inputs. The dotted green lines show the results as predicted by the Lin *et al.* [2010] model, which requires solar wind dynamic and thermal pressures, IMF B_Z, and dipole tilt angle as inputs.

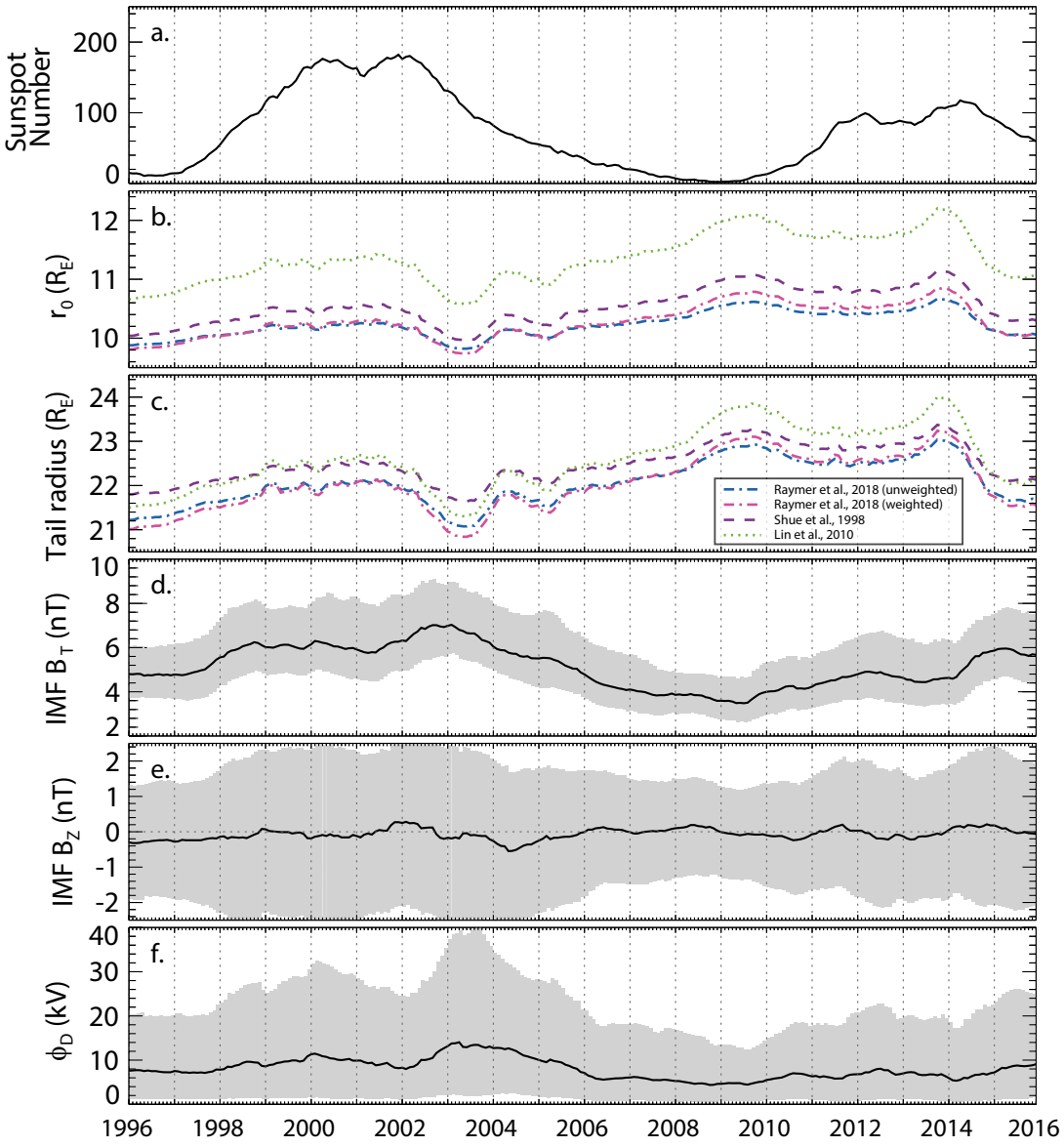

Figure 5.3: a. 12-month sliding mean sunspot numbers provided by the SILSO World Data Center [2016]. b. and c. show the calculated subsolar magnetopause standoff distance, r_0, and radius of the magnetotail calculated at 20 R_E downtail for the different models. d-f. 12-month sliding median and quartiles for different solar wind parameters from the OMNI dataset. They respectively show: total IMF strength, IMF B_Z, and the dayside reconnection rate [Milan *et al.*, 2012].

For this study however, we have set the dipole tilt angle to zero, since it primarily influences the location of the magnetic cusps, which do not have a strong effect on the location of the magnetopause in the equatorial plane. As the Lin *et al.* [2010] model is three-dimensional

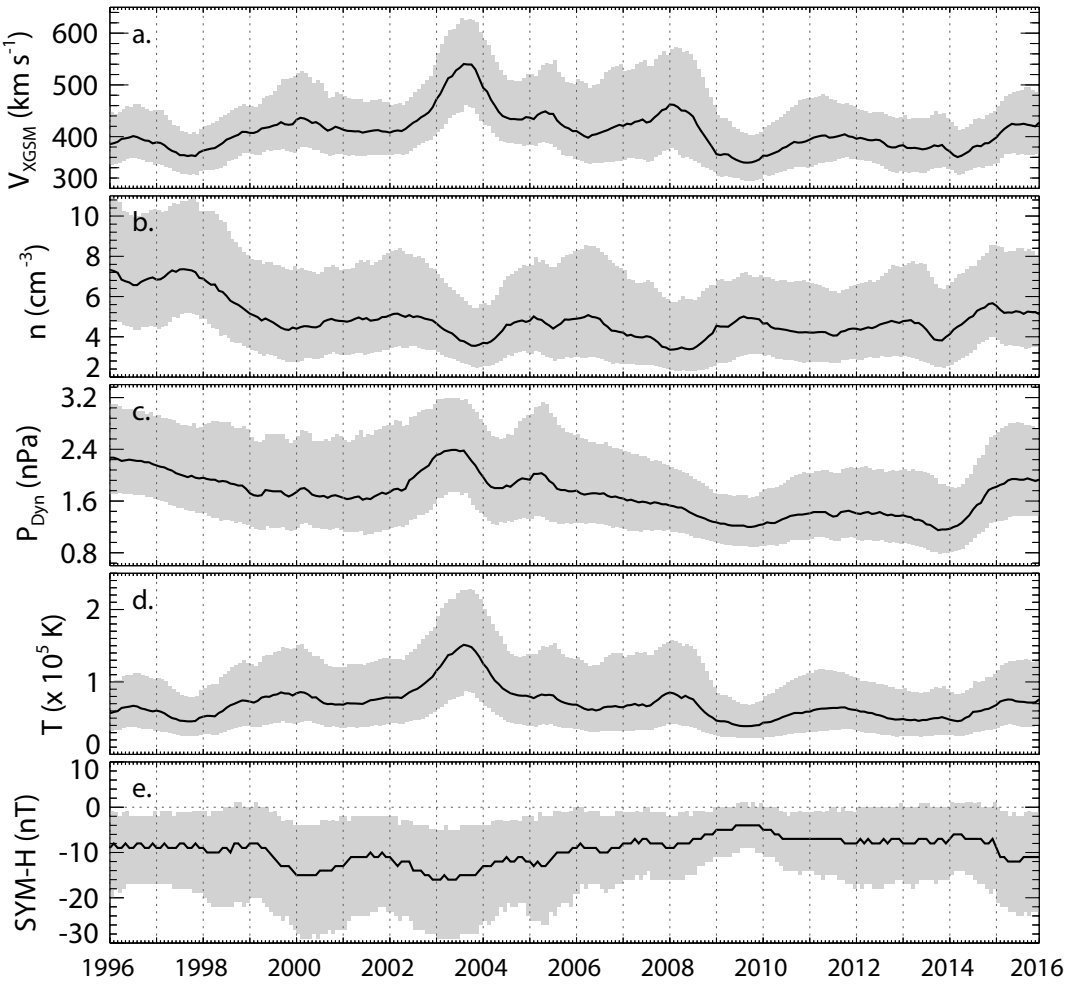

Figure 5.4: a. to e. respectively show the magnitude of the solar wind velocity in the X_{GSM} direction, the density, solar wind dynamic pressure, plasma temperature and the SYM-H index. 12-month sliding medians are indicated by the black solid line with quartile ranges shaded in grey.

and asymmetric, only the model predictions in the $X-Y$ plane and for positive Y'_{GSM} have been considered, although there are only small differences between positive and negative Y'_{GSM}.

Panels d., e., and f. show the median and quartile ranges of the total IMF strength, the IMF B_Z component, and the solar wind-magnetosphere coupling function, ϕ_D. The coupling function describes the relationship between the dayside reconnection rate and the upstream solar wind conditions, and hence is a measure of the amount of magnetic flux being opened at the dayside magnetopause (section 3.1.4). Milan *et al.* [2012] defined

this coupling function based on upstream solar wind measurements combined with in situ spacecraft measurements, auroral images, and ground-based measurements as

$$\phi_D = \Lambda V_X^{4/3} B_{YZ} \sin^{9/2} \frac{1}{2}\theta \tag{5.4}$$

where $\Lambda = 3.3 \times 10^5$ m$^{2/3}$ s$^{1/3}$, V_X is the velocity of the solar wind the X_{GSM} direction, B_{YZ} is the transverse component of the IMF ($B_{YZ}^2 = B_Y^2 + B_Z^2$), and θ is the clock angle, the angle that the projection of the IMF in the Y-Z plane makes to the Z-axis. ϕ_D maximises when IMF B_Z is directed southwards.

The panels in Figure 5.4 respectively show: a. the magnitude of the solar wind velocity in the X_{GSM} direction, b. the solar wind density, c. the solar wind dynamic pressure, d. the solar wind plasma temperature, and e. the ring current strength measured by the SYM-H indices. The black line indicates the medians of the parameters, and the grey shaded regions show the quartiles.

Figure 5.3d. indicates that the IMF strength is well correlated with sunspot number such that at solar minimum the average IMF strength is low. In 1996 the IMF strength was approximately 4.5 nT, but during the next minimum in 2009 it was lower; approximately 3.5 nT. As the Sun's magnetic field becomes more disordered during the solar cycle, the average IMF magnitude increases. It peaks just after solar maximum during the two solar cycles shown in panel d. Peak average values are approximately 7 nT and 6 nT for solar cycle 23 and 24 respectively. The coupling function, shown in panel f., is highest during 2003, and lowest during the deep solar minimum of 2007 to 2010.

The velocity of the solar wind also varies over the cycle (Figure 5.4c.). The highest velocities are observed during the declining phase in 2003 reaching an average of $\sim$550 km s^{-1}, whereas the lowest velocities ($\sim$350 km s^{-1}) were observed in 2009. The solar wind density begins quite high averaging around 7 cm^{-3} in the first few years of this study as can be seen in Figure 5.4b. From 1999 onwards, the solar wind density consistently averaged around 4-5 cm^{-3}, decreasing to $\sim$3 cm^{-3} in 2003 and 2009. The solar wind dynamic pressure (Figure 5.4c.), which is equal to the solar wind density multiplied by the velocity squared, varies by about a factor of two over the solar cycle. High dynamic pressures are observed during the first solar minimum and in both of the declining phases (2003 and 2015). The solar wind temperature (Figure 5.4d.) has a similar variation to the solar wind velocity. The

solar wind temperature is highest during the declining phase of solar cycle 23 reaching a median value of approximately 1.5 $\times 10^5$ K. The lowest temperatures are observed during both solar minima. The solar wind temperature is on average comparatively lower during solar cycle 24 compared to solar cycle 23.

Panel e. in Figure 5.4 shows the median SYM-H index over the two solar cycles. The SYM-H index is significantly lower during solar cycle 23 compared to solar cycle 24, indicating that the ring current was much stronger. The ring current strength increases during geomagnetic storms (see section 3.1.5 for a discussion on geomagnetic storms). More geomagnetic storms occurred during the solar maximum of solar cycle 23 compared to solar cycle 24 and they were generally stronger. The ring current strength is weakest during the two solar minima. The ring current strength starts to increase again during the second solar maximum phase (2015).

Since the empirical model presented in this study depends only on the solar wind dynamic pressure as an input, the contraction and expansion of the magnetopause model reflects the solar cycle variation in dynamic pressure. At the beginning of the period being studied, the solar wind is characterised by relatively strong dynamic pressures, and the whole magnetosphere is compressed. High velocities cause a large increase in dynamic pressure in 2003, corresponding to a contraction of the magnetosphere. During the extended solar minimum and into solar cycle 24, the solar wind dynamic pressure is unusually low. Throughout this time the magnetosphere remains expanded at both the nose and in the magnetotail. At the end of the period, the dynamic pressure increases, and the magnetopause undergoes a compression.

The differences between the weighted and unweighted empirical models developed in this thesis (dot-dashed pink and blue lines respectively) are generally small. The largest differences occur during more extreme times over the solar cycle. In 2003, the weighted fit indicates that the magnetosphere was more compressed than the unweighted fit at both the day- and nightside. However, over the years 2009 to 2014, the weighted fit shows that the magnetosphere was slightly more inflated than the unweighted fit. This implies that the magnetopause crossings that were identified under extreme solar wind dynamic pressures (both high and low) were located in spatial bins where Geotail spent less time, and so after accounting for this orbital bias these magnetopause crossings have been weighted

more heavily.

Differences between the three empirical magnetopause models are expected as they are dependent on different parameters. Solar wind dynamic pressure has the strongest influence on magnetopause location and shape, so all three models follow a similar trend. However, both the Shue *et al.* [1998] and Lin *et al.* [2010] models predict a more expanded magnetosphere on average than the model presented in this study. The differences between our model (dot-dashed pink lines) and that of Shue *et al.* [1998] (dashed purple lines) are quite small for r_0 and the magnetotail radius. Although Shue *et al.* [1998] use the same function to characterise the magnetopause as in this thesis, the two solutions are different due to being based upon different datasets and including different parameters. The magnetopause crossing database used in the Shue *et al.* [1998] study to develop their model contains fewer magnetopause crossings than our study, and are largely located on the dayside of the magnetosphere. The magnetopause crossings are identified during a different solar cycle spanning primarily 1977 to 1987, which was characterised by different conditions to solar cycles 23 and 24. The Lin *et al.* [2010] model differs in that it predicts a much more expanded dayside magnetopause than the other two models. The Lin *et al.* [2010] model is developed from a larger magnetopause crossing than that of Shue *et al.* [1997] and Shue *et al.* [1998], but is still significantly smaller than the database we have presented. There are only small differences between the models in the magnetotail radius.

5.4 Summary

In this chapter the magnetopause crossings identified from 20 years of Geotail data have been investigated on a year by year basis. The Shue *et al.* [1997, 1998] function was fitted to the weighted magnetopause crossings for each year to find the best fit values for the subsolar magnetopause standoff distance, r_0, and the flaring in the magnetotail, α. The best fit magnetopause for each year was compared to the average magnetopause for the entire magnetopause crossing database. It was found that during the first few years there is not a large difference between the two. During solar maximum the magnetosphere is more compressed than the average location. From 2006 through to 2015, the magnetosphere is more expanded than the average location. This is attributed to the unusually weak

and extended solar minimum at the end of solar cycle 23 and the relatively weak activity of solar cycle 24. Comparisons were then drawn between phases of the two solar cycles. The magnetosphere was much more inflated during the second solar minimum than the first. The same affects were observed when comparing the two solar maxima; both the dayside and nightside magnetopause was more inflated during the solar maximum of solar cycle 24. During the declining phases, the magnetopause undergoes a slightly larger compression during solar cycle 23. Overall, during solar cycle 24 the magnetopause was more inflated than it was during solar cycle 23.

The second part of this chapter looked at how solar wind parameters change over the solar cycle and at how the model developed in section 4.2 varies. The model was compared to models developed by Shue *et al.* [1998] and Lin *et al.* [2010]. It was found that the empirical model developed in this thesis predicts a more compressed magnetopause than the other two models. Differences between the three models are to be expected for several reasons. Firstly, each model is created from different magnetopause crossing databases. The magnetopause crossing database employed in this thesis includes more magnetopause crossings identified downtail compared to the other two. The vast majority of magnetopause crossings identified and used to create the Shue *et al.* [1997, 1998] and Lin *et al.* [2010] models are at distances of $X_{GSM} \geq$ -10 R_E, and therefore both models may have limitations when used to describe the nightside magnetotail. Secondly, this study uses data from a much longer time period than the other two, spanning almost two solar cycles. Shue *et al.* [1997] have used data mainly from 1977 to 1987 during a more active solar cycle than the solar cycles investigated in this study. The model presented by Shue *et al.* [1998] is an improvement on their previous model and includes an extreme event observed in January 1997. Lin *et al.* [2010] have created their model by utilising data from December 1994 to January 2008 which covers all of solar cycle 23. Solar activity varies greatly between solar cycles. Unique solar activity has been observed during the solar cycles examined in this study, including the deep and extended solar minimum, and the relatively low activity of solar cycle 24.

In the following two chapters, firstly we will investigate how well the model magnetopause describes the observed magnetopause shape and examine what is causing the discrepancies between the predictions and observations, and secondly, we will consider the effects of solar wind and magnetospheric processes on magnetopause location.

Chapter 6

Comparison between the predicted and observed magnetopause location

6.1 Introduction

The location of the magnetopause is largely governed by upstream solar wind conditions, of which, solar wind dynamic pressure is the main controlling factor. At the magnetopause nose, the solar wind flow is normal to the magnetopause surface and hence solar wind dynamic pressure has the greatest influence on the magnetopause in this region. At the flanks and in the magnetotail, the flow becomes more tangential to the magnetopause and the effect of solar wind dynamic pressure on magnetopause location decreases, although it does not completely diminish (for example, see Figure 4.9 in section 4.2.2). Many other physical processes influence magnetopause location such as the strength and direction of the interplanetary magnetic field (IMF) and conditions inside the magnetosphere.

In Chapter 4, the identified magnetopause crossings were normalised for solar wind dynamic pressure and the shape and location of the magnetopause was modelled with the functional form of the Shue *et al.* [1997, 1998] empirical magnetopause model to determine new functions for the magnetopause subsolar standoff distance, r_0, and the flaring of the magnetotail, α. This allowed us to predict the location of the magnetopause for a given upstream solar wind dynamic pressure and investigate the long-term changes in magnetopause shape and location over the two most recent solar cycles. This chapter will be a continuation of the previous chapter. We examine the magnetopause location further

by comparing the empirical model predictions with the observed location of the magnetopause over the 20 years. Times when the model characterises magnetopause position well are identified and what causes the observations to deviate from model predictions are discussed. We further investigate some specific cases where atypical magnetopause crossings were observed as a result of extreme solar wind conditions and discuss their potential influence on the average magnetopause location.

6.2 Instruments and methods

The magnetopause crossing database that was identified from Geotail magnetic field and plasma data from January 1996 to December 2015 in Chapter 4 is used here. Details on how the magnetopause crossings were identified are described in section 4.1 and techniques used to minimise biases in the dataset are described in section 4.2.1. The resulting database contains 8050 magnetopause crossings that can be used for the analysis in this chapter. As described in section 4.2, an empirical model is then developed from the magnetopause crossing database. The model allows us to predict the location of the magnetopause for a given solar wind dynamic pressure. The relationship is given by

$$r = r_0 \left(\frac{2}{1 + \cos\theta} \right)^{\alpha} \tag{6.1}$$

where

$$r_0 = 11.082 P_{Dyn}^{-1/6.75} R_E \tag{6.2}$$

$$\alpha = 0.605 - 0.010 P_{Dyn} \tag{6.3}$$

where r is the radial distance and θ is the solar zenith angle, r_0 is the magnetopause standoff distance, and α describes the level of flaring in the magnetotail. The magnetopause crossings have been weighted by dwell time prior to developing the model.

Solar wind data is provided by the OMNI dataset (see section 2.1.2) and sunspot numbers are provided by the SILSO World Data Center [2016] (see section 2.2.3).

To examine how the location of the magnetopause varies over the 20-year period, we separate the magnetopause crossings into 12-month sliding intervals and fit the function defined by Shue *et al.* [1997, 1998] (equation 6.1) to each 12-month interval. The starting

point of each 12-month interval is shifted by one month. Similar to the fitting process described section 4.2.2, to minimise the effects of orbital biases, magnetopause crossings have been weighted by how long Geotail spends in a particular spatial bin over each 12-month sliding interval. A value for r_0 and α are calculated for each of the sliding 12-month intervals. r_0 and α can then be plotted as a function of time enabling the observed average magnetopause shape and position to be investigated over the 20-year period.

6.3 Results and discussion

Variations in magnetopause location and solar wind parameters for the whole 20-year period (1996 to 2016) are presented and discussed first. This is followed by a detailed examination of intervals during which the empirical magnetopause model does not describe the location of the observed magnetopause sufficiently. Reasons for the discrepancies are discussed and examples of magnetopause crossings that are detected during extreme solar wind conditions are presented.

6.3.1 1996 to 2016

Sunspot numbers, the observed magnetopause location and model predictions, and solar wind data are presented in Figures 6.1 and 6.2. Figure 6.1a. displays the monthly mean sunspot numbers (grey solid line) and 12-month sliding mean sunspot numbers (black solid line) [SILSO World Data Center, 2016]. Sunspot numbers are an indication of solar activity and are used to define the solar cycle (see section 1.3.2 for more detail). Panels b. and c. show the predicted (dot-dashed lines) and observed (red solid line) magnetopause location at the subsolar standoff distance, r_0, and the magnetotail radius calculated at 20 R_E downtail, respectively. 12-month sliding median solar wind dynamic pressure is input in equations 6.2 and 6.3 to produce the pink dot-dashed lines, and one-month medians are used to produce the grey dot-dashed lines. Corresponding solar wind parameters are presented in Figure 6.1d-f. and in Figure 6.2a-e. The black solid line shows the 12-month sliding median values with upper and lower quartiles shaded in grey. The grey solid lines show the one-month median values. Figure 6.1d. and 6.1e. present the IMF B_T and B_Z conditions over the 20 years. Figure 6.1f. shows the dayside reconnection rate, ϕ_D, which is calculated

using equation 3.4 described in section 3.1.4 defined by Milan *et al.* [2012]. Figure 6.2a-e. respectively show: the magnitude of the solar wind velocity in the X_{GSM} direction, the solar wind density, the solar wind dynamic pressure, the solar wind temperature, and the SYM-H index.

The observed magnetopause has been calculated by fitting the Shue *et al.* [1997, 1998] function (equation 6.1) to 12-month sliding intervals of magnetopause crossings to find best-fit values for r_0 and α. Different methods of weighting the crossings were tested. The results shown in Figure 6.1 show the average location of the magnetopause when the magnetopause crossings have been weighted with a 12-month sliding interval dwell time. Although not shown in the figure, weighting the crossings with the 20-year dwell time as opposed to the 12-month sliding interval dwell time was investigated, but it was found that this weighted some magnetopause crossings too heavily and therefore did not produce a very good fit to the magnetopause crossings. Similar to the best fit values shown in Table 5.1, the fitting has only been carried out to two decimal places due to computational constraints. This means that when it is plotted it is not as smooth as the model. It was decided to not bin the magnetopause crossings into intervals any shorter than 12 months because it takes 12 months for Geotail's apogee to cover all MLTs, and so a shorter time interval would not cover all MLTs.

In the previous chapter, how the solar wind and magnetopause varied over the 20 years was described in detail, so therefore the variations observed in solar wind conditions and the magnetosphere shown in Figures 6.1 and 6.2 will only be briefly reviewed here before the differences between the model prediction and observations are discussed. On average, the magnetopause nose and magnetotail (Figures 6.1b. and c.) are more compressed during solar cycle 23 compared to solar cycle 24. The largest compressions are observed during the declining phase of solar cycle 23. The magnetopause is highly inflated during the deep and extended solar minimum and during solar cycle 24; between 2007 and 2014.

The total magnetic field strength, presented in Figure 6.1d., correlates with solar activity, or sunspot number. The maximum in B_T occurs just after solar maximum, and it decreases to its lowest values at solar minimum. The 12-month sliding median IMF B_Z (panel e.) mainly fluctuates around 0 nT, although larger deviations are observed. For example, in 2004, the IMF B_Z was on average directed southwards reaching an average of $\sim$ -0.5 nT. The

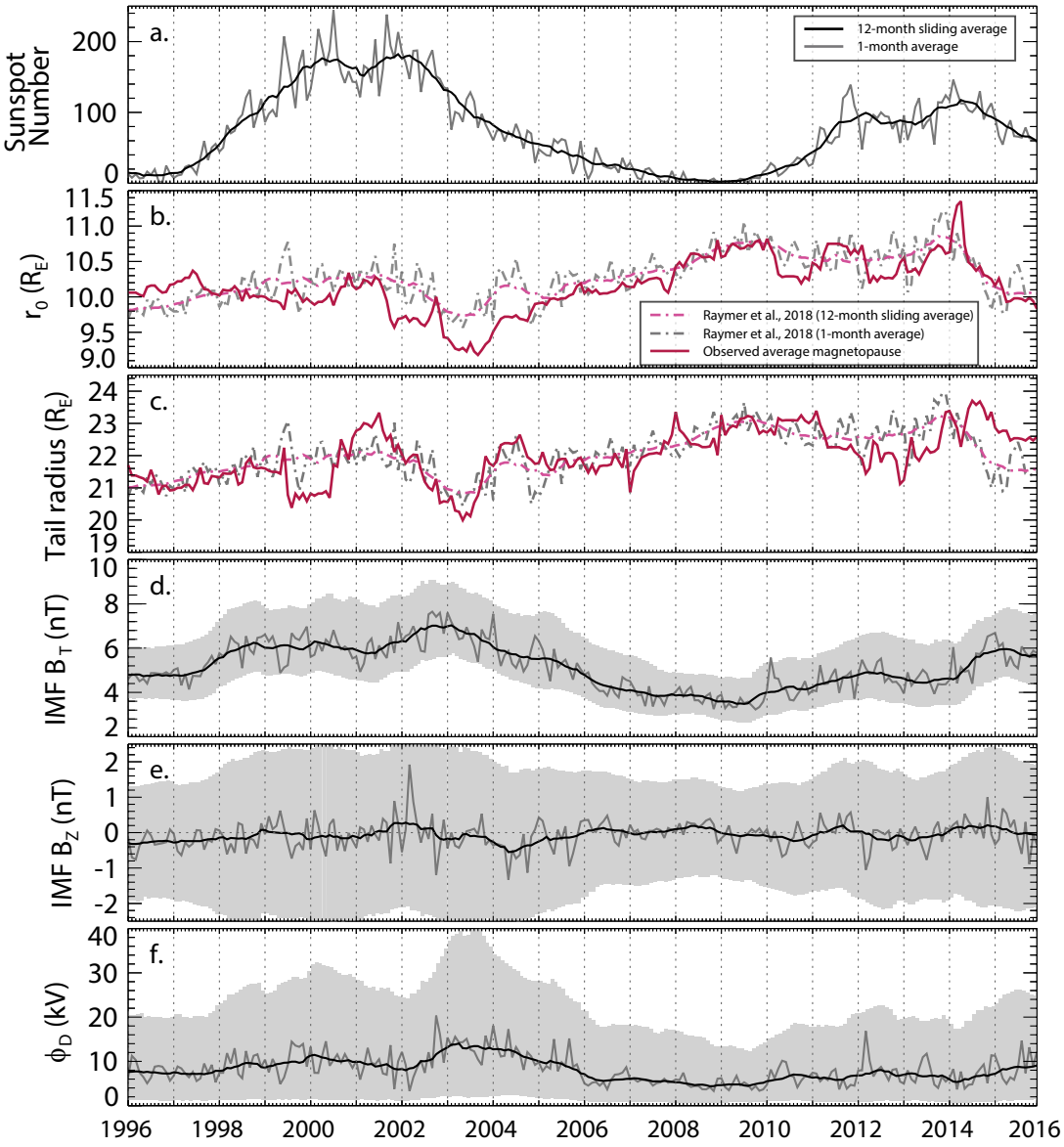

Figure 6.1: a. 12-month sliding mean sunspot numbers (provided by the SILSO World Data Center [2016]) in black, and one-month mean sunspot numbers in grey. b. Subsolar standoff distance, r_0, for the model (pink and grey dot-dashed lines) and the observed average magnetopause (red solid line). c. Radius of the magnetotail calculated at 20 R_E downtail for the model (pink and grey dot-dashed lines) and the observed average magnetopause (red solid line). d. and e. IMF B_T and B_Z respectively. f. displays the dayside reconnection rate, ϕ_D, which is calculated using equation 3.4. 12-month sliding medians are indicated by the black solid line with upper and lower quartile ranges shaded in grey. One-month medians are indicated by the grey solid line.

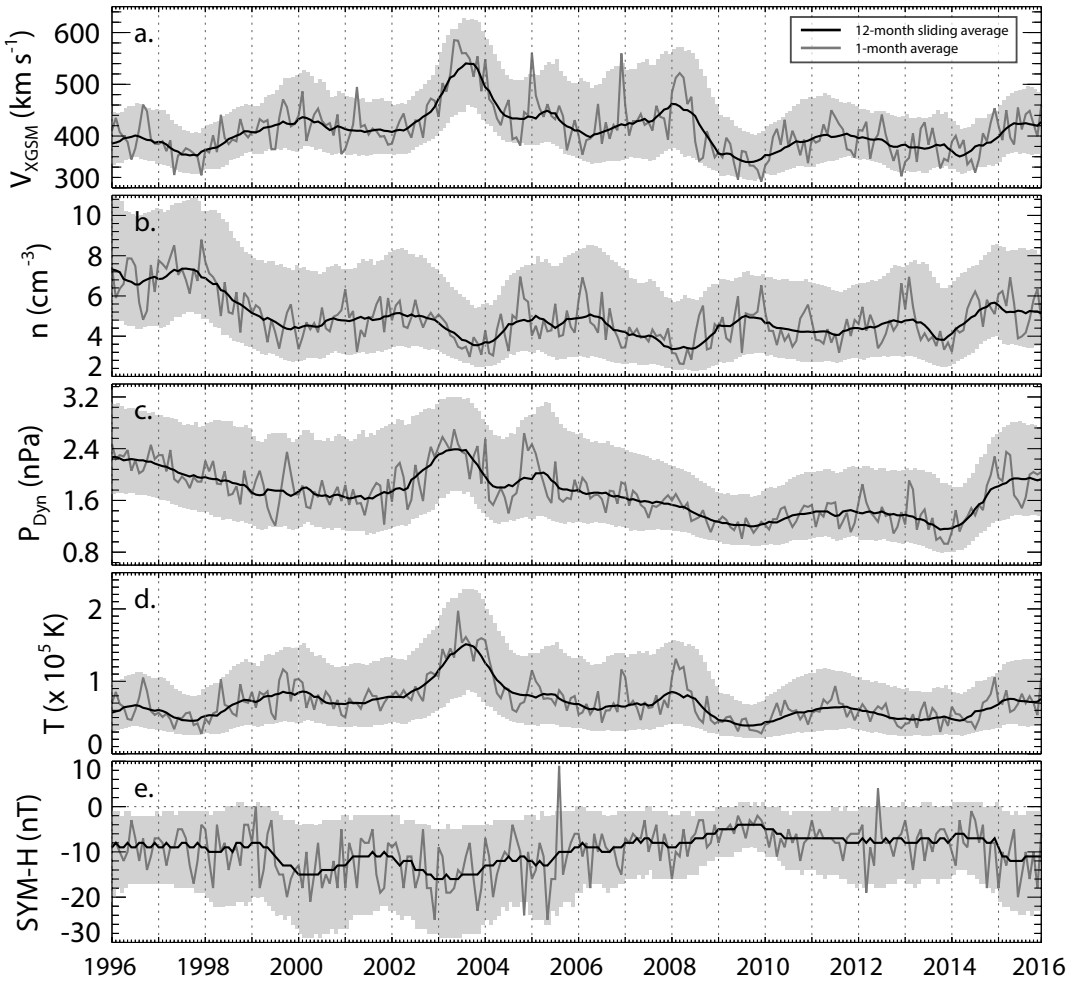

Figure 6.2: a. to e. respectively show the magnitude of the solar wind velocity in the X_{GSM} direction, the density, solar wind dynamic pressure, plasma temperature and the SYM-H index. 12-month sliding medians are indicated by the black solid line with quartile ranges shaded in grey. 1-month medians are indicated by the grey solid line.

dayside reconnection rate (panel f.) peaks in 2003. This coincides with the largest compression observed in both r_0 and the tail radius.

There are large changes in the median solar wind velocity over the 20-year period (Figure 6.2a.). During the declining phase of solar cycle 23, the median velocity increased to $\sim$ 550 km s^{-1}, compared with a minimum of $\sim$ 350 km s^{-1} at solar minimum in 2009. The solar wind density (panel b.) shows that it is also highly varied over the given period. It is maximum in the beginning of the period (1996 to 1999), and does not correlate with solar cycle as the density did not increase again during the beginning of the next solar cycle. Solar wind

dynamic pressure (panel c.) is calculated from the solar wind density and velocity. It varies by approximately a factor of two over the solar cycle. Solar wind dynamic pressure is highest during the first solar minimum (1996), and during the two declining phases (2003 and 2015). The solar wind temperature (panel d.) peaks in 2003 similar to the other parameters. Finally, the ring current strength (panel e.) varies over the solar cycle. The ring current is strongest during the declining phases (2003 and 2015) as expected based on the other parameters, but it is also strong between 1999 and 2000.

Figure 6.1b. and 6.1c. show that generally, there is a close overall agreement between the model predictions (pink and grey dot-dashed lines) and the observed 12-month sliding average magnetopause location (red solid line). Beginning with panel b., which shows the variations in dayside subsolar standoff distance, during the years 2005 to 2010, the model predicts the average location of the magnetopause fairly accurately. This is during the deep and extended solar minimum when solar wind dynamic pressure is low. There is also very good agreement during the second half of 2014 and during 2015, and reasonably good agreement from 1998 to 2001. During the years 1996 to 1997, at the first solar minimum, the dayside magnetopause is slightly more expanded than predicted by the model. The solar wind dynamic pressure was high during this interval due to an increase in solar wind plasma density. The largest differences between the model and average magnetopause location occur from the end of 2001 to the end of 2004, during which the magnetopause nose is located much closer to the planet than predicted. There are also discrepancies between the model and the average magnetopause location from 2010 to mid-2014. Differences between the model and the observed magnetopause location are expected because the model is parameterised by solar wind dynamic pressure only; it does not take other solar wind processes into account, such as dayside reconnection which is known to have an effect on the nose of the magnetopause as it erodes the magnetic flux in this region.

Moving on to panel c., which shows the radius of the nightside magnetotail, overall, the model predicts the average shape and location of the magnetopause in the tail with reasonable accuracy. There is close agreement between the model and the average magnetopause location during the years 1996 to mid-1999, and again from 2002 to 2012. Larger differences occur in 2000, 2001 and towards the end of the 20-year time period from 2012 onwards. Greater variations between the model magnetopause and the observed magnetopause are

expected in the flanks and magnetotail region because the solar wind flow becomes more tangential to the magnetopause and so the influence of solar wind dynamic pressure is lower. The magnetopause nose experiences a solar wind flow normal to its surface, and therefore variations in solar wind dynamic pressure will have a larger influence on this region, and a model parameterised by solar wind dynamic pressure will describe the location more accurately. Furthermore, a greater number of magnetopause crossings are observed at the dayside magnetopause, and therefore the magnetopause in this region will be more accurately constrained.

The other models presented in Chapter 5 predict a more expanded magnetopause than the predictions made by the model presented in this study for all solar wind conditions. As discussed in section 5.4, differences are expected as the models are developed from different datasets of magnetopause crossings that were identified during different solar wind conditions. As models developed by Shue *et al.* [1998] and Lin *et al.* [2010] are parameterised by other solar wind parameters such as IMF B_Z, it might be expected that they would predict the behaviour of the magnetopause more accurately. Despite this, they do not fit the observations any better than the model developed in this study.

Although we do not believe there will be a large difference between the solar wind dynamic pressure measured at the bow shock and what is measured downtail, this could have an effect. It would take the solar wind approximately 12 minutes to reach 20 R_E downtail depending on upstream conditions. This propagation time from upstream spacecraft to Geotail has not been taken into account in this study as it is difficult to quantify, and this could have a small influence on the analysis presented here.

The remaining sections in this chapter will investigate the periods during which the model does not characterise the magnetopause well in greater detail. We will focus on the magnetopause nose and magnetotail separately, as we expect that solar wind conditions will influence the two regions differently. We will investigate the following periods: 1999 to 2002, during which the magnetotail is firstly more compressed than predicted, and then more inflated; 2001 to 2005, during which r_0 is more eroded than predicted; and finally 2012 to 2016, which includes both a short period where the dayside magnetopause becomes much more expanded than predicted, and includes discrepancies between the model and observations in the magnetotail. In addition, a selection of magnetopause crossings that

were identified during extreme solar wind conditions are presented.

6.3.2 1999 to 2002

The first period that is being examined in greater detail spans 1999 to 2002. Two intervals are highlighted during which the observed magnetopause diverges from the predicted magnetopause. During the first interval which is highlighted in pink and labelled (i) in Figure 6.3, the magnetotail undergoes a ∼1 to 1.5 R_E compression which lasts from approximately July 1999 to June 2000. During the second interval which is highlighted and labelled (ii) in Figure 6.3, the magnetotail radius is slightly more expanded than predicted by the empirical model by $\sim 1\ R_E$. This occurs from approximately December 2000 to November 2001. In this section I will discuss the possible causes for the observed differences.

During the first interval (i) in Figure 6.3, the solar wind conditions are relatively quiet. There is a slight increase in dayside reconnection rate (panel e.) due to periods of southward directed IMF B_Z (panel d.), however the increase in dayside reconnection and southward IMF B_Z does not persist through the entire period. There is also a slight increase in solar wind velocity in the X_{GSM} direction (panel f.), but this increase coincides with a decrease in solar wind density (panel g.), so the solar wind dynamic pressure remains relatively constant during the period (panel h.). Only small geomagnetic disturbances are observed (panel i.).

As the observed magnetopause is calculated from fitting the Shue *et al.* [1997, 1998] to 12-month sliding intervals of magnetopause crossings, the observed compression in the magnetotail could be caused by extreme magnetopause crossings influencing the fitting process. To investigate this, I have examined the 12-month sliding intervals of magnetopause crossings that occur during this time-period (not shown). There are a few cases where the magnetotail is observed to be highly compressed. The most extreme of these events occurred on 4$^{\text{th}}$ December 1999 in which Geotail repeatedly encountered a highly compressed magnetopause during a 9-hour period. Figure 6.4a. displays the locations of the magnetopause crossings (red crosses) identified by the automated routine in the $X'_{GSM} - \rho'_{GSM}$ plane (where ρ' is defined as $\sqrt{Y'^2_{GSM} + Z^2_{GSM}}$). The dot-dashed line represents a model bow shock determined from the average solar wind conditions during this interval [Peredo *et al.*, 1995] and the dashed line represents the predicted magnetopause location determined by the model developed in this thesis, where r_0 and α are indicated under the panel. The path

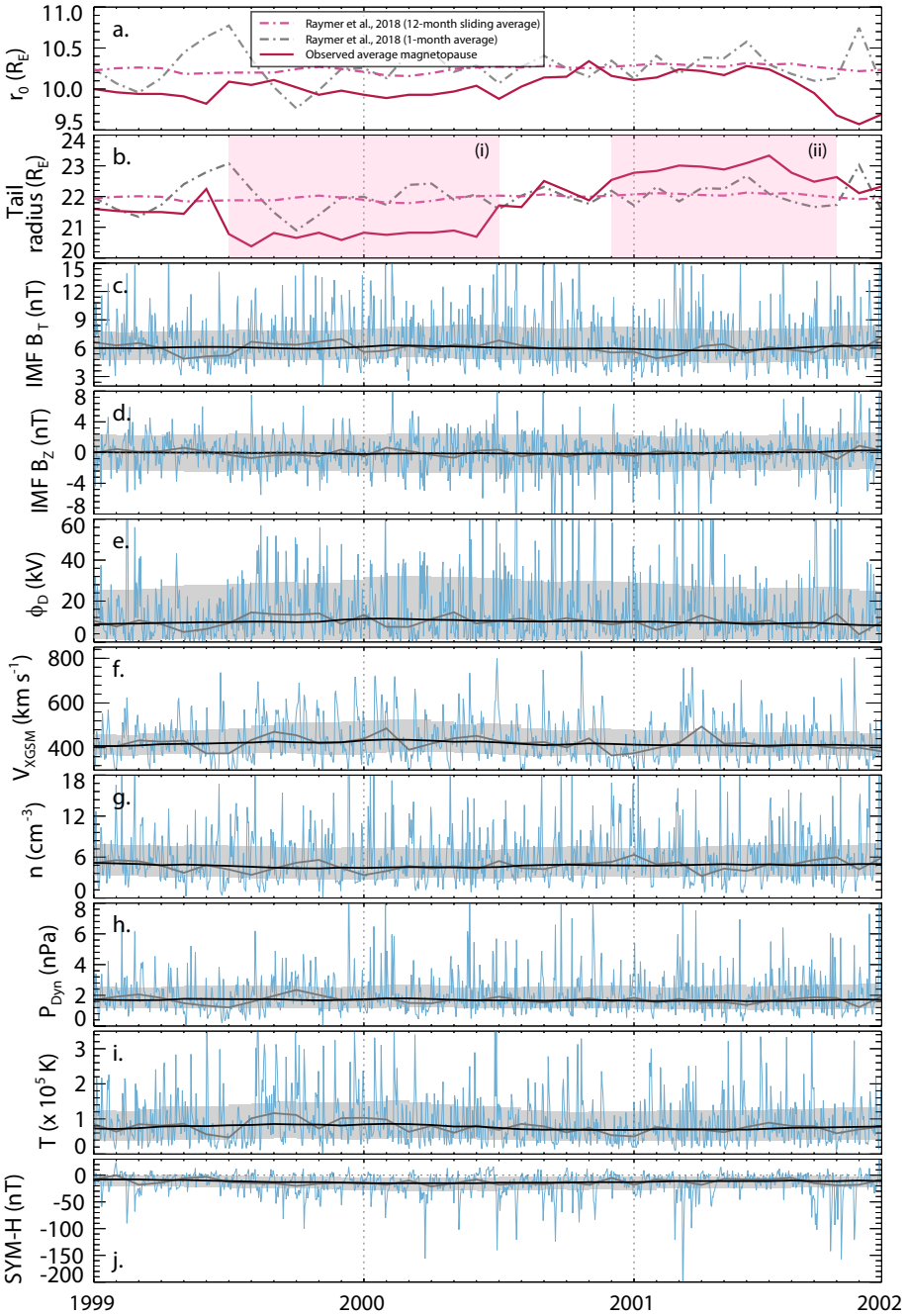

Figure 6.3: a. and b. Subsolar standoff distance, r_0, and the radius of the magnetotail calculated at 20 R_E downtail respectively, for the model (pink and grey dot-dashed lines) and the observed average magnetopause (red solid line). c. to j. IMF B_T; IMF B_Z; the dayside reconnection rate, ϕ_D; solar wind velocity; solar wind density; solar wind dynamic pressure; solar wind temperature; and the SYM-H index. 12-month sliding medians are indicated by the black solid line with upper and lower quartile ranges shaded in grey. One-month medians are indicated by the grey solid line and daily medians are shown by the blue solid line.

of Geotail for the 24-hour interval is represented by the red arrowed dotted line. Panels b. to e. show the magnetic field and plasma conditions Geotail observed and the red dotted lines show the identified magnetopause crossings. Coordinates are displayed below the panels.

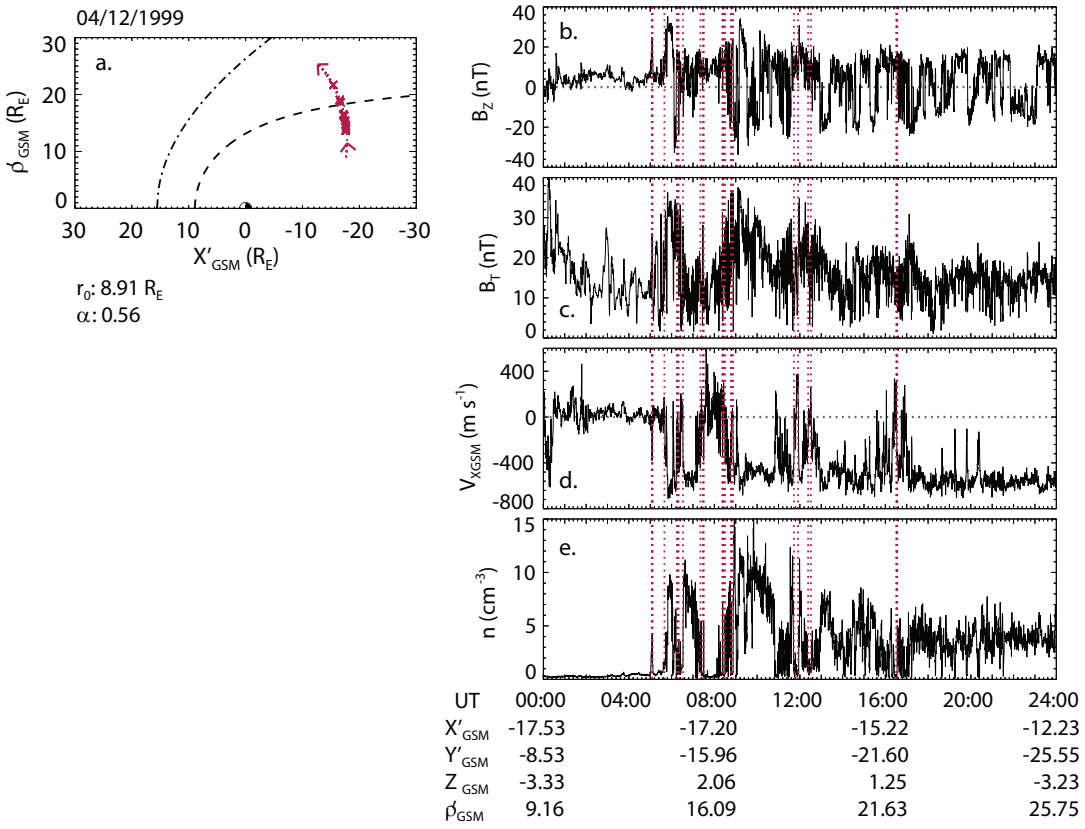

Figure 6.4: a. Orbital path of Geotail (red dotted arrowed line) on 4th December 1999 in the $X'_{GSM} - \rho'_{GSM}$ plane (where ρ' is defined as $\sqrt{Y'^2_{GSM} + Z^2_{GSM}}$). The locations of the magnetopause crossings detected by the algorithm are indicated by the red crosses. The dot dash line indicates a model bow shock [Peredo *et al.*, 1995] and the dashed line represents the predicted magnetopause location using the model developed in this study. r_0 and α values are indicated below the plot. Average solar wind conditions from this time interval have been used as an input for both models. b. to e. display the magnetic field strength in the Z direction; the total magnetic field strength; the velocity of the plasma in the X_{GSM} direction; and the density of the plasma during the 24-hour period.

At the start of this period, Geotail is located in the magnetospheric side of the the dawn magnetopause. This is characterised by northward directed B_Z, plasma velocities fluctuating around 0 km s^{-1}, and near-zero plasma density. At approximately 05:00 UT, the first

magnetopause crossing is detected. It is registered because it satisfies the flank and magnetotail crossing identification criteria described in section 4.1.1.2. The bulk plasma tailwards velocity decreases suddenly and is accompanied by an increase in the plasma density and a more varied total magnetic field strength. About 30 minutes after this first magnetopause crossing, another is detected, followed by subsequent multiple crossings until approximately 16:30 UT. The corresponding OMNI observations from this interval (not shown) indicate that there was a solar wind dynamic pressure enhancement to $\sim$6 nPa, IMF B_Z was strongly northwards ($\sim$ 15 nT) prior to the magnetopause encounter, before turning southwards after the crossing, and the solar wind velocity in the X_{GSM} direction increased in magnitude to $\sim$650-700 km s^{-1}. SYM-H measurements show that the period was geomagnetically quiet, $\sim$-20 to -40 nT, so we do not believe these extreme events were caused by a geomagnetic storm.

The plasma on the magnetospheric side was stagnant with a low density, while the plasma in the magnetosheath was flowing tailward with plasma density of 5-10 cm^{-3}, indicating the existence of a velocity shear across the magnetopause. Large fluctuations in the plasma density suggest that wavy or vortical structures were present at the dusk side magnetopause [Nishino *et al.*, 2011]. These wavy/vortical structures may be caused by the sudden pressure change [Sibeck, 1990], or they could be caused by Kelvin-Helmholtz Instabilities (KHI) [Kivelson & Chen, 1995]. KHI vortices are well-known fluid instabilities that occur on the interface between two fluids that are flowing with different velocities relative to one another [e.g. Chandrasekhar, 1961; Hasegawa, 2012]. KHI play an important role in plasma transport across the magnetopause when the IMF B_Z component is directed northwards [e.g. Scholer & Treumann, 1997; Fairfield *et al.*, 2000; Hasegawa *et al.*, 2004].

During this interval, although Geotail encounters the magnetopause multiple times, not all boundary crossings are identified by the algorithm. The algorithm determines whether the mean plasma conditions within a 3-minute interval are either magnetospheric or magnetosheath conditions. Therefore, if Geotail encounters the magnetopause multiple times in short timescales, then a second crossing may occur within the 3-minute window and the crossing will not register. A different technique would be required in order to catch these additional magnetopause crossings and this is beyond the scope of this thesis.

The multiple magnetopause crossings identified on 4$^{\text{th}}$ December 1999 are the main

cause of the observed compression occurring between July 1999 to June 2000. These magnetopause crossings, in combination with some other magnetopause crossings that are observed when the magnetopause is undergoing a compression, influence the fitting process. Since the fit is being weighted by dwell time, these extreme magnetopause crossings are being weighted more heavily than others. They have not been removed because we wanted to include extreme conditions as well as quiet conditions.

From December 2000 to November 2001 (interval (ii) in Figure 6.3), the magnetotail is more flared than predicted by $\sim$1 R_E. Prolonged periods of southward directed IMF B_Z, which adds open magnetic flux to the magnetosphere and inflates the magnetotail could be producing this observed inflation. This would also lead to increased dayside reconnection rates. During this interval there are some periods with strong southward IMF B_Z and high dayside reconnection rates (panels d. and e.).

Another process that may affect magnetopause location is the strength of the ring current. The ring current flows toroidally around the Earth and extends to distances of $\sim$2 to 9 R_E in the equatorial plane [e.g. Daglis *et al.*, 1999]. Increased geomagnetic activity caused by geomagnetic storms (see section 3.1.5) causes an enhancement in the ring current strength. The magnetic field that accompanies the ring current decreases the Earth's magnetic field inside of the ring current and a reduction in SYM-H indices is measured (see section 2.2.1). Outside the ring current however, the magnetic field increases and can cause the magnetopause to inflate.

In this interval (ii), which spans most of 2001, a number of geomagnetic storms are observed (panel i.). It should be noted that the blue line only indicates the median daily observations, therefore it does not capture the full intensity of the storms. For this, we have looked at geomagnetic storm lists [e.g. Hutchinson *et al.*, 2011; Kilpua *et al.*, 2015]. The increased number of geomagnetic storms may have a role in causing the differences between the predicted and observed magnetopause location. During the main phase of a storm we would expect to observe a compression of the magnetopause in combination with the erosion of magnetic flux from the dayside magnetosphere (see section 3.1.5). During the recovery phase it is expected that the magnetic field accompanying the ring current will cause an inflation in the magnetotail.

The recovery phase of a geomagnetic storm can last several days depending on the

strength of the storm. In a study of the storms that occurred during solar cycle 23, Hutchinson *et al.* [2011] found that the recovery phase for weak storms (-150 nT < SYM-H $\leq$ -80 nT) was $\sim$1.5 days, for moderate storms (-300 nT < SYM-H $\leq$ -150 nT) it was over 2 days, and for intense storms (SYM-H $\leq$ -300 nT) it was over 3 days. Milan [2009] also investigated storm-time recovery by examining the behaviour of the auroral oval from IMAGE observations. They found that the auroral oval radius increases sharply at storm onset, associated with increased dayside driving. During the recovery phase, the oval radius gradually decreases mirroring the decay observed in SYM-H indices. In the period highlighted (ii), a number of weak, moderate and intense storms were observed. The ring current is likely to have continued to inflate the magnetotail over a number of days during the recovery phases of these storms, and this is a possible explanation for the differences between the model and observations seen in the tail radius (panel b., (ii)).

6.3.3 2001 to 2005

During the period shown in Figure 6.5, 2001 to 2005, differences are observed between the model magnetopause and the observed magnetopause standoff distance, r_0. The interval that will be focused on in this section is highlighted in pink and spans approximately September 2001 to December 2004 during which the observed magnetopause nose was located closer to the planet than predicted. Panels c. to h. display the upstream solar wind conditions and dayside reconnection rate (e.), ϕ_D, which is calculated using equation 3.4 [Milan *et al.*, 2012]. Panel i. displays the SYM-H index which is a measure of ring current strength. Daily medians are shown by the blue line, monthly medians are shown by the grey line and 12-month sliding medians which are calculated in the same way as described previously are shown by the black line, with lower and upper quartiles shaded in grey.

Throughout this interval, the observed standoff distance is offset by approximately 0.5 R_E (panel a.). At the magnetotail (panel b.), the model predicts the observed tail radius with better accuracy than it does at the dayside. There are discrepancies of up to $\sim 0.5\ R_E$, but as discussed previously, larger variations between the model and observations at the magnetotail are expected as the magnetotail is not as constrained by solar wind dynamic pressure.

To explain the differences between the model and observed magnetopause other param-

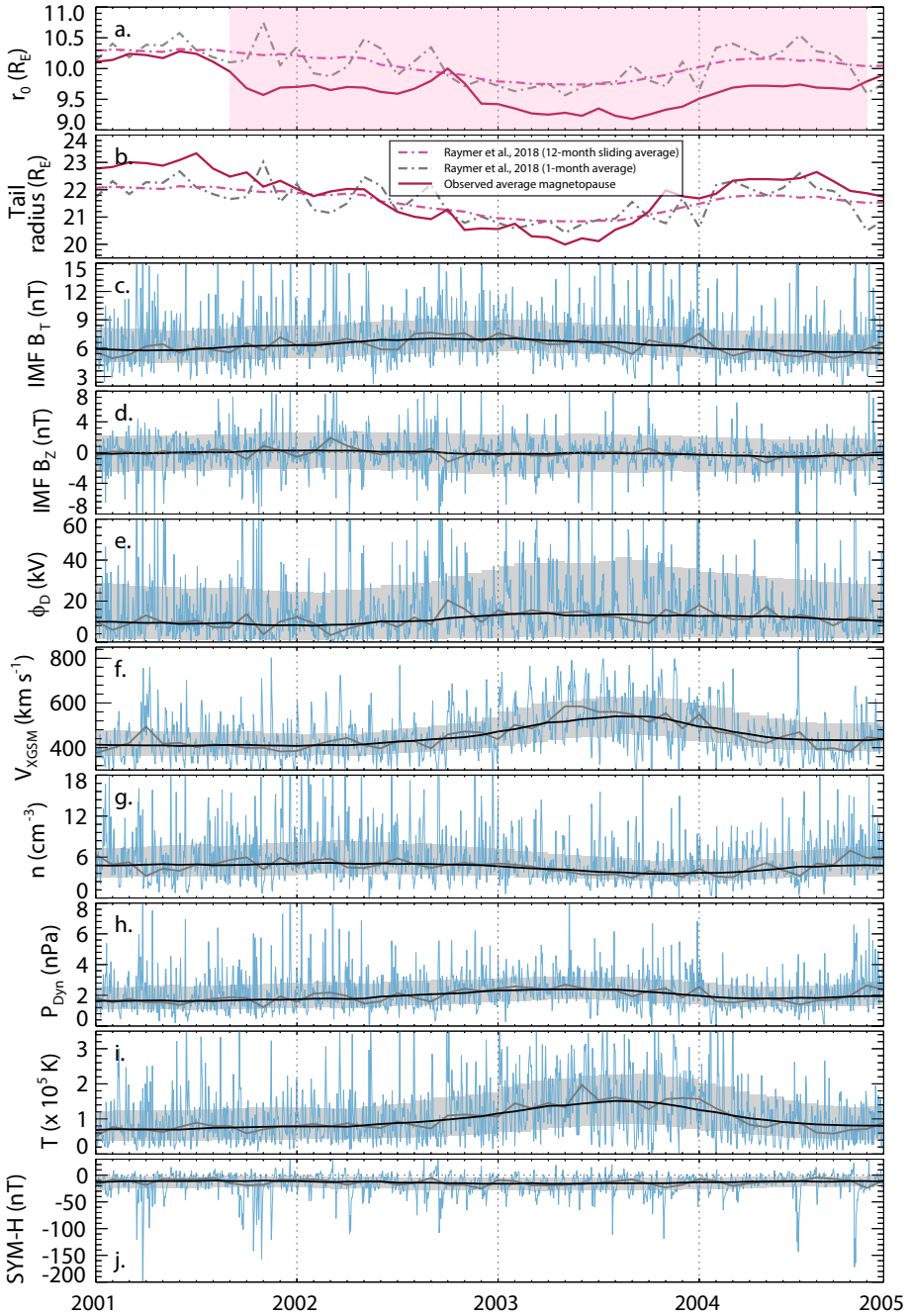

Figure 6.5: a. and b. Subsolar standoff distance, r_0, and the radius of the magnetotail calculated at 20 R_E downtail respectively, for the model (pink and grey dot-dashed lines) and the observed average magnetopause (red solid line). c. to j. IMF B_T; IMF B_Z; the dayside reconnection rate, ϕ_D; solar wind velocity; solar wind density; solar wind dynamic pressure; solar wind temperature; and the SYM-H index. 12-month sliding medians are indicated by the black solid line with upper and lower quartile ranges shaded in grey. One-month medians are indicated by the grey solid line and daily medians are shown by the blue solid line.

eters need to be considered. The strength and direction of the IMF can affect magnetopause location, particularly at the dayside magnetopause. During this interval, the total IMF strength, B_T, is at its strongest over the 20 years (panel c.). The dayside reconnection rate is also at its highest (panel e.). IMF B_Z is varied (panel d.), although from approximately October 2002 to after the end of the interval being examined, on average IMF B_Z is directed southwards (see Figure 6.1 where it is clearer). Additionally, in the first few months of this interval, there are numerous days where the daily median IMF B_Z is strongly southwards and ϕ_D is high. This increase in solar wind driving will cause more reconnection to take place at the dayside magnetopause and an erosion of magnetic flux will be observed.

In 2003, the largest erosion of the dayside magnetopause nose is observed. This coincides with the biggest peak in solar wind velocity and dynamic pressure. The model developed in this thesis may not be as accurate in describing the magnetopause under these conditions because throughout the majority of the 20-year period, the solar wind velocity and dynamic pressure are on average lower than the 2003 observations. The solar wind dynamic pressure is also high in 1996, but this is caused by an enhancement in plasma density rather than solar wind velocity. The model is further limited because it is not possible to identify magnetopause crossings inside of Geotail's perigee, so this could mean that the magnetopause nose was at times more eroded than observed here.

A further physical process that might cause the differences observed between the predicted and observed magnetopause location is the strength of the ring current (panel i.). During geomagnetically disturbed intervals, the dayside magnetopause is eroded by increased coupling between the solar wind and magnetosphere, and is compressed by the impacting CME or CIR [Gosling *et al.*, 1991; Taylor *et al.*, 1994; Tsurutani *et al.*, 1995; Hutchinson *et al.*, 2011]. Therefore, we would expect to observe magnetopause crossings closer to the planet at the dayside during geomagnetically disturbed periods. During this time interval, which spans September 2001 to December 2004 including the solar maximum and declining phase of solar cycle 23 (see section 3.2.1), many of the largest storms of solar cycle 23 are observed [e.g. Gonzalez *et al.*, 2007]. The increased number of geomagnetic storms will contribute to the compression of the magnetopause nose observed in the Geotail magnetopause crossings.

6.3.4 2012 to 2016

In the period shown in Figure 6.6, which spans 2012 to 2016, there are three intervals where there are significant differences between the predicted magnetopause location and observed magnetopause location (panels a. and b.). The first interval that will be examined, highlighted in pink (i), covers a period where the observed dayside magnetopause was approximately 0.5 to 1 R_E more expanded than predicted. This inflation occurs between January 2014 and June 2014. The second two intervals which will be investigated further, (ii) and (iii), cover periods where the magnetotail was more compressed than predicted (ii), and where it was more expanded (iii). These two intervals span January 2012 to November 2013 (ii) and June 2014 to the end of December 2015 (iii); the end of the dataset.

During the first interval (i), the dayside magnetopause undergoes the largest expansion observed during the 20-year period being studied. During this interval, there is a small increase in IMF B_T, however it does not persist throughout the entire observed expansion. The IMF B_Z magnitude and dayside reconnection rate remained low, and no irregular behaviour in the other solar wind parameters was observed. Therefore, it is likely that this short-lived expansion observed in r_0 could be caused by a handful of magnetopause crossings observed under extreme conditions influencing the fitting procedure. Similar to the examination carried out in section 6.3.2, I have looked through the 12-month sliding windows of magnetopause crossings to identify magnetopause crossings that were observed when the magnetopause was highly inflated. Whilst the majority of magnetopause crossings observed in these intervals are true crossings, some are not. In this interval, there are a few cases where the identified magnetopause crossing is actually a bow shock crossing. Additionally, there is an event which is registered as a magnetopause crossing but unfortunately has occurred due to no data being recorded by Geotail for a short interval. Although it is likely that these false positives are contributing to the observed expansion, there are also cases where the magnetopause was highly inflated when Geotail encountered it. An example of a magnetopause crossing that was identified by the algorithm when the magnetopause was highly inflated is shown in Figure 6.7.

The panels and geometry shown in Figure 6.7 are identical to Figure 6.4. Figure 6.7 shows a 16-hour period from the 15$^{\text{th}}$ January 2014. At the start of the interval, Geotail is located inside the magnetosphere at the dayside. At approximately 14:00 UT, Geotail

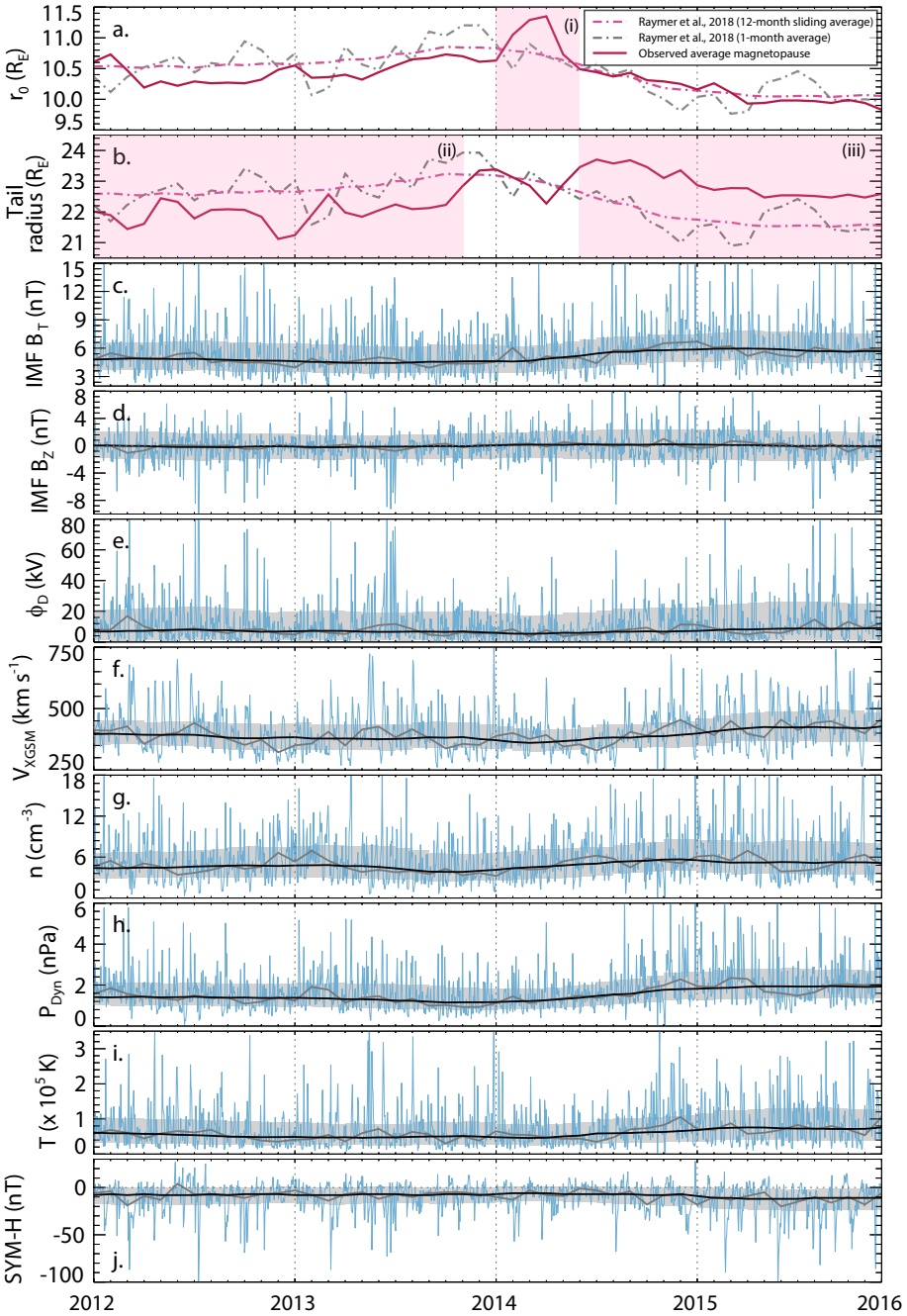

Figure 6.6: a. and b. Subsolar standoff distance, r_0, and the radius of the magnetotail calculated at 20 R_E downtail respectively, for the model (pink and grey dot-dashed lines) and the observed average magnetopause (red solid line). c. to j. IMF B_T; IMF B_Z; the dayside reconnection rate, ϕ_D; solar wind velocity; solar wind density; solar wind dynamic pressure; solar wind temperature; and the SYM-H index. 12-month sliding medians are indicated by the black solid line with upper and lower quartile ranges shaded in grey. One-month medians are indicated by the grey solid line and daily medians are shown by the blue solid line.

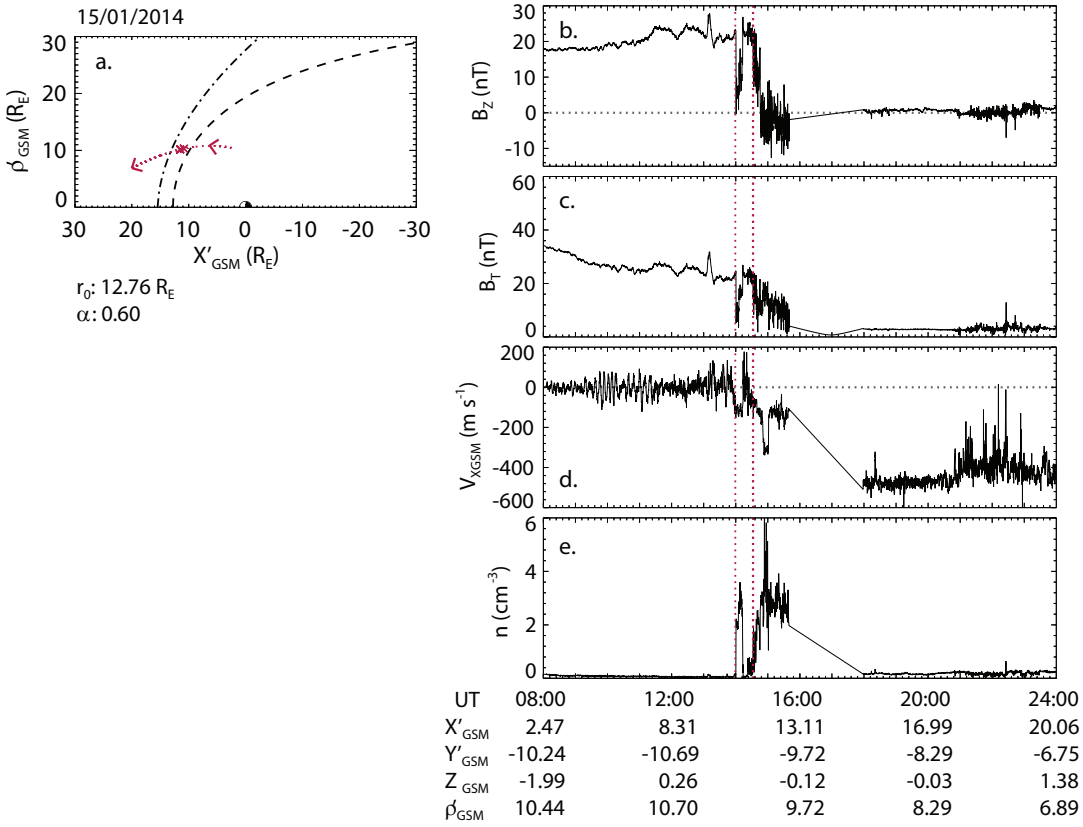

Figure 6.7: a. Orbital path of Geotail (red dotted arrowed line) on 15$^{\text{th}}$ January 2014 in the $X'_{GSM} - \rho'_{GSM}$ plane (where ρ' is defined as $\sqrt{Y'^2_{GSM} + Z^2_{GSM}}$). The locations of the magnetopause crossings detected by the algorithm are indicated by the red crosses. The dot dash line indicates a model bow shock [Peredo *et al.,* 1995] and the dashed line represents the predicted magnetopause location using the model developed in this study. r_0 and α values are indicated below the plot. Average solar wind conditions from this time interval have been used as an input for both models. b. to e. display the magnetic field strength in the Z direction; the total magnetic field strength; the velocity of the plasma in the X_{GSM} direction; and the density of the plasma during the 24-hour period.

encounters the magnetopause for the first time and a magnetopause crossing is detected after satisfying the magnetopause nose criteria (section 4.1.1.1). There is a sharp change from strongly northward B_Z to weaker northward B_Z coinciding with a reduction in B_T. The magnetic field within the magnetosheath is much more varied than the magnetospheric magnetic field. Shortly after this first magnetopause crossing, Geotail is located within the magnetosphere once more, before crossing the magnetopause and leaving the magneto-

sphere permanently for the rest of this period. These multiple traversals suggest that the magnetopause was in motion. At the times of these magnetopause crossings, the solar wind dynamic pressure was very low ($\sim$0.4 nPa), the solar wind velocity in the X_{GSM} direction was $\sim$-500 km s^{-1}, and the IMF B_Z was low and varying between being directed north- and southward. These weak solar wind conditions may explain why the magnetopause was so inflated in this particular case. In panel a., the dashed line indicates where the model predicts the magnetopause to be for the solar wind conditions at the time of the magnetopause crossings. Although the model predicts a very expanded magnetopause, the observations show that the magnetopause was even more expanded than predicted. About an hour after the second magnetopause crossing there is a 2.5 hour period where there are no measurements. After this, the observations suggest that Geotail was located in the solar wind. This is one of the examples when the magnetopause was observed outside the location predicted by the model. We suggest that the reason the model has not accounted for these low solar wind conditions in this example, because fewer observations take place when the solar wind is that weak and so these conditions are not fairly accounted for in the magnetopause crossing database.

The second period highlighted in pink (ii) in Figure 6.6 that will be discussed spans just under two years, January 2012 to November 2013. During this interval, the magnetotail is compressed by approximately 1 R_E, increasing to $\sim$1.5 R_E in December 2012. The compression is not continuous throughout the period, it varies. Once again, there is no obvious explanation from the solar wind conditions as to what is causing this compression. Upon studying the magnetopause crossings in more detail, there are some crossings that have been observed under a compressed magnetopause, but there are also very few crossings observed when the magnetopause is very inflated. We believe a combination of these two factors has led us to conclude that this is the cause of the slight compression observed in the observations.

The final part of Figure 6.6 to be examined is the interval that occurred between June 2014 and the end of December 2015 (iii). In this period, the observations of the magnetotail indicate a more expanded tail than predicted by the model. Conversely, the model and the observed magnetopause location agree remarkably well for the dayside magnetopause. This interval is marked by a small increase in IMF B_T and the dayside reconnection rate. This

could contribute to an increase in the amount of open magnetic flux content in the magnetosphere which can cause an inflation of the magnetotail. Furthermore, as discussed in section 6.3.2, the increased number of geomagnetic storms observed in this interval may contribute to the observed expansion. The changes observed in the tail show the time history of reconnection and the rate of returned closed field lines, which is difficult to incorporate into the model.

6.4 Summary

In this chapter, comparisons between the predicted magnetopause and the observed magnetopause are made. The model used to predict the magnetopause location was developed in section 4.2 of this thesis and can predict the magnetopause for a given solar wind dynamic pressure. The observed magnetopause is determined from fitting the Shue *et al.* [1997, 1998] function to 12-month sliding windows of magnetopause crossings to find values for r_0 and α across the 20-year period. Overall, the model magnetopause characterises the shape and location of the the observed magnetopause with reasonable accuracy. As the model is only parameterised by solar wind dynamic pressure, differences between the model and observations are expected. It is the aim of this chapter to explain these differences by considering both solar wind and magnetospheric conditions.

Across the entire 20-year period, there are parts of the solar cycle where the model describes the observations well. Both the dayside subsolar standoff distance and the location of the magnetotail are characterised by the model remarkably well during the deep and extended solar minimum that occurs between solar cycles 23 and 24. The model predicts the observations with high accuracy in the magnetotail between 1996 and mid-1999, and between 2002 and 2012. The largest discrepancies between the model and the observed magnetopause occur at solar maximum and in the declining phases of the solar cycles, during which solar activity is much higher than it is at other phases.

The first difference between the predicted and observed magnetopause that is examined spans July 1999 to June 2000 where a compression of $\sim$1 to 1.5 R_E is observed in the magnetotail. It is found that this compression is caused by some extreme magnetopause crossings that are observed during the interval, the most extreme of which occurred on 4$^{\text{th}}$ December

1999 where multiple magnetopause crossings are observed at the dawn magnetopause. It is not known exactly what causes the magnetotail to be compressed by this much, however large variations in the velocity and density are indicative of Kelvin-Helmholtz Instabilities. In addition, Geotail encountered the magnetopause at dawn and the IMF B_Z component was directed northwards, both of with are indicative of KHI. These magnetopause crossings, in combination with some other extreme magnetopause crossings (which were not shown in this chapter), influence the fitting procedure and cause the observed compression.

Between December 2000 and November 2001, observations of the magnetotail show that it is more flared than predicted by the model. We attribute this to the increased number of geomagnetic storms which occur in 2001. During geomagnetic storms, the ring current becomes enhanced and acts to inflate the nightside magnetopause. After a geomagnetic storm, the ring current can take days to recover depending on the severity of the storm. Therefore, it could mean that Geotail observes a more inflated magnetopause during these periods.

During the period spanning September 2001 to December 2004, the magnetopause nose is eroded by approximately 0.5 R_E more than predicted. Throughout this interval, both the total magnetic field strength and dayside magnetic reconnection rate are at their highest. There are intervals of strongly southward directed IMF B_Z, coupled with high dayside reconnection rates, so it is likely that the magnetopause nose is being eroded by magnetic reconnection, which the model does not account for. During this period, some of the largest geomagnetic storms of solar cycle 23 are observed. This too is likely to be causing increased erosion and a compression of the dayside magnetopause.

Over the period 2012 to 2016, there are a number of cases where the predicted magnetopause did not match the observations. In 2014, there was a six-month period during which the observed dayside magnetopause was briefly more inflated than the model. We find that the cause of this brief inflation is a number of magnetopause crossings influencing the fitting procedure. Whilst some of these magnetopause crossings turned out to be false positives, most were true crossings, and we investigate one example in detail. In this particular case, the magnetopause was highly inflated, and the model cannot predict the observations for the given conditions.

The final two intervals that we investigate in greater detail focus on the discrepancies

in the magnetotail radius and span January 2012 to November 2013, and June 2014 to December 2015. It is concluded that the first of these discrepancies is caused by a combination of magnetopause crossings being observed both under a more compressed configuration and crossings either not being identified when the magnetopause is highly inflated, or the magnetopause was just not inflated. During the final interval, the tail magnetopause was more inflated than predicted by the model. B_T and ϕ_D were slightly increased, and there were an increased number of geomagnetic storms occurring. We suggest that a combination of these conditions act to inflate the magnetotail.

In this chapter we have investigated the long-term differences between the model and observed magnetopause. We have shown that long-term changes in the average location of the magnetopause are related to solar cycle variations in several different parameters of the solar wind and in the magnetosphere. Although generally the model characterises the behaviour of the observations very well, there are times when it does not. This is in part a result of the model only accounting for solar wind dynamic pressure, but also in some instances, a result of magnetopause crossings that were identified under extreme solar wind conditions, influencing the fitting procedure and therefore influence the observed average magnetopause location.

Chapter 7

Solar wind and magnetospheric influences on the shape and location of the magnetopause

7.1 Introduction

The magnetopause separates the Earth's magnetic field from the interplanetary magnetic field and prevents solar wind plasma from entering the Earth's magnetosphere. Its location and shape are primarily governed by the pressure balance between the two regions. There are well developed theories to describe magnetopause shape and location dependence on solar wind dynamic pressure. As shown in Chapters 4, 5 and 6, solar wind dynamic pressure is the most dominant factor in ordering the shape and location of the magnetopause. However, other internal and external parameters play a role and the extent to which they influence the magnetopause will be investigated in this chapter.

The direction of the north-south component of the interplanetary magnetic field (IMF) plays a significant role in influencing magnetopause shape [e.g. Aubry *et al.*, 1970, 1971; Maezawa, 1974; Fairfield, 1991, 1995; Sibeck *et al.*, 1991; Roelof & Sibeck, 1993; Sibeck *et al.*, 2000]. When the IMF B_Z is directed southwards, magnetic reconnection with the Earth's northward directed magnetic field erodes the magnetopause nose. On the nightside however, open magnetic flux is added to the magnetosphere causing it to inflate [Milan *et al.*, 2004, e.g.]. Coupling functions are used to parameterise magnetospheric activity in terms of

upstream solar wind observations (see section 3.1.4 for more detail on coupling functions). Being able to estimate how much open magnetic flux is being added to the magnetosphere from upstream solar wind conditions, (the dayside reconnection rate), will tell us more about the changing shape of the magnetopause.

After magnetic flux is opened at the dayside magnetopause, it is transported to the nightside magnetosphere via the Dungey cycle before it is closed by magnetic reconnection in the magnetotail (see section 3.1.1). The quantity of open magnetic flux in the magnetosphere will affect the size and shape of the magnetopause. Although the dayside reconnection rate provides an estimate for how much open magnetic flux has been added to the magnetosphere, it does not provide any indication about how much magnetic flux is already in the magnetosphere or how much is being closed in the magnetotail. Measuring the size of the polar caps, the area of open magnetic flux at the poles, is a commonly used method to determine the amount of open magnetic flux in the magnetosphere [e.g. Cowley & Lockwood, 1992]. As it is difficult to measure directly, proxies are often used such as the location of the open/closed field line boundary from auroral imagery [Milan *et al.*, 2003; Hubert *et al.*, 2006; Østgaard *et al.*, 2007; Boakes *et al.*, 2009; Milan, 2009; Milan *et al.*, 2009b; Longden *et al.*, 2010], or the Heppner-Maynard Boundary (HMB) [Imber *et al.*, 2013a,b] (see section 3.1.3 for more detail).

It has been theorised that the strength of the ring current will order magnetopause size and shape in the equatorial plane. The ring current flows toroidally around the Earth extending to distances of around 2-9 $\mathrm{R_E}$ [e.g Daglis *et al.*, 1999]. It is thought that when the ring current is enhanced due to increased geomagnetic activity caused by storms (see section 3.1.5), the ring current will cause an inflation of the nightside magnetopause. The magnetic field that accompanies the ring current decreases the Earth's magnetic field inside the ring current, hence a reduction in geomagnetic indices is measured. However, outside the ring current the magnetic field increases and this may cause the nightside magnetopause to inflate. At the dayside magnetopause however, it is expected that the magnetopause will be eroded by the increased solar wind-magnetosphere coupling.

In this chapter the influence of both internal and external parameters on magnetopause location will be examined. This will be achieved by comparing the location of the magnetopause predicted by the empirical model presented in Chapter 4 with the internal and

external parameters discussed above. How these parameters affect the magnetopause under different solar wind dynamic pressure strengths will also be investigated. Instruments and methods will be discussed in the next section, followed by the results and discussion, and lastly a summary of the findings.

7.2 Instruments and methods

Akin to the previous two chapters, 20 years of magnetic field and plasma observations from the Geotail spacecraft have been used to identify both dayside and nightside magnetopause crossings. The magnetopause crossings were identified using an automated routine (described in section 4.1.1) which detected magnetopause crossings from changes in magnetic field and plasma properties across the magnetopause boundary. To account for the motion of the Earth around the Sun, the magnetopause crossings are aberrated (see section 4.1.2.1). Furthermore, magnetopause crossings beyond a point which is normal to the average magnetopause at 25 $\mathrm{R_E}$ are removed (section 4.2.1), resulting in a dataset of 8050 magnetopause crossings. The identified magnetopause crossings are then used with corresponding solar wind data to develop a simple model to predict the location of the magnetopause for a given solar wind dynamic pressure. Solar wind conditions are determined from the OMNI dataset from NASA/GSFC's OMNIWeb. The simple model is given by

$$r = r_0 \left(\frac{2}{1 + \cos\theta} \right)^{\alpha} \tag{7.1}$$

$$r_0 = 11.082 P_{Dyn}^{-1/6.75} \mathrm{R_E} \tag{7.2}$$

$$\alpha = 0.605 - 0.010 P_{Dyn} \tag{7.3}$$

where r is the radial distance and θ is the solar zenith angle, r_0 is the magnetopause standoff distance, and α describes the level of flaring in the magnetotail. r_0 and α have been calculated by firstly weighting the magnetopause crossings by how long Geotail spends in a 1×1 $\mathrm{R_E}$ spatial bin, then by separating the magnetopause crossings into solar wind dynamic pressure ranges and fitting the function to each pressure range (see section 4.2.2 for detail).

The model developed in this study is dependent only on solar wind dynamic pressure. Although this parameter has the largest influence on magnetopause location, other internal and external factors affect the shape and position of the magnetopause. To investigate how the dayside reconnection rate, the open flux content, and the ring current influence magnetopause location, we compare the location of each individual magnetopause crossing with the location of the magnetopause as predicted by the model (defined by equations 7.1, 7.2 and 7.3). First, the solar wind dynamic pressure observed at the time of the magnetopause crossing is put into the model to find the predicted magnetopause location. The next step is to find the point on the model magnetopause curve which is perpendicular to the magnetopause crossing. This is done by calculating the difference between the magnetopause crossing and the model magnetopause. The sum of the squared differences is calculated for multiple points along the model magnetopause curve. The point on the model magnetopause that is perpendicular to the magnetopause crossing is where the sum of the squared differences is minimum. The perpendicular offset is then calculated as follows

$$\text{perpendicular offset} = (X_{crossing} - X_{model}) + (\rho_{crossing} - \rho_{model}) \tag{7.4}$$

Figure 7.1 shows the perpendicular offset for two example magnetopause crossings. The perpendicular offset is positive when the magnetopause is more inflated than predicted by the model, and the offset is negative when the magnetopause is more compressed than predicted. We further look at how the effects of these parameters on magnetopause location differ between the dayside magnetosphere ($X'_{GSM} > 0\ R_E$) indicated by the blue region and nightside magnetosphere ($X'_{GSM} < 0\ R_E$) indicated by the grey region.

To examine how the dayside magnetic reconnection influences magnetopause location, IMF B_Z and the dayside reconnection rate, ϕ_D, are compared with the perpendicular offsets. IMF B_Z is calculated from the OMNI dataset and is integrated over 30 minutes prior to the time of each magnetopause crossing so that it is possible to see how much the magnetopause has eroded rather than the instantaneous observation. To calculate the dayside reconnection rate, the solar wind-magnetosphere coupling function derived by Milan *et al.* [2012] (discussed in section 3.1.4) is used. This function requires solar wind data as an input. Like IMF B_Z, the dayside reconnection rate is integrated over the preceding 30 minutes for each magnetopause crossing.

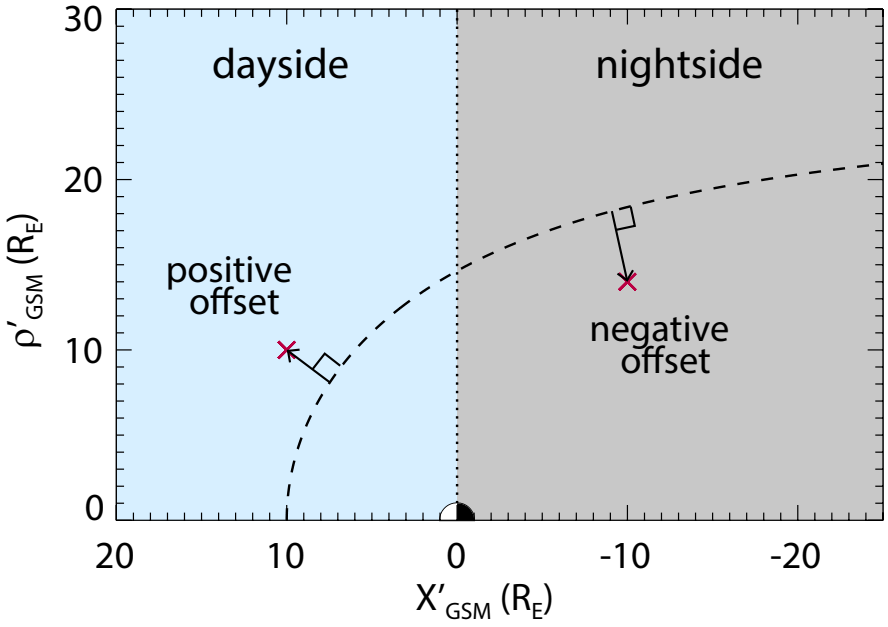

Figure 7.1: An example model magnetopause is shown by the dashed line in the $X'_{GSM} - \rho'_{GSM}$ plane. Red crosses indicate two example magnetopause crossings and black arrows show the perpendicular offset. When the offset is positive, the magnetopause is more inflated than the model magnetopause, and when the offset is negative, the magnetopause is more compressed than the model magnetopause. The dotted line drawn at $X'_{GSM} = 0\ R_E$ shows where dayside (blue region) and nightside (grey region) magnetopause crossings are separated.

A further parameter expected to order the size and shape of the magnetopause is the quantity of open flux in the magnetosphere. Different methods of measuring the quantity of open magnetic flux inside the magnetosphere were discussed in section 3.1.3. In this chapter, two different proxies to estimate open magnetic flux content are trialled. The first tool used is global auroral imagery. Data from the Imager for Magnetopause-to-Aurora Global Exploration (IMAGE) mission [Burch, 2000] (see section 2.1.3 for detail on the spacecraft) is used to deduce the radius of the auroral oval and open flux content. How these parameters are calculated is briefly described in section 2.1.4 and described in greater detail in Shukhtina & Milan [2014]. To examine how well the model describes the magnetopause, the oval radius and open flux content at the time of each magnetopause crossing needs to be determined. As the IMAGE spacecraft was only operational between June 2000 and October 2005 [Burch, 2000; Mende *et al.*, 2000a], only a subset of magnetopause crossings can be utilised. The magne-

topause crossing dataset is further limited because there are often no IMAGE measurements when a magnetopause crossing takes place. This is caused by either orbital limitations, or when the oval radius cannot be determined from the observations due to either the presence of dayglow; when the auroral boundaries are not sharp; or when the aurora is faint due to sensitivity limitations of the camera [Shukhtina & Milan, 2014]. The second proxy used to estimate the amount of open magnetic flux in the magnetosphere is the Heppner-Maynard Boundary (HMB). The HMB is calculated from SuperDARN convection maps (see section 2.2.2.2 for the discussion of how the HMB is calculated) and represents the latitudinal extent of the ionospheric convection pattern. As discussed by Imber *et al.* [2013a,b], a threshold of at least 150 vectors per map must be met for the HMB latitude to be used. The latitude of the HMB at 24 MLT is then compared with the perpendicular offsets.

Finally, the last parameter that is investigated in this chapter is the effect that the ring current strength has on magnetopause location. To do this, the SYM-H geomagnetic index is used (see section 3.1.5).

7.3 Results and discussion

7.3.1 IMF B_Z and dayside reconnection rate

Figure 7.2 shows the comparison of the perpendicular offset between the magnetopause crossings identified by the automated routine and the model magnetopause location for IMF B_Z. The magnetopause crossings have been separated into the dayside (panel a.) and the nightside (panel b.). The colours represent how many magnetopause crossings are in a $0.5\ R_E \times 1$ nT bin. Grey crosses and error bars indicate the median and interquartile ranges for each row.

In panel a. of Figure 7.2, the results show that for strongly southwards directed IMF, when B_Z is less than ~ -3 nT, the dayside magnetopause is located closer to the Earth than predicted by the model which only takes solar wind dynamic pressure into account. This is indicative of magnetic reconnection occurring at the dayside subsolar magnetopause causing the erosion of magnetic flux. When the IMF B_Z is close to 0 nT or directed northwards with field strengths of up to ~ 5 nT, a slight expansion of the dayside magnetopause is observed. There are only a small number of magnetopause crossings with field strengths

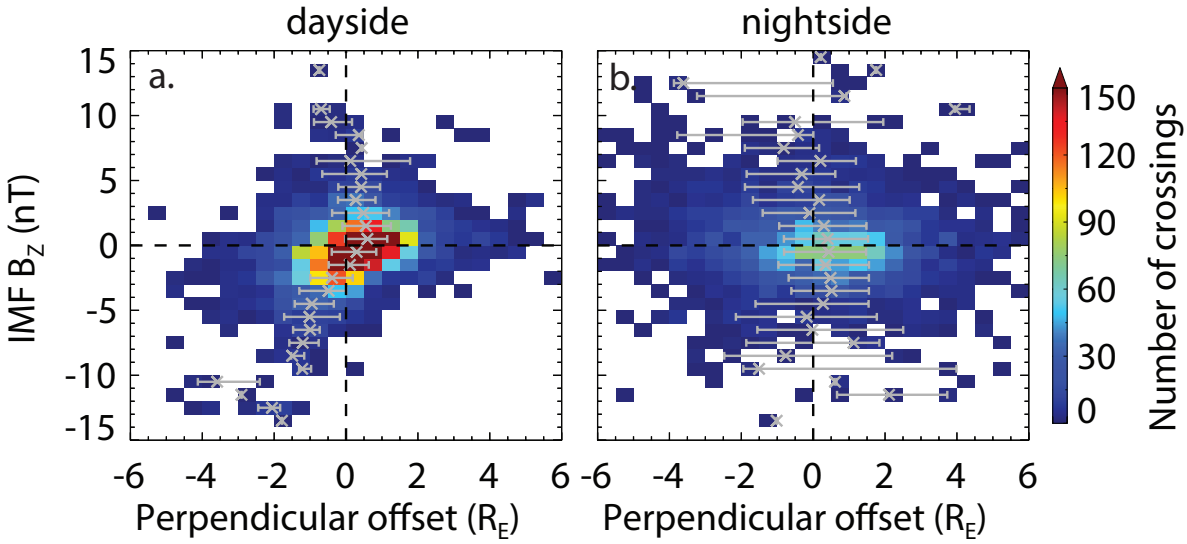

Figure 7.2: A comparison of the perpendicular offset between the identified magnetopause location and the model magnetopause location for IMF B_Z. Panel a. shows the results for dayside magnetopause crossings ($X'_{GSM} > 0\ R_E$) and panel b. shows the results for nightside magnetopause crossings ($X'_{GSM} < 0\ R_E$). The colours indicate the number of magnetopause crossings in a $0.5\ R_E \times 1$ nT bin. The grey crosses and error bars show the median perpendicular offset and interquartile ranges for each row respectively.

above 5 nT and so it is not possible to draw any conclusions for strongly northward IMF.

Nightside magnetopause crossings are shown in panel b. of Figure 7.2. The perpendicular offsets are more varied than those observed for the dayside magnetopause. This is expected as the nightside magnetopause is able to move around more compared to the dayside magnetopause and is less ordered by solar wind dynamic pressure. For southward IMF, between 0 nT and -5 nT, the nightside magnetopause appears to be slightly inflated, however it is difficult to draw any conclusions given the spread of the magnetopause crossings. An inflated magnetosphere is expected for southward directed IMF as magnetic flux that has been reconnected at the dayside magnetopause is transported to the nightside.

To investigate the effect of IMF B_Z on magnetopause location further, Figure 7.3 shows the comparison between perpendicular offsets and IMF B_Z for increasing solar wind dynamic pressure. The panels are calculated in the same way as the previous figure but are also binned by solar wind dynamic pressure. It is clear that the strength and direction of the IMF B_Z has a larger effect on magnetopause location at the dayside for weaker solar wind dynamic

pressures (panels a., c., and e.). When B_Z is directed southwards, the magnetopause nose is located closer to the Earth and as B_Z turns northwards, the dayside magnetopause expands. In higher pressure ranges (panels g., i., and k.) this effect is less pronounced due to the magnetopause already being compressed. Similar to Figure 7.2 nightside magnetopause crossings are highly varied and it is difficult to draw any conclusions.

Figure 7.4 shows the comparison of the perpendicular offsets with the dayside reconnection rate, ϕ_D. For the dayside magnetopause crossings shown in panel a., as the dayside reconnection rate increases, the magnetopause moves closer to the planet, which is indicative of erosion of magnetic flux caused by reconnection. Results show that when very little reconnection is taking place, when ϕ_D is low, the dayside magnetopause is slightly expanded. Although the spread of perpendicular offsets is greatest in this region. Similar to the results for IMF B_Z, there is much more variability in nightside magnetopause locations (panel b.). It is expected that the nightside magnetopause will become more inflated as the dayside reconnection rate increases and more open magnetic flux is added to the magnetosphere. For ϕ_D measurements less than ~ 40 kV, the magnetopause is located at distances further away from the planet than predicted by solar wind dynamic pressure alone. For higher dayside reconnection rates, there are far fewer nightside magnetopause crossings and so it is not possible to determine whether the nightside magnetopause will continue to expand or whether the expansion will saturate.

Similar to Figure 7.3, Figure 7.5 shows the comparison of perpendicular offsets with the dayside reconnection rate binned by solar wind dynamic pressure. Results show that the dayside reconnection rate has a larger influence on dayside magnetopause location when the solar wind dynamic pressure is weaker (panels a., c., and e.). More magnetic flux is eroded at the dayside magnetopause when dynamic pressure is weaker. As the dynamic pressure increases, the perpendicular offsets are smaller and the model describes the dayside magnetopause well (panels g., i., and k.). At the nightside magnetopause, although there is high variability in the perpendicular offsets, generally as ϕ_D increases, the offsets are positive, indicating a small expansion of the nightside magnetosphere.

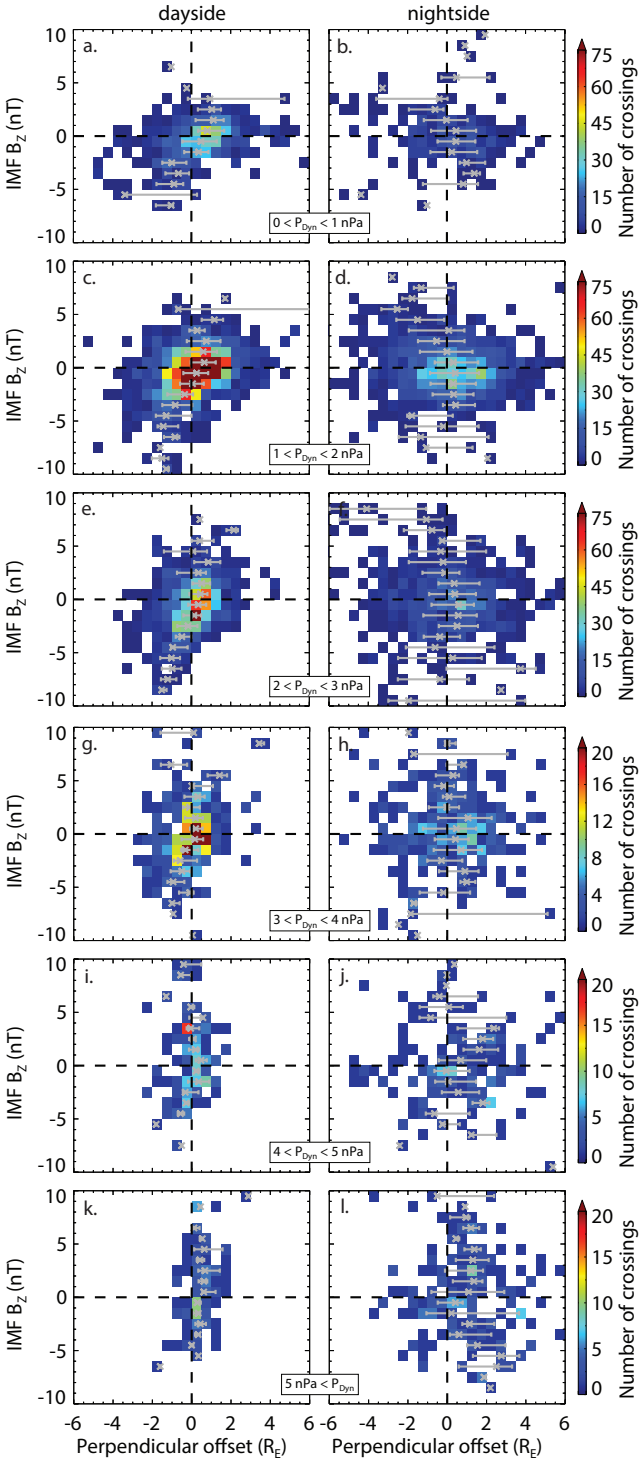

Figure 7.3: A comparison of the perpendicular offset between the identified magnetopause crossing location and the model magnetopause location for IMF B_Z binned by increasing solar wind dynamic pressure. The colours indicate the number of magnetopause crossings in a 0.5 R_E $\times 1$ nT bin. The grey crosses and error bars show the median perpendicular offset and interquartile ranges for each row respectively.

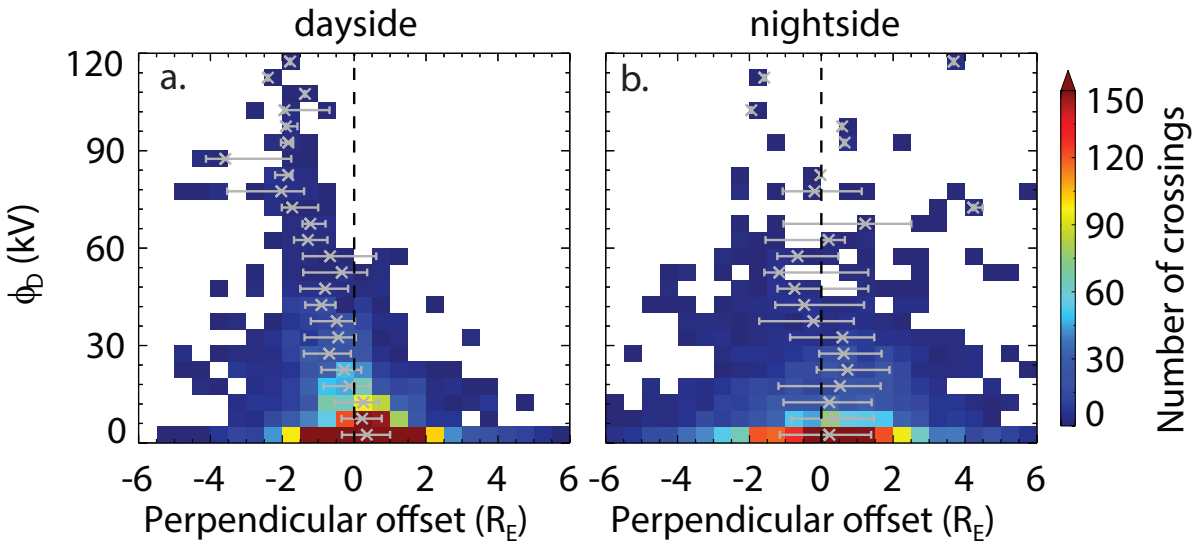

Figure 7.4: A comparison of the perpendicular offset between the identified magnetopause crossing location and the model magnetopause location for the dayside reconnection rate, ϕ_D. Panel a. shows the results for dayside magnetopause crossings ($X'_{GSM} > 0\ R_E$) and panel b. shows the results for nightside magnetopause crossings ($X'_{GSM} < 0\ R_E$). The colours indicate the number of magnetopause crossings in a $0.5\ R_E$ $\times 5$ kV bin. The grey crosses and error bars show the median perpendicular offset and interquartile ranges for each row respectively.

7.3.2 Open magnetic flux content

The following section is divided into two parts: firstly, results from comparing the perpendicular offsets with IMAGE observations of the auroral oval radius and calculated open flux content are presented; and secondly, results from comparing the perpendicular offsets with HMB measurements are shown.

7.3.2.1 Oval radius and open flux content calculated from IMAGE observations

To compare the perpendicular offset between the magnetopause crossing location and the model for both the auroral oval radius and the open flux content, IMAGE data at the time of the magnetopause crossing must be found. As discussed in the methods section, often there is no data at the time of the magnetopause crossing. Different time windows around the time of the magnetopause crossing were trialled. Figure 7.6 shows the results for a time window of ± 20 minutes. Unfortunately, even with a large time window, there are very

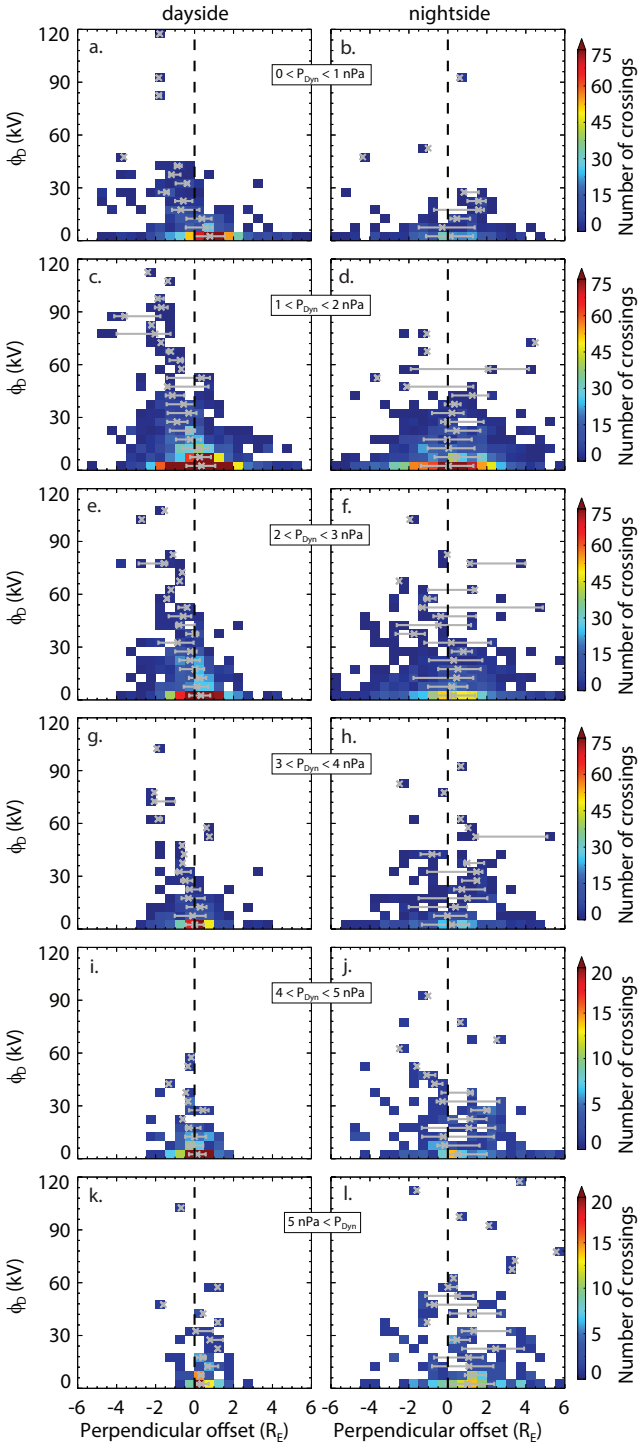

Figure 7.5: A comparison of the perpendicular offset between the identified magnetopause crossing location and the model magnetopause location for the dayside reconnection rate, ϕ_D, binned by increasing solar wind dynamic pressure. The colours indicate the number of magnetopause crossings in a 0.5 $R_E\times$ 5 kV bin. The grey crosses and error bars show the median perpendicular offset and interquartile ranges for each row respectively.

few crossings available for the analysis, so we must be cautious when drawing conclusions about the results. The panels in Figure 7.6 are presented in the same way as the previous results in this chapter, with the top two panels (a. and b.) showing results for the auroral oval radius, and the bottom two panels (c. and d.) showing results for the open flux content in the magnetosphere estimated from the size of the polar cap.

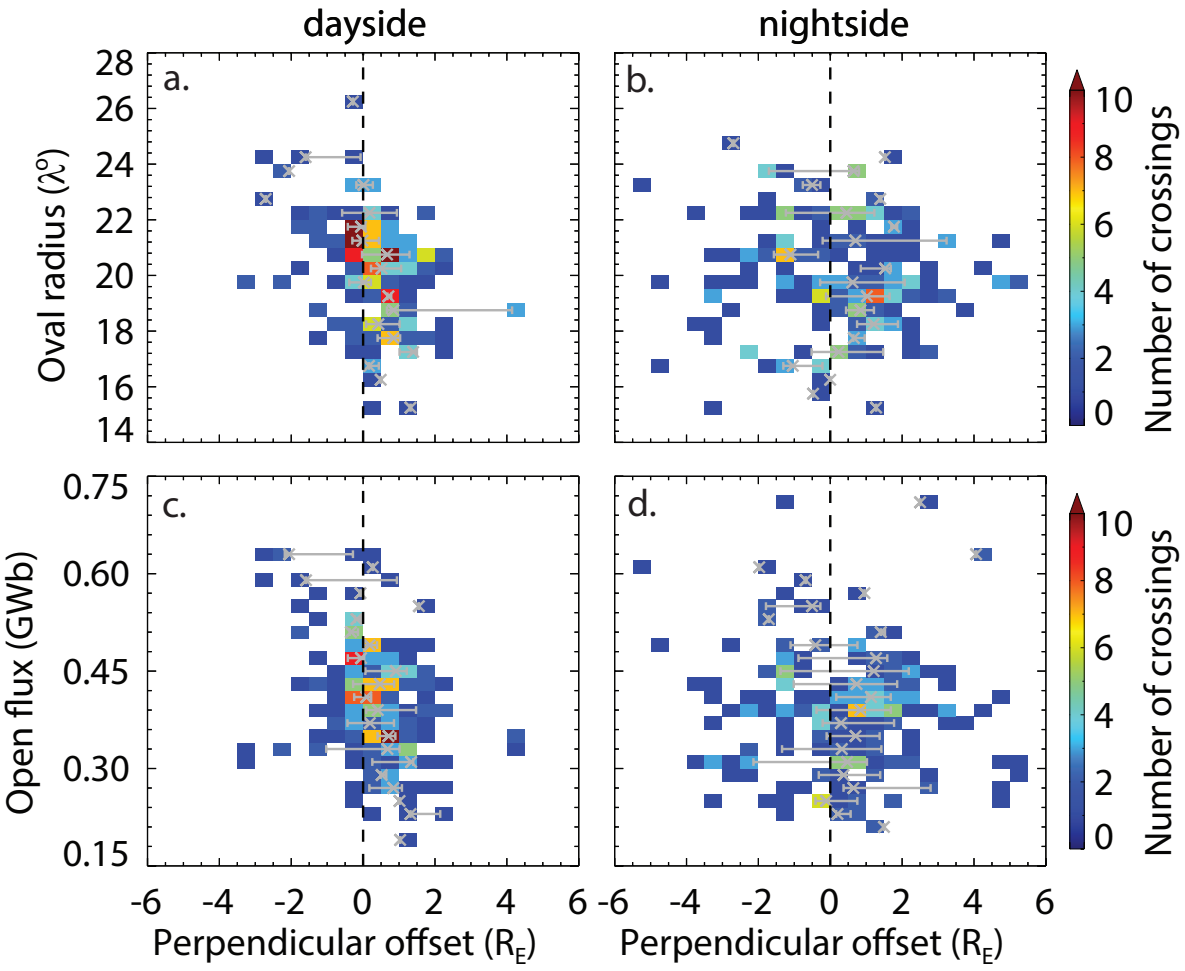

Figure 7.6: A comparison of the perpendicular offset between the identified magnetopause crossing location and the model magnetopause location for the auroral oval radius (panels a. and b.) and open magnetic flux content (panels c. and d.) as measured by IMAGE. The panels on the left show the results for dayside magnetopause crossings ($X'_{GSM} > 0\ R_E$) and the panels on the right show the results for nightside magnetopause crossings ($X'_{GSM} < 0\ R_E$). The colours indicate the number of magnetopause crossings in a 0.5 R_E $\times 1°$ bin for the oval radius and 0.5 R_E $\times 0.002$ GWb bin for the open flux content. The grey crosses and error bars show the median perpendicular offset and interquartile ranges for each row respectively.

Panel a. of Figure 7.6 shows a slight correlation between the perpendicular offset and oval radius for the dayside magnetopause. When the oval radius is smaller, the dayside magnetopause tends to be more expanded than predicted by the model. A small auroral oval suggests that the recent history of dayside reconnection is low and the quantity of open magnetic flux in the magnetosphere is small, and hence the dayside magnetopause nose has not been eroded. Looking at panel c., the comparison between perpendicular offsets and open flux content, similar conclusions can be made. A small expansion of the dayside magnetopause is observed when the open flux content is low. Conversely, as the amount of open flux in the magnetosphere increases, the magnetopause nose is eroded by magnetic reconnection. We would expect the nightside magnetopause to expand with increasing open flux content as more open magnetic field lines are transported to the nightside magnetosphere by the Dungey cycle. Although it looks like there could be a slight expansion with increasing open flux content in panel d., the magnetopause crossings are very sparse.

7.3.2.2 Heppner-Maynard Boundary

As only HMB data between 1996 and 2012 was readily available, the number of magnetopause crossings was reduced to 7644. To find the corresponding HMB latitude for the time of each magnetopause crossing, a time window of ± 2 minutes was used. As discussed by Imber *et al.* [2013a,b], a threshold for the number of SuperDARN vector measurements used to produce the HMB must be set. Imber *et al.* [2013a] implement a minimum threshold of 200 vectors, whereas Imber *et al.* [2013b] implement a minimum threshold of 150 vectors. Thresholds of 100, 150 and 200 vectors were trialled in this thesis (not shown) and each produced similar results. As it did not impact the results hugely, a minimum of 150 vectors was chosen in this thesis as Imber *et al.* [2013b] found this was the optimum value for providing large statistics with little impact on the ability of the maps to determine the HMB. With this threshold, the total number of magnetopause crossings is reduced to 2960.

Figure 7.7 shows the comparison between the perpendicular offsets and the HMB latitude. At the dayside magnetopause, panel a., as the HMB expands to lower latitudes, the amount of open magnetic flux in the magnetosphere increases and an erosion of the dayside magnetopause is observed as shown by the negative offsets. This indicates that dayside magnetic reconnection has taken place. As the HMB shrinks to higher latitudes, the amount

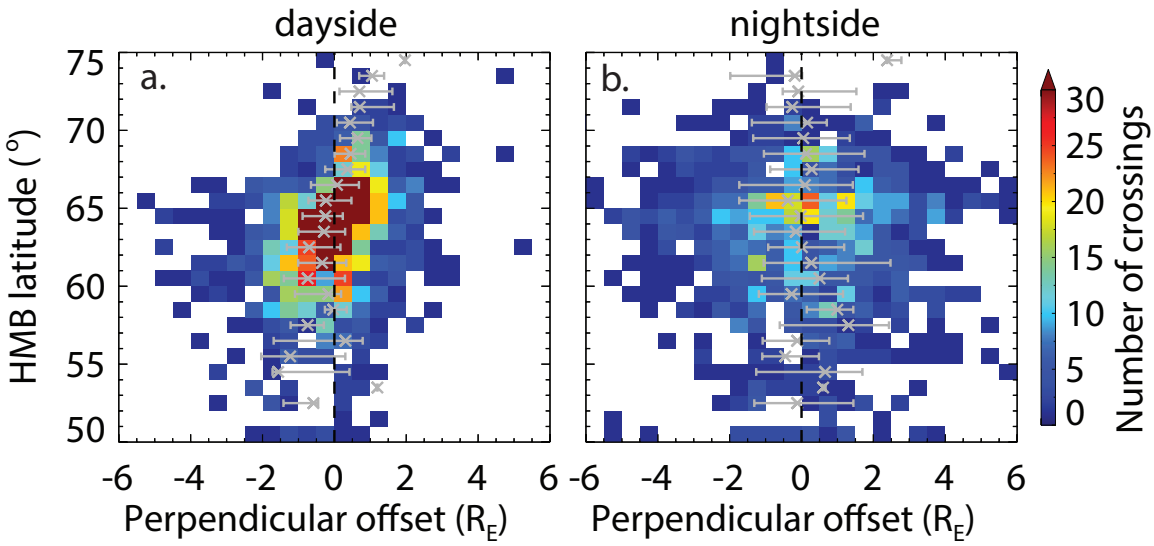

Figure 7.7: A comparison of the perpendicular offset between the identified magnetopause crossing location and the model magnetopause location for the HMB latitude. Panel a. shows the results for dayside magnetopause crossings ($X'_{GSM} > 0$ R_E) and panel b. shows the results for nightside magnetopause crossings ($X'_{GSM} < 0$ R_E). The colours indicate the number of magnetopause crossings in a 0.5 R_E $\times 1°$ bin. The grey crosses and error bars show the median perpendicular offset and interquartile ranges for each row respectively.

of open magnetic flux in the magnetosphere decreases and an expansion of the dayside magnetopause is observed, which is indicative of reduced dayside reconnection or enhanced tail reconnection. At the nightside magnetopause, panel b., no trend is observed. We would expect to see an expansion of the nightside magnetopause as the HMB expands to lower latitudes and more open magnetic flux is added to the magnetosphere. As the HMB shrinks to higher latitudes due to a reduction in the quantity of open magnetic flux in the magnetosphere, we would expect the nightside magnetopause to respond by contracting.

7.3.3 Ring current

Figure 7.8 displays the comparison of the perpendicular offset between the magnetopause crossing locations and where the magnetopause is predicted to be located based on solar wind dynamic pressure under different ring current strengths. It is expected that an enhanced ring current will affect magnetopause location. Panel a. shows the results for the dayside

magnetopause. It indicates that during increasingly geomagnetically disturbed times, a slight compression of the magnetopause is observed. There are a couple of reasons why this is observed. The ring current becomes enhanced after a solar wind event like a CME or CIR impacts the dayside magnetosphere and causes a compression (see section 3.1.5). Geomagnetic storms result from prolonged periods of solar wind-magnetosphere coupling, and so this will further cause an erosion of the magnetic flux at the dayside magnetopause. The majority of magnetopause crossings occur during geomagnetically quiet times.

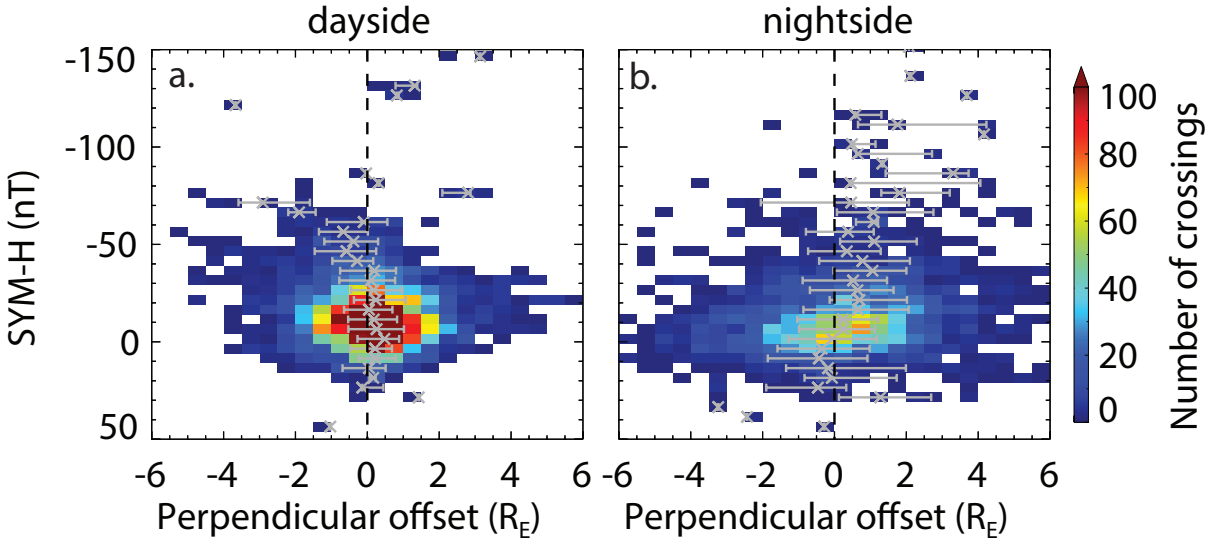

Figure 7.8: A comparison of the perpendicular offset between the identified magnetopause crossing location and the model magnetopause location for the ring current strength. Panel a. shows the results for dayside magnetopause crossings ($X'_{GSM} > 0\ R_E$) and panel b. shows the results for nightside magnetopause crossings ($X'_{GSM} < 0\ R_E$). The colours indicate the number of magnetopause crossings in a $0.5\ R_E \times 5$ nT bin. The grey crosses and error bars show the median perpendicular offset and interquartile ranges for each row respectively.

At the nightside, in Figure 7.8 panel b., during geomagnetically disturbed periods, the magnetopause inflates. This inflation is caused by the magnetic field that accompanies the ring current. During geomagnetically disturbed times, inside of the ring current, the accompanying magnetic field reduces the Earth's magnetic field and a reduction in SYM-H is observed. Outside of the ring current however, the accompanying magnetic field is in the same direction as the Earth's magnetic field and it acts to inflate the magnetopause. Although there are very few magnetopause crossings occurring during moderate (-150 nT < SYM-H

< -300 nT) or strong storms (-300 nT > SYM-H) [Hutchinson *et al.*, 2011], the magnetopause crossings that occur during weak storms (-80 nT < SYM-H < -150 nT) shown in this figure, indicate that the magnetopause is more inflated than predicted by the model.

7.4 Summary

In this chapter internal and external parameters that influence magnetopause location have been examined. This is achieved by using the magnetopause crossings identified from 20 years of Geotail observations presented earlier in this thesis (section 4.1). The magnetopause crossings were used to develop a simple magnetopause model which can predict the location of the magnetopause based on the upstream solar wind dynamic pressure. Comparisons are made between the perpendicular offset between the identified magnetopause crossing and the model magnetopause location for IMF B_Z, the dayside reconnection rate, ϕ_D, open flux content, and the ring current.

As expected, it is found that both the IMF B_Z and dayside reconnection rate order the dayside magnetopause. As the dayside reconnection rate increases, or as the IMF becomes more southward, the dayside magnetopause is eroded via magnetic reconnection. It is further found that both parameters have the largest effect on the dayside magnetopause location when the solar wind dynamic pressure is smallest. For higher ram pressures, the erosion of the magnetopause nose saturates. Results are not as clear for the nightside magnetopause. The magnetopause in this region is not as restricted by the incoming solar wind and the tail magnetopause is able to vary in location more freely. Despite this, a small inflation of the nightside magnetopause is observed under southward IMF conditions, and an inflation is observed with increasing ϕ_D up to ~ 40 kV.

To examine how the quantity of open magnetic flux inside the magnetosphere affects magnetopause shape and location, proxies have been used. The first proxy for open flux content investigated in this thesis was auroral imagery from the IMAGE spacecraft. Due to limitations discussed such as the limited years IMAGE was operational, only a very small subset of magnetopause crossings could be used for this analysis. No clear conclusions can be drawn about the oval radius and open flux content effect on magnetopause location, although results indicate a small expansion of the dayside magnetopause when the auroral

oval radius shrinks and when the open flux content is small. To investigate the effects of open flux content on magnetopause location with a larger database of magnetopause crossings, the HMB was used. A minimum threshold of 150 SuperDARN vector measurements per map was set, resulting in a database of 2960 magnetopause crossings for the analysis. Results for the dayside magnetopause showed that as the HMB expands to lower latitudes, the quantity of open magnetic flux in the magnetosphere increases and the dayside magnetopause nose is eroded. As the HMB shrinks to higher latitudes, the amount of open magnetic flux in the magnetosphere decreases, and the dayside magnetopause expands due to reduced dayside reconnection. No trend is observed at the nightside magnetopause.

Finally, effects of the ring current strength on magnetopause shape and position are explored. During increasingly geomagnetically disturbed times, i.e. when SYM-H becomes more negative, a compression of the dayside magnetopause and an inflation of the magnetotail are observed. The dayside magnetopause is compressed by both the impact of a CME or CIR on the terrestrial magnetosphere, which are linked to geomagnetic storms; and the intense periods of solar-wind-magnetosphere coupling which produce storms. The nightside magnetopause is inflated by the magnetic field that accompanies the ring current.

To conclude, we have demonstrated that the dayside magnetopause is strongly ordered by IMF B_Z and ϕ_D, especially under low solar wind dynamic pressures, but the nightside is not. We have further shown that for a long-term statistical study such as this one, the HMB can be used as a proxy for the amount of open flux inside the magnetosphere, and the erosion of the dayside magnetopause responds to the expansion and contraction of the HMB latitude. Finally, we have demonstrated that the ring current influences both the dayside and nightside magnetopause location.

Chapter 8

Conclusions and future work

This thesis has examined influences on the location of the Earth's magnetopause. An extensive magnetopause crossing database was identified, enabling a simple empirical magnetopause model to be developed. Using the model and magnetopause crossing database, solar cycle, solar wind and magnetospheric effects on the shape and location of the magnetopause were studied. In this final chapter, the results from this thesis are summarised and main conclusions are presented, followed by a discussion of the areas of future work that could be carried out.

8.1 Summary and conclusions

The first key result obtained in this thesis is the development of a new automated magnetopause crossing detection routine that is able to identify when Geotail, the primary spacecraft used in this thesis, traverses the magnetopause nose, magnetopause flanks and magnetotail. Whilst the criteria for the detection of magnetopause nose crossings are based on those described by Ivchenko *et al.* [2000] and Case & Wild [2013], the criteria for the detection of flank and tail crossings are developed in this study. The routine is applied to 20 years of Geotail plasma and magnetic field observations to produce a database of over 8000 magnetopause crossings. This new magnetopause crossing database spans almost two solar cycles (1996-2015) and includes magnetopause crossings from further downtail than many previous studies. We also investigated methods to reduce any bias which may be caused by both the automated routine and by the orbital properties of Geotail. One such technique

was to weight the magnetopause crossings by the dwell time of the spacecraft. Weighting the magnetopause crossings in this way means that any model that is developed using these crossings will be more reliable and robust because they will not be influenced by orbital bias.

Using the weighted magnetopause crossings, a new empirical magnetopause model was created. The new model can predict the location of the magnetopause for a given upstream solar wind dynamic pressure. Developing a new model rather than using a model defined by previous authors was decided upon, because it is able to more accurately describe the magnetopause crossings identified in this study than models developed using different datasets. The magnetopause crossing database identified in this study contains a greater number of magnetopause crossings than previous studies and includes crossings from much further downtail than previous studies, during the two most recent solar cycles. This model enabled us to study what influences magnetopause location.

Solar cycle variations in the shape and location of the magnetopause are studied in Chapter 5. The two most recent solar cycles, solar cycle 23 and 24, contain some unusual features including a deep and extended solar minimum. Solar activity over these two cycles, and in particular during the most recent cycle (24), is the weakest it has been in the space age. Comparisons are drawn between the two solar cycles and we find the magnetopause was much more inflated in solar cycle 24. The magnetopause is most compressed during the declining phases of the solar cycles, when solar wind dynamic pressure and magnetic reconnection is highest. Additionally in this chapter, we compare the predictive capabilities of the model developed in this thesis with previous models defined by Shue *et al.* [1998] and Lin *et al.* [2010]. We find that both the Shue *et al.* [1998] and Lin *et al.* [2010] models consistently predict a more expanded magnetopause than the model we have developed.

In Chapter 6, we investigate the differences between the model location of the magnetopause and the observed magnetopause. We find that even though the model only takes solar wind dynamic pressure into account, it generally predicts the location of the magnetopause with high accuracy. The model is least accurate at predicting the location of the magnetopause during the solar maxima, and during the declining phase of solar cycle 23, in which many of the solar wind parameters were the most extreme.

In Chapter 7, the solar wind and magnetospheric influences on the shape and location of the magnetopause were examined. In particular, we investigated the effects of IMF B_Z,

the dayside reconnection rate, ϕ_D, the open magnetic flux content in the magnetosphere, and the strength of the ring current on magnetopause location. We found that both IMF B_Z and the dayside reconnection rate order the dayside magnetopause. As the dayside reconnection rate increases, or as the IMF becomes more southward, the dayside magnetopause is eroded due to magnetic reconnection. They both have the largest effect on the dayside magnetopause location when the solar wind dynamic pressure is lowest. For higher ram pressures, the erosion of the magnetopause nose saturates. The effect of IMF B_Z and the dayside reconnection rate on magnetopause location is not as clear for the nightside. The magnetopause in this region is not as restricted by the incoming solar wind and the tail magnetopause is able to vary in location more freely.

We further demonstrate in Chapter 7, that the Heppner-Maynard Boundary can be used as a proxy for the amount of open magnetic flux in the magnetosphere. As the HMB expands to lower latitudes, the quantity of open magnetic flux in the magnetosphere increases, and the dayside magnetopause nose is eroded. As the HMB shrinks to higher latitudes, the amount of open magnetic flux in the magnetosphere decreases, and the dayside magnetopause expands due to reduced dayside reconnection. The final result presented in Chapter 7 showed that the strength of the ring current has an influence on magnetopause location. During increasingly geomagnetically disturbed times, i.e. when the SYM-H index becomes more negative, a compression of the dayside magnetopause and an inflation of the magnetotail are observed. The dayside magnetopause is compressed by the impact of a coronal mass ejection of a corotating interaction region on the magnetosphere, which are linked to geomagnetic storms; and is eroded due to the intense periods of solar-wind-magnetosphere coupling which produce storms. The nightside magnetopause is inflated by the magnetic field that accompanies the ring current during geomagnetically disturbed periods.

To conclude, the results contained in this thesis further our current knowledge of what influences the location of the Earth's magnetopause. It demonstrates that in order to improve our understanding of how the magnetopause protects the Earth from varying space weather conditions, it is vital to consider both solar wind and magnetospheric effects on magnetopause location.

8.2 Future work

An obvious area of future work would be to extend the Geotail magnetopause crossing database to the current day, and include magnetopause crossings from additional spacecraft, such as the Cluster or THEMIS (Time History of Events and Macroscale Interactions during Substorms) missions. The Cluster mission consists of four satellites in elliptical polar orbits and has been in operation since 2000. The THEMIS mission consists of five identical probes which are in an equatorial orbit, which have different apogees. The THEMIS probes have both a smaller perigee than Geotail and bigger apogees. Using additional spacecraft like Cluster and THEMIS would mean that we can sample the magnetopause in different regions and build a more accurate picture of the magnetopause.

In Chapter 6, it was found that there are periods when the model developed in this thesis, as well as the models developed by Shue *et al.* [1998] and Lin *et al.* [2010], do not characterise the location of the magnetopause accurately. One area of future work would be to investigate the reasons for the discrepancies further to determine how future models can better predict the magnetopause location. This would be particularly useful for studies which take place during the most recent two solar cycles (23 and 24) and in future solar cycles. As discussed in section 3.2, it has been hypothesised that the Sun is now entering a Grand Solar Minimum, during which solar activity is greatly reduced. Therefore, our current understanding of magnetopause location, which is heavily based on studies that have been carried out under more active solar conditions, may not be able to accurately predict how the magnetopause responds during such low activity.

One of the case studies presented in Chapter 6 showed Kelvin-Helmholtz Instabilities (KHI) identified in the magnetotail. Subsequent analysis on the magnetopause crossing database could be carried out to investigate the statistics of KHI. For example, it would be interesting to examine how often KHI occur, where they occur, is there a dawn-dusk asymmetry present, and how far do KHI penetrate in the magnetotail.

In addition to the solar wind and magnetospheric effects on magnetopause location discussed in Chapter 7, it would be interesting to study the effects of other parameters. For example, it is well-established that the tilt of the Earth's dipole influences magnetopause location. Since the orbit of Geotail is mostly confined to the equatorial plane in this study,

we did not consider any dipole tilt effects. However, if we were to extend our magnetopause crossing database to include magnetopause crossings from other spacecraft with higher latitude orbits, it would be an area worth studying. Further parameters that could be studied are the effects of other current systems on the magnetopause. One such current system that could have an effect on magnetopause location is the Region 1 field-aligned currents, which close on the magnetopause.

Bibliography

Abreu, J. A., Beer, J., Steinhilber, F., Tobias, S. M., & Weiss, N. O. 2008. For how long will the current grand maximum of solar activity persist? *Geophysical Research Letters*, **35**(20), 2–5.

Akasofu, S.-I, Chapman, S, & Venkatesan, D. 1963. The main phase of great magnetic storms. *Journal of Geophysical Research*, **68**(11).

Alfvén, H. 1943. On the existence of electromagnetic-hydrodynamic waves. *Arkiv for Astronomi*, **29**, 1–7.

Aubry, M. P., Russell, C. T., & Kivelson, M. G. 1970. Inward motion of the magnetopause before a substorm. *Journal of Geophysical Research*, **75**(34), 7018–7031.

Aubry, M. P., Kivelson, M. G., & Russell, C. T. 1971. Motion and structure of the magnetopause. *Journal of Geophysical Research*, **76**(7), 1673–1696.

Axford, W. I., & Hines, C. O. 1961. A unifying theory of high-latitude geophysical phenomena and geomagnetic storms. *Canadian Journal of Physics*, **39**(10), 1433–1464.

Baumjohann, W., & Treumann, R. A. 1997. *Basic Space Plasma Physics*. London: Imperial College Press.

Beer, J., Tobias, S. M., & Weiss, N.O. 2017. On long-term modulation of the Sun's magnetic cycle. *Monthly Notices of the Royal Astronomical Society*, **1602**, 1596–1602.

Berchem, J., & Russell, C. T. 1982. The thickness of the magnetopause current layer - ISEE 1 and 2 observations. *Journal of Geophysical Research*, **87**(A4), 2108–2114.

Boakes, P. D., Milan, S. E., Abel, G. A., Freeman, M. P., Chisham, G., & Hubert, B. 2009. A statistical study of the open magnetic flux content of the magnetosphere at the time of substorm onset. *Geophysical Research Letters*, **36**(4), 3–7.

Boardsen, S. A., Eastman, T. E., Sotirelis, T., & Green, J. L. 2000. An empirical model of the high-latitude magnetopause. *Journal of Geophysical Research: Space Physics*, **105**(A10), 23193–23219.

Borovsky, J. E. 2008. The rudiments of a theory of solar wind/magnetosphere coupling derived from first principles. *Journal of Geophysical Research: Space Physics*, **113**(8), 1–14.

Burch, J. L. 2000. IMAGE mission overview. *Space Sci. Rev.*, **91**(c), 1–14.

Caan, M. N., McPherron, R. L., & Russell, C. T. 1977. Characteristics of the Association Between the Interplanetary Magnetic Field and Substorms. *Journal of Geophysical Research*, **82**(29), 4837–4842.

Case, N. A., & Wild, J. A. 2013. The location of the Earth's magnetopause: A comparison of modeled position and in situ Cluster data. *Journal of Geophysical Research: Space Physics*, **118**(October), 6127–6135.

Chandrasekhar, S. 1961. *Hydrodynamic and hydromagnetic stability*. International Series of Monographs on Physics, Oxford: Clarendon, 1961.

Chao, J. K., Wu, D. J., Lin, C. H., Yang, Y. H., Wang, X. Y., Kessel, M., Chen, S. H., & Lepping, R. P. 2002. Models for the size and shape of the earth's magnetopause and bow shock. *COSPAR Colloquia Series*, **12**, 127–135.

Chapman, S. 1962. Earth storms: Retrospect and Prospect. *Journal of the Physical Society of Japan Supplement*, **17**, 6.

Chapman, S., & Bartels, J. 1940. *Geomagnetism, Vol. 1.* Clarendon Press.

Chapman, S., & Ferraro, V. C. A. 1931. A new theory of magnetic storms. *Journal of Geophysical Research*, **36**, 77–97.

Chisham, G., & Pinnock, M. 2002. Assessing the contamination of SuperDARN global convection maps by non-F-region backscatter. *Annales Geophysicae*, **20**(1), 13–28.

Chisham, G., Lester, M., Milan, S. E., Freeman, M. P., Bristow, W. A., Grocott, A., McWilliams, K. A., Ruohoniemi, J. M., Yeoman, T. K., Dyson, P. L., Greenwald, R. A., Kikuchi, T., Pinnock, M., Rash, J. P.S., Sato, N., Sofko, G. J., Villain, J. P., & Walker, A. D.M. 2007. A decade of the Super Dual Auroral Radar Network (SuperDARN): Scientific achievements, new techniques and future directions. *Surveys in Geophysics*, **28**(1), 33–109.

Clausen, L. B. N., Baker, J. B. H., Ruohoniemi, J. M., Milan, S. E., & Anderson, B. J. 2012. Dynamics of the region 1 Birkeland current oval derived from the active magnetosphere and planetary electrodynamics response experiment (AMPERE). *Journal of Geophysical Research: Space Physics*, **117**(6), 1–11.

Clausen, L. B.N., H. Baker, J. B., Ruohoniemi, J. M., Milan, S. E., Coxon, J. C., Wing, S., Ohtani, S., & Anderson, B. J. 2013. Temporal and spatial dynamics of the regions 1 and 2 Birkeland currents during substorms. *Journal of Geophysical Research: Space Physics*, **118**(6), 3007–3016.

Cliver, E. W., Boriakoff, V., & Bounar, K. H. 1998. Geomagnetic activity and the solar wind during the Maunder Minimum. *Geophysical Research Letters*, **25**(6), 897–900.

Coroniti, F. V., & Kennel, C. F. 1973. Can the ionosphere regulate magnetospheric convection? *Journal of Geophysical Research*, 7**8**(16), 2837–2851.

Cowley, S. W. H. 1982. The causes of convection in the Earth's magnetosphere: A review of developments during the IMS. *Reviews of Geophysics*, **20**(3), 531–565.

Cowley, S. W. H., & Lockwood, M. 1992. *Excitation and decay of solar wind-driven flows in the magnetosphere-ionophere system*.

Daglis, I., Thorne, M., Baumjohann, W., & Orsini, S. 1999. The terrestrial ring current: origin, formation and decay. *Reviews of Geophysics*, **37**(4), 407–438.

Daglis, I. A., & Kozyra, J. U. 2002. Outstanding issues of ring current dynamics. *Journal of Atmospheric and Solar-Terrestrial Physics*, **64**(2), 253–264.

Dmitriev, A, & Suvorova, A. V. 2000. Three-dimensional artificial neural network model of the dayside magnetopause. *Journal of Geophysical Research*, **105**(A8), 18909–18918.

Dmitriev, A., Suvorova, A., & Chao, J. K. 2011. A predictive model of geosynchronous magnetopause crossings. *Journal of Geophysical Research: Space Physics*, **116**(A05208), 1–13.

Dungey, J. W. 1961. Interplanetary magnetic field and the auroral zones. *Physical Review Letters*, **6**(2), 6–7.

Dungey, J. W. 1963. Interactions of solar plasma with the geomagnetic field. *Planetary and Space Science*, **10**, 233–237.

Dušik, Š., Granko, G., Šafránková, J., Němeček, Z., & Jelínek, K. 2010. IMF cone angle control of the magnetopause location: Statistical study. *Geophysical Research Letters*, **3**7(19), 2–5.

Eastman, T. E, Boardsen, S. A, Chen, S.-H., Fung, S. F., & Kessel, R. L. 2000. Configuration of high-latitude and high-altitude boundary layers. *Journal of Geophysical Research*, **105**, 23221–23238.

Eastwood, J. P., Biffis, E., Hapgood, M. A., Green, L., Bisi, M. M., Bentley, R. D., Wicks, R., McKinnell, L. A., Gibbs, M., & Burnett, C. 2017. The Economic Impact of Space Weather: Where Do We Stand? *Risk Analysis*, **3**7(2), 206–218.

Eddy, J.A. 1976. The Maunder Minimum. *Science*, **192**(4245), 1189–1202.

Elsen, R. K., & Winglee, R. M. 1997. The average shape of the Magnetopause: A comparison of three-dimensional global MHD and empirical models. *Journal of Geophysical Research*, **102**(A3), 4799.

Evans, L. C., & Stone, E. C. 1972. Electron polar cap and the boundary of open geomagnetic field lines. *Journal of Geophysical Research*, 77(28), 5580–5584.

Fairfield, D. H. 1971. Average and Unusual Locations of the Earth's Magnetopause and Bow Shock. *J. Geophys. Res.*, 7**6**(28), 6700–6716.

Fairfield, D. H. 1979. On the average configuration of the geomagnetic tail. *Journal of Geophysical Research*, **84**(A5), 1950–1958.

Fairfield, D. H. 1991. Solar wind control of the size and shape of the magnetosphere. *J. Geomagn. Geoelectr.*, **43**(Suppl.), 117–127.

Fairfield, D. H. 1995. *Observations of the shape and location of the magnetopause: A review*. American Geophysical Union. Pages 53–60.

Fairfield, D. H., Otto, a., Mukai, T., Kokubun, S., Lepping, R. P., Steinberg, J. T., Lazarus, a. J., & Yamamoto, T. 2000. Geotail observations of the Kelvin-Helmholtz instability at the equatorial magnetotail boundary for parallel northward fields. *Journal of Geophysical Research*, **105**(A9), 21159.

Farris, M. H., & Russell, C. T. 1994. Determining the standoff distance of the bow shock: Mach number dependence and use of models. *Journal of Geophysical Research*, **99**(A9), 681–689.

Freeman, M. P., & Southwood, D. J. 1988. The effect of magnetospheric erosion on mid- and high-latitude ionospheric flows. *Planetary and Space Science*, **36**(5), 509–522.

Gonzalez, W. D., Tsurutani, B. T., Gonzalez, Alicia L. C., & Smith, J. 1989. Solar wind-magnetosphere coupling during intense magnetic storms (1978-1979). *Journal of Geophysical Research*, **94**(A7), 8835–8851.

Gonzalez, W. D., Joselyn, J. a., Kamide, Y., Kroehl, H. W., Rostoker, G., Tsurutani, B. T., & Vasyliunas, V. M. 1994. What is a geomagnetic storm? *Journal of Geophysical Research*, **99**(A4), 5771–5792.

Gonzalez, W. D., Tsurutani, B. T., & Clúa de Gonzalez, A. L. 1999. Interplanetary origin of geomagnetic storms. *Space Science Reviews*, **88**(3/4), 529–562.

Gonzalez, W. D., Echer, E., Clua-Gonzales, A. L., & Tsurutani, B. T. 2007. Interplanetary origin of intense geomagnetic storms (Dst < - 100 nT) during solar cycle 23. *Geophysical Research Letters*, **34**(6), 2–5.

Gordeev, E. I., Sergeev, V. A., Pulkkinen, T. I., & Palmroth, M. 2011. Contribution of magnetotail reconnection to the cross-polar cap electric potential drop. *Journal of Geophysical Research: Space Physics*, **116**(8), 1–10.

Gosling, J. T., Asbridge, J. R., Bame, S. J., & Feldman, W. C. 1976. Solar wind speed variations: 1962-1974. *Journal of Geophysical Research*, **81**(28), 5061–5070.

Gosling, J. T., Bame, S. J., McComas, D. J., & Phillips, J. L. 1990. Coronal mass ejections and large geomagnetic storms. *Geophysical Research Letters*, **17**(7), 901–904.

Gosling, J. T., McComas, D. J., Phillips, J. L., & Bame, S. J. 1991. Geomagnetic activity associated with Earth passage of interplanetary shock disturbances and coronal mass ejections. *Journal of Geophysical Research*, **96**(A5), 7831–7839.

Greenwald, R. A., Baker, K. B., Dudeney, J. R., Pinnock, M., Jones, T. B., Thomas, E. C., Villain, J.-P., Cerisier, J.-C, Senior, C., Hanuise, C., Hunsucker, R. D., Sofko, G. J., Koehler, J., Nielsen, E., Pellinen, R., Walker, A. D.M., Sato, N., & Yamagishi, H. 1995. DARN/SuperDARN. A global view of the dynamics of high-latitude convection. *Space Sci. Rev.*, **71**, 761–796.

Grocott, A., Milan, S. E., Imber, S. M., Lester, M., & Yeoman, T. K. 2012. A quantitative deconstruction of the morphology of high-latitude ionospheric convection. *Journal of Geophysical Research: Space Physics*, **117**(5), 1–16.

Grzedzielski, S, & Lazarus, A J. 1993. 2- to 3-kHz continuum emissions as possible indications of global heliospheric "breathing". *Journal of Geophysical Research*, **98**(A4), 5551–5558.

Haaland, S., Reistad, J, Tenfjord, P, Gjerloev, J, Maes, L, Dekeyser, J, Maggiolo, R, Anekallu, C, & Dorville, N. 2014. Characteristics of the flank magnetopause: Cluster observations. *Journal of Geophysical Research: Space Physics*, **119**, 9019–9037.

Hale, G. E., Ellerman, F., Nicholson, S. B., & Joy, A. H. 1919. The Magnetic polarity of sunspots. *American Astronomical Society*, **49**(26), 153–185.

Hardy, D. A., Schmitt, L. K., Gussenhoven, M. S., Marshall, F. J., & Yeh, H. C. 1984. *Precipitating electron and ion detectors (SSJ/4) for the block 5D/flights 6 – 10 DMSP satellites: Calibration and data presentation*. Tech. rept. Air Force Geophysics Laboratory.

Hasegawa, H. 2012. Structure and Dynamics of the Magnetopause and Its Boundary Layers. *Monographs on Environment, Earth and Planets*, **1**(2), 71–119.

Hasegawa, H., Fujimoto, M., Phan, T.-D., Rème, H., Balogh, A., Dunlop, M. W., Hashimoto, C., & Tandokoro, R. 2004. Transport of solar wind into Earth's magnetosphere through rolled-up Kelvin-Helmholtz vortices. *Nature*, **430**, 755–758.

Hathaway, D. H. 2015. The Solar Cycle. *Living Reviews in Solar Physics*, **12**(1), 4.

Heppner, J. P. 1977. Empirical models of high-latitude electric fields. *Journal of Geophysical Research*, **82**(7), 1115–1125.

Heppner, J. P., & Maynard, N. C. 1987. Empirical high-latitude electric field models. *Journal of Geophysical Research*, **92**(A5), 4467–4489.

Holzer, R. E., & Slavin, J. A. 1978. Magnetic flux transfer associated with expansions and contractions of the dayside magnetosphere. *Journal of Geophysical Research*, **83**(A8), 3831–3839.

Hospodarsky, G. B. 2016. Spaced-based search coil magnetometers. *Journal of Geophysical Research: Space Physics*, **121**(12), 12,068–12,079.

Hubert, B., Milan, S. E., Grocott, A., Blockx, C., Cowley, S. W.H., & Gérard, J. C. 2006. Dayside and nightside reconnection rates inferred from IMAGE FUV and Super Dual Auroral Radar Network data. *Journal of Geophysical Research: Space Physics*, **111**(3), 1–16.

Hughes, W. J. 1995. The magnetopause, magnetotail, and magnetic reconnection. *Chap. 9, pages 227–287 of:* Kivelson, Margaret G, & Russell, Christopher T (eds), *Introduction to Space Physics*. Cambridge University Press.

Hunt, G. 2016. Analyses of field-aligned currents in Saturn's nightside magnetosphere.

Hutchinson, J. A., Wright, D. M., & Milan, S. E. 2011. Geomagnetic storms over the last solar cycle: A superposed epoch analysis. *Journal of Geophysical Research: Space Physics*, **116**(9), 1–16.

Iijima, T., & Potemra, T. A. 1978. Large-scale characteristics of field-aligned currents associated with substorms. *Journal of Geophysical Research*, **83**(A2), 599.

Imber, S. M., Milan, S. E., & Lester, M. 2013a. Solar cycle variations in polar cap area measured by the superDARN radars. *Journal of Geophysical Research: Space Physics*, **118**(10), 6188–6196.

Imber, S. M., Milan, S. E., & Lester, M. 2013b. The Heppner-Maynard Boundary measured by SuperDARN as a proxy for the latitude of the auroral oval. *Journal of Geophysical Research: Space Physics*, **118**(2), 685–697.

Ivchenko, N. V., Sibeck, D. G., Takahashi, K., & Kokubun, S. 2000. A statistical study of the magnetosphere boundary crossing by the Geotail satellite. *Geophysical Research Letters*, **27**(18), 2881–2884.

Iyemori, T. 1990. Storm-time magnetospheric currents inferred from mid-latitude geomagnetic field variations. *Journal of geomagnetism and geoelectricity*, **42**(11), 1249–1265.

Iyemori, T., Takeda, M., Nose, M., Odagi, Y., & Toh, H. 2010. Mid-latitude Geomagnetic Indices "ASY" and "SYM" for 2009 (Provisional). **200**(3).

Javaraiah, J. 2017. Will solar cycles 25 and 26 be weaker than cycle 24? *Solar Physics*, **292**(11), 172.

Kalegaev, V. V., & Lyutov, Y. G. 2000. The solar wind control of the magnetopause. *Advances in Space Research*, **25**(7/8), 1489–1492.

Kamide, Y. 1992. Is substorm occurrence a necessary condition for a magnetic storm? *J. Geomag. Geoelectr.*, **44**, 109–117.

Kamide, Y., Baumjohann, W., Daglis, I. a., Gonzalez, W. D., Grande, M., Joselyn, J. a., McPherron, R. L., Phillips, J. L., Reeves, E. G. D., Rostoker, G., Sharma, a. S., Singer, H. J., Tsurutani, B. T., & Vasyliunas, V. M. 1998. Current understanding of magnetic storms: Storm-substorm relationships. *Journal of Geophysical Research: Space Physics*, **103**(A8), 17705–17728.

Kan, J. R., & Lee, L. C. 1979. Energy coupling function and solar wind-magnetosphere dynamo. *Geophys. Res. Lett.*, **6**(7).

Kawano, H., Petrinec, S. M., Russell, C. T., & Higuchi, T. 1999. Magnetopause shape determinations from measured position and estimated flaring angle. *J. Geophys. Res.*, **104**(A1), 247–261.

Kilpua, E. K. J., Hietala, H., Turner, D. L., Koskinen, H. E. J., Pulkkinen, T. I., Rodriguez, J. V., Reeves, G. D., Claudepierre, S. G., & Spence, H. E. 2015. Unraveling the drivers of the storm-time radiation belt response. *Geophysical Research Letters*, n/a–n/a.

Kivelson, M. G., & Chen, S.-H. 1995. The magnetopause: surface waves and instabilities and their possible dynamical consequences. *Pages 257–268 of:* Song, P., Sonnerup, B. U Ö, & Thomsen, M. F. (eds), *Physics of the Magnetopause*, geophysica edn. Washington, DC: American Geophysical Union.

Kokubun, S., Yamamoto, T., Acuña, M. H., Hayashi, K., Shiokawa, K., & Kawano, H. 1994. *The Geotail magnetic field experiment*.

Kozyra, J., Fok, M., Sanchez, E. R., Evans, D. S., Hamilton, D. C., & Nagy, A. F. 1998. The role of precipitation losses in producing the rapid early recovery phase of the Great Magnetic Storm of February 1986. *Journal of Geophysical Research*, **103**(97), 6801.

Kuznetsov, S. N., & Suvorova, A. V. 1996. Solar wind control of the magnetopause shape and location. *Radiation Measurements*, **26**(3), 413–415.

Kuznetsov, S. N., & Suvorova, A.V. 1998. Solar wind magnetic field and pressure during magnetopause crossings at geosynchronous orbit. *Advances in Space Research*, **22**(1), 63–66.

Lin, R. L., Zhang, X. X., Liu, S. Q., Wang, Y. L., & Gong, J. C. 2010. A three-dimensional asymmetric magnetopause model. *Journal of Geophysical Research*, **115**, 1–12.

Lockwood, M. 1991. On flow reversal boundaries and transpolar voltage in average models of high-latitude convection. *Planetary and Space Science*, **39**(3), 397–409.

Lockwood, M., & Cowley, S. W. H. 1992. Ionospheric convection and the substorm cycle. *Proceedings of the International Conference on Substorms (ICS-1)*, **1**, 99–109.

Lockwood, M., & Fröhlich, C. 2007. Recent oppositely directed trends in solar climate forcings and the global mean surface air temperature. *Proceedings of the Royal Society A: Mathematical, Physical and Engineering Sciences*, **463**(2086), 2447–2460.

Lockwood, M., & Owens, M. J. 2014. Implications of the recent low solar minimum for the solar wind during the Maunder Minimum. *Astrophysical Journal Letters*, 7**81**(L7), 1–5.

Lockwood, M., Owens, M., & Rouillard, A. P. 2009a. Excess open solar magnetic flux from satellite data: 1. Analysis of the third perihelion Ulysses pass. *Journal of Geophysical Research: Space Physics*, **114**(11), 1–9.

Lockwood, M., Rouillard, A. P., & Finch, I. D. 2009b. The rise and fall of open solar flux during the current grand solar maximum. *Astrophysical Journal*, 7**00**(2), 937–944.

Lockwood, M., Hairston, M., Finch, I., & Rouillard, A. 2009c. Transpolar voltage and polar cap flux during the substorm cycle and steady convection events. *Journal of Geophysical Research: Space Physics*, **114**(1), 1–19.

Longden, N., Chisham, G., Freeman, M. P., Abel, G. A., & Sotirelis, T. 2010. Estimating the location of the open-closed magnetic field line boundary from auroral images. *Annales Geophysicae*, **28**(9), 1659–1678.

Maezawa, K. 1974. Dependence of the magnetopause position on the southward interplanetary magnetic field. *Planetary and Space Science*, **22**(10), 1443–1453.

McComas, D. J., Ebert, R. W., Elliott, H. A., Goldstein, B. E., Gosling, J. T., Schwadron, N. A., & Skoug, R. M. 2008. Weaker solar wind from the polar coronal holes and the whole Sun. *Geophysical Research Letters*, **35**(18), 1–5.

Mead, G. D., & Beard, D. B. 1964. Shape of the geomagnetic field solar wind boundary. *Journal of Geophysical Research*, **69**(7), 1169–1179.

Mende, S. B., Heetderks, H., Frey, H. U., Lampton, M., Geller, S. P., Stock, J. M., Abiad, R., Siegmund, O. H. W., Tremsin, a. S., & Habraken, S. 2000a. Far Ultraviolet imaging from the IMAGE spacecraft. 1. System design. *Space Science Reviews*, **91**, 243–270.

Mende, S. B., Heetderks, H., Frey, H. U., Lampton, M., Geller, S. P., Abiad, R., Siegmund, O. H. W., Tremsin, A. S., Spann, J., Dougani, H., Fuselier, S. A., Magoncelli, A. L., Bumala, M. B., Murphree, S., & Trondsen, T. 2000b. Far Ultraviolet imaging from the IMAGE spacecraft. 2. Wideband FUV imaging. *Space Science Reviews*, **91**, 271–285.

Mende, S. B., Heetderks, H., Frey, H. U., Stock, J. M., Lampton, M., Geller, S. P. P., Abiad, R., Siegmund, O. H. W., Habraken, S., Renotte, E., Jamar, C., Rochus, P., Gerard, J.-C., Sigler, R., & Lauche, H. 2000c. Far ultraviolet imaging from the IMAGE spacecraft. 3. Spectral imaging of Lyman alpha and OI 135.6 nm. *Space Science Reviews*, **91**, 287–318.

Meng, C.-I., & Makita, K. 1986. Dynamic variations of the polar cap. *Pages 605–631 of:* Kamide, Y., & Slavin, James A. (eds), *Solar Wind Magnetosphere Coupling*. Terra Scientific.

Milan, S. E. 2009. Both solar wind-magnetosphere coupling and ring current intensity control of the size of the auroral oval. *Geophysical Research Letters*, **36**(18), 2–5.

Milan, S. E. 2015. Sun et Lumiere: Solar wind-magnetosphere coupling as deduced from ionospheric flows and polar auroras. *Chap. 2, pages 33–64 of:* Cowley, S. W.H., Southwood, D. J., & Mitton, Simon (eds), *Magnetospheric Plasma Physics: The Impact of Jim Dungey's Research*. Springer International Publishing.

Milan, S. E., Lester, M., Cowley, S. W. H., Oksavik, K., Brittnacher, M., Greenwald, R. A., Sofko, G. J., & Villain, J.-P. 2003. Variations in the polar cap area during two substorm cycles. *Annales Geophysicae*, **21**, 1121–1140.

Milan, S. E., Cowley, S. W H, Lester, M., Wright, D. M., Slavin, J. a., Fillingim, M., Carlson, C. W., & Singer, H. J. 2004. Response of the magnetotail to changes in the open flux content of the magnetosphere. *Journal of Geophysical Research*, **109**(A04220), 1–16.

Milan, S. E., Wild, J. A., Hubert, B., Carr, C .M., Lucek, E. A., Bosqued, J. M., Watermann, J. F., & Slavin, J. A. 2006. Flux closure during a substorm observed by Cluster, Double Star, IMAGE FUV, SuperDARN, and Greenland magnetometers. *Annales Geophysicae*, **24**, 751–767.

Milan, S. E., Provan, G., & Hubert, B. 2007. Magnetic flux transport in the Dungey cycle: A

survey of dayside and nightside reconnection rates. *Journal of Geophysical Research: Space Physics*, **112**, 1–13.

Milan, S. E., Boakes, P. D., & Hubert, B. 2008. Response of the expanding/contracting polar cap to weak and strong solar wind driving: Implications for substorm onset. *Journal of Geophysical Research: Space Physics*, **113**(A9), n/a–n/a.

Milan, S. E., Grocott, A., Forsyth, C., Imber, S. M., Boakes, P. D., & Hubert, B. 2009a. A superposed epoch analysis of auroral evolution during substorm growth, onset and recovery: open magnetic flux control of substorm intensity. *Annales Geophysicae*, **27**(2), 659–668.

Milan, S. E., Hutchinson, J., Boakes, P. D., & Hubert, B. 2009b. Influences on the radius of the auroral oval. *Annales Geophysicae*, **27**(7), 2913–2924.

Milan, S. E., Gosling, J. S., & Hubert, B. 2012. Relationship between interplanetary parameters and the magnetopause reconnection rate quantified from observations of the expanding polar cap. *Journal of Geophysical Research: Space Physics*, **117**, 1–16.

Milan, S. E., Clausen, L. B.N., Coxon, J. C., Carter, J. A., Walach, M. T., Laundal, K., Østgaard, N., Tenfjord, P., Reistad, J., Snekvik, K., Korth, H., & Anderson, B. J. 2017. Overview of Solar Wind–Magnetosphere–Ionosphere–Atmosphere Coupling and the Generation of Magnetospheric Currents. *Space Science Reviews*, **206**(1-4), 547–573.

Moldwin, M. B. 2008. *An Introduction to Space Weather*. Cambridge University Press.

Mukai, T., Machida, S, Saito, Y., Terasawa, T, Kaya, N., Obara, T., Ejiri, M., & Nishida, A. 1994. The Low Energy Particle (LEP) experiment onboard the GEOTAIL satellite. *J. Geomagn. Geoelectr.*, **46**, 669–692.

Neugebauer, M. 1975. Large-scale and solar cycle variations of the solar wind. *Space Science Reviews*, **17**, 221–254.

Newell, P. T., Wing, S., Meng, C.-I., & Sigillito, V. 1991. The auroral oval position, structure, and intensity of precipitation from 1984 onward: An automated on-line data base. *Journal of Geophysical Research*, **96**(A4), 5877.

Newell, P. T., Sotirelis, T., Liou, K., Meng, C. I., & Rich, F. J. 2007. A nearly universal solar wind-magnetosphere coupling function inferred from 10 magnetospheric state variables. *Journal of Geophysical Research: Space Physics*, **112**(1), 1–16.

Nishida, A. 1994. The Geotail Mission. *Geophysical Research Letters*, **21**(25), 2871–2873.

Nishino, M. N., Hasegawa, H., Fujimoto, M., Saito, Y., Mukai, T., Dandouras, I., Rème, H., Retinò, A., Nakamura, R., Lucek, E., & Schwartz, S. J. 2011. A case study of Kelvin-Helmholtz vortices on both flanks of the Earth's magnetotail. *Planetary and Space Science*, **59**(7), 502–509.

Østgaard, N., Mende, S. B., Frey, H. U., Sigwarth, J. B., Åsnes, A., & Weygand, J. M. 2007. Auroral conjugacy studies based on global imaging. *Journal of Atmospheric and Solar-Terrestrial Physics*, **69**(3), 249–255.

Owens, M. J., & Forsyth, R. J. 2013. The Heliospheric Magnetic Field Imprint / Terms of Use. *Living Reviews in Solar Physics*.

Owens, M. J., Lockwood, M., Barnard, L., & Davis, C. J. 2011. Solar cycle 24: Implications for energetic particles and long-term space climate change. *Geophysical Research Letters*, **38**(19), n/a–n/a.

Parker, E. N. 1958. Dynamics of the interplanetary gas and magnetic fields. *Astrophysical Journal*, 664–676.

Peredo, M., Slavin, J. A., Mazur, E., & Curtis, S. A. 1995. Three-dimensional position and shape of the bow shock and their variation with Alfvénic, sonic and magnetosonic Mach numbers and interplanetary magnetic field orientation. *Journal of Geophysical Research*, **100**(A5), 7907.

Perreault, P., & Akasofu, S.-I. 1978. A study of geomagnetic storms. *geophys. J. R. astr. Soc.*, **54**, 547–573.

Petrinec, S. M., & Russell, C. T. 1993. An empirical model of the size and shape of the near-Earth magnetotail. *Geophys. Res. Lett.*, **20**(23), 2695–2698.

Petrinec, S. M., & Russell, C. T. 1995. An examination of the effect of dipole tilt angle and cusp regions on the shape of the dayside magnetopause. *Journal of Geophysical Research*, **100**(A6), 9559–9566.

Petrinec, S. M., & Russell, C. T. 1996. Near-Earth magnetotail shape and size as determined from the magnetopause flaring angle. *Journal of Geophysical Research*, **101**(A1), 137–152.

Petrinec, S. P., Song, P., & Russell, C. T. 1991. Solar cycle variations in the size and shape of the magnetopause. *Journal of Geophysical Research*, **96**(A5), 7893.

Reeves, G. D. 2003. Acceleration and loss of relativistic electrons during geomagnetic storms. *Geophysical Research Letters*, **30**(10), 1–4.

Richardson, J. D., Belcher, J. W., Lazarus, A. J., Paularena, K. I., & Gazis, P. R. 1996. Statistical properties of the solar wind. *Pages 483–486 of: AIP Conference Proceedings*, vol. 382. AIP.

Roelof, E. C., & Sibeck, D. G. 1993. Magnetopause shape as a bivariate function of interplanetary magnetic field Bz and solar wind dynamic pressure. *J. Geophys. Res.*, **99**(93), 8787–8788.

Ruohoniemi, J. M., & Baker, K. B. 1998. Large-scale imaging of high-latitude convection with Super Dual Auroral Radar Network HF radar observations. *Journal of Geophysical Research*, **103**(A9), 20797.

Ruohoniemi, J. M., & Greenwald, R. A. 1996. Statistical patterns of high-latitude convection obtained from Goose Bay HF radar observations. *Journal of Geophysical Research*, **101**(A10), 21743.

Russell, C. T. 1972. Configuration of the magnetosphere. *Critical Problems of Magnetospheric Physics, Proceedings of the Symposium held 11-13 May, 1972 in Madrid, Spain*, **1**.

Šafránková, J., Dušík, Š, & Němeček, Z. 2004. The shape and location of the high-latitude magnetopause. *Advances in Space Research*, **36**(10), 1934–1939.

Sandhu, J. K., Yeoman, T. K., Fear, R. C., & Dandouras, I. 2016. *A statistical study of magnetospheric electron density using the Cluster spacecraft*.

Schield, M. A. 1969. Pressure balance between solar wind and magnetosphere. *Journal of Geophysical Research: Space Physics*, **74**(5), 1275–1286.

Scholer, M., & Treumann, R. A. 1997. *The low-latitude boundary layer at the flanks of the magnetopause*.

Schwabe, H. 1844. Sonnen-Beobachtungen im Jahre 1843. *Astron. Nachr.*, **21**(495), 233–236.

Scurry, L., & Russell, C. T. 1991. Proxy studies of energy transfer to the magnetosphere. *Journal of Geophysical Research*, **96**(A6), 9541.

Shepherd, S. G., & Ruohoniemi, J. M. 2000. Electrostatic potential patterns in the high-latitude ionosphere constrained by SuperDARN measurements. *Journal of Geophysical Research: Space Physics*, **105**(A10), 23005–23014.

Shue, J.-H., Chao, J. K., Fu, H. C., Russell, C. T., Song, P., Khurana, K. K., & Singer, H. J. 1997. A new functional form to study the solar wind control of the magnetopause size and shape. *Journal of Geophysical Research*, **102**(1), 9497.

Shue, J.-H., Song, P., Russell, C. T., Steinberg, J. T., Chao, J. K., Zastenker, G., Vaisberg, O. L., Kokubun, S., Singer, H. J., Detman, T. R., & Kawano, H. 1998. Magnetopause location under extreme solar wind conditions. *Journal of Geophysical Research*, **103**, 17691.

Shukhtina, M. A., & Gordeev, E. 2015. In situ magnetotail magnetic flux calculation. *Ann. Geophys*, **33**, 769–781.

Shukhtina, M. A., & Milan, S. E. 2014. *ECLAT system level data products report (D430.1)*. Tech. rept. ECLAT.

Sibeck, D. G. 1990. A model for the transient magnetospheric response to sudden solar wind dynamic pressure variations. *Journal of Geophysical Research*, **95**(A4), 3755–3771.

Sibeck, D. G., Lopez, R. E., & Roelof, Edmond C. 1991. Solar wind control of the magnetopause shape, location, and motion. *Journal of Geophysical Research*, **96**(A4), 5489–5495.

Sibeck, D. G., Kudela, K., Lepping, R. P., Lin, R., Nemecek, Z., & Nozdrachev, M. N. 2000. Magnetopause motion driven by interplanetary magnetic field variations. *Journal of Geophysical Research*, **105**(A11), 25155–25169.

SILSO World Data Center. 2016. - Sunspot number and long-term solar observations. *Royal Observatory of Belgium, on-line sunspot number catalogue: http://www.sidc.be/SILSO/*, **1995-2016**.

Siscoe, G. L., & Huang, T. S. 1985. Polar Cap Inflation and Deflation. *Journal of Geophysical Research*, **90**(A1), 543–547.

Siscoe, G. L., Crooker, N. U., & Siebert, K. D. 2002. Transpolar potential saturation: Roles of region 1 current system and solar wind ram pressure. *Journal of Geophysical Research: Space Physics*, **107**(A10), 1–9.

Slavin, J. A., & Holzer, R. E. 1981. Solar Wind Flow About the Terrestrial Planets, 1. Modeling Bow Shock Position and Shape. *J. Geophys. Res.*, **86**(A13), 11401–11418.

Smith, E. J., & Wolfe, J. H. 1976. Observations of interaction regions and corotating shocks between one and five AU: Pioneers 10 and 11. *Geophys. Res. Lett.*, **3**(3), 137–140.

Song, P., & Russell, C. T. 1992. Model of the Formation of the Low-Latitude Boundary Layer for Strongly Northward Interplanetary Magnetic Field. *Journal of Geophysical Research*, **97**(A2), 1411–1420.

Sonnerup, B. U. Ö. 1980. Theory of the Low-Latitude Boundary Layer. *J. Geophys. Res.*, **85**(A5), 2017–2026.

Sotirelis, T., & Meng, C.-I. 1999. Magnetopause from pressure balance. *Journal of Geophysical Research*, **104**(A4), 6889.

Störmer, C. 1907. Sur les trajectories des corpuscles electrises dans l'espace sous l'action du magnetisme terrestre avec application aux aurores boreales. *Arch. Sci. Phys. Nat.*, **24**, 317–364.

Taylor, J. R., Lester, M., & Yeoman, T. K. 1994. A superposed epoch analysis of geomagnetic storms. *Annales Geophysicae*, **12**(7), 612–624.

Taylor, J. R., Yeoman, T. K., Lester, M., Emery, B. A., & Knipp, D. J. 1996. Variations in the polar cap area during intervals of substorm activity on 20-21 March 1990 deduced from AMIE convection patterns. *Annales Geophysicae*, **14**(9), 879–887.

Tsurutani, B. T., Gonzalez, W. D., Tang, F., & Lee, Y. T. 1992. Great magnetic storms. *Geophysical Research Letters*, **19**(1), 73–76.

Tsurutani, B. T., Gonzalez, W. D., Gonzalez, A. L. C., Tang, F., Arballo, J. K., & Okada, M. 1995. Interplanetary origin of geomagnetic activity in the declining phase of the solar cycle. *Journal of Geophysical Research: Space Physics*, **100**(A11), 21717–21733.

Usoskin, I. G. 2017. A History of solar activity over millennia. *Living Reviews in Solar Physics*, **5**(1), 1–88.

Usoskin, I. G., Mursula, K., & Kovaltsov, G. A. 2001. Heliospheric modulation of cosmic rays and solar activity during the Maunder minimum. *Journal of Geophysical Research*, **106**(A8), 16039–16046.

Usoskin, I. G., Arlt, R., Asvestari, E., Hawkins, E., Kapylä, M. J., Kovaltsov, G. A., Krivova, N., Lockwood, M., Mursula, K., O'Reilly, J., Owens, M. J., Scott, C. J., Sokoloff, D. D., Solanki, S. K., Soon, W., Vaquero, J. M., & O'Reilly, J. 2015. The Maunder minimum (1645-1715) was indeed a grand minimum: A reassessment of multiple datasets. *Astronomy and Astrophysics*, **581**, A95.

Vasyliunas, V. M., Kan, J. R., Siscoe, G. L., & Akasofu, S. I. 1982. Scaling relations governing magnetospheric energy transfer. *Planetary and Space Science*, **30**(4), 359–365.

Verigin, M. I., Kotova, G. A., Bezrukikh, V. V., Zastenker, G. N., & Nikolaeva, N. 2009. Analytical model of the near-Earth magnetopause according to the data of the Prognoz and Interball satellite data. *Geomagnetism and Aeronomy*, **49**(8), 1176–1181.

Wang, Y. M., Robbrecht, E., & Sheeley, N. R. 2009. On the weakening of the polar magnetic fields during solar cycle 23. *Astrophysical Journal*, 7**07**(2), 1372–1386.

Wanliss, J. A., & Showalter, K. M. 2006. High-resolution global storm index: Dst versus SYM-H. *Journal of Geophysical Research: Space Physics*, **111**(2), 1–10.

Webb, D. F., & Howard, R. A. 1994. The solar cycle variation of coronal mass ejections and the solar wind mass flux. *Journal of Geophysical Research*, **99**, 4201–4220.

Webb, D. F., & Howard, T. A. 2012. Coronal mass ejections: Observations. *Living Reviews in Solar Physics*, **9**(3).

Winningham, J. D., & Heikkila, W. J. 1974. Polar cap auroral electron fluxes observed with Isis 1. *Journal of Geophysical Research*, **79**(7), 949–957.

Wolf, R. 1861. "Abstract of his latest Results". *Mon. Not. R. Astron. Soc.*, **21**, 77–78.

Yokoyama, N., & Kamide, Y. 1997. Statistical nature of geomagnetic storms. *Journal of Geophysical Research: Space Physics (1978–2012)*, **102**(A7), 14215–14222.

Zhang, J., Liemohn, M. W., Kozyra, J. U., Thomsen, M. F., Elliott, H. A., & Weygand, J. M. 2006. A statistical comparison of solar wind sources of moderate and intense geomagnetic storms at solar minimum and maximum. *Journal of Geophysical Research: Space Physics*, **111**(1), 1–13.

Zmuda, A. J., Armstrong, J. C., & Heuring, F. T. 1970. Characteristics of transverse magnetic disturbances observed at 1100 kilometers in the auroral oval. *Journal of Geophysical Research*, **75**(25), 4757–4762.